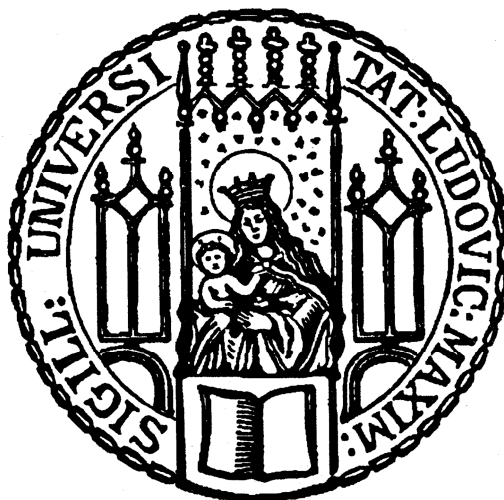


DISSERTATION ZUR ERLANGUNG DES DOKTORGRADES
DER FAKULTÄT FÜR CHEMIE UND PHARMAZIE
DER LUDWIG-MAXIMILIANS-UNIVERSITÄT MÜNCHEN



INTERACTIONS OF FORMULATION AND
DISPOSABLES IN BIOPHARMACEUTICAL DRUG
PRODUCT MANUFACTURING

Verena Saller

aus

Starnberg, Deutschland

2015

ERKLÄRUNG

Dieser Dissertation wurde im Sinne von § 7 der Promotionsordnung vom 28. November 2011 von Herrn Prof. Dr. Wolfgang Frieß betreut.

EIDESSTATTLICHE VERSICHERUNG

Diese Dissertation wurde eigenständig und ohne unerlaubte Hilfe erarbeitet.

München, den

.....

Dissertation eingereicht am: 06.11.2015

1. Gutachter: Prof. Dr. Wolfgang Frieß

2. Gutachter: Prof. Dr. Gerhard Winter

Mündliche Prüfung am: 21.12.2015

„SCIENCE IS BUILT UP WITH FACTS, AS A HOUSE IS WITH STONES.
BUT A COLLECTION OF FACTS IS NO MORE A SCIENCE THAN A HEAP OF STONES IS A HOUSE.“

Henri Poincaré
in: La Science et l'Hypothèse (1902)

ACKNOWLEDGEMENTS

My deepest thanks go to my supervisor at the LMU, Prof. Dr. W. Frieß, for his outstanding guidance and support. During nearly 3.5 years in his group, I experienced him as a real “Doktorvater” – always bubbling over with ideas on how to address upcoming scientific questions and providing confidence in my work. Thank you so much for giving me the opportunity to grow not only scientifically but also personally during this time. I always enjoyed being part of your group.

Many thanks also go to Prof. Dr. G. Winter, not only for taking over the co-referee of this thesis, but also for providing excellent working conditions at the chair of Pharmaceutical Technology and Biopharmaceutics.

I also want to express my deep gratitude to the collaboration partners from F. Hoffmann-La Roche for their great support. Thank you very much to Karoline Bechtold-Peters for initiating this project and for always taking your time to give valuable input during our telecons! I am greatly indebted to Julia Matilainen: As my supervisor at Roche she strongly pushed this project forward and managed all logistics smoothly – from material supply to the organization of my several stays in Basel to the approval of publications and many more. Thank you so much! Many thanks to Christian Rothkopf for taking over the supervising during the last six months of this project and for putting so much effort in the discussions about the mathematical model for the preservative loss! In this context, I want to say thank you to Daniel Serafin who invested many hours in the implementation of the mathematical model in MatLab. Unfortunately, we were not fully successful in the end, but we had many valuable discussions and I highly appreciate your efforts! My acknowledgements also go to Ulla Grauschopf. Based on her initial studies, the online-turbidity monitoring setup was implemented. Moreover, the realization of the silicone particle spiking studies was strongly driven by her commitment. Thank you for all your valuable scientific input and for giving me the opportunity to perform the spiking study in the Late Stage Pharmaceutical and Processing Development labs in Basel! Many heartfelt thanks go to Constanze Hediger who supported me during the preparation and conduction of these studies. It was really great to work together with you! Thank you very much to Hanns-Christian Mahler for the publication reviews and the confidence shown to me. My extended thanks go to all the other Roche colleagues that contributed to various parts of this work: Thank you to Holger Roehl, Christian Matz, Andreas Graser, Stefanie Keller, Ingeborg Krämer-Pittrof, Margot Reth and Arno Wortmann from Roche Basel, thank you to Michael Schneider, Julia Krusemark, and Tina Schwarzkopf from Roche Mannheim and thanks also to the Penzberg colleagues, especially for providing the model protein.

Thank you very much to Anacelia Ríos Quiroz. She shared her experience on particle analytics gained during her PhD thesis in Basel with me, introduced me to the NTA technique and contributed to an intensified knowledge about MFI. In order for me to finish the never-ending MFI samples, she stayed with me at the Roche campus until late in the evening. I will never forget about that. Thank you also to Emilien Folzer who every now and then jumped in to unlock the MFI computer.

Thank you also to Dr. Yuan Yang and Mrs. Porobin from the group of Prof. Dr. Thomas Groth at the Martin-Luther-University Halle-Wittenberg for performing the SurPASS measurement with the Flexboy bag film. Additional thanks go to Daniel Weinbuch from Coriolis Pharma for enabling access to the FlowCam test instrument and the introduction to this instrument. A big thank you also goes to Christian Minke from the LMU for taking all the great SEM images.

Thank you so much to all my colleagues at the chair of Pharmaceutical Technology and Biopharmaceutics who made my PhD time so enjoyable and unforgettable. You were always great company and I enjoyed all the moments we shared during skiing or hiking trips, our annual Oktoberfest visits, conference visits, coffee breaks, and all other social and sports events. Since I cannot name them all without risking to forget someone, I want to mention at least my closest colleagues: Thank you very much to my predecessor working in the field of protein adsorption, Kerstin Höger, who introduced me to the SDS desorption method and protein adsorption in general. Stefanie Funke – it was a real pleasure having you on board in the Roche collaboration! Thank you so much for the many scientific discussions that we had, working and travelling together with you always worked out really great and I think we learned a lot from each other. Thank you so much also to my long-term lab mates in the “Damen-Sauna”, Madeleine Witting und Kay Strüver. Sharing the same lab for nearly three years really welds together. Thank you for always listening and giving advice with regards to work-related but also personal issues. I hope we all stay in touch!

Thank you to all the students who supported the project for varying time periods: Josefine Pott, Daniel Perez, Daniela Maier, Marlene Burisch, Nathalie Winke, Vincent Kreipe, Abdulhaq Babelli, and Tilly Stubbs. I especially want to highlight the work of Josefine Pott, who was a great support for all the online-turbidity monitoring experiments and Marlene Burisch, who contributed substantially to the adsorption studies during her Master thesis. You did a great job and I always enjoyed working with you!

I also want to mention my friends from school and university: Manu, Andy, Anna, Nea, Tina, Huifeng, Eva, Marika, Roman – thank you for your friendship and for the great times that we spent together. I am sure that there are still many more moments together waiting for us! Thank you also to my former football team at TSV Neuried – playing football together with you was great fun and a good distraction from work.

My heartfelt thanks go to my family, my father Franz, my mother Anneliese, and my brother Stephan – thank you for always being there for me and for supporting me in any situation! It is wonderful to know that there will always be someone who trusts in me and who I can rely on.

Last but not least, thank you so much to Raimund for all your love and support and all the cappuccini that you prepared for me... You have become such an important part of my life and I am very grateful and lucky to have you by my side.

TABLE OF CONTENTS

CHAPTER I

GENERAL INTRODUCTION & OBJECTIVES..... 1

1	General Introduction	1
1.1	Disposables in Biopharmaceutical Manufacturing	1
1.2	The Benefits and Challenges Associated with Single-Use Systems	2
1.3	Possible Interactions between Disposables and Drug Product	3
2	Objectives of the Thesis	4
3	References	5

CHAPTER II

ADSORPTION OF A MODEL ANTIBODY TO SINGLE-USE BIOPROCESS BAGS..... 9

<i>Abstract</i>	9	
1	Introduction.....	10
1.1	Single-Use Bioprocess Bags	10
1.1.1	Implementation of Single-Use Bags during Different Steps of the Manufacturing Process	10
1.1.2	Characteristics and Manufacturing of Single-Use Bags.....	10
1.1.3	Investigated Bags and the Characteristics of their Fluid Contact Layers	11
1.2	Protein Adsorption to Solid Surfaces.....	13
2	Materials and Methods.....	16
2.1	Materials.....	16
2.1.1	Chemicals	16
2.1.2	Model Antibody.....	16
2.1.3	Investigated Bags	16
2.2	Methods	16
2.2.1	Bag Characterization	16
2.2.2	IgG Charge Characterization.....	18
2.2.3	Sample Preparation.....	19
2.2.4	HPLC Adsorption Studies.....	19
2.2.5	Gold Staining of Adsorbed IgG	20
2.2.6	Replacement Studies with Fluorescently-Labeled IgG	21
2.2.7	Data Analysis and Statistics	21
3	Results	22
3.1	Characterization of the Fluid Contact Layers.....	22
3.1.1	Morphology.....	22
3.1.2	ATR-IR Microscopy	22
3.1.3	Surface Free Energy.....	23
3.2	Charge Characterization of IgG and Contact Layer Materials.....	25
3.3	Adsorption Studies with HP-SEC Quantification	26
3.3.1	Adsorption Isotherms.....	26
3.3.2	Influence of Adsorption and Desorption Time	27

3.3.3	Influence of pH and Ionic Strength on IgG Adsorption	28
3.3.4	IgG Adsorption to 5 mL Flexboy® Bags	29
3.4	Verification of SDS Desorption Efficiency via Gold Staining	30
3.5	Reversibility of IgG Adsorption	31
4	Discussion	34
4.1	The Influence of IgG and Surface Characteristics on IgG Adsorption	34
4.2	Adsorption Isotherms and the Interplay of Hydrophobic and Electrostatic Forces	36
4.3	Impact of IgG Adsorption on Protein Loss in the Bulk	37
4.4	Evaluation of the Applied Quantification Method	40
4.5	Adsorption Reversibility and Consequences	41
5	Summary and Outlook	42
6	Abbreviations	44
7	References	45
CHAPTER III		
STUDYING PROTEIN ADSORPTION WITH QUARTZ CRYSTAL MICROBALANCE (QCM)..... 52		
Abstract		52
1	Introduction.....	53
1.1	Methods for Studying Protein Adsorption in Situ	53
1.2	Adsorption Studies with Quartz Crystal Microbalance (QCM)	54
2	Materials and Methods.....	57
2.1	Materials.....	57
2.1.1	Chemicals	57
2.1.2	Model Antibody.....	57
2.1.3	Polymers for QCM chip coating.....	57
2.2	Methods	58
2.2.1	QCM Chip Coating	58
2.2.2	Microscopy	58
2.2.3	Sample Preparation.....	58
2.2.4	QCM Measurements	58
2.2.5	Calculations	59
2.2.6	IgG Size Determination with Dynamic Light Scattering (DLS)	61
2.2.7	Viscosity measurements	61
2.2.8	HP-SEC Quantification of IgG Adsorbed to the QCM Chip Surface	61
2.2.9	HP-SEC Quantification of IgG Adsorbed to Bag Pieces In the Presence of Surfactant	62
2.2.10	Statistics	62
3	Results	63
3.1	QCM Chip Coating Development and Morphology	63
3.2	QCM Method Development	64
3.3	Influence of pH on IgG Adsorption	65
3.3.1	Adsorbed Amount	65
3.3.2	Adsorption Kinetics	66
3.3.3	Viscoelastic Properties of the Adsorbed IgG Layer	67

3.3.4	Influence of pH on IgG Size Distribution	68
3.4	Influence of Ionic Strength on IgG Adsorption	68
3.4.1	Adsorbed Amount	69
3.4.2	Adsorption Kinetics and Viscoelastic Properties	69
3.5	Influence of Non-Ionic Surfactants on IgG Adsorption to EVA surfaces.....	71
3.5.1	Influence of Three Different Surfactants on Adsorption.....	71
3.5.2	HP-SEC Determination of the Amount of Adsorbed IgG	73
3.5.3	Influence of PS 80 Concentration.....	74
3.6	Verification of QCM Results with HP-SEC Quantification	74
4	Discussion.....	76
4.1	Implementation of QCM Measurements for Adsorption Studies with Single-Use Bag Polymer Surfaces	76
4.2	Quantification of Protein Adsorption with QCM	76
4.3	Insights into Adsorption Kinetics	78
4.4	Viscoelastic Properties of Adsorbed IgG Layers	80
4.5	Influence of Surfactants on IgG Adsorption	81
4.5.1	Adsorption Behavior of Surfactants	81
4.5.2	Sequential Adsorption and Co-Adsorption of IgG and Surfactants	82
4.5.3	Importance of Surfactant Concentration	84
4.6	Comparison of Results Obtained with Real Bag Surfaces and Casted Polymer Films	84
5	Summary and Outlook	85
6	Abbreviations	86
7	References.....	87

CHAPTER IV

PARTICLE SHEDDING FROM SILICONE TUBING UPON PERISTALTIC PUMPING..... 93

Abstract

1	Introduction.....	94
2	Materials and Methods.....	96
2.1	Materials.....	96
2.2	Methods	96
2.2.1	Online-Turbidity Monitoring	96
2.2.2	Determination of Pump Rate	98
2.2.3	Dynamic light scattering (DLS)	98
2.2.4	Light Obscuration (LO).....	98
2.2.5	Analysis of Particle Morphology.....	98
2.2.6	Fourier-Transform-Infrared-Spectroscopy (FTIR).....	99
2.2.7	Nanoparticle Tracking Analysis (NTA)	99
2.2.8	Scanning Electron Microscopy (SEM).....	99
2.2.9	3D Laser Scanning Microscopy	100
2.2.10	Evaluation of a Second Type of Pump Head	101
2.2.11	Simulated Post-Curing Process	101
2.2.12	Determination of Mechanical Properties	101
2.2.13	Thermogravimetric Analysis (TGA).....	102

2.2.14	Statistics	102
3	Results	103
3.1	Online-Turbidity Monitoring.....	103
3.2	Particle Characterization	104
3.3	Tubing Wear	109
3.4	Influence of Tubing ID.....	111
3.5	Influence of Tubing Batch.....	113
3.6	Effect of Pumping on Mechanical Properties of Tubing	117
3.7	Influence of Pump Head	118
3.8	Influence of Post-Curing	121
4	Discussion	122
5	Summary and Conclusion.....	126
6	Abbreviations	127
7	References	128

CHAPTER V

INFLUENCE OF PARTICLE SHEDDING FROM SILICONE TUBING ON ANTIBODY STABILITY..131

Abstract	131
1 Introduction.....	132
2 Materials and Methods.....	133
2.1 Materials.....	133
2.1.1 Chemicals	133
2.1.2 Silicone Tubing	133
2.1.3 Model Antibodies	133
2.1.4 Packaging Material	133
2.2 Methods	133
2.2.1 Preparation of Recirculates.....	133
2.2.2 Sample Preparation and Stability Study.....	133
2.2.3 Visual Inspection	134
2.2.4 Turbidity	134
2.2.5 Subvisible Particle Analysis.....	134
2.2.6 High Performance Size Exclusion Chromatography (HP-SEC)	134
2.2.7 Dynamic Light Scattering (DLS)	135
2.2.8 Nanoparticle Tracking Analysis (NTA)	135
2.2.9 Leachable Analysis via GC-MS	135
2.2.10 3D Laser Scanning Microscopy	135
3 Results	136
3.1 Recirculate Characterization.....	136
3.1.1 Particle Characterization	136
3.1.2 Leachables Analysis	138
3.1.3 Surface Roughness of Tubing	138
3.2 Stability Data	139

3.2.1	Monomer Content.....	139
3.2.2	Turbidity Data.....	141
3.2.3	Subvisible Particle Levels.....	142
3.2.4	Visual Inspection	143
4	Discussion	144
5	Summary and Conclusion.....	146
6	Abbreviations	146
7	References	147
8	Appendix	150

CHAPTER VI

PRESERVATIVE LOSS FROM SILICONE TUBING DURING FILL & FINISH.....154

<i>Abstract</i>	154
1 Introduction.....	155
2 Materials and Methods.....	157
2.1 Materials.....	157
2.1.1 Chemicals	157
2.1.2 Silicone Tubing	157
2.2 Methods	157
2.2.1 Sample Preparation.....	157
2.2.2 Sorption Experiments.....	157
2.2.3 UV Absorption Measurements.....	158
2.2.4 Determination of the Partition Coefficient k	158
2.2.5 Determination of the Diffusivity D	158
2.2.6 Determination of the Evaporation Characteristics.....	159
2.2.7 Modelling of Data with Fick's Law of Diffusion	159
3 Results	160
3.1 Preservative Loss during Static Incubation in Silicone Tubing.....	160
3.2 Influence of Preservative Concentration.....	160
3.3 Determination of the Partition Coefficient k	161
3.4 Determination of the Diffusivity D	162
3.5 Determination of the Evaporation Characteristics.....	163
3.6 Modelling of Data with Fick's Law of Diffusion	164
4 Discussion	166
5 Summary and Conclusion.....	170
6 Abbreviations	170
7 References	171
8 Appendix	173

CHAPTER VII

FLUOROPOLYMER TUBING AS AN ALTERNATIVE TO SILICONE TUBING.....175

1	Introduction.....	175
2	Materials and Methods.....	176
2.1	Materials.....	176
2.1.1	Chemicals	176
2.1.2	Fluoropolymer Tubing.....	176
2.2	Methods	176
2.2.1	Sample Preparation.....	176
2.2.2	Sorption Experiments.....	176
2.2.3	UV Absorption Measurements.....	176
2.2.4	Online-Turbidity Monitoring	177
2.2.5	Determination of Pump Rate	177
2.2.6	Dynamic Light Scattering (DLS)	177
2.2.7	Light Obscuration (LO).....	177
2.2.8	3D Laser Scanning Microscopy.....	178
2.2.9	Leachable Analytics via GC-MS.....	178
3	Results	179
3.1	Preservative Loss during Static Incubation.....	179
3.2	Online-turbidity monitoring	179
3.3	Particle characterization.....	179
3.4	Tubing wear	180
3.5	Leachable Analytics	180
4	Discussion	182
5	Summary and Conclusion.....	183
6	Abbreviations	183
7	References	184
8	Appendix	185

CHAPTER VIII

FINAL SUMMARY & OUTLOOK186

Abbreviations..... 188

References 189

GENERAL INTRODUCTION & OBJECTIVES

1 GENERAL INTRODUCTION

1.1 Disposables in Biopharmaceutical Manufacturing

During recent years, the number of disposables that are available for biopharmaceutical manufacturing has increased substantially and more and more biopharmaceutical companies start establishing disposable concepts [1–7]. Disposables are defined as single-use components that are typically provided gamma-sterilized and therefore ready-to-use. Nowadays, available disposables include single-use bioreactors, bioprocess bags, mixing systems, tubing, pumps, sensors, connectors, filter cartridges, and chromatography systems [5,6]. Disposables can be implemented during any step of biopharmaceutical production [4,8,9] – from cell culture and fermentation to purification, formulation, storage and filling. Hence, a fully disposable manufacturing site has become feasible [7,10]. Figure I-1 visualizes the potential layout of a fully disposable compounding site. Stainless steel tanks only act as support for the flexible disposable bags that are made from plastic materials and used for intermediate storage or mixing. The transfer of drug product is realized with disposable silicone tubing and a peristaltic pump. For the future, it is anticipated that disposables will increasingly replace traditional stainless steel manufacturing equipment or at least be essential parts of hybrid settings that combine the benefits of both traditional and disposable elements [4].



Figure I-1: Possible set-up of a fully disposable biopharmaceutical manufacturing site for the final formulation step. Reproduced from <http://microsite.sartorius.com/single-use-technology/engineering/configurable-single-use-systems.html> (accessed May 9th, 2015).

1.2 The Benefits and Challenges Associated with Single-Use Systems

The main benefit of disposable systems arises from the lower risk of cross-contaminations and thus increased patient safety [11]. Sites that use stainless steel equipment have to carry out time-consuming cleaning validation studies or implement dedicated equipment in order to avoid such risks. Initial capital investments for a disposable plant are typically lower than for costly stainless steel equipment, resulting in capital expenditure savings of up to 60-70 % [12,13]. In general, the savings associated with disposables depend on the production scale and seem to be favorable mainly for small-scale production, e.g. for early clinical phases [14]. Since cleaning-in-place and sterilization-in-place cycles are not required for disposables, product change-over times can be significantly shortened [4,5]. By implementing single-use 3D bags for buffer preparation, Weitbrecht *et al.* were able to increase the number of produced batches per week significantly due to time savings of 4 to 6 hours per batch [2]. In a case study by Liderfelt *et al.*, the total downstream process time for mAb purification could be shortened from 45.5 h to 23 h by using disposables [15]. Moreover, waiving cleaning cycles leads to substantial savings with regards to electricity, water, and cleaning material [16]. As a conclusion, operation expenditures can be reduced by 20-25 % [12] and the overall carbon dioxide balance for disposable processes is assumed to be lower than for traditional processes employing stainless steel despite the increased amount of waste that is produced with disposables [10,16–18]. When handling highly toxic drugs, disposables might help to protect the manufacturing personal from contact with the drug [5]. In times of personalized medicine with a variety of highly potent drugs that are manufactured in volumes well below those of traditional ‘blockbusters’, the flexibility associated with disposables is highly appreciated [1,4]. Therefore, disposable concepts are often favored for pilot plants and the production of material for clinical Phases I and II [6,19]. Moreover, flexibility in terms of the layout of the manufacturing site is increased and the facility footprint is reduced [20]. A modular approach with flexible tubing and mobile tanks enables a customized configuration of unit operations that can be adapted in a product-specific way [12,21]. In this context, the “ballroom concept” as a facility layout consisting of one large, unclassified manufacturing area with minimal segregation due to the use of movable and functionally contained equipment was introduced [22]. How all of these factors can combine to significant savings in R&D and manufacturing costs is shown in different case studies [23–25].

Potential challenges include the implementation of an efficient waste management system [17,18] and the higher ongoing costs for consumables. Since standardization of disposables is not established yet, vendor dependency is highly increased and considered business critical [9,11]. Proper supplier qualification and auditing is essential in order to ensure that disposables are manufactured to defined quality standards [26], especially with regards to sterility, lack of endotoxins, extractables and leachables [27], and particle contamination [28]. The volume per batch is limited by the bag sizes that are maximally realizable with plastic materials due to physical constraints [4]. The brittleness of single-use bags with tubing connectors that are stored frozen requires careful handling by well-educated personal. The most important challenge is the lack of experience which is currently still associated with disposable use [6]. More comprehensive studies are needed in order to evaluate a possible impact on the quality of a drug product prior to implementation of disposables.

1.3 Possible Interactions between Disposables and Drug Product

In general, possible interactions between contact materials and a drug product are classified into sorption, migration, and diffusion events (Figure I-2). Surfaces and their leachables can impair the stability of biopharmaceuticals in various ways [29,30].

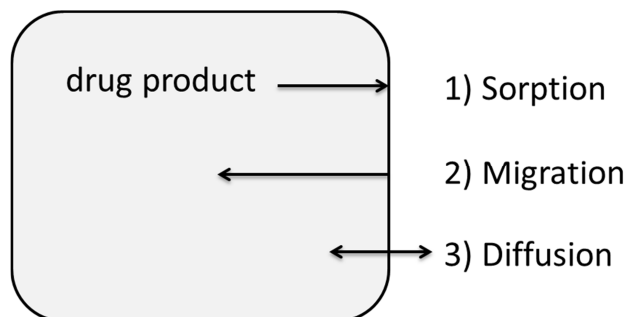


Figure I-2: Possible interactions between drug product and contact material.

Sorption processes may include the adsorption as well as absorption of drug product components by the contact material. Especially proteinaceous drugs and excipients like surfactants are prone to adsorption [31–33]. In extreme cases, sorption can lead to substantial losses of the active ingredient [34,35] or excipients. This needs to be avoided in order to meet the specifications and to ensure stability and efficacy of the final drug product. With regards to proteins, also desorption events of potentially altered protein structures need to be considered [36,37]. More details regarding protein adsorption will be discussed in Chapter II and III.

Migration of packaging components into the drug product solution is of increased concern with polymeric materials and therefore carefully evaluated during extractables and leachables studies with disposables [38]. Extractables are all potential substances that can be extracted from plastic materials using solvents and possibly harsh extraction conditions like increased temperature or extreme pH values [39,40]. Also the impact of gamma irradiation has to be considered in this context [41]. Leachables are defined as the substances that can be found in the finished drug product during its intended use and are often a subset of all possible extractables [39,40]. However, reactions between migrating substances and the drug product can result in leachables that were not pre-defined as extractables [39,42]. Extractables and leachables can be of organic (monomers, antioxidants, plasticizers, stabilizers, degradation products) [43] as well as of inorganic (e.g. metals) origin [40]. Extraction studies and a toxicological evaluation of potential leachables together with a safety risk assessment are demanded by the authorities for packaging components and all other contact materials encountered during manufacturing [39,43–46]. Currently, the leachables topic is considered as one of the most critical issues associated with disposables [3]. Since harmonized extractable and leachables guidelines and standardized testing methods do not exist so far [4,39], a comparative evaluation of the extractable data provided by the manufacturers is hardly feasible. Pharmaceutical companies have to define an appropriate way of how to perform extractable and leachable studies themselves [42,47]. The assessment of leachables is product-specific and was therefore not in the focus of this thesis, but included whenever reasonable. Migration might not only include substances on a molecular basis like leachables, but also particles (Chapter IV and V).

Diffusion of oxygen, water vapor, carbon dioxide or other volatile substances can occur in two directions and is potentially increased with disposables since plastic materials are characterized by a

higher permeability than glass or stainless steel. Diffusion of oxygen into the headspace of sensitive products can accelerate oxidation [48]. Loss of water vapor eventually leads to a concentrating of the drug. Preservatives in multi-use drug products are typically volatile substances that might also diffuse through the packaging material [49,50] (Chapter VI and VII).

2 OBJECTIVES OF THE THESIS

It is the aim of this thesis to contribute to a better knowledge around disposables with regards to the properties of employed materials and in particular to possible interactions with the drug product itself. The materials investigated included single-use bioprocess bags and tubing used for peristaltic pumping. The general outline of this thesis is depicted in Figure I-3.

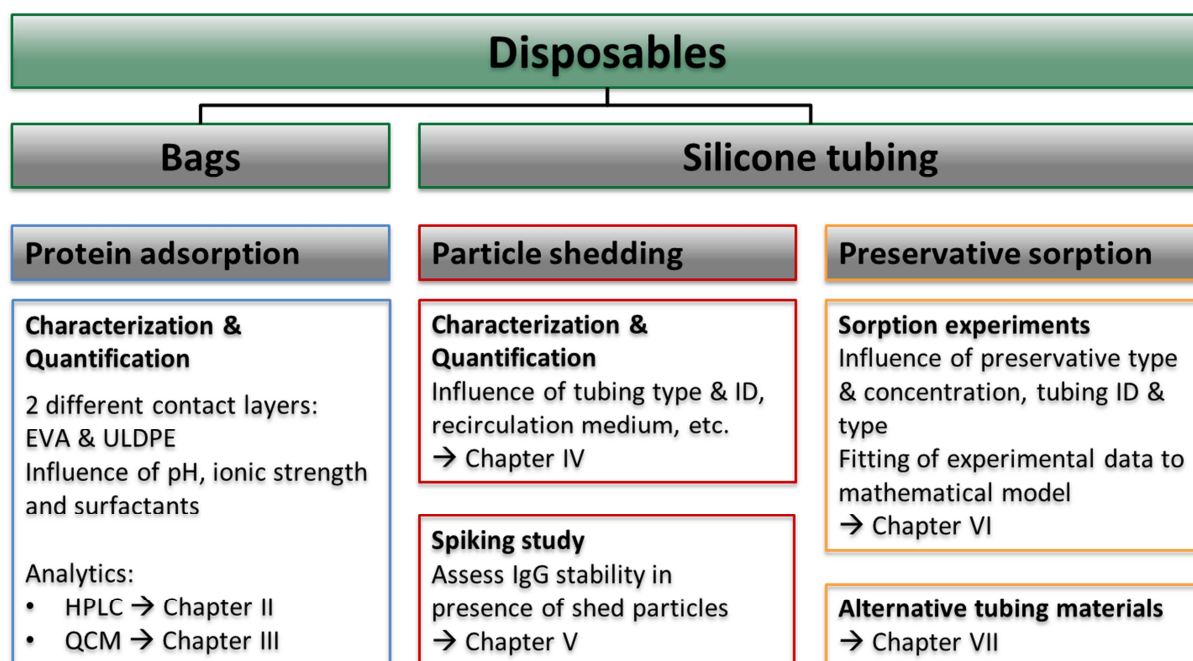


Figure I-3: Outline of the thesis.

Investigations with single-use bags focused on the characterization of the two commonly used bag materials ethylene-vinyl acetate (EVA) and ultra-low density polyethylene (ULDPE) as well as the quantification of monoclonal antibody adsorption (Chapter II). In addition, the quartz crystal microbalance (QCM) technique was implemented to gain a deeper understanding of the kinetics of mAb adsorption (Chapter III).

Silicone tubing was extensively characterized for its particle shedding behavior during peristaltic pumping (Chapter IV). A possible impact of shed particles on the stability of two model monoclonal antibodies was evaluated by means of spiking studies (Chapter V). The permeability of silicone tubing for preservatives was assessed with sorption experiments (Chapter VI). An alternative tubing material that can help to avoid preservative losses during filling is presented and its performance in terms of sorption and particle shedding was evaluated (Chapter VII).

3 REFERENCES

- [1] P. Krämer, R. Müller, Single-Use-/Disposables-Prozesskomponenten: Eine Technologiealternative. Teil 1: Technologische Einsatzgrenzen aus bioverfahrenstechnischer Sicht, *Pharm. Ind.* 74 (2012) 323–327.
- [2] T. Weitbrecht, G. Kallmeyer, U. Klotz, T. Posset, A. Mang, Einsatz von Disposables in der Pharma-Parenteralia-Produktion, *Pharm. Ind.* 75 (2013) 1810–1823.
- [3] E. Langer, Ten Years Later: Innovation Driving Single-Use Technology Advances, *BioPharm Int.* (2013) s4–s8.
- [4] C. Mintz, Single-Use, Disposable Products: A “State of the Industry” Update, *Life Sci. Lead.* (2009).
- [5] M.W. Jornitz, J.-M. Cappia, T.H. Meltzer, Disposable Components in Aseptic Processing, *Pharm. Technol.* (2009).
- [6] T. Kapp, J. Boehm, J. Chase, J. Craig, K. Davis, V. Gupta, et al., Road Map to Implementation of Single-Use Systems, *Bioprocess Int.* 8 (2010) Supplement 10–19.
- [7] W.G. Whitford, Single-Use Systems As Principal Components in Bioproduction, *Bioprocess Int.* 8 (2010) 34–42.
- [8] G. Rao, A. Moreira, K. Brorson, Disposable bioprocessing: the future has arrived., *Biotechnol. Bioeng.* 102 (2009) 348–56.
- [9] D. Eibl, T. Peuker, R. Eibl, Single-Use Equipment in Biopharmaceutical Manufacture: A Brief Introduction, in: R. Eibl, D. Eibl (Eds.), *Single-Use Technology in Biopharmaceutical Manufacture*, John Wiley & Sons, Inc., Hoboken, New Jersey, USA, 2011: pp. 3–11.
- [10] L. McLeod, The Road to a Fully Disposable Protein Purification Process: Single-Use Systems Eliminate Time-Consuming, Non-Revenue-Generating Activities, *Bioprocess Int.* 7 (2009) Supplement 4–8.
- [11] E. Isberg, The Overlooked Benefits of Single-Use Technology: Improved Quality and Increased Patient Safety, *BioPharm Int.* (2013) s9–s10.
- [12] P. Galliher, A. Pralong, When the Process Becomes the Product: Single-Use Technology and the Next Biomanufacturing Paradigm, *BioPharm Int.* (2013) s27–s30.
- [13] J. Novais, N. Titchener-Hooker, M. Hoare, Economic comparison between conventional and disposables-based technology for the production of biopharmaceuticals, *Biotechnol. Bioeng.* 75 (2001) 143–153.
- [14] S.S. Farid, Process economics of industrial monoclonal antibody manufacture., *J. Chromatogr. B. Analyt. Technol. Biomed. Life Sci.* 848 (2007) 8–18.
- [15] J. Liderfelt, G. Rodrigo, A. Forss, The Manufacture of mAbs - A Comparison of Performance and Process Time between Traditional and Ready-to-Use Disposable Systems, in: R. Eibl, D.

- Eibl (Eds.), *Single-Use Technology in Biopharmaceutical Manufacture*, John Wiley & Sons, Inc., Hoboken, New Jersey, USA, 2011: pp. 333–340.
- [16] B.A. Sinclair, L. Leveen, M. Monge, J. Lim, S. Cox, The Environmental Impact of Disposable Technologies, (2008) 1–9.
- [17] B. Rawlings, H. Pora, A Prescriptive Approach to Management of Solid Waste from Single-Use Systems, *Bioprocess Int.* 7 (2009) 40–46.
- [18] U. Baier, Waste Generation, Treatment Options, and the Environmental Impact of Single-Use Systems, in: R. Eibl, D. Eibl (Eds.), *Single-Use Technology in Biopharmaceutical Manufacture*, John Wiley & Sons, Inc., Hoboken, New Jersey, USA, 2011: pp. 173–182.
- [19] M. Jornitz, T. Paust, The Evolution of Single-Use Technologies in Aseptic Processing, *Pharm. Technol.* 34 (2010).
- [20] A. Sinclair, M. Monge, Biomanufacturing for the 21st century: Designing a Concept Facility Based on Single-Use Systems, *Bioprocess Int.* 2 (2004) Supplement 26–31.
- [21] T. Peuker, D. Eibl, Biopharmaceutical Manufacturing Facilities Integrating Single-Use Systems, in: R. Eibl, D. Eibl (Eds.), *Single-Use Technology in Biopharmaceutical Manufacture*, John Wiley & Sons, Inc., Hoboken, New Jersey, USA, 2011: pp. 145–158.
- [22] B. Bodeker, Improving Biologic Manufacturing Operations and Plant Design through Single-Use Technologies Application, *Pharm. Outsourcing.* 13 (2012).
- [23] A. Ravisé, E. Cameau, G. De Abreu, A. Pralong, Hybrid and disposable facilities for manufacturing of biopharmaceuticals: pros and cons., *Adv. Biochem. Eng. Biotechnol.* 115 (2010) 185–219.
- [24] A. Sinclair, M. Monge, Concept Facility Based on Single-Use Systems, Part 2: Leading the Way for Biomanufacturing in the 21st Century, *Bioprocess Int.* 3 (2005) Supplement 51–55.
- [25] A. Seeger, D. Estapé, Production Costs in Biotech Facilities: Single-Use versus Multiple-Use Equipment for Antibody Manufacture, in: R. Eibl, D. Eibl (Eds.), *Single-Use Technology in Biopharmaceutical Manufacture*, John Wiley & Sons, Inc., Hoboken, New Jersey, USA, 2011: pp. 351–361.
- [26] K.D. Lear, N. Collier, K. Bader, Securing and Qualifying Single-Use Technologies, *BioPharm Int.* (2013) s18–s23.
- [27] T. Merseburger, An Introduction to the Validation and Qualification of Disposables Used in Biomanufacture - A User's Perspective, in: R. Eibl, D. Eibl (Eds.), *Single-Use Technology in Biopharmaceutical Manufacture2*, John Wiley & Sons, Inc., Hoboken, New Jersey, USA, 2011: pp. 159–172.
- [28] B.M. Belongia, J.A. Allay, Characterization, Qualification, and Validation of a Disposable Final Filling Process for Parenteral and Ophthalmic Drugs, *Pharm. Technol.* (2006).
- [29] J.S. Bee, T.W. Randolph, J.F. Carpenter, S.M. Bishop, M.N. Dimitrova, Effects of surfaces and leachables on the stability of biopharmaceuticals., *J. Pharm. Sci.* 100 (2011) 4158–70.

-
- [30] H.-C. Mahler, S. Fischer, T.W. Randolph, J.F. Carpenter, Protein Aggregation and Particle Formation: Effects of Formulation, Interfaces and Drug Product Manufacturing Operations, in: W. Wang, C.J. Roberts (Eds.), *Aggregation of Therapeutic Proteins*, John Wiley & Sons, Inc., Hoboken, New Jersey, USA, 2010: pp. 301–331.
- [31] K. Nakanishi, T. Sakiyama, K. Imamura, On the adsorption of proteins on solid surfaces, a common but very complicated phenomenon, *J. Biosci. Bioeng.* 91 (2001) 233–44.
- [32] W. Norde, J. Lyklema, Why proteins prefer interfaces, *J. Biomater. Sci. Polym. Ed.* 2 (1991) 183–202.
- [33] L. Shen, A. Guo, X. Zhu, Tween surfactants: Adsorption, self-organization, and protein resistance, *Surf. Sci.* 605 (2011) 494–499.
- [34] A. Hawe, W. Friess, Development of HSA-free formulations for a hydrophobic cytokine with improved stability, *Eur. J. Pharm. Biopharm.* 68 (2008) 169–82.
- [35] A.G. McLeod, I.R. Walker, S. Zheng, C.P. Hayward, Loss of factor VIII activity during storage in PVC containers due to adsorption, *Haemophilia.* 6 (2000) 89–92.
- [36] F. Felsovalyi, P. Mangiagalli, C. Bureau, S.K. Kumar, S. Banta, Reversibility of the adsorption of lysozyme on silica, *Langmuir.* 27 (2011) 11873–82.
- [37] M. Wahlgren, Protein adsorption to solid surfaces, *Trends Biotechnol.* 9 (1991) 201–208.
- [38] I. Markovic, Evaluation of safety and quality impact of extractable and leachable substances in therapeutic biologic protein products: a risk-based perspective., *Expert Opin. Drug Saf.* 6 (2007) 487–91.
- [39] D. Jenke, Evaluation of the chemical compatibility of plastic contact materials and pharmaceutical products; safety considerations related to extractables and leachables, *J. Pharm. Sci.* 96 (2007) 2566–2581.
- [40] P. Kushwaha, A.K. Madan, Extractables and Leachables: An Overview of Emerging Challenges, *Pharm. Technol.* 32 (2008).
- [41] J. Wood, E. Mahajan, M. Shiratori, Strategy for selecting disposable bags for cell culture media applications based on a root-cause investigation., *Biotechnol. Prog.* 29 (2013) 1535–49.
- [42] A.A. Wakankar, Y.J. Wang, E. Canova-Davis, S. Ma, D. Schmalzing, J. Grieco, et al., On developing a process for conducting extractable–leachable assessment of components used for storage of biopharmaceuticals, *J. Pharm. Sci.* 99 (2010) 2209–2218.
- [43] C. Ducker, M. Kolodziejski, M. Jacques, J. Roark, A. Blakinger, T. Lehman, The Risks of Single-Use Bioprocess Containers, *Am. Pharm. Rev.* (2014).
- [44] J.S. Kauffman, Identification and Risk-Assessment of Extractables and Leachables, *Pharm. Technol.* (2006).
- [45] J. Bennan, F. Bing, N. Boone, J. Fernandez, B. Seely, H. van Deinse, et al., Evaluation of extractables from product-contact surfaces, *Biopharm Int.* 15 (2002) 22–34.
-

- [46] D. Bestwick, R. Colton, Extractables and Leachables from Single-Use Disposables, *Bioprocess Int.* (2009) February Supplement p.88–94.
- [47] X. Yu, D. Wook, X. Ding, Extractables and Leachables Study Approach for Disposable Materials Used in Bioprocessing, *BioPharm Int.* 21 (2008).
- [48] W. Wang, S. Singh, D.L. Zeng, K. King, S. Nema, Antibody structure, instability, and formulation., *J. Pharm. Sci.* 96 (2007) 1–26.
- [49] S.M. Bahal, J.M. Romansky, Sorption of parabens by flexible tubings., *Pharm. Dev. Technol.* 6 (2001) 431–40.
- [50] S.M. Bahal, J.M. Romansky, Sorption of benzoic acid, sorbic acid, benzyl alcohol, and benzalkonium chloride by flexible tubing., *Pharm. Dev. Technol.* 7 (2002) 49–58.

ADSORPTION OF A MODEL ANTIBODY TO SINGLE-USE BIOPROCESS BAGS

ABSTRACT

During implementation of single-use bioprocess bags in biopharmaceutical drug product manufacturing, protein adsorption has to be considered and studied in detail. In order to quantify protein adsorption, we adapted a previously introduced method for studying protein adsorption to glass vials (Mathes & Friess 2011) to bags with EVA and ULDPE contact layers. The correct HP-SEC analysis relies on the quantitative desorption of adsorbed protein with SDS which was proven for an IgG using gold staining. To enhance a better understanding of the ongoing adsorption process of a model IgG1 antibody, bag surfaces and the antibody were characterized in terms of morphology, surface free energy and surface charge, respectively. Additionally, studies with varying incubation time, pH, and ionic strength were conducted. Adsorption reversibility was investigated using fluorescently labelled antibody molecules. It was found that not only hydrophobic interactions are of importance during protein adsorption, but especially electrostatic interactions led to an increased adsorbed amount of IgG on the more polar EVA bag surface in comparison to the nonpolar ULDPE surface. Adsorption isotherms indicated that the antibody shows a higher affinity to the ULDPE polymer. Depending on the pH value, adsorbed amounts were in the range of 2 to 5 mg/m². Loss due to protein adsorption was demonstrated not to be of concern, especially with higher concentrated formulations and at maximal bag filling volumes.

Parts of the following chapter are intended for publication.

Protein adsorption measurements to ULDPE bags as well as the characterization of these surfaces was performed by Stephanie Marlene Burisch during her Master thesis project entitled "IgG adsorption to single-use bioprocess bags with ULDPE contact layer" (2014).

1 INTRODUCTION

1.1 Single-Use Bioprocess Bags

1.1.1 Implementation of Single-Use Bags during Different Steps of the Manufacturing Process

Single-use bag systems have become available for many applications in biopharmaceutical manufacturing where traditionally containers made from glass or stainless steel are employed. The most basic form of single-use bags are tank liners. They are well suited for buffer and media preparation in open container systems and create a barrier between the liner content and the container wall. Rather flat, “two-dimensional” bags as shown in Figure II-4a facilitate sampling, storage, freezing and transportation of limited volumes (usually 50 mL to 50 L) of drug substance, buffer and media. Different bag types vary in the position and number of ports, connectors, pinch clamps, tubing, and filters which can be customized for individual purposes. A suitable handling system, e.g. stackable trays, for safe storage and transportation might be needed. “Three-dimensional” cubical or cylindrical bags with integrated stirring units as shown in Figure II-4b have been designed specifically for mixing purposes and larger liquid volumes of up to 2500 L. An outer container as mechanical support is mandatory [1]. Single-use bioreactors with ports for (single-use) pH and oxygen sensors can be implemented during cell cultivation and fermentation [2]. Bags of any type are usually provided fully assembled and gamma sterilized, and are therefore ready-to-use.

1.1.2 Characteristics and Manufacturing of Single-Use Bags

Single-use bags are fabricated from polymeric materials that may have drawbacks in terms of product compatibility, gas permeability, or mechanical instability, when compared to traditional materials like glass and stainless steel. The performance in terms of required container properties of typically used polymers like polyvinyl chloride (PVC), low-density polyethylene (LDPE), and ethylene vinyl acetate (EVA) is listed in Table II-1.

Table II-1: Performance of major plastic polymers in terms of required container properties. Modified from Sacha et al. 2010 [3].

Property	PVC	LDPE	EVA
Compatibility with contained drug products	Poor	Good	Fair
Resistance to moisture permeation	Very poor	Good	Very poor
Heat sterilization	Fair	Poor	Very poor
Transparency	Good	Fair	Fair
Collapsibility	Excellent	Poor	Good
Disposability	Poor	Good	Fair

In order to obtain bags with optimal performance in all quality attributes, bag films are manufactured as multilayers from several polymeric materials. Generally, such multilayer films are composed of a fluid contact layer, a barrier layer, and an outer layer providing mechanical stability [4].

The most important feature of the fluid contact layer is its inertness and compatibility with the contained product. In early years, PVC was commonly used for plastic containers. PVC films usually contain high amounts of plasticizers, e.g. diethylhexylphthalate (DEHP), at levels up to 40 % which can result in substantial amounts of extractables and leachables [3]. Due to this poor compatibility with the contained product, PVC is nowadays typically replaced by materials like ultra-low density polyethylene (ULDPE), polypropylene (PP), and EVA. However, PVC is still commonly used in intravenous (IV) and blood bags [5]. Bags with ULDPE and EVA contact layers were investigated in this study. More details on characteristics of these polymers are provided in the next section.

Plastic films are manufactured by extrusion techniques. During extrusion, the raw material in the form of polymer granules is melted, homogenized and finally reshaped into a film. When applying blown film extrusion or cast film extrusion, multilayer films can directly be produced via coextrusion. Otherwise, during extrusion lamination a suitable tie layer is extruded between already existing films. Different tie-layer materials can be incorporated as adhesives between the individual layers. Other additives can be incorporated into the polymer mixture to improve bag performance or manufacturability, but manufacturers often do not disclose the exact composition of their films. Other possibly present, but unwanted compounds might include unreacted monomers, solvents, polymerization catalysts, surfactants, or polymer degradation products. Therefore, extractables and leachables studies are important to qualify the single-use bag prior to implementation.

Materials used for film manufacturing are thermosetting polymers and can thus be simply welded together to form the final bag geometry. Other parts like connectors are shaped separately via injection molding. In a final assembly step, these fitments are joined to the bag via welding, mechanical fastening or chemical bonding with e.g. cyclohexanone [3]. In the end, functional elements (e.g. filters, clamps, sampling bags) are connected to the fitments via tubing sets. Gamma sterilization of the assembled bag system needs to be carefully validated as this process can increase cross-linking inside the polymers or lead to polymer degradation.

Bag manufacturers include many companies like Thermo Fisher Scientific, Sartorius Stedim, ATMI Life Sciences, Millipore, Xcellerex, Meissner, HyNetics Corporation, and GE Healthcare. Composition and quality of the bag materials vary with the bag manufacturer. Also offered designs, bag volumes, and available functionalization via ports, tubings, and in-line filters depend on the manufacturer. Typically, standard as well as customer-specific solutions are provided [5].

1.1.3 Investigated Bags and the Characteristics of their Fluid Contact Layers

In this study, investigated bags included the Flexboy® bag with EVA contact layer (Sartorius Stedim, Stedim 71) as well as two bags with ULDPE contact layer, namely Flexel® bags (Sartorius Stedim, Stedim 40) and bags made from PureFlex™ film (Millipore). Film compositions as well as total film thicknesses of these bags are listed in Table II-2.

2D Flexboy® bags from Sartorius Stedim (Figure II-4a) are intended for the preparation, storage, and transport of biopharmaceutical solutions, intermediates, and final bulk products. This bag type is available in bag chamber volumes between 5 mL and 50 L [6].

The Flexel® series for LevMixer® comprises cubical 3D bags that have a magnetic impeller inside (Figure II-4b). Together with the corresponding stainless steel container Palletank® and the LevMixer® drive unit, this bag can be employed for mixing during buffer and media preparation, bulk

intermediate resuspension, product (re-)formulation, or pooling. Nominal bag capacities of Flexel® bags for LevMixer® range from 50 L to 1000 L [7], other Flexel® 3D bags are available for nominal fill volumes of up to 3,000 L [8].

The Mobius® system by Millipore provides integrated disposable platform solutions including bags made from PureFlex™ films. Millipore uses this coextruded bag material throughout all applications during drug manufacturing, from media and buffer preparation, cell culture, mixing, product storage, to sterile sampling. For large volume operations of more than 500 L, the PureFlex™ Plus film was developed. This film consists of a LLDPE outer layer with otherwise identical film composition and an increased film thickness of 300 µm [9].

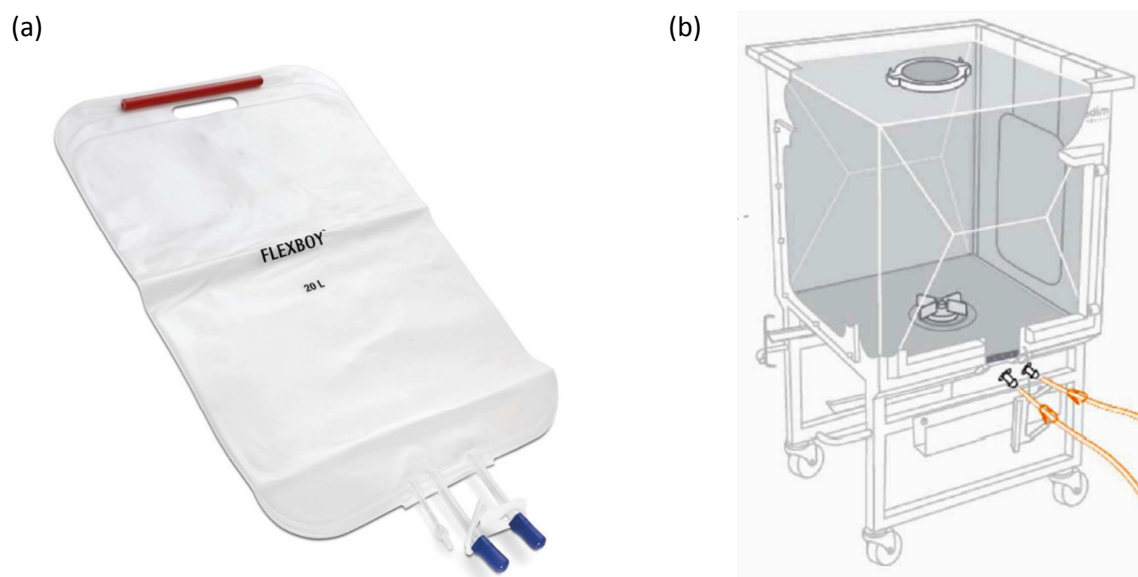


Figure II-4: Images of (a) a 2D Flexboy® bag and (b) a 3D Flexel® bag for Levmixer® with magnetic impeller inside a stainless steel Palletank® support tray. Images from <http://www.sartorius.com>.

Table II-2: Multilayer composition of investigated bags. PET: Polyethylene Terephthalate, PA: Polyamide, EVOH: Ethyl Vinyl Alcohol, ULDPE: Ultra-Low Density Polyethylene, EVA: Ethylene Vinyl Acetate.

Layer	Flexboy® (Sartorius) [10] Stedim 71 film	Flexel® (Sartorius) [11] Stedim 40 film	PureFlex™ (Millipore) [9]
Fluid contact layer	EVA	ULDPE	ULDPE
Gas barrier layer	EVOH	EVOH	EVOH
Outer layer	EVA	PA PET	EVA ULDPE
Total thickness	300 ± 25 µm (360 ± 45 µm for 50 L bag)	200 ± 25 µm	250 µm

The fluid contact layer of Flexboy® bags is made from EVA, which is a copolymerization product of ethylene and vinyl acetate units. The properties of this random copolymer mainly depend on the vinyl acetate (VA) content, which is limited to 25 % for use in containers for parenterals by the European Pharmacopeia [12]. For film applications, the VA content usually ranges from 4 to 18 % [5]. With higher VA content, crystallinity, melting point, and stiffness decrease, whereas density and

toughness increase. Higher VA level grades are used as contact or heat sealing layers in coextrusion of multilayer structures. Due to its mechanical resistance at low temperatures, it is also used for freeze / thawing bags like Celsius®-Paks from Sartorius [13]. According to Vanhamel and Masy [5], EVA is the primary replacement material for PVC.

Both, the Flexel® bag (Stedim 40) and the PureFlex™ film, are produced with a ULDPE contact layer. ULDPE belongs to the polyethylene (PE) family and mainly consists of polymerized ethylene units. Different types of PE can be fabricated through varying reactor type, reaction conditions, presence and type of catalyst, and addition of co-monomers. ULDPE is obtained from polymerization with octene as a co-monomer in levels ranging from 10 to 30 % (w/w) [5]. ULDPE is a special case of linear low-density polyethylene (LLDPE), which is produced with a metal coordination catalyst [14]. The production process results in many short-chain branches on the linear polymer and the final density of the material is in the range of 0.880-0.915 g/cm³. ULDPE copolymers are characterized by good mechanical properties, sealability, flexibility, and transparency. Its oxygen permeability is higher than for other PEs, but similar to values for EVA. The water vapor transmission rate of ULDPE is similar to those of other PEs [13]. Due to its mechanical flexibility which is superior to EVA, ULDPE is considered a good choice for contact layers in disposable bag films [5].

All investigated bags feature an ethylene vinyl alcohol (EVOH) gas barrier layer. EVOH is produced by controlled hydrolysis of EVA. EVOH is characterized by outstanding oxygen and odor barrier properties. Varying the ethylene content impacts barrier properties as well as mechanical properties. Due to its sensitivity towards humidity, EVOH always needs to be embedded between two layers with good humidity barrier properties [5,13]. Another suitable material for gas barrier layers is polyvinylidene dichloride (PVDC).

Outer layer materials are meant to increase the mechanical stability of the whole bag film. Apart from EVA and ULDPE, polyamide (PA) and polyethylene terephthalate (PET) are commonly used. PA and PET additionally show good barrier properties and temperature stability [5].

1.2 Protein Adsorption to Solid Surfaces

One of the challenges associated with drug product manufacturing is protein adsorption. Proteins are large, amphiphilic molecules and intrinsically surface active [15]. Therefore, proteins readily adsorb to any kind of exposed surface. Only with structurally stable proteins and equally charged interaction partners, adsorption might not be a concern [16]. The underlying driving force for adsorption is the higher standard free energy of an interface in comparison to the bulk phase. A thermodynamic equilibrium is thus achieved by the adsorption of substances that are different from the solvent molecules [17].

Protein adsorption and subsequent desorption consists of several steps (Figure II-5) [18,19]. Firstly, transport to the surface is governed by diffusion and convection and influenced by the charge conditions on the surface. Even in a well-stirred system, this step can be rate-determining due to the stagnant layer close to the surface. Subsequent interactions of the protein with the surface foster protein attachment to the surface. With increasing surface coverage, attachment of newly arriving molecules is significantly influenced by lateral interactions with already adsorbed proteins. During this step, changes in the secondary or tertiary structure of the protein can occur. This results in an increase of the number of protein – surface interaction sites over time and can cause substantial alterations in the protein structure. The generally accepted irreversibility of protein adsorption is suggested to be a result of these structural changes. All of the formed interaction bonds between

protein and surface would have to break at the same time in order to enable desorption. Nevertheless, desorption can be induced by changes of pH or ionic strength. Generally, at least a fraction of adsorbed protein is expected to be in exchange with protein molecules in the bulk. Moreover, lateral diffusion of adsorbed proteins can occur. As a result from desorption, conformationally altered protein molecules might arrive in the bulk. In this context, immunogenicity issues are discussed. However, in many cases the protein might as well recover its native state [18].

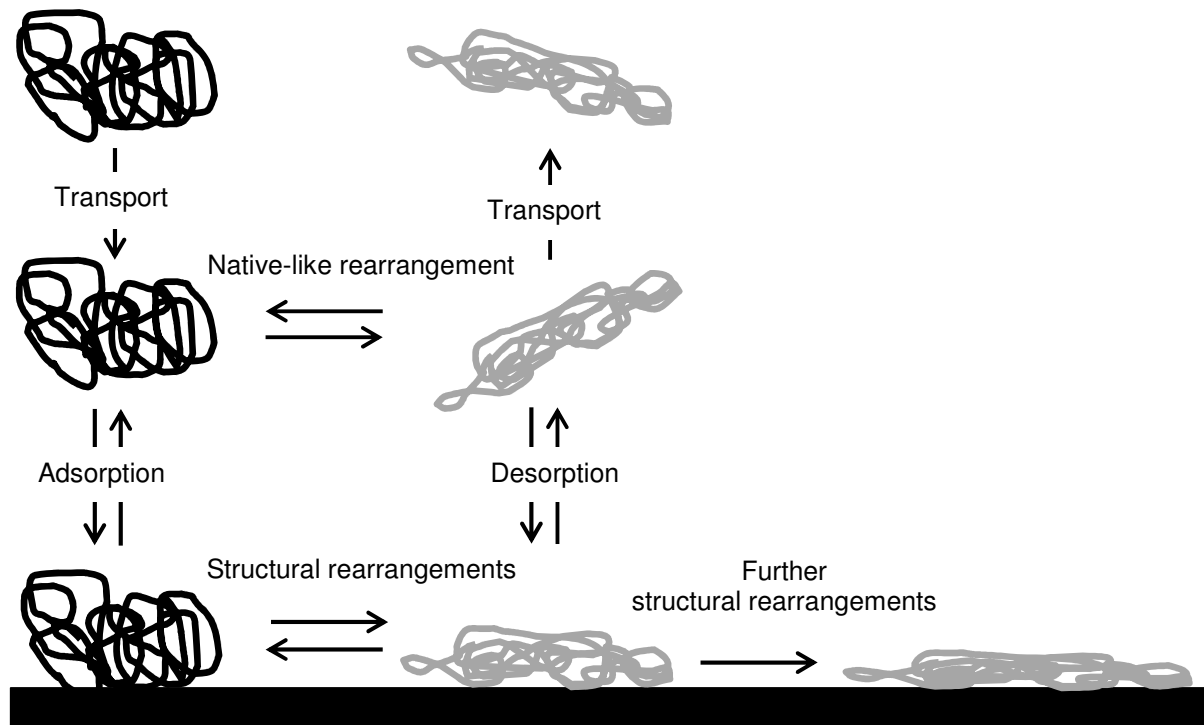


Figure II-5: Kinetic model of protein adsorption. Modified from Felsovalyi et al. 2011 [20], Norde & Haynes 1995 [19], and Wahlgren & Arnebrant 1991 [18].

The main contribution to protein attachment arises from hydrophobic interactions and the corresponding entropy gain upon dehydration of the surface. Further important interactions occur via dispersion and electrostatic forces. Moreover, structure loss of the protein leads to additional entropy gain [21]. The extent to which the different interaction forces contribute to protein adsorption depends on factors that are often specific for the studied system, namely the protein itself, the surface under investigation, and formulation as well as environmental conditions. Some of these influencing factors are listed in Table II-3.

Table II-3: Main factors that influence interaction forces and thus protein adsorption to surfaces.

Protein properties	Surface properties	General formulation factors
Charge / Isoelectric point (IEP)	Charge / Zero point of charge (ZPC)	pH
Size	Hydrophilicity / Hydrophobicity	Ionic strength (IS)
Stability ("hard" or "soft")	Chemical composition	Temperature
Hydrophobicity	Roughness	Time
Steric conformation		Concentration

Protein adsorption is a widely studied phenomenon. Nakanishi et al. give a detailed overview of published adsorption studies including experimental conditions, adsorbed amounts and applied analytics [17]. However, most of the studies so far investigated adsorption of model proteins like lysozyme and albumin. The employed surfaces were often chosen according to their suitability for methods like ellipsometry or for measuring adsorption via depletion. Thus, modified silica, gold, mica, or particles made from polystyrene or glass are typical sorbents for adsorption studies [22]. Another main focus is on adsorption of plasma proteins to biomaterials. In this context, Young *et al.* published on adsorption of albumin, transferrin, three model antibodies, fibrinogen, and α_2 -macroglobulin to polyethylene, silicone rubber, and polyvinylchloride (PVC) tubing [23,24]. Only few studies actually assess adsorption of therapeutic proteins to relevant surfaces encountered during manufacturing or storage of a drug product. For example, Mathes and Friess addressed IgG adsorption to glass vials and the follow-up study by Höger *et al.* dealt with IgG adsorption to siliconized glass vials [25,26]. McLeod and coworkers quantified the loss of factor VIII activity upon contact to PVC mini-bags [27]. Eu *et al.* visualized adsorption of a therapeutic protein to siliconized glass prefilled syringes with gold nanoparticles [28]. Vials made from plastic CZ-resin (Daikyo Crystal Zenith) were evaluated as packaging material for protein-based parenteral formulations by Qadry *et al.*, also in terms of protein adsorption [29]. In summary, there is limited knowledge about adsorption of relevant therapeutic proteins like monoclonal antibodies (mAb) to bioprocess materials so far. Only few methods exist that can be applied to real, imperfect surfaces. Although influences of pH and ionic strength on protein adsorption were studied manifold, the impact on mAb adsorption to single-use bag surfaces is hard to predict due to the unique characteristics of a specific protein – surface system. Experiments with varying formulation parameters and a thorough characterization of the interacting partners is thus needed in order to elaborate the applicability of general concepts (e.g. impact of hydrophobicity and electrostatic interactions) to the system under investigation.

The present study introduces a setup that can be applied to quantify adsorption of a therapeutic immunoglobulin G (IgG) to single-use bioprocess bags. In total, three different bags with EVA and ULDPE contact layers were employed. Via gold staining, the effectivity of the applied desorption method is proven. The influence of factors like incubation concentration, incubation time, and desorption time was studied in order to further evaluate the method. The impact of varying pH and ionic strength was interpreted in conjunction with charge characteristics of sorbent and adsorbate in order to gain a deeper understanding of the underlying interaction mechanisms. In this context, adsorption isotherms helped to elucidate differences in IgG adsorption to the two contact layer materials. Moreover, the significance of morphology, hydrophobicity, and chemical composition of the three contact layers on adsorption was considered. Reversibility of protein adsorption was addressed with exchange studies employing labeled and unlabeled IgG molecules. Finally, conclusions about expected protein losses due to adsorption are drawn and possible risks arising from structural alterations and the inherent reversibility of adsorption are discussed.

2 MATERIALS AND METHODS

2.1 Materials

2.1.1 Chemicals

NaHCO₃, Na₂CO₃, and dimethylsulfoxid (DMSO) were purchased from Merck Chemicals (Darmstadt, Germany). NaCl, KCl, Na₂HPO₄, and NaH₂PO₄ were supplied by VWR International (Darmstadt, Germany). NaOH (1 M), HCl (1 M), sodium dodecyl sulfate (SDS), and Rhodamine B isothiocyanate (Rh B ITC) were obtained from Sigma-Aldrich (Taufkirchen, Germany). Polysorbate 20 (PS 20) was kindly donated by Croda GmbH (Nettetal, Germany). Tetrahydrofurane (THF) was obtained from J.T. Baker (Deventer, Netherlands). Highly purified water used for buffer preparation was obtained from an arium® pro DI Ultrapure Water System (Sartoris Stedim Biotech GmbH, Goettingen, Germany) or a USF ELGA PURELAB Plus UV/UF purification system (ELGA LabWater, Celle, Germany). Buffer filtration (volumes ≥ 500 mL) was performed with pressurized nitrogen and 0.2 µm cellulose acetate filters (47 mm ø, Sartorius Stedim Biotech GmbH).

2.1.2 Model Antibody

A 33.4 mg/mL IgG1 antibody (148 kDa) drug substance solution in 20 mM histidine buffer (pH 5.4) was kindly donated by Roche GmbH (Penzberg, Germany).

2.1.3 Investigated Bags

Investigated bags included Flexboy® bags (50 L, Ref. FFB102340, Lot 10A22412) and a Standard Flexel® cubical Levmix bag (50 L, Ref. FXB111567, Lot 13A16150), both manufactured by Sartorius Stedim Biotech SA (Aubagne, France), as well as a PureFlex™ bag from Millipore Corporation (Billerica, MA, USA).

2.2 Methods

2.2.1 Bag Characterization

2.2.1.1 Laser Microscopy

Inner bag surface morphology was visualized using a Keyence VK-X210 3D laser scanning microscope (Keyence GmbH, Neu-Isenburg, Germany). The roughness parameters arithmetic mean roughness R_a and maximum height R_z were calculated according to the JIS standard B0601:2001 in the multi-line roughness mode with VK Analyzer Plus software version 3.3.0.0 from an average of $2 \cdot n + 1$ horizontal lines with $n=30$ and 10 skipped lines in-between. Cut-off values were set to $\lambda_c = 2.5$ mm and $\lambda_s = 8$ µm. Curvature was corrected via the 'correct tilt – sec curved surf. (auto)' function.

2.2.1.2 ATR-IR Microscopy

Infrared (IR) spectra of the inner bag surfaces as well as EVA reference films were recorded using the ATR-IR microscope Hyperion 2000 (Bruker Optics, Ettlingen, Germany) attached to a Bruker Tensor 27 Fourier Transform IR spectrometer. In order to reduce spectral contributions from atmospheric water vapor and carbon dioxide the system was purged with dry nitrogen and cooled with liquid nitrogen. The absorbance of every sample was recorded from 4000 to 1000 cm⁻¹ at three different

spots on the surface. Spectra were recorded with 120 scans using an ATR crystal at a contact pressure setting of 1 and a resolution of 4 cm⁻¹. Spectral data was evaluated using the Bruker Opus 6.5 software. All displayed spectra were vector normalized, smoothed (performed with 17 smoothing points), and baseline corrected via the concave rubberband method using 100 iterations. The three spectra obtained for one bag were averaged.

For the determination of the vinyl acetate (VA) content of the EVA layer of the Flexboy® bag, EVA reference films were cast from Elvax materials (see Table II-4). All Elvax grades were kindly donated by DuPont Packaging & Industrial Polymers (Neu-Isenburg, Germany). 0.1 g of each reference material (n=2) were dissolved in 10 mL of THF under stirring and heating to max. 60°C. The resulting solutions were poured into cleaned glass petri dishes (ø of 5 cm) and the solvent was allowed to evaporate under the fume hood. For further drying, the films were stored in an exsiccator for one week at room temperature. IR spectra of each reference film were recorded as described above. After vector standardization, the ratio of the peak heights at the absorption maxima at around 1737 cm⁻¹ and 1465 cm⁻¹ were calculated and plotted against the VA content.

Table II-4: EVA reference materials used for film casting.

Reference material	VA content [%]
Elvax 660A	12
Elvax 3150A	15
Elvax 460A	18
Elvax 3190A	25
Elvax 265A	28

2.2.1.3 Contact Angle Measurements

A Krüss Drop Shape Analyzer DSA25 (Krüss GmbH, Hamburg, Germany) was used to measure the contact angles of deionized water and diiodomethane on the EVA surface of the Flexboy® bag and on the ULDPE surface of the Flexel® bag via the sessile drop method. Using water, a drop of 2 µL was placed on the surface under investigation, for diiodomethane the drop volume was set to 1 µL. After manual baseline adjustment, contact angles on both sides of the drop were fitted by the Ellipse (Tangent-1) method. For every drop, three measurements were performed 20 seconds after the drop formation with 1 second delay between measurements. For the determination of the surface free energy of the polymer surfaces, the Owens-Wendt-Rabel-Kaelble analysis was applied to the contact angle data. This measurement procedure was repeated on three different spots on the two tested bags. Data evaluation was obtained using the ADVANCE software v1.1.0.2 and the surface tension values for the test liquids as stated in Table II-5.

Table II-5: Surface tension parameters of the test liquids used for contact angle measurements (according to Ström [30]).

Liquid	Surface tension [mN/m]	Polar component [mN/m]	Dispersive component [mN/m]
Water	72.8	51.0	21.8
Diiodomethane	50.8	0.0	50.8

2.2.1.4 Determination of Surface Tension with Test Inks

Alternatively, blue arcotest® test inks (Arcotest GmbH, Mönshheim, Germany) with defined surface tensions from 18 to 32 mN/m were applied to the Flexboy® and Flexel® bag surface for the determination of surface tension.

2.2.1.5 Zeta Potential Measurements

Zeta potential of the inner Flexboy® bag surface was measured using a SurPASS device (Anton Paar, Graz, Austria). Two bag pieces were fixed on opposite metal stamps using an adjustable gap cell with the inner surfaces pointed towards the measuring cell. The gap was adjusted so that the flow rate was between 100 and 150 mL/min under a maximum pressure of 300 mbar. A flow check was applied to obtain a constant flow in both directions. Before starting the measurement, the pH value of the 1 mM KCl model electrolyte solution was adjusted to pH 10.5 using 1 M NaOH. Automated titration from pH 10.5 to pH 2.25 was performed using 0.1 M HCl.

For measuring the zeta potential of a polyethylene surface similar to the Flexel® ULDPE contact layer, PE particles were produced with a Retsch CryoMill ball mill (Retsch®, Haan, Germany) from bag pieces made of pure polyethylene (Stomacher®, VWR, Darmstadt, Germany). The stainless steel milling jar with two milling balls (15 mm ϕ) was continuously cooled with liquid nitrogen before and during the milling process. After an initial cooling phase of 10 minutes at 5 Hz, two milling cycles of 5 minutes at 24 Hz with an intermediate cooling phase of 3 minutes at 5 Hz were applied. About 80 mg of the obtained PE particles were suspended in 11 mL of a filtrated (0.2 μ m PES) solution of 10 mM NaCl with 0.02 % polysorbate 20. The non-ionic surfactant had to be added to ensure proper particle wetting. Using 0.01 M NaOH and 0.01 M HCl, the pH was adjusted to defined values of 2, 3, 4, 6, 8, and 10. Zeta potential measurements of 800 μ L aliquots of these samples were performed in disposable folded capillary cells using a Zetasizer Nano-ZS (Malvern Instruments Ltd., Herrenberg, Germany) with three runs of 10 to 30 sub runs each. Analysis was performed at 25°C and a voltage of 50 V with automatic attenuator selection. Zeta potentials were calculated by the Zetasizer software v6.32 applying Smoluchowski theory and the 'auto mode' analysis model.

2.2.2 IgG Charge Characterization

2.2.2.1 Zeta Potential Measurements

The model IgG was dialyzed into 1 mM KCl using Vivaspin 20 ultrafiltration spin columns (Sartorius AG, Göttingen, Germany) with a molecular weight cut-off of 30,000 Da. Centrifugation was performed at 4000 rpm and 4°C for several times until buffer replacement was completed. The final IgG concentration was adjusted to 6 mg/mL. A filtrated (0.2 μ m PES) aliquot of 9 mL was transferred into a stirred polypropylene tube and by means of a Malvern MPT-2 Autotitrator, the pH of the sample was titrated from pH 2 to pH 10 in increments of 0.5 using 0.1 M NaOH and 0.1 M HCl. Zeta potential was measured in a connected disposable zeta cell placed inside a Zetasizer Nano-ZS (Malvern Instruments Ltd., Herrenberg, Germany) with three measurements per pH value of 10 to 30 sub runs each. Analysis was performed at 25°C and at a voltage of 50 V in 'monomodal mode' with automatic attenuation selection. The IEP of the IgG was calculated by the Zetasizer Software v6.32.

2.2.2.2 Isoelectric Focusing (IEF)

For the determination of the isoelectric point (IEP) of the model IgG, isoelectric focusing was performed on a Multiphor II™ electrophoresis system with an EPS 3501 XL power supply and a Multitemp III thermostatic circulator (GE Healthcare Europe GmbH, Freiburg, Germany). Precast Servalyt® Blank Precotes® electrophoresis gels with a pH gradient from 6 to 9 were used (Serva Electrophoresis GmbH, Heidelberg, Germany). As protein standard, 5 µL of the Serva Liquid Mix IEF Marker 3-10 were used. The protein concentration of the sample was 2 mg/mL in 20 mM histidine buffer pH 5.4. A volume of 10 µL was loaded on the gel. The Serva Violet 17 staining kit was used for gel staining. The staining protocol as recommended by the manufacturer was followed.

2.2.3 Sample Preparation

Adsorption isotherm experiments were conducted with diluted IgG solutions of concentrations between 0.1 and 5 mg/mL in 20 mM histidine buffer pH 5.4. In all following studies, IgG concentration was set to 2 mg/mL. Experiments with varying adsorption and desorption times were performed without further additives. For studies with varying pH and ionic strength (IS), various 20 mM histidine buffers were prepared via pH adjustment with 1 M NaOH and 1 M HCl. Ionic strength was set to either 50 or 100 mM via the addition of adequate amounts of NaCl. The iterative calculation process for the required amounts of salt is described in detail by Mathes [31]. The spreadsheet template was adapted to the histidine buffer system with $pK_{a1} = 1.8$, $pK_{a2} = 6.0$ and $pK_{a3} = 9.3$ as given by Lieberman, Marks and Peet [32]. IgG stock solution was diluted using the corresponding buffer to the final concentration of 2 mg/mL. The pH of all samples was checked using a Mettler Toledo MP220 pH meter (Mettler Toledo, Greifensee, Switzerland). Finally, all samples were filtered (0.2 µm PES). Protein concentration was verified by UV absorption at 280 nm using a Nanodrop Micro-Volume UV-Vis spectrometer (Nano Drop 2000, Thermo Scientific, Wilmington, USA) and an extinction coefficient of 1.51 cm²/mg.

2.2.4 HPLC Adsorption Studies

2.2.4.1 Standard Adsorption and Desorption Procedure

Pieces of 1.2 cm width and 2.2 cm length were cut out of the polymer bags. The outer faces of two pieces were mounted together using double-sided adhesive tape (tesa® Verlegeband, Ref. 05681-00018, Beiersdorf, Hamburg, Germany). Care was taken not to touch the inner surface of the bag at any time. Each piece was transferred into a flat base tube (VWR International, Darmstadt, Germany). The dimensions of the bag pieces were chosen so that they fitted exactly into the tube. Each bag piece was incubated with 3 mL of the appropriate IgG solution at room temperature for at least two hours (n=3). For isotherm determination, the equilibrium IgG concentration in the supernatant after incubation was determined using UV spectroscopy as described above. Subsequently, incubated bag pieces were rinsed five times with 3.5 mL of the corresponding placebo buffer. Therefore, tubes were centrifuged upside down using short spins of up to 1000 rpm between each washing step to remove excessive liquid. After cutting off the bag piece edges, each sample was transferred into a fresh tube and 2.8 mL of desorption medium (10 mM phosphate buffer with 145 mM NaCl and 0.05 % SDS, pH 7.2) was added. After desorption at room temperature for at least two hours, aliquots from the supernatant were transferred into HPLC glass vials (VWR, Darmstadt, Germany) and the IgG content was quantified via HP-SEC. The measures of each incubated bag piece were calipered and the corresponding adsorbed amount per unit surface area was determined.

For comparison, 5 mL Flexboy® bags were employed for adsorption studies. Incubation was performed with 4 mL of a 2 mg/mL IgG solution in 20 mM histidine buffer pH 5.4. For better handling, one side of the small-scale bags was cut open prior to performing seven washing steps with 4 mL placebo buffer each. Desorption medium volume was 4 mL.

2.2.4.2 HP-SEC Analysis of Desorbed IgG

The desorbed amount of IgG was determined via high-performance size-exclusion chromatography (HP-SEC) with an Agilent 1200 device (Agilent Technologies GmbH, Boeblingen, Germany) equipped with a HP 1046A fluorescence detector (Hewlett Packard, Palo Alto, CA, USA). A TSK Gel G3000 SWXL column with a SEC guard column was used (Tosoh Bioscience GmbH, Stuttgart, Germany). The mobile phase equaled the desorption medium (0.05 % SDS in 10 mM phosphate buffer pH 7.2 with 145 mM sodium chloride). Flow rate was set to 0.7 mL/min and injection volume was 300 μ L. A 6-point calibration curve was included in every run with reference concentrations of 0.01, 0.005, 0.001, 0.0005, 0.0002 and 0.0001 mg/mL IgG in desorption medium. All chromatograms were integrated manually using ChemStation software Rev. B.02.01-SR2 (Agilent Technologies GmbH). Fluorescence characteristics of the model IgG were evaluated with a Varian Cary Eclipse fluorescence spectrophotometer (Varian Deutschland GmbH, Darmstadt, Germany). IgG solutions at a concentration of 0.05 mg/mL in 20 mM histidine buffer pH 5.4 as well as in desorption medium containing 0.05 % SDS were analyzed as described by Mathes [31]. The resulting spectra shown in Figure II-6 indicate increased fluorescence intensity in the presence of SDS and the maximum quantum yield was obtained at an excitation wavelength of 279 nm and an emission wavelength of 336 nm. Accordingly, fluorescence quantification during HPLC analysis was performed at these wavelengths.

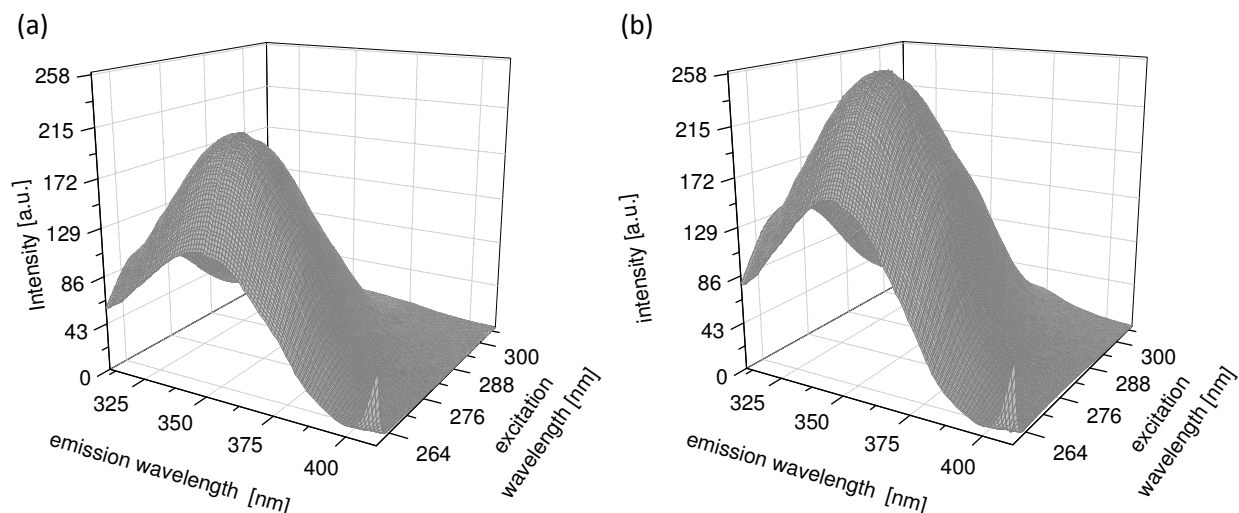


Figure II-6: Fluorescence spectra of IgG in (a) 20 mM histidine and (b) 10 mM phosphate buffer with 145 mM NaCl and 0.05% SDS.

2.2.5 Gold Staining of Adsorbed IgG

In order to visualize protein adsorbed to the different bag surfaces after incubation or remaining protein after SDS desorption, gold staining was performed. Bag pieces for staining were obtained via the above described adsorption and desorption process from incubation with IgG samples of pH 2, 6, and 10, all at 100 mM ionic strength. All pieces were washed using the corresponding placebo buffer and subsequently with deionized water in order to remove residual salts on the surface that might interfere with the gold staining [33]. Each bag pieces was transferred into a new tube and 3 mL gold

staining solution (Colloidal gold total protein stain, BioRad Laboratories, Munich, Germany) were added. After incubation at room temperature for 3 days, specimen were washed with deionized water and dried. For semi-qualitative information, reference staining included bag pieces that were incubated with IgG solutions of 0.0001 mg/mL, 0.001 mg/mL, and 0.01 mg/mL in 20 mM histidine buffer pH 5.4.

2.2.6 Replacement Studies with Fluorescently-Labeled IgG

Fluorescent labeling of IgG was performed using Rhodamine B isothiocyanate (Rh B ITC) dye (Sigma Aldrich GmbH, Taufkirchen, Germany). The model IgG was dialyzed into 1 M bicarbonate buffer pH 9 using a Vivaspin 20 tube (Sartorius Stedim biotech GmbH, Goettingen, Germany) with a molecular weight cut-off of 30,000 Da and centrifugation at 4000 rpm and 5°C. The final concentration was adjusted to 6 mg/mL. While stirring slowly, 105.6 μ L of a 20 mg/mL Rh B ITC stock solution in DMSO (Merck Chemicals, Darmstadt, Germany) were added to 10 mL of IgG solution under light protection. After incubation for 2 hours at room temperature, the conjugation buffer was again replaced by 20 mM histidine buffer pH 5.4 using ultrafiltration. Several centrifugation steps were performed to remove excess dye from the sample. The labeled IgG solution was filtered (0.2 μ m PES) and the final IgG concentration as well as the degree of labeling (DOL) were determined from UV absorbance at 280 nm and 557 nm using a Nanodrop Micro-Volume UV-Vis spectrometer. Calculations were performed as described elsewhere [34]. For replacement studies, the labeled IgG solution (IgG-Rho B, 9 mg/mL and DOL of 15 %) was diluted 1:500 with unlabeled IgG and concentration was adjusted to 2 mg/mL.

Bag pieces with 1.2 cm length and 0.8 cm width were cut out of the polymer bags. During incubation, the outer bag surface was covered with adhesive tape (tesa®, Beiersdorf, Hamburg, Germany), which was removed prior to microscopy due to its strong background fluorescence. In a first step, bag specimens were incubated with unlabeled IgG (2 mg/mL) for two hours. After washing with histidine buffer, samples were transferred into new 2 mL reaction tubes (Eppendorf AG, Hamburg, Germany) and subsequently incubated under light protection with the diluted IgG-Rho B solution for fixed time frames of 5 minutes to 48 hours. The same procedure was performed in reversed order (incubation with IgG-Rho B first followed by incubation with unlabeled IgG, both under light protection). After final rinsing with histidine buffer and deionized water, the dried bag pieces were fixed to a carefully cleaned object slide with the inner bag surface directed upwards. The positive control was incubated with fluorescently-labeled IgG only and the negative control with unlabeled IgG only for 48 hours. Microscopic measurements were accomplished using a Biozero BZ-8000 fluorescence microscope (Keyence GmbH, Neu-Isenburg, Germany) with a TexasRed filter system (λ_{ex} / λ_{em} : 560 nm / 630 nm) and 10x magnification. With a blank specimen that was in contact with histidine buffer only, exposure time was adjusted to 0.5 seconds.

2.2.7 Data Analysis and Statistics

Unless otherwise stated, results are presented as mean values with standard deviations (n=3). F-tests (equality of variances) were conducted with p=0.95. Significance testing was performed via the t-test function in Microsoft Excel 2010. Significance levels are indicated by asterisks: p < 0.05 (*), p < 0.01 (**), and p < 0.001 (***). Adsorption isotherms were calculated in Origin 8G (OriginLab Corporation, Northampton, MA, USA) using non-linear least square curve fitting with the Levenberg-Marquardt algorithm. Displayed HP-SEC chromatograms were obtained after curve smoothing using the Savitzky-Golay function in Origin 8G.

3 RESULTS

3.1 Characterization of the Fluid Contact Layers

3.1.1 Morphology

The micrographs shown in Figure II-7 depict significant differences in the morphology of the three tested bag types. The inner surface of the Flexboy® bag revealed a grid-like structure (see Figure II-8a). In contrast, the Flexel® surface exhibited a completely flat sheet structure with regular marks probably arising from polymer foil handling with rollers during film production [35]. The PureFlex™ film revealed unregular elevations of approximately 2 μm (see Figure II-8b). R_z and R_a values of the different bag surfaces were determined to be 1.108 μm / 0.167 μm for the Flexboy® bag, 0.736 μm / 0.091 μm for the Flexel® bag, and 1.137 μm / 0.129 μm for the PureFlex™ film.

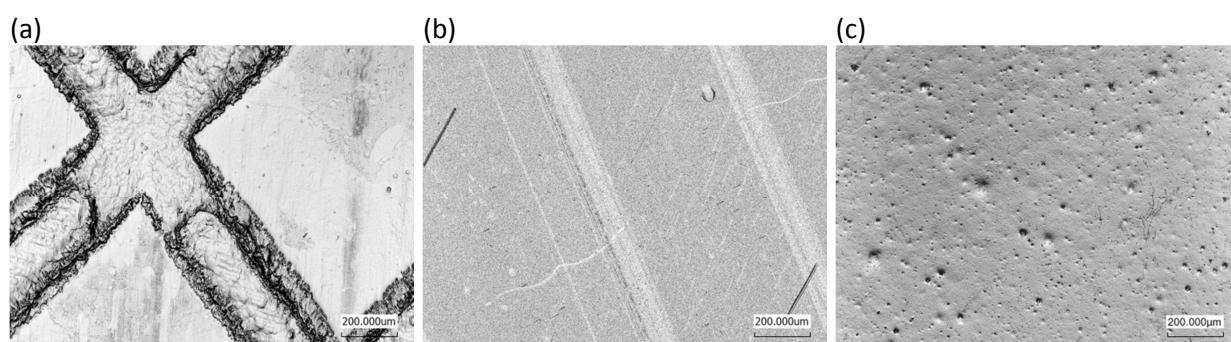


Figure II-7: The inner surface of (a) Flexboy®, (b) Flexel®, and (c) PureFlex™ bags examined with 3D laser microscopy with 10x magnification.

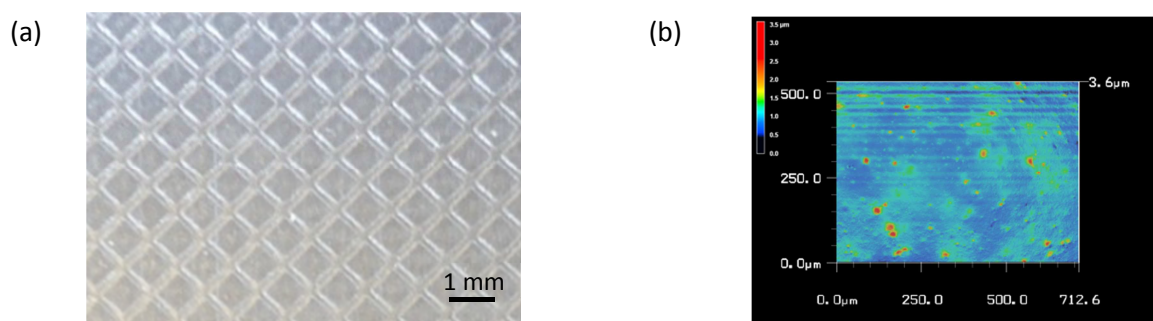


Figure II-8: (a) Photograph of the inner surface of a Flexboy® bag showing the regular grid-like morphology. (b) 3D display of the elevations on the surface of a PureFlex™ bag.

3.1.2 ATR-IR Microscopy

In order to confirm the composition of the fluid contact layers of the different bags, specifically to determine the vinyl acetate (VA) content of the inner Flexboy® bag surface, IR spectra were recorded in attenuated total reflection mode with an IR microscope (see Figure II-9). All spectra showed typical peaks arising from ethylene adsorption bands at 2920, 2850, and 1465 cm^{-1} [36]. In the Flexboy® bag spectrum, additional peaks from the vinyl acetate subunits could be identified at 1740, 1375, 1240, and 1020 cm^{-1} [12]. The PureFlex™ spectrum revealed two smaller extra peaks at 1639 and 1560 cm^{-1} , which might be related to not further specified additives [3,37,38].

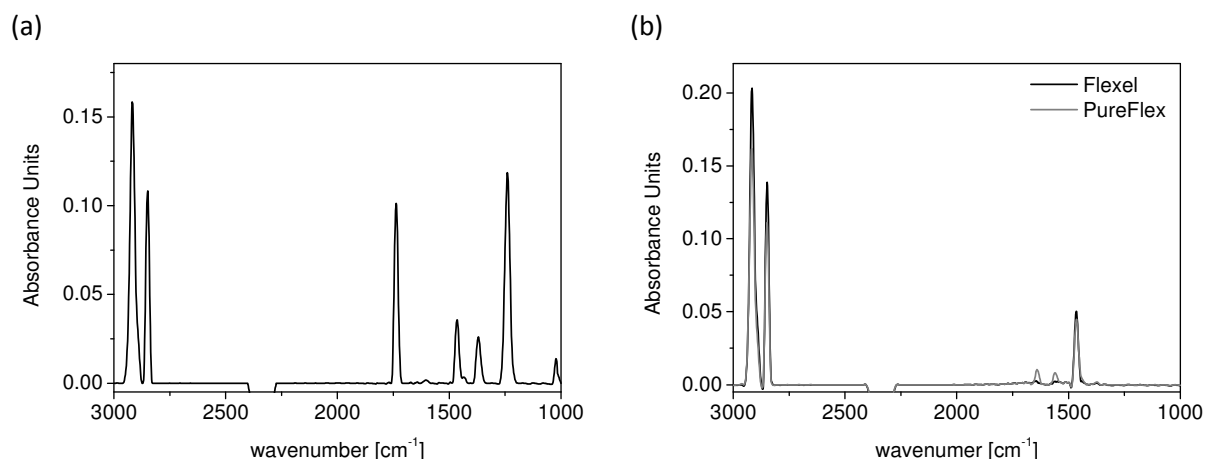


Figure II-9: FT-IR spectra of the inner surface of (a) the EVA contact layer of a Flexboy® bag and (b) the ULDPE contact layers of a Flexel® and a PureFlex™ bag.

As shown in Figure II-10, the VA content of the Flexboy® bag surface could be determined via the peak height ratio of the valence vibration of the carbonyl group in the VA subunit at 1737 cm^{-1} and the deformation vibration of the C-H bond in the ethylene subunit at 1465 cm^{-1} [39]. With a peak ratio of 2.75 ± 0.04 , the VA content of the bag material was 24.0 %. For EVA materials used for containers, the European Pharmacopeia limits the VA content to 25 % [12].

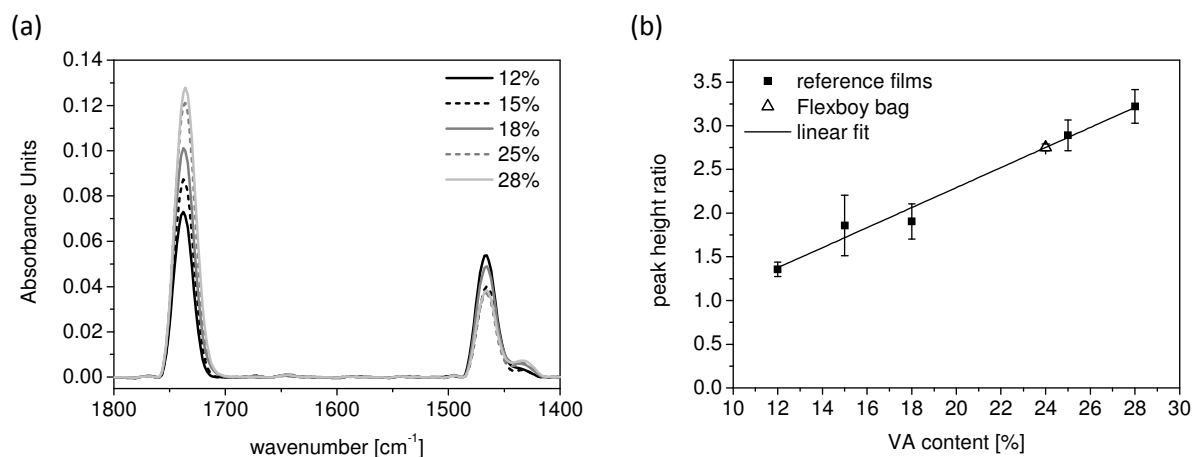


Figure II-10: (a) IR spectra of EVA reference films with varying VA content. (b) Plot of peak height ratio of the bands at 1737 and 1465 cm^{-1} versus VA content in %. Linear fit: $y = -7.7\text{E-}4 + 0.11466 \cdot x$ ($R^2 = 0.97508$).

3.1.3 Surface Free Energy

3.1.3.1 Contact Angle Measurements

The surface free energy as an important solid surface property can be obtained via measuring the contact angles with liquids of different surface tension and polarity. Drop shape analysis of the contact angles obtained for water and diiodomethane on Flexboy® and Flexel® bag pieces are shown in Figure II-11. The corresponding contact angles are summarized in Table II-6. Both bag surfaces exhibited high water contact angles of 87° and 97° , respectively. Upon contact with diiodomethane, the contact angles were 60° for the Flexboy® bag and 50° for the Flexel® surface.

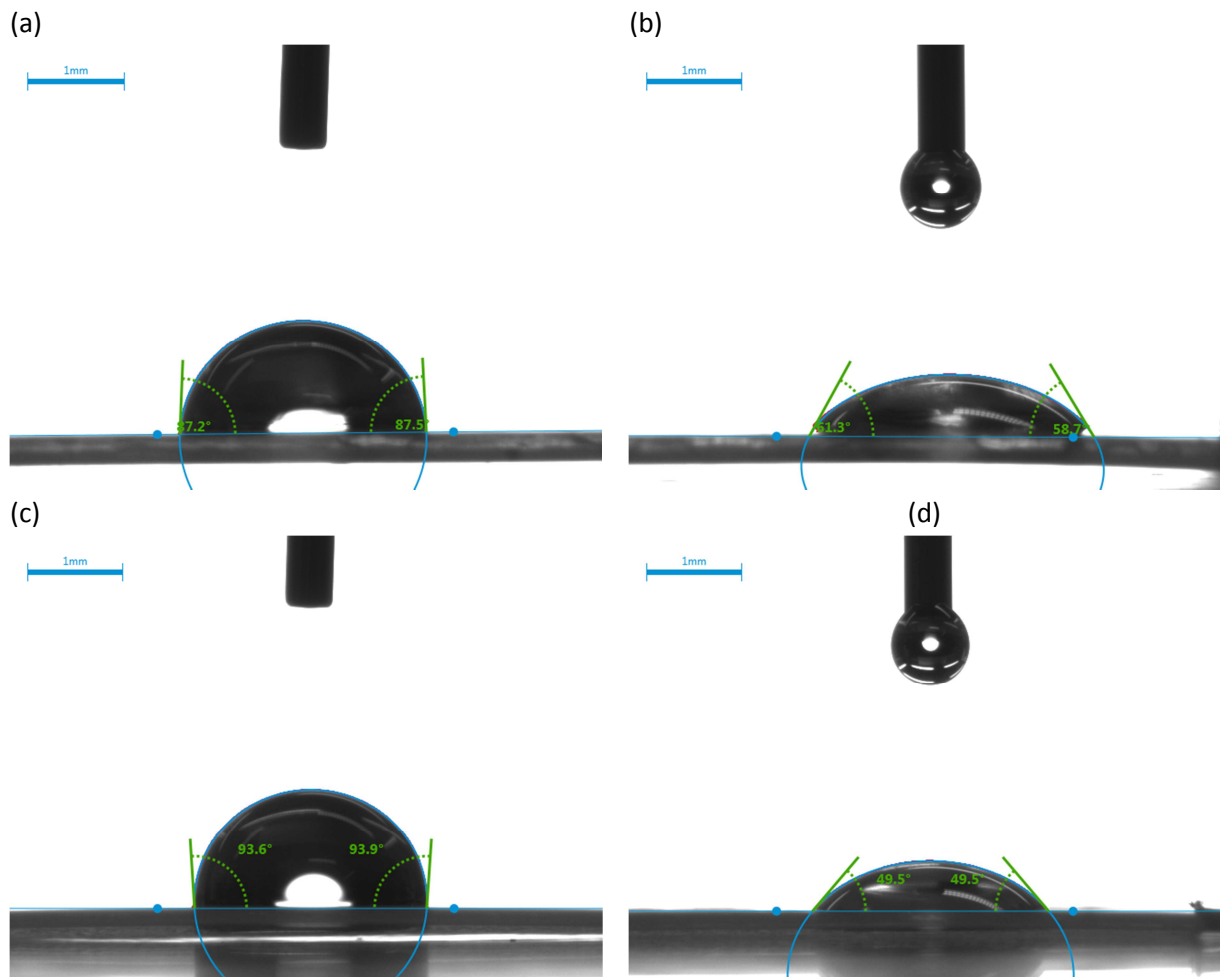


Figure II-11: Contact angle measurements with (a+b) Flexboy® and (c+d) Flexel® bag pieces. On the left side, drops of water on the bag surface are shown, the right side depicts measurements with diiodomethane.

Table II-6: Contact angles of Flexboy® and Flexel® bags with water and diiodomethane (n=3 with 3 sub measurements each).

Bag	Water	Diiodomethane
Flexboy	$86.6 \pm 1.1^\circ$	$60.0 \pm 2.6^\circ$
Flexel	$96.9 \pm 3.5^\circ$	$49.9 \pm 1.3^\circ$

Using the dispersive and polar components of the test liquid surface tensions as stated in Table II-5, the Owens-Wendt-Rabel-Kaelble analysis (see Table II-7) demonstrated that the polar components contributed about 12 % to the overall surface tension of 31.8 mN/m for the Flexboy® bag. The surface tension value for the Flexel® bag was slightly higher with hardly any polar contribution.

Table II-7: Surface free energy of the bag surfaces as obtained from the Owens-Wendt-Rabel-Kaelble analysis.

Bag	Surface tension [mN/m]	Polar component [mN/m]	Dispersive component [mN/m]
Flexboy	31.8 ± 1.0	3.7 ± 0.2	28.2 ± 0.7
Flexel	34.9 ± 0.5	0.5 ± 0.5	34.3 ± 0.9

3.1.3.2 Determination of Surface Tension with Test Inks

The surface tension of the polymer bags was additionally tested with a second method. Drops of test inks with defined surface tensions were placed on the surface of a Flexboy® and a Flexel® bag. As shown in Figure II-12, the test ink with 29 mN/m spread on both surfaces, whereas the test ink with 32 mN/m formed a defined drop and did not wet. Thus the surface tension of the two bag surfaces must be higher than or equal to 29 mN/m, but lower than 32 mN/m.

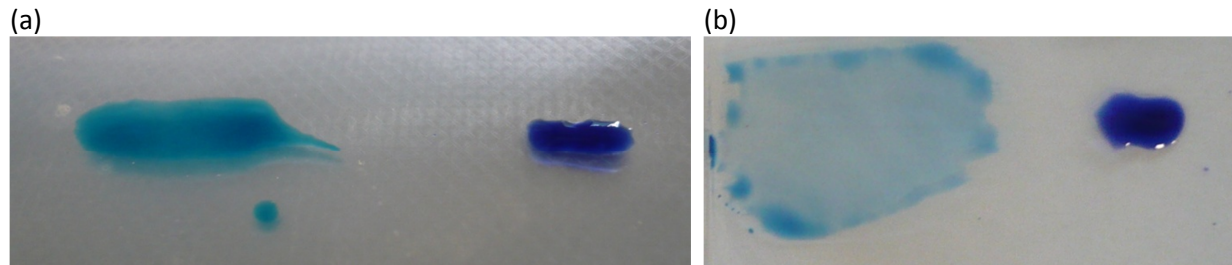


Figure II-12: Two different test inks (left: 29 mN/m and right: 32 mN/m) on the surface of the (a) Flexboy® bag and (b) Flexel® bag.

3.2 Charge Characterization of IgG and Contact Layer Materials

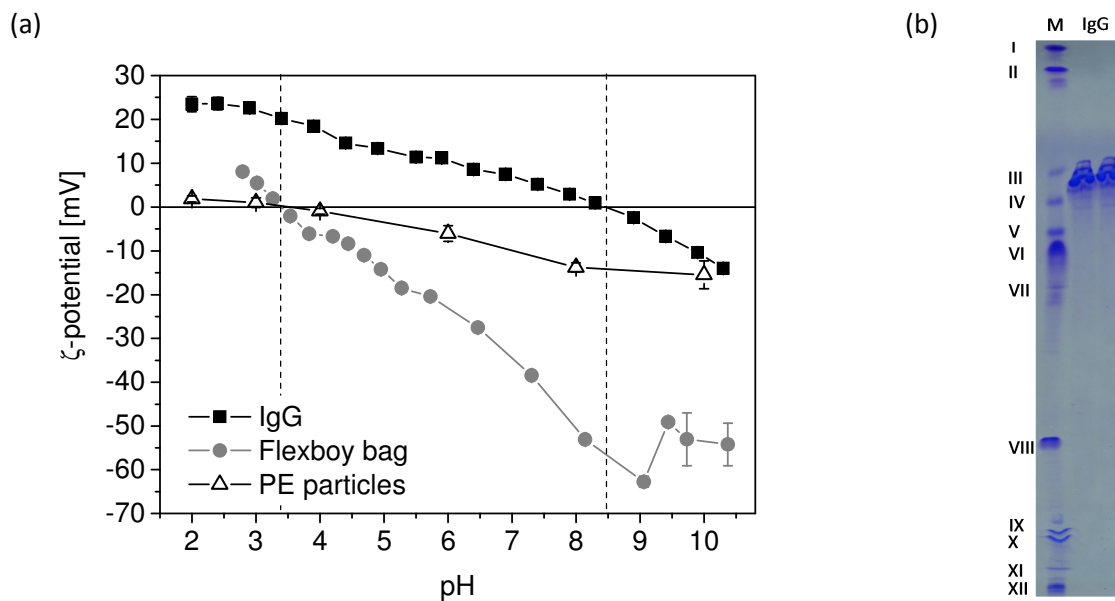


Figure II-13: (a) Electric charge of IgG, Flexboy® bag and PE particles depending on pH value determined from zeta potential measurements. (b) Isoelectric focusing gel for IEP determination of the model IgG. Marker (M) bands correspond to IEP values of I) 10.7, II) 9.5, III) 8.3, IV) 8.0, V) 7.8, VI) 7.4, VII) 6.9, VIII) 6.0, IX) 5.3, X) 5.2, XI) 4.5, XII) 4.2.

For the interpretation of electrostatic interaction forces between bag and protein, the surface charge of the bag surfaces and the IgG was determined via zeta potential measurements (see Figure II-13a). Below their zero point of charge at around pH 3.5, both polymer surfaces bear a limited positive charge. At pH 10, the zeta potential of PE particles was around -15 mV. The EVA surface of the Flexboy® bag was more negatively charged with a zeta potential of -54 mV. The IEP of the model IgG as determined from automatic titration with concurrent zeta potential measurement was 8.5. At lower pH values, IgG molecules are positively charged with a maximum of 23 mV at pH 2. At alkaline conditions of pH 10, the IgG molecules elicited a negative zeta potential of -14 mV.

Depending on the titration sequence, the IEP of the protein was found to vary slightly. Therefore, IEP was confirmed with isoelectric focusing (IEF). The IgG sample showed a dominant band between marker bands III and IV, indicative for an IEP between 8.0 and 8.3 (Figure II-13b). Only rather faint isoform bands were visible below and above the main band.

3.3 Adsorption Studies with HP-SEC Quantification

3.3.1 Adsorption Isotherms

The influence of IgG concentration on the adsorbed amount and therefore IgG affinity to the bag surfaces is shown in Figure II-14. Saturation was reached at around 2 mg/mL for the Flexboy® bag surface, for the Flexel® pieces surface coverage was already maximal at an IgG concentration of 1 mg/mL. Consequently, the IgG incubation concentration was chosen to be 2 mg/mL for all following experiments.

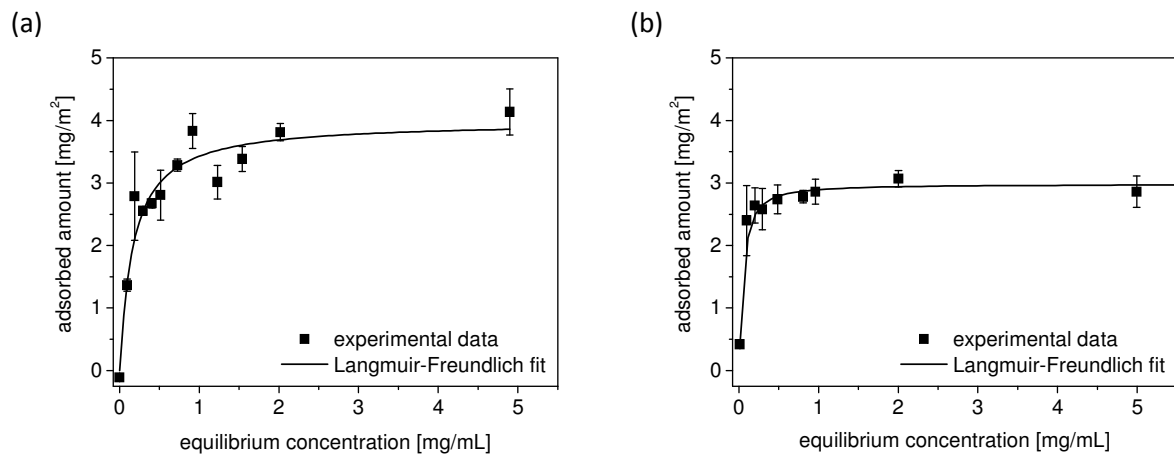


Figure II-14: Adsorption isotherms of the model IgG for adsorption to (a) Flexboy® and (b) Flexel® bag pieces.

Adsorption isotherms can be described by several fit functions including the Langmuir and the Langmuir-Freundlich fit. The Langmuir adsorption model was originally developed for the adsorption of gases to homogeneous and independent interaction sites on solids and is described by the following equation [40,41]:

$$\Gamma = \frac{\Gamma_{max} K c_{eq}}{1 + K c_{eq}}$$

$\Gamma_{(max)}$ equals the (maximum) adsorbed amount per unit surface area, K is described as equilibrium constant and c_{eq} is the equilibrium concentration of the adsorbing molecule, in this case the IgG concentration in the supernatant. As the assumptions made by the Langmuir model are often argued to be inadequate for describing the process of protein adsorption [41,42], a modification in the form of the Langmuir-Freundlich model was derived [43]:

$$\Gamma = \frac{\Gamma_{max} (K_m c_{eq})^n}{1 + (K_m c_{eq})^n}$$

In this model, K_m represents the mean binding affinity and equals K in the Langmuir equation for $n = 1$ [42]. The Langmuir-Freundlich fit assumes heterogeneous binding affinities that follow a quasi-Gaussian distribution function. The width of this distribution function is characterized by the heterogeneity index n with $0 < n < 1$ [42,44]. According to this definition, n values of less than 1

indicate surface heterogeneity. The mathematically equivalent Hill equation accounts for adsorption to homogeneous surfaces [44]. In this case, n is defined as the Langmuir-Freundlich coefficient number that serves as an indicator for the type and extent of adsorption cooperativity due to lateral interactions between the adsorbing molecules [41,44,45].

Table II-8: Parameters obtained by applying non-linear curve fitting to IgG adsorption isotherms.

Bag	Langmuir fit			Langmuir-Freundlich fit			
	Γ_{\max} [mg/m ²]	K [mL/g]	R^2	Γ_{\max} [mg/m ²]	K_m [mL/g]	n	R^2
Flexboy	4.01	5.90	0.899	3.98	5.95	1.03	0.887
Flexel	3.09	14.41	0.996	2.98	19.66	1.18	0.997

Both models resulted in fittings of comparable quality as indicated by the coefficient of determination R^2 in Table II-8. Independent of the applied model, the maximum adsorbed amount of IgG (in 20 mM histidine buffer pH 5.4, without further additives) was calculated to be 4 mg/m² for the Flexboy® bag surface and 3 mg/m² for the Flexel® bag. In both cases, the K or K_m values for IgG adsorption to the Flexel® surface were about three times higher than the constants for IgG adsorption to Flexboy® bags. This fact was accompanied by a slightly increased n -value in the Langmuir-Freundlich fit parameters for the Flexel® bag.

3.3.2 Influence of Adsorption and Desorption Time

To further characterize the IgG adsorption process, the incubation time was varied. The results in Figure II-15a indicate that IgG adsorption to the EVA surface of the Flexboy® bag pieces was completed after two hours. Longer incubation period did not lead to an increase in the amount of adsorbed IgG. For the Flexel® bag, the maximum adsorbed amount was already reached within the first hour of IgG incubation (see Figure II-15b). All samples contained 2 mg/mL of IgG in 20 mM histidine buffer pH 5.4.

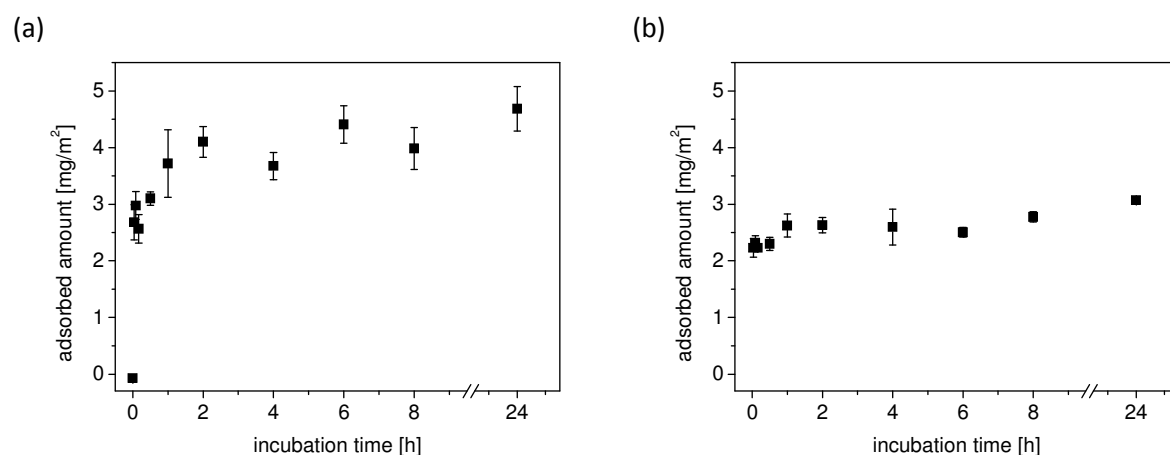


Figure II-15: Influence of incubation time on the adsorbed amount of IgG for (a) Flexboy® and (b) Flexel® bag.

Upon contact with the desorption buffer containing 0.05 % SDS, IgG was readily desorbed from the Flexboy® bag surface (see Figure II-16a). Desorption from the Flexel® bag surface took up to one hour to be completed (see Figure II-16b). In both cases, longer desorption periods did not result in an increase in the amount of IgG available for quantification. In contrast, increasing desorption times lead to increased tape extractable peaks in HP-SEC chromatograms as shown in Figure II-17. This

extra peak might impact IgG peak integration negatively and therefore desorption times should be kept to a minimum.

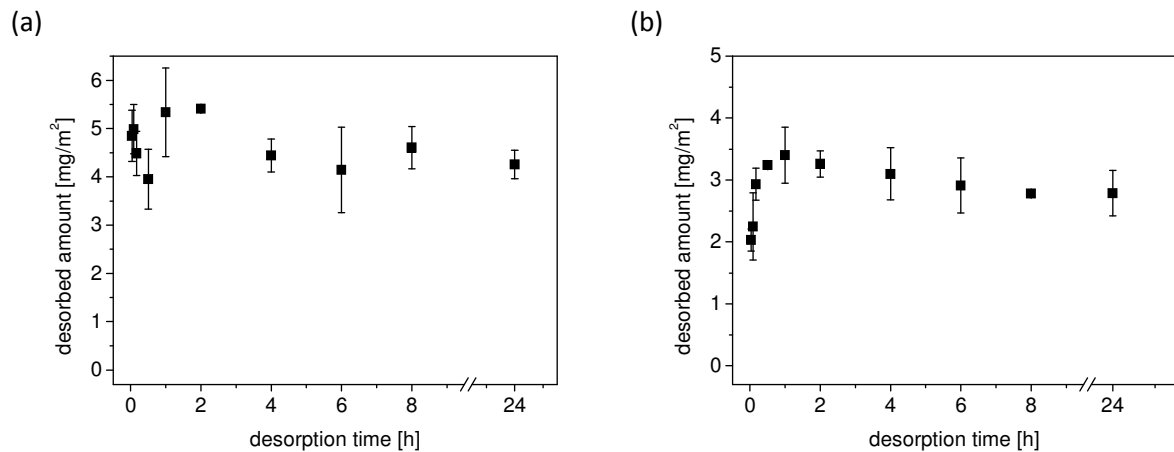


Figure II-16: Influence of desorption time on the amount of IgG available for HP-SEC quantification for (a) Flexboy® and (b) Flexel® bag.

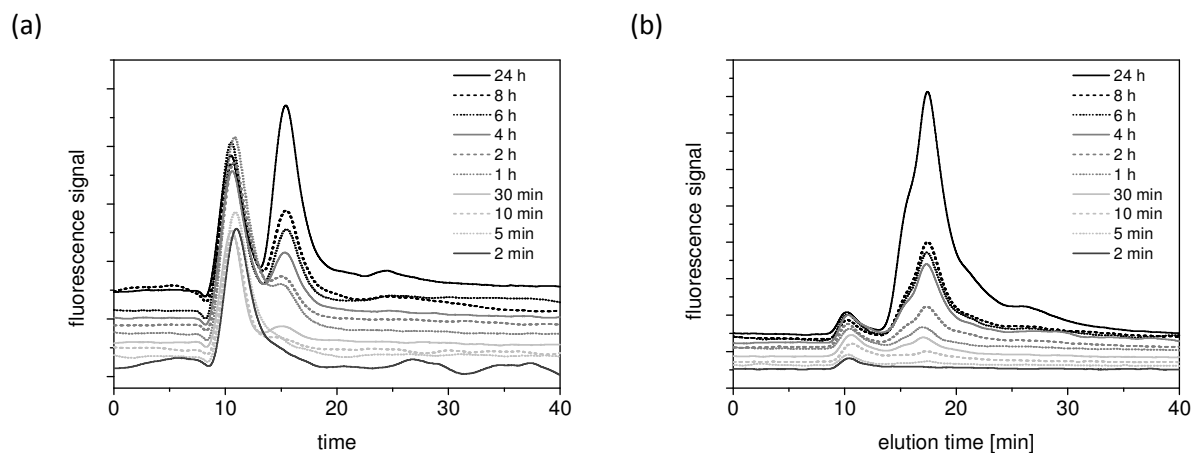


Figure II-17: HP-SEC chromatograms after IgG desorption from (a) Flexboy and (b) Flexel bag pieces. The peak at around 11 min RT corresponds to the IgG, the second peak at a RT of approx. 17 min was due to extractables from the double-sided adhesive tape used for bag piece preparation.

3.3.3 Influence of pH and Ionic Strength on IgG Adsorption

All previous experiments were conducted to gain insights into adsorption kinetics and to establish the experimental parameters for reliable quantification of IgG adsorption to bag films. By varying the formulation pH and ionic strength, the relevance of electrostatic interactions as potential driving forces for the adsorption process was evaluated.

Figure II-18a demonstrates the pronounced effect of pH on the adsorbed amount of IgG to the Flexboy® bag surface. For an ionic strength of 50 mM, the adsorption maximum was at pH 6 with an adsorbed amount of around 4 mg/m². Towards more acidic and more alkaline pH values, the adsorbed amount decreased to 2 mg/m². Samples with an increased ionic strength of 100 mM tended to result in slightly higher adsorbed amounts. Due to the overall rather high relative standard deviations of up to 30 %, this trend is only significant for pH 4 ($p < 0.05$). Hardly any influence of pH on the adsorbed amount to the Flexel® bag surface was observed (see Figure II-18b). Over the range of pH 3 to 9, the adsorbed amount was constantly between 2.7 and 3.8 mg/m², independent of the ionic strength of the applied formulation. At pH 2, the adsorbed amount was more than 4.5 mg/m²

and therefore comparably higher for both tested ionic strength values. The adsorbed amount at pH 10 was slightly decreased in comparison to all other tested pH values.

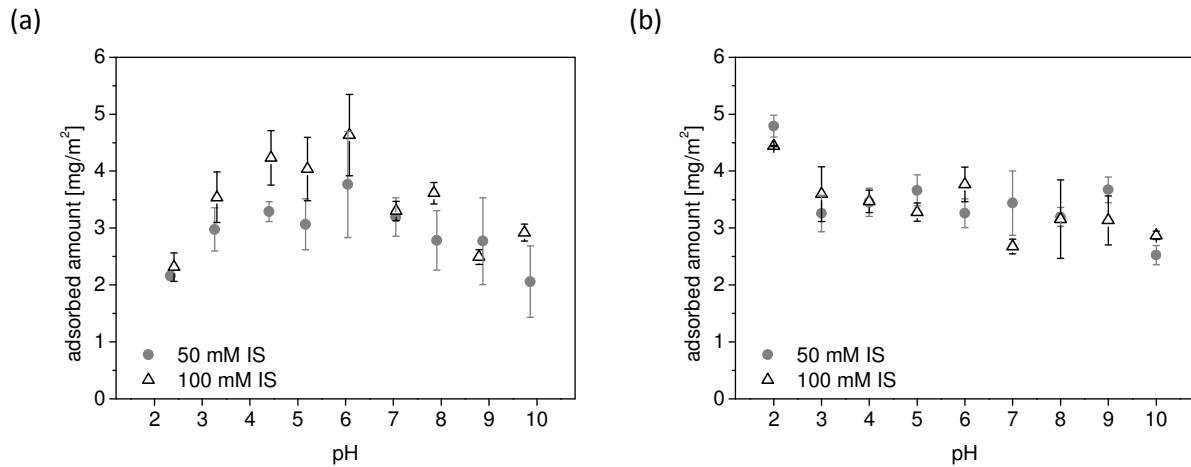


Figure II-18: Influence of pH and ionic strength (IS) on the adsorbed amount of IgG for (a) Flexboy® and (b) Flexel® bag.

IgG adsorption to the two bags with ULDPE contact layer, the Flexel® bag from Sartorius and the PureFlex™ bag from Millipore, was compared at pH 6 with 50 and 100 mM ionic strength. Figure II-19 shows that adsorption to the PureFlex™ film was slightly higher than adsorption to the Flexel® bag, especially for elevated ionic strengths of 100 mM ($p < 0.01$).

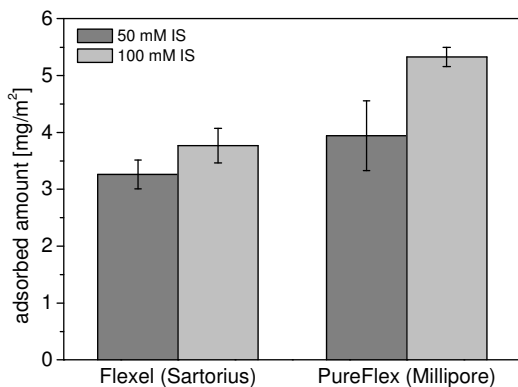


Figure II-19: Comparison of the adsorbed amount of IgG to two different bags with ULDPE contact layer: (a) Flexel® bag from Sartorius, (b) PureFlex™ film from Millipore.

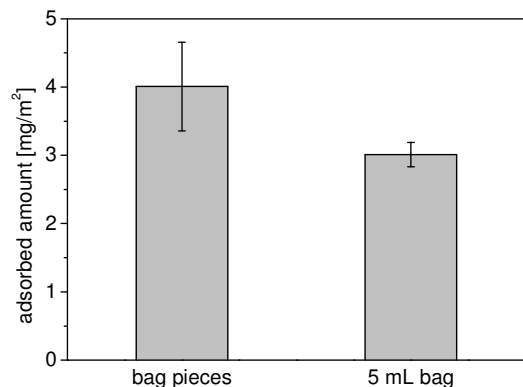


Figure II-20: Comparison of adsorbed amounts obtained for adsorption to (a) model bag pieces from Flexboy® bags and (b) 5 mL small-scale Flexboy® bags.

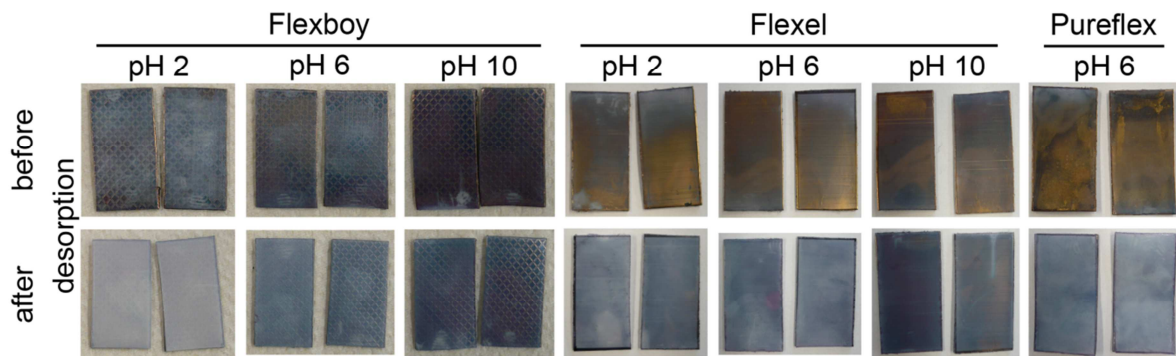
3.3.4 IgG Adsorption to 5 mL Flexboy® Bags

The setup with pieces produced from bag material was established due to its easy handling, the possibility for higher sample through-put, and for economic reasons as well. The validity of this model setup was confirmed by comparative testing with 5 mL small-scale Flexboy® bags as a whole on the other side. The adsorbed IgG amounts (see Figure II-20) were not identical, but comparable as indicated by significance testing ($p > 0.05$).

3.4 Verification of SDS Desorption Efficiency via Gold Staining

Analysis of IgG adsorption with the described setup relies on quantitative desorption of previously adsorbed IgG with SDS containing buffer. For verification of this assumption, gold staining as described by Eu *et al.* [28] was performed. Photographs of stained bag pieces of all three tested bag types before and after SDS desorption as well as reference stainings for semi-quantitative evaluation of the remaining amount of IgG after desorption are depicted in Figure II-21.

(a)



(b)

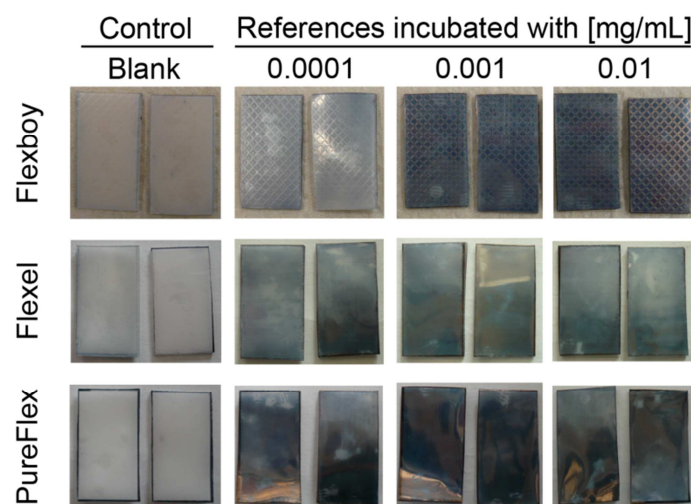


Figure II-21: Photographs of gold stained bag pieces. (a) Comparison of staining before and after desorption with SDS buffer. (b) References for semi-quantitative evaluation of the amount of IgG on the surface of stained bag pieces.

After incubation with IgG, gold staining of bag pieces resulted in a dark blue coloring (see Figure II-21a). Flexboy® bag pieces incubated at pH 10 appeared darker than after incubation at pH 2 or 6. For the ULDPE bag types, the coloring after IgG incubation with various pH values was comparable. After desorption with SDS containing buffer, the Flexboy® bag piece incubated at pH 2 was nearly colorless. All bag pieces incubated at pH 6 showed a light blue staining after desorption, whereas the coloring of both Flexel® and Flexboy® bag pieces incubated at pH 10 was slightly darker. Comparison with the references (see Figure II-21b) led to the conclusions that already highly diluted incubation solutions caused a significant blue coloring of the bag pieces. The amounts of IgG adsorbed onto Flexboy® and Flexel® bag pieces after incubation with these defined concentrations could be estimated with the calculated adsorption isotherms (see 3.3.1). The results are stated in Table II-9.

Table II-9: Received adsorbed amounts [mg/m²] on reference bag pieces determined using the Langmuir-Freundlich equation and corresponding fitting parameters.

adsorbed amount [mg/m ²]	Reference concentration [mg/mL]		
	0.0001 (Ref 1)	0.001 (Ref 2)	0.01 (Ref 3)
Flexboy®	0.0020	0.021	0.21
Flexel®	0.0019	0.029	0.38

Comparison of the degree of staining of bag pieces after desorption with the references enabled estimation of the amount of IgG remaining on the bag surface after desorption. For nearly all conditions, desorption efficiency was calculated to be 99 % or higher (see Table II-10). As anticipated from the slightly darker staining of samples incubated at pH 10, desorption efficiency – especially for the Flexboy® bag samples – was decreased, but still well above 90 %.

Table II-10: Calculation of SDS desorption efficiency.

Bag piece	Flexboy®			Flexel®			PureFlex™
	pH 2	pH 6	pH 10	pH 2	pH 6	pH 10	pH 6
Total adsorbed amount [mg/m ²]	2.3	4.6	2.9	4.4	3.8	2.9	5.3
Staining comparable to	Ref 1	Ref 2	Ref 3	Ref 1	Ref 1	Ref 2	Ref 1
Remaining protein [%]	0.09	0.45	7.2	0.04	0.05	1.0	0.04
Desorption efficiency [%]	99.9	99.5	92.8	> 99.9	> 99.9	99.0	> 99.9

3.5 Reversibility of IgG Adsorption

After buffer rinsing, IgG adsorbed to the bag surfaces could only be removed by means of a detergent like SDS. Nevertheless, IgG adsorption is claimed to be reversible in a sense that already adsorbed IgG molecules are in constant exchange with free IgG molecules from the bulk [22,46]. Replacement studies with fluorescently-labeled and native IgG molecules were performed in order to visualize this suggested reversibility. Figure II-22 clearly shows that samples pre-equilibrated with native IgG revealed faint fluorescence already after 30 minutes of contact with labeled IgG. The fluorescence signal increased steadily with longer contact times to labeled IgG solutions. Figure II-23 visualizes this reversibility for the replacement of labeled IgG molecules by native IgG as fluorescence signals diminished with increasing secondary incubation times. This control served as proof that replacement in the first experiment was not only due to an increase in the hydrophobicity of the IgG due to labelling [47]. In general, fluorescence signals were not evenly spread across the micrographs, but distinct clusters and structures with notably stronger fluorescence were observable.

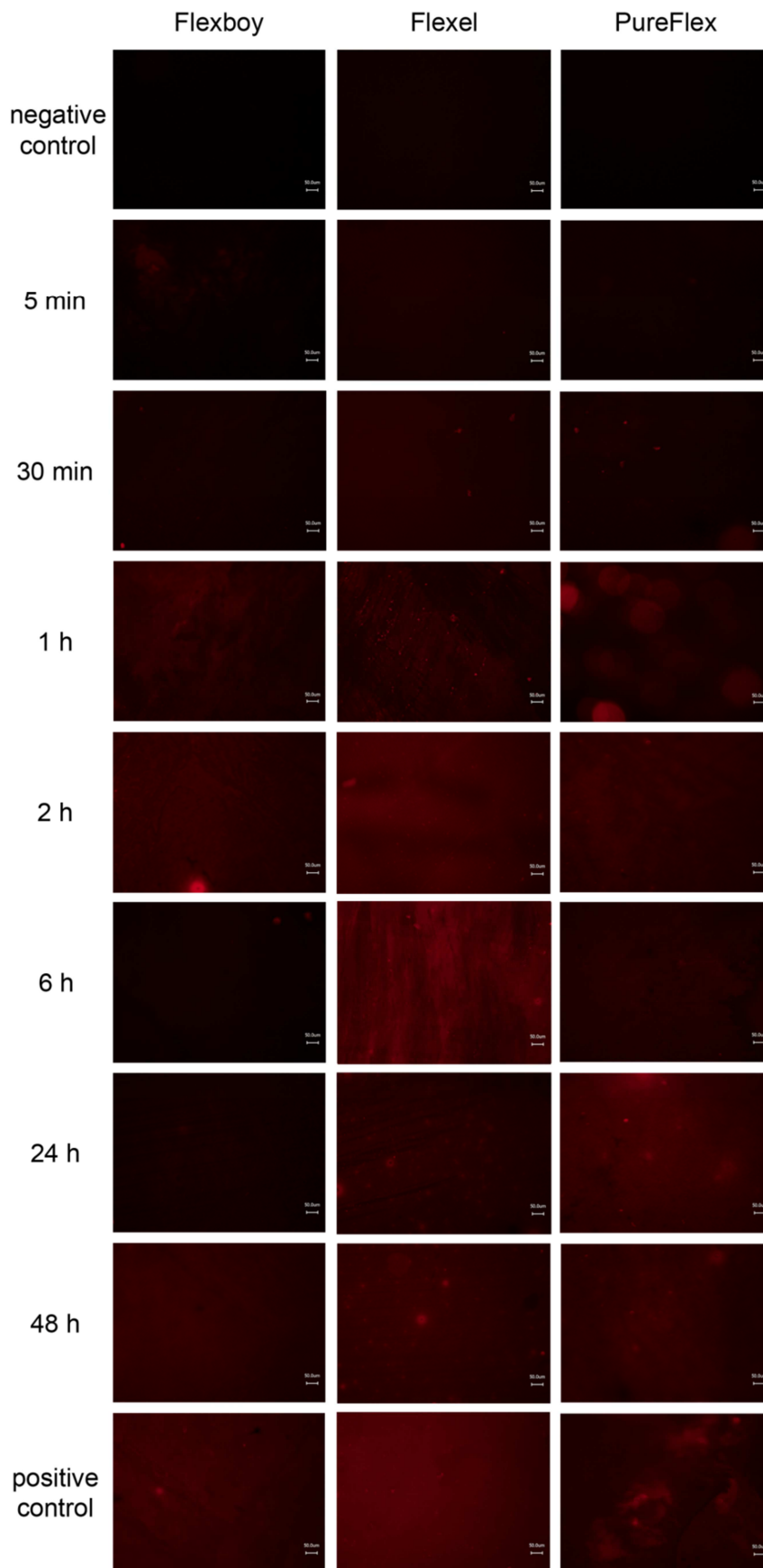


Figure II-22: Micrographs of bag pieces after pre-incubation with unlabeled IgG and subsequent incubation with Rhodamine B-labeled IgG. Incubation with labeled IgG was varied from 5 minutes to 48 hours.

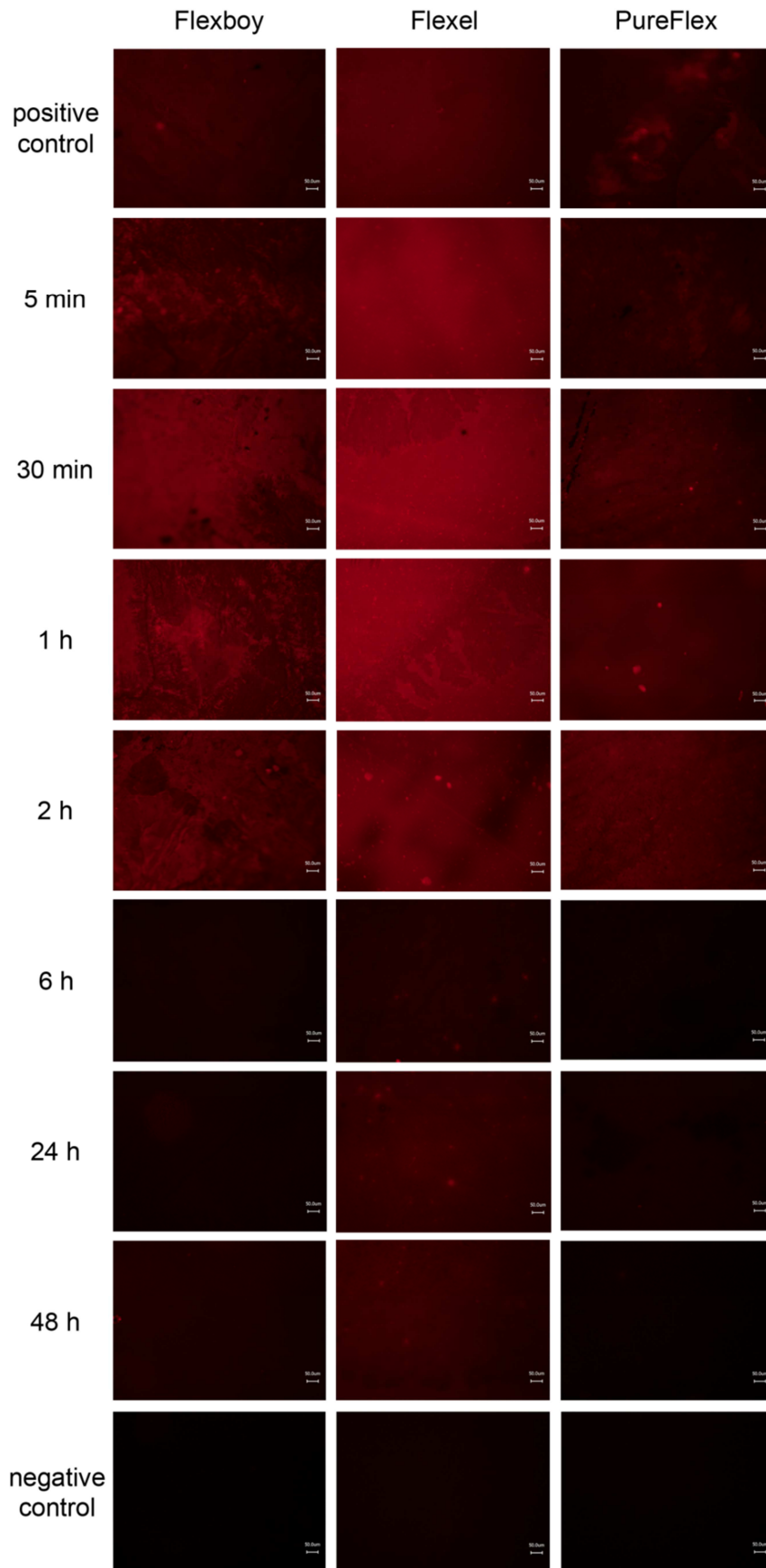


Figure II-23: Micrographs of bag pieces after pre-incubation with Rhodamine B-labeled IgG and subsequent incubation with unlabeled IgG. Incubation with unlabeled IgG was varied from 5 minutes to 48 hours.

4 DISCUSSION

4.1 The Influence of IgG and Surface Characteristics on IgG Adsorption

In the course of this study, the surfaces of single-use bioprocess bags as well as the model antibody were characterized in order to gain a detailed picture of the adsorption process. The characteristics of the interacting partners strongly influence the extent and also the kinetics of protein adsorption. In this context, important surface properties include morphology, surface energy, polarity, and charge [22].

The three investigated bags revealed distinct differences in surface morphology upon microscopic investigation. The EVA Flexboy® surface and the ULDPE PureFlex™ film were found to have similar surface roughness values, whereas R values for the Flexel® bag were on average 30 to 45 % lower. A possible influence of surface roughness on the adsorbed amount of protein has to be considered when comparing adsorption data. As an example, adsorption to the PureFlex™ surface was slightly increased in comparison to adsorption to the Flexel® bag despite otherwise identical chemical composition of the fluid contact layer. There are several studies that indicate enhanced protein adsorption with increasing surface roughness which is beyond the corresponding increase in specific surface area. The focus here is on roughness in the nano-scale range [48,49]. Rechendorff *et al.* [50] report increased adsorption for the anisotropically shaped fibrinogen to evaporated tantalum films when increasing root-mean-square roughness from 2.0 to 32.9 nm. However, adsorption of bovine serum albumin, a nearly globular protein, was less influenced by surface roughness. Elter *et al.* [51] demonstrated that the adsorbed amount of fibronectin to silicon wafers was higher on areas with a topographic nanostructure than on the planar reference. Deligianni *et al.* [52] also found higher adsorbed amounts of fibronectin on titanium alloys of increased surface roughness (R_a values of 0.320, 0.490, and 0.874 μm), whereas human serum albumin was adsorbed preferentially onto the smooth substrate. In contrast, from their studies on collagen adsorption to surfaces of controlled topography and surface chemistry, Denis and coworkers [53] concluded that surface topography does not influence the adsorbed amount, but the supramolecular organization of the adsorbed layer.

The determination of surface free energies via contact angle measurements is well accepted [54]. However, results have to be interpreted with care since surface roughness and chemical heterogeneity might have an impact on observed contact angles [55–57]. Moreover, it is often stated that the number and type of standard liquids as well as the calculation method strongly influence the obtained surface free energy values [55,58,59]. The surface free energy values obtained for the bag surfaces are nonetheless considered reliable since widely accepted standard test liquids were used and also the applied Owens-Wendt-Rabel-Kaelble analysis is known to result in useful and qualitatively reasonable data [58,59]. Additionally, experimentally determined value of 32 and 35 mN/m for EVA and PE, respectively, were close to the surface tension values obtained with test inks and to reported literature values. Owens and Wendt [60] report a surface tension of 33.2 mN/m for low-density polyethylene with a hydrogen bonding component of zero. Surface tension values between 17 mN/m and 32 mN/m were measured by Ali for various LDPE/EVA blends [61]. Michalski states a surface free energy value for EVA with 70 % VA content of 27.4 mN/m, with a nondispersive component contribution of 6.6 mN/m [59]. In a study by Devallencourt *et al.*, the surface free energy of an EVA film with 19 % VA content is given with 30.4 mN/m [62]. Although surface tension values for both bags were comparable, it became clear that the surface free energies of EVA and ULDPE differ in the contribution from polar components: ULDPE is a completely nonpolar material and

mainly hydrophobic interactions are expected during protein adsorption. By contrast, with EVA distinct contributions from polar interactions are anticipated.

A common rule of thumb claims that the more hydrophobic the surface, the greater is the extent of protein adsorption [15,17]. In the present case, this would implicit higher adsorbed amounts on ULDPE bags than on the EVA bag. When comparing the maximum adsorbed amounts Γ_{\max} obtained from isotherm fitting at pH 5.4, this hypothesis cannot be confirmed in our case. 4 mg/m² of IgG adsorbed to the EVA surface of the Flexboy[®] bag, whereas only 3 mg/m² were quantified on the ULDPE surface of the Flexel[®] bag. Only at a relative extreme acidic pH of 2 that induces protein unfolding, this relation is inverted. Indeed, Uettwiller *et al.* [63] did find higher adsorbed amounts on LDPE than on EVA with a bovine IgG formulated at 1 mg/mL in phosphate-buffered saline (PBS) pH 7.2. But there are several examples in literature that also give exceptions to this rule of thumb. Van der Veen *et al.* [64] measured higher plateau values for α -lactalbumin adsorption to the hydrophilic interface than to the hydrophobic one when choosing a protein concentration of 0.1 g/L. This effect was ascribed to faster spreading rates on the hydrophobic surface. In a study by Ho and Hlady [65] on the adsorption of low-density lipoprotein to a gradient surface with hydrophilic silica at one end and a self-assembled C-18 monolayer at the other, higher adsorption capacities and affinities were found at the hydrophilic end. Adsorption processes may therefore not always be entirely determined by hydrophobicity [15,66].

The zeta potential titration curves clearly indicated pH ranges for which electrostatic attraction or repulsion has to be considered. With a zero point of charge around 3.5, the zeta potential profiles of EVA and PE resemble typical polymer titration curves [67]. The absolute charge value for the PE particles was generally lower than for the EVA surface of the Flexboy[®] bag. This seems reasonable as the PE surface is very nonpolar, whereas EVA with a VA content of 24 % possesses a significant number of polarizable chemical groups. Of course, the influence of the varying solution properties employed during zeta potential measurements should be considered. However, it seems unlikely that a slightly increased ionic strength and the presence of a non-ionic surfactant during measurements with the PE particles would make up for such a considerable difference in absolute zeta potential values [67]. The presence of protein isoforms as visible in the IEF gel arises from protein fermentation and cannot be avoided [68]. For this model IgG, one isoform was strongly prevailing and the additional isoform bands were limited and rather faint. In conclusion, below a pH of 3.5 and above the IgG's IEP of around 8.0-8.5, both interaction partners were equally charged and electrostatic repulsive forces dominate. In-between these pH values, IgG and the bag surface were oppositely charged and electrostatically attracted each other. Due to the absolute charge values, this effect should be more pronounced with the EVA surface. Indeed, pH variations considerably affected the extent of IgG adsorption to EVA and resulted in an adsorption maximum at pH 6. Conversely, the adsorbed amount on the ULDPE bag surface stayed rather constant over a broad pH range. Likewise, an increase in ionic strength did not influence adsorption to the Flexel[®] bag, but slightly increased adsorption to the EVA surface. From his early studies on bovine serum albumin adsorption to hydrophobic and hydrophilic silica surfaces, MacRitchie also concluded that adsorption at a more hydrophilic surface is more sensitive to electrical factors [69].

However, the fact that even under electrostatic repulsive conditions a significant amount of IgG adsorbs to the polymer surfaces underpins the prevailing theory that not electrostatic forces but rather hydrophobic interactions are the main driving force for protein adsorption [16]. The entropy gain due to the release of surface bound water molecules and salt ions as well as due to

conformational changes of the protein compensates electrostatically unfavorable forces [22,70,71]. Especially immunoglobulins are considered to be “soft” proteins that readily undergo structural alterations during adsorption [17,22]. Moreover, nonuniformity of a protein’s local charge distribution in the 3D structure enables adsorption under overall repelling charge conditions as surface attachment can be promoted via distinct regional charge patches of opposite sign [72]. The often observed adsorption maximum at the protein’s IEP [22] could not be confirmed in this study. It is argued that at the IEP, electrostatic protein-protein repulsions are minimized and therefore a higher packing density on the surface is enabled [22]. For EVA, the adsorbed amount at pH 8, which is close to the IgG’s IEP, was lower than at pH 6, and for ULDPE the adsorbed amount was constant in the range of pH 3 to 9. An adsorption maximum shifted away from the IEP of the protein was also found by other authors. Mathes and Friess [25] investigated a monoclonal IgG1 with an IEP of approx. 8 and located the maximum of adsorption to glass vials at pH 4. Likewise, the maximum adsorbed amount of IgG1 on siliconized glass vials in a study by Höger *et al.* [26] was located at pH 4 to 5, with a second smaller maximum around the IEP of the protein.

4.2 Adsorption Isotherms and the Interplay of Hydrophobic and Electrostatic Forces

Electrostatic interactions also impact adsorption kinetics. The adsorption rate is anticipated to be higher with electrostatic attraction due to an accelerated protein migration towards the surface [22]. Analyzing the influence of incubation time on the amount of adsorbed IgG revealed that adsorption to the nonpolar ULDPE bag surface was completed within one hour. Saturation of the EVA surface was not achieved until two hours of incubation time. Consequently, the hydrophobicity aspect might be once again more important in this case. Besides, a denser packing of 4 mg/m² on EVA compared to 3 mg/m² on ULDPE may be a result of re-arrangement of individual IgG molecules, which simply might take more time. Overall, IgG adsorption was fast as already after a few minutes a substantial amount of IgG was found on the investigated surfaces. In his review, Gray schedules initial protein adsorption events even to microseconds to milliseconds [72].

The fact that hydrophobicity is an important factor for IgG affinity to the bag surfaces can also be concluded from the three times higher ULDPE equilibrium constant K / mean binding affinity K_m obtained from isotherm calculations (see 3.3.1). An increased K value indicates a higher adsorption than desorption rate [66]. Moreover, adsorption saturation at the ULDPE surface was reached at lower equilibrium concentrations. Both observations might direct towards increased spreading and structural adaptations of IgG molecules on the more hydrophobic ULDPE surface. Generally, structural alterations are supposed to be more likely with soft proteins and hydrophobic surfaces [16] as well as at low surface-coverages [18]. Upon spreading, the IgG molecule’s footprint on the adsorbing surface increases and saturation is achieved with less IgG molecules and thus lower adsorbed amounts. It might also be argued that IgG adsorption to EVA and ULDPE occurs in different favored molecular orientations including end-on with Fab-up or Fab-down orientation, side-on, and flat-on [15,73,74]. For cytochrome c, Lee and Saavedra [74] showed that molecular orientation and therefore adsorbed amounts indeed can vary with surfaces of different chemical properties. Since the jamming limit of surface coverage is usually unknown, calculating the favored orientation based on actual adsorbed amounts seems rather speculative. Although protein adsorption was observed to result in mainly monolayers, surface filling can range from closely-packed molecules to incomplete surface coverage [70,75]. Hlady and Buijs [76] indicate that under most conditions, IgG adsorbs in an end-on orientation probably with the Fc part directed towards the surface. Under the assumption of an end-

on orientation in a closely-packed monolayer, Buijs *et al.* state adsorbed IgG amounts between 2.6 and 5.5 mg/m² [77]. The results for IgG adsorption to both ULDPE and EVA were within this range. Additionally, the absence of steps or inflection points in the adsorption isotherms supports the suggested formation of a monolayer only [78].

For both bag materials isotherms approached a plateau, which is typical for protein adsorption [16,17]. Coefficients of determination were comparable for both applied fitting functions, namely the Langmuir and the Langmuir-Freundlich fit. Therefore, the Langmuir model seemed to be suitable for the description of IgG adsorption in this case despite its inappropriate postulates based on the reversible adsorption of gases to solids [79]. However, this agreement might be only accidental and isotherms should be interpreted carefully [40,69]. Due to the fact that during protein adsorption each molecule usually forms several surface interaction sites, interacts with other protein molecules, and adsorbs irreversibly to the surface, many authors prefer the Langmuir-Freundlich fit [41–43,66]. This fitting function includes the parameter n , which can be an indicator for cooperativity during adsorption. The value of n is influenced by both interactions between protein and surface and lateral interactions between adsorbing proteins. Luo and Andrade describe the degree of cooperativity to be partially positive for n values between 1 and 1.5 [45]. The values obtained for IgG adsorption to the EVA and ULDPE bag surfaces were within this range. Koopal *et al.* confirmed that positive cooperativity in general is more common than negative cooperativity [44], although e.g. J. Mathes and K. Höger obtained n values of less than 1 for IgG and lysozyme adsorption to borosilicate glass vials [31,80]. Due to the two different possible definitions for n with regards to cooperativity or heterogeneity, the calculated, apparent n value might be influenced by contributions from both intrinsic heterogeneity of the surface and adsorbate-specific nonideal behavior. The extended Langmuir-Freundlich equation for monocomponent adsorption by Koopal *et al.* takes both factors into account [44]. Moreover, Luo and Andrade found cooperativity to be dependent on protein concentration when studying adsorption of several model proteins like lysozyme, BSA, transferrin, and lactoferrin onto hydroxyapatite. With the help of Hill plots, they could define three stages of cooperativity in most of the studied adsorption isotherms [45]. The calculated n values of 1.03 and 1.18 for EVA and ULDPE, respectively, might thus represent an overall cooperativity value only and individual n values for different stages during adsorption might partly be even higher. Similarly, Rabe *et al.* discuss apparent non-cooperativity as a result from balanced positive and negative cooperative effects [22]. The different phases during protein adsorption and the corresponding interaction forces that determine cooperativity will be discussed in more detail in the next chapter.

4.3 Impact of IgG Adsorption on Protein Loss in the Bulk

From an industrial point of view, protein losses are of main interest in adsorption studies. Protein losses in percent were calculated based on the maximum adsorbed amount of 4 mg/m² as determined for IgG adsorption to the Flexboy® surface and the inner surface areas of various bag sizes as stated by the manufacturer (Table II-11). For the calculations, nominal fill volumes were assumed. Especially with higher concentrated IgG solutions of 100 mg/mL, the expected loss is below 0.04 % in any case and therefore most likely not even detectable. Only in small bags with higher surface area to volume ratios and at low protein concentrations in the bulk or only partial filling, protein loss might be measurable. For example, at an IgG concentration of 1 mg/mL, the loss upon storage in a 5 mL bag was calculated to be 0.4 %. For a bag filled at only 25 %, losses would increase to 1.3 %. For IgG adsorption to Flexel ULDPE bag, even lower percentages of losses are to be expected. In this case, the maximum adsorbed amount was only 3 mg/m² and bag capacities range

from 50 up to 1000 L. These findings are confirmed by Uettwiller *et al.*, who calculated IgG losses (1 mg/mL, 5°C storage) to be 0.22 % in a 30 mL Celsius-Pak with EVA contact layer and 0.011 % in a 50 mL Flexel 3D bag with LDPE contact layer. The basis for this extrapolation were adsorbed IgG amounts of 4.8 mg/m² for the Stedim 71 (EVA) material and 5.6 mg/m² for the Stedim 40 (LDPE) film material [63].

In summary, loss due to protein adsorption is negligible for the studied system. An overview given by Nakanishi *et al.* indicates that for most systems studied in literature, adsorbed amounts were in the lower mg/m² range [17]. Therefore, as a general rule, loss due to protein adsorption does not seem to be crucial [20]. Exceptions to that rule are of course highly diluted protein solutions. As an example, Hawe and Friess [81] report losses of a hydrophobic cytokine formulated at 0.25 mg/mL due to adsorption to glass vials of up to 10 %, and McLeod *et al.* [27] attributed Factor VIII activity losses of up to 60 % upon storage in PVC mini-bags to adsorption effects.

Table II-11: Anticipated protein loss in the bulk due to adsorption to the bag surfaces based on a maximum adsorbed amount of 4 mg/m². *: nominal filling according to stated bag size. A 15 % overfill can typically be applied.

Bag size	inner surface [cm ²]	adsorbed IgG [mg]	loss in concentration at nominal* filling [µg/mL]	Loss in bulk [%] at nominal filling			loss in concentration at 25% filling [µg/mL]	Loss in bulk [%] at 25 % filling		
				1 mg/mL IgG	10 mg/mL IgG	100 mg/mL IgG		1 mg/mL IgG	10 mg/mL IgG	100 mg/mL IgG
5 mL	42	0.017	3.36	0.3360	0.0336	0.0034	13.44	1.3440	0.1344	0.0134
50 mL	143	0.057	1.14	0.1144	0.0114	0.0011	4.58	0.4576	0.0458	0.0046
150 mL	275	0.110	0.73	0.0733	0.0073	0.0007	2.93	0.2933	0.0293	0.0029
250 mL	329	0.132	0.53	0.0526	0.0053	0.0005	2.11	0.2106	0.0211	0.0021
500 mL	452	0.181	0.36	0.0362	0.0036	0.0004	1.45	0.1446	0.0145	0.0014
1 L	707	0.283	0.28	0.0283	0.0028	0.0003	1.13	0.1131	0.0113	0.0011
3 L	1346	0.538	0.18	0.0179	0.0018	0.0002	0.72	0.0718	0.0072	0.0007
5 L	1929	0.772	0.15	0.0154	0.0015	0.0002	0.62	0.0617	0.0062	0.0006
10 L	3528	1.411	0.14	0.0141	0.0014	0.0001	0.56	0.0564	0.0056	0.0006
20 L	4826	1.930	0.10	0.0097	0.0010	0.0001	0.39	0.0386	0.0039	0.0004
50 L	8106	3.242	0.06	0.0065	0.0006	0.0001	0.26	0.0259	0.0026	0.0003

4.4 Evaluation of the Applied Quantification Method

As the relative amount of adsorbed protein was low, it was not possible to measure the adsorbed amount via depletion in the bulk solution. The depletion method combined with simple UV quantification of the protein content with or without preceding SEC analysis was applied in many studies using model surfaces with high surface areas like polystyrene latex particles [82], micro- and nanoparticles made from various materials [83], or glass beads [84,85]. For real container surfaces, more sensitive detection methods have to be applied. With the help of radioisotope-labeled molecules, adsorption can be measured directly on the surface of interest [86–88] or again via depletion in the incubation solution [89]. Other methods like total organic carbon (TOC) analysis after oxidative hydrolysis use rather harsh conditions in order to remove adsorbed protein quantitatively from the sorbent surface [31,90]. Such harsh conditions are not applicable to plastic polymers of single-use bags due to compatibility issues. Therefore, Uettwiller and coworkers [63] analyzed the adsorbed amounts of IgG and BSA on single-use containers via quantitative amino acid analysis including a desorption step with 5% acetic acid under sonication. Subsequently, acid hydrolysis with 6 N HCl was performed at 110°C for 24 hours followed by amino acid derivatization with phenylisothiocyanate (PITC). PITC conjugation made amino acids accessible to UV quantification after reversed-phase HPLC. In contrast, the herein described method is rather simple, fast, and at the same time applicable to the real bag surface. Adsorbed protein was available for quantification via HP-SEC with fluorescence detection after one single desorption step with a phosphate buffer containing 0.05 % SDS. This method was adapted from previous studies by J. Mathes [31] and K. Höger [80] and benefits from the high sensitivity of fluorescence spectroscopy in combination with higher quantum yields in the presence of SDS. Via gold staining before and after IgG desorption and upon visual comparison with stained references, the almost quantitative desorption of IgG from the studied EVA and ULDPE bag surfaces by the detergent SDS was proven. Adsorption isotherms together with the stained references were employed to estimate the amount of protein remaining on the bag surfaces after desorption. In most cases, desorption efficiency was determined to be 99 % or higher. As an exception, IgG adsorbed to the EVA surface at pH 10 could be removed less efficiently at an extent of 92.8 %. The maximum desorbed amount available for quantification was obtained within one hour of incubation with SDS. In literature it is described that SDS is very well suited to desorb proteins from various surfaces. Brash and Horbett claim that one possible mechanism for this process is solubilization involving complex formation between adsorbed proteins and surfactant [15]. In their studies, Liu and Craig showed that a buffer solution containing 17 mM SDS was able to remove 90% of lysozyme from a hydrophobic model surface [91]. Likewise, Mulzer and Brash used tris buffer containing 2 % SDS for the desorption of plasma proteins adsorbed to glass beads [92].

For experimental validation and qualification studies during the implementation of bag systems, commercially available small-scale bags, but also bag pieces as described here can be used for adsorption studies. During the course of this study, adsorbed amounts were not only quantified with Flexboy® bag pieces, but also with 5 mL Flexboy® bags. Thus, the validity of results obtained from studies with bag pieces was verified. Adsorbed amounts were slightly, but not significantly reduced when performing adsorption studies with 5 mL bags. This tendency might have different reasons. The surface area to volume ratio for the small-scale bag setup was 0.1 cm²/mL and therefore only half as for the setup with bag pieces in tubes (surface area to volume ratio of 0.2 m²/mL including tube walls). Moreover, diffusion of IgG molecules to the surface might be hindered in small-scale bags. Despite near maximal filling, the 5 mL bag remained rather flat and especially in the edge regions

capillary effects might inhibit free diffusion of protein molecules to unoccupied spots on the inner bag surface. Wahlgren and Arnebrant describe transport to the surface as the first important step during the whole adsorption process [18]. Several authors claim that this step might even be adsorption rate-determining [24,87]. Incubation time was chosen long enough to achieve saturation, but when keeping the ongoing spreading of adsorbed proteins on the respective surface in mind, it becomes clear that hindered diffusion might indeed reduce the amount of adsorbed protein [16]. Consecutively, rather slowly arriving molecules might not be able to occupy initially free space on the surface because in the meantime, this spot might be covered by previously adsorbed, spreading molecules [64]. In conclusion, the established model setup with bag pieces was found to be appropriate to study protein adsorption. With this setup, sample handling is facilitated and higher sample through-put than with small-scale bags is feasible. Additionally, resource consumption in the form of protein solution and bag material is reduced.

4.5 Adsorption Reversibility and Consequences

One of the paradoxes in protein adsorption described by Ramsden is the shown concentration dependency of adsorption that is normally expected for a reversible process only [75]. It is well accepted that the adsorption process is usually not reversible upon dilution or rinsing with buffer [15–17,87], because the multiple interaction sites between protein and surface would all have to break at the same time to enable desorption [15]. Nevertheless, at equilibrium a constant exchange of adsorbed molecules with molecules from the bulk solution is assumed [22,46]. In this context, fibrinogen turnover on glass was demonstrated by Chan and Brash via replacement studies with differently radioisotope-labeled proteins [86]. In the present study, IgG replacement between adsorbed and free molecules was studied with fluorescently-labeled IgG molecules. Artefacts can arise from increased hydrophobicity of labeled molecules and the thus increased propensity for non-specific adsorption [22,47]. This was taken into account by utilizing two experimental setups: incubation of bag surfaces with labeled IgG molecules and subsequent exposure to unlabeled IgG, and vice versa. With both incubation schemes, replacement of the previously adsorbed species during the second incubation step could be observed. This confirms the prevailing theory that adsorbed proteins diffuse back into the bulk solution [18–20]. It is discussed whether detached molecules which became structurally perturbed at the surface can have negative immunogenic effects or serve as seeds for aggregation.

Fluorescence of adsorbed IgG-Rho B was not evenly distributed over the investigated bag areas. On the contrary, localized spots with high fluorescence signals indicated some kind of clustering of adsorbed IgG molecules. Rabe et al. ascribe this surface clustering of molecules to either diffusion of surface bound molecules towards precursor aggregates or the direct adsorption of bulk monomers in close proximity to already adsorbed molecules or aggregates. This guiding of newly arriving molecules implies cooperativity between adsorbed and adsorbing molecules. Alternatively, protein assemblies formed in solution can direct deposit onto the surface and result in clusters [22]. Using atomic force microscopy (AFM), Herrig *et al.* were able to visualize surface clusters of the protein ezrin when adsorbed to supported lipid bilayers [93]. AFM pictures from studies by Hoehne *et al.* [85] and Mathes [31] also indicate an uneven distribution of model antibodies upon adsorption to glass. The phenomenon of cluster formation is especially well studied for lysozyme adsorption on mica surfaces [94–96].

5 SUMMARY AND OUTLOOK

The described setup is well-suited for quantifying adsorption of therapeutic proteins to disposable bag materials. Bag pieces for incubation were prepared by sticking two film sheets together using double-sided adhesive tape, with the inner bag surfaces facing outside. After incubation with the protein solution under investigation and few washing steps, adsorbed protein was readily desorbed with SDS containing buffer. Subsequently, the IgG content could easily be analyzed with HP-SEC and fluorescence detection. Desorption efficiency was visualized by gold staining and for most cases estimated to be $\geq 99\%$. Initial adsorption as well as desorption events occurred within minutes and were completed within one to two hours at a maximum. Adsorbed amounts obtained with small-scale bags were comparable and thus confirmed the validity of the more convenient experimental setup with bag pieces.

The present study showed that adsorption of a model IgG (IEP of approx. 8.2) to single-use bag surfaces with ULDPE and EVA contact layer was governed by hydrophobic as well as electrostatic interactions. With the more polar surface EVA, electrostatic interactions were more important than for the non-polar ULDPE surface. The adsorption maximum for the EVA surface was located at pH 6 and increased ionic strength led to slightly higher adsorbed amounts of around 5 mg/m^2 . On ULDPE, adsorbed amounts were consistently around 3.5 mg/m^2 for pH values between 3 and 9, variations in ionic strength did not have any impact at all. With the help of adsorption isotherms, the higher affinity of the model IgG to the more hydrophobic ULDPE was shown.

“General truths” that attribute adsorption maxima to the IEP or commonly expect increased adsorption on more hydrophobic surfaces could thus not be confirmed. These assumptions have to be verified on a case-by-case basis, since adsorption is strongly influenced by surface and protein properties. Even the amount of adsorbed protein on the two ULDPE surfaces differed slightly, indicating that different bag types indeed have specific characteristics based on their production and final processing conditions [5]. Polymer surfaces can be comprehensively characterized by the described methods. Surface morphology was visualized using 3D laser scanning microscopy, FT-IR measurements confirmed the chemical composition of the polymers, surface charge was analyzed with zeta or streaming potential measurements, and surface tensions were determined using contact angle measurements and test inks. The model protein was characterized in terms of its overall surface charge at different pH values. When comparing adsorption of different proteins, further influencing factors like size, stability, and hydrophobicity of each protein have to be investigated as well.

Depending on pH, adsorbed amounts were in the range of 2 to 5 mg/m^2 . Loss due to protein adsorption at relevant conditions was therefore demonstrated to be negligible, especially with higher concentrated formulations and at maximal filling volumes. More critical might be structural alterations due to adsorption in conjunction with the proven exchange of adsorbed molecules with molecules in the bulk. However, assessing structural alterations directly when adsorbed to real, imperfect surfaces is challenging. The detection of desorbed protein in the bulk is equally ambitious, since the fraction of exchanged and perturbed molecules in the bulk is expected to be rather small. Moreover, most spectroscopical methods perform an averaging of protein structure signals over the observed protein population [15,76]. The occurrence and the extent of structural perturbations might be different for every single molecule, depending on its residence time and available space on the surface [97]. Brash and Horbett assume that the structure of adsorbed proteins ranges from

native to, at most, partially unfolded [15]. Nevertheless, several authors found significantly perturbed structures for desorbed proteins using circular dichroism. Soderquist and Walton report marked decreases in α -helical content of albumin and fibrinogen after desorption from copolypeptide and silicone surfaces. Similarly, γ -globulin lost most of its β -sheet structure [98]. Chan and Brash eluted human fibrinogen from a Pyrex glass surface using a highly concentrated Tris buffer (1 M) and suggest a 50 % loss in α -helical content due to adsorption [99]. After desorbing bovine serum albumin (BSA) and hen's egg lysozyme from silica particles via displacement with morpholine, Norde and Favier found reduced α -helical contents at low surface coverages. At saturation conditions, the reduction in α -helical content was insignificant for lysozyme, and BSA recovered most of its native structure during displacement [100]. With regards to therapeutic proteins, Hoehne *et al.* investigated structural changes of three humanized antibodies upon adsorption to glass particles. Infrared spectroscopy and front-face fluorescence quenching measurements revealed only minor perturbations in secondary and tertiary structure, respectively [85]. In the context of possible structural alterations arising from protein adsorption, immunogenicity of adsorbed proteins is discussed. Shomali *et al.* [101] as well as van Beers *et al.* [102] addressed this issue in immunogenicity studies with mice by injecting glass and other particles with adsorbed antibodies or recombinant human interferon beta, respectively. Immunogenicity resulting from protein adsorption could not be proven conclusively, especially as a potential immunogenic impact of the particles themselves should be considered.

Apart from investigations on protein structure after adsorption, more detailed insights into adsorption kinetics and the adsorption process itself are of interest. An elaborated study on IgG adsorption kinetics using quartz crystal microbalance (QCM) with ULDPE and EVA model surfaces is described in the next chapter.

6 ABBREVIATIONS

ATR-IR	attenuated total reflectance infrared
C_{eq}	equilibrium concentration of the adsorbing molecule
CZ	Crystal Zenith
DEHP	diethylhexylphthalate
DMSO	dimethylsulfoxid
DOL	degree of labeling
EVA	ethylene vinyl acetate
EVOH	ethyl vinyl alcohol
HP-SEC	high-performance size-exclusion chromatography
IEF	isoelectric focusing
IEP	isoelectric point
IgG	immunoglobulin G
IgG-Rho B	IgG labeled with Rhodamine B
IS	ionic strength
IV	intravenous
K	equilibrium constant
K_m	mean binding affinity
LDPE	low-density polyethylene
LLDPE	linear low-density polyethylene
M	molar
mAb	monoclonal antibody
n	heterogeneity index / Langmuir-Freundlich coefficient number
NaCl	sodium chloride
\emptyset	diameter
PA	polyamide
PBS	phosphate-buffered saline
PE	polyethylene
PES	polyethersulfone
PET	polyethylene terephthalate
PP	polypropylene
PS 20	polysorbate 20
PVC	polyvinyl chloride
PVDC	polyvinylidene dichloride
R_a	arithmetic mean roughness
RhB ITC	Rhodamine B isothiocyanate
rpm	revolutions per minute
RT	retention time
R_z	maximum height
SDS	sodium dodecyl sulfate
THF	tetrahydrofuran
ULDPE	ultra-low density polyethylene
VA	vinyl acetate
ZPC	zero point of charge
$\Gamma_{(max)}$	(maximum) adsorbed amount per unit surface area

7 REFERENCES

- [1] N. Riesen, R. Eibl, Single-Use Bag Systems for Storage, Transportation, Freezing, and Thawing, in: R. Eibl, D. Eibl (Eds.), *Single-Use Technology in Biopharmaceutical Manufacture*, John Wiley & Sons, Inc., Hoboken, New Jersey, USA, 2011: pp. 13–20.
- [2] R. Eibl, M. Löffelholz, D. Eibl, Single-Use Bioreactors - An Overview, in: R. Eibl, D. Eibl (Eds.), *Single-Use Technology in Biopharmaceutical Manufacture*, John Wiley & Sons, Inc., Hoboken, New Jersey, USA, 2011: pp. 33–51.
- [3] G.A. Sacha, W. Saffell-Clemmer, K. Abram, M.J. Akers, Practical fundamentals of glass, rubber, and plastic sterile packaging systems, *Pharm. Dev. Technol.* 15 (2010) 6–34.
- [4] M. Barbaroux, A. Sette, Properties of materials used in single-use flexible containers: Requirements and analysis, *Biopharm Int.* (2006). Available online at: <http://www.biopharminternational.com/properties-materials-used-single-use-flexible-containers-requirements-and-analysis> (accessed November 8, 2011).
- [5] S. Vanhamel, C. Masy, Production of Disposable Bags: A Manufacturer's Report, in: R. Eibl, D. Eibl (Eds.), *Single-Use Technology in Biopharmaceutical Manufacture*, John Wiley & Sons, Inc., Hoboken, New Jersey, USA, 2011: pp. 113–134.
- [6] Sartorius Stedim Biotech GmbH, Standard Flexboy® bioprocessing bags, Data Sheet Vers. 07/2011. Available online at: http://www.sartorius.de/fileadmin/DID/pdf/DID_Lit_Collection/Data_Flexboy_Standard_Bags_SPL2003-e.pdf (accessed December 5, 2014).
- [7] Sartorius Stedim Biotech GmbH, Flexel® Palletank® for LevMixer®, Data Sheet Ver. 03/2010.14. Available online at: http://www.sartorius.de/fileadmin/DID/pdf/DID_Lit_Collection/Data_Flexel3D_LevMix_System_for_Palletank_SPT2012-e.pdf (accessed December 5, 2014).
- [8] Sartorius Stedim Biotech GmbH, Flexel® 3D Bags for Palletank®. Available online at: <https://www.sartorius.com/en/products/bioprocess/single-use-bioprocess-bags/flexel-bags/flexel-3d-bags-for-palletank/> (accessed August 23, 2015).
- [9] EMD Millipore Corporation, PureFlex™ Single-Use Process Container Films, Specification Sheet 2014. Available online at: http://www.emdmillipore.com/Web-US-Site/en_CA/-/USD/ShowDocument-Pronet?id=201306.14007 (accessed December 5, 2014).
- [10] Sartorius Stedim Biotech GmbH, Technical Specifications for Flexboy® Bags, Data Sheet Ver. 08/2012. Available online at: http://www.sartorius.de/fileadmin/fm-dam/DDM/Bioprocess-Solutions/Fluid_Management/Flexboy_Bags/Data_Sheets/Technical_Specifications_Flexboy_Bags_SL-1102-e.pdf (accessed December 5, 2014).
- [11] Sartorius Stedim Biotech GmbH, Technical Specifications for Flexel® 3D Bags, Data Sheet Ver. 08/2012. Available online at: http://www.sartorius.de/fileadmin/fm-dam/DDM/Bioprocess-Solutions/Fluid_Management/Flexel_3D_Bags/Data_Sheets/Technical_Specifications_Flexel_3D_Bags_SL-1101-e.pdf (accessed December 5, 2014).

- [12] European Directorate for the Quality of Medicine (EDQM), 3.1.7 Poly(ethylene-vinyl acetate) for containers and tubing for total parenteral nutrition preparations, in: European Pharmacopoeia, 7th ed., 2011.
- [13] R.J. Hernandez, Food Packaging Materials, Barrier Properties, and Selection, in: K.J. Valentas, E. Rotstein, R.P. Singh (Eds.), Handbook of Food Engineering Practice, CRC Press LLC, Boca Raton, Florida, USA, 1997: pp. 286–355.
- [14] K.K. Dohrer, L.G. Hazlitt, N.F. Whiteman, Short Chain Branching Distribution of ULDPE, *J. Plast. Film Sheeting*. 4 (1988) 214–226.
- [15] J.L. Brash, T.A. Horbett, Proteins at Interfaces: An Overview, in: T.A. Horbett, J.L. Brash (Eds.), Proteins at Interfaces II - Fundamentals and Applications, American Chemical Society, Washington, DC, 1995: pp. 1–23.
- [16] W. Norde, My voyage of discovery to proteins in flatland ...and beyond, *Colloids Surf. B. Biointerfaces*. 61 (2008) 1–9.
- [17] K. Nakanishi, T. Sakiyama, K. Imamura, On the adsorption of proteins on solid surfaces, a common but very complicated phenomenon, *J. Biosci. Bioeng.* 91 (2001) 233–44.
- [18] M. Wahlgren, Protein adsorption to solid surfaces, *Trends Biotechnol.* 9 (1991) 201–208.
- [19] W. Norde, C.A. Haynes, Reversibility and the Mechanism of Protein Adsorption, in: T.A. Horbett, J.L. Brash (Eds.), Proteins at Interfaces II - Fundamentals and Applications, American Chemical Society, Washington, DC, 1995: pp. 26–40.
- [20] F. Felsovalyi, P. Mangiagalli, C. Bureau, S.K. Kumar, S. Banta, Reversibility of the adsorption of lysozyme on silica, *Langmuir*. 27 (2011) 11873–82.
- [21] W. Norde, Proteins at Solid Surfaces, in: A. Baszkin, W. Norde (Eds.), Physical Chemistry of Biological Interfaces, Marcel Dekker, Inc., New York, 2000: pp. 115–135.
- [22] M. Rabe, D. Verdes, S. Seeger, Understanding protein adsorption phenomena at solid surfaces, *Adv. Colloid Interface Sci.* 162 (2011) 87–106.
- [23] B.R. Young, W.G. Pitt, S.L. Cooper, Protein adsorption on polymeric biomaterials I. Adsorption isotherms, *J. Colloid Interface Sci.* 124 (1988) 28–43.
- [24] B.R. Young, W.G. Pitt, S.L. Cooper, Protein adsorption on polymeric biomaterials II. Adsorption Kinetics, *J. Colloid Interface Sci.* 125 (1988) 246–260.
- [25] J. Mathes, W. Friess, Influence of pH and ionic strength on IgG adsorption to vials, *Eur. J. Pharm. Biopharm.* 78 (2011) 239–47.
- [26] K. Höger, J. Mathes, W. Frieß, IgG1 Adsorption to Siliconized Glass Vials-Influence of pH, Ionic Strength, and Nonionic Surfactants., *J. Pharm. Sci.* 104 (2015) 34–43.
- [27] A.G. McLeod, I.R. Walker, S. Zheng, C.P. Hayward, Loss of factor VIII activity during storage in PVC containers due to adsorption, *Haemophilia*. 6 (2000) 89–92.

- [28] B. Eu, A. Cairns, G. Ding, X. Cao, Z.-Q. Wen, Direct visualization of protein adsorption to primary containers by gold nanoparticles, *J. Pharm. Sci.* 100 (2011) 1663–70.
- [29] S.S. Qadry, T.H. Roshdy, H. Char, S. Del Terzo, R. Tarantino, J. Moschera, Evaluation of CZ-resin vials for packaging protein-based parenteral formulations, *Int. J. Pharm.* 252 (2003) 207–12.
- [30] G. Strom, Contact angles, work of adhesion, and interfacial tensions at a dissolving Hydrocarbon surface, *J. Colloid Interface Sci.* 119 (1987) 352–361.
- [31] J.M. Mathes, Protein Adsorption to Vial Surfaces – Quantification, Structural and Mechanistic Studies, Cuvillier Verlag, Göttingen, Germany, 2010.
- [32] M. Lieberman, A. Marks, A. Peet, Marks' Basic Medical Biochemistry, 4th ed., Lippincott Williams & Wilkins, Philadelphia, PA, 2013.
- [33] Bio-Rad Laboratories Product Information: Colloidal Gold Total Protein Stain. Available online at: http://www.bio-rad.com/LifeScience/pdf/Bulletin_9112.pdf (accessed October 22, 2014).
- [34] Thermo Scientific, 2011. Tech Tip #31: Calculate dye:protein (F/P) molar ratios. Available online at: <http://www.piercenet.com/files/TR0031-Calc-FP-ratios.pdf> (accessed October 22, 2014).
- [35] J. Helbig, E. Spingler, Kunststoffe für die Pharmazeutische Verpackung, Wissenschaftliche Verlagsgesellschaft mbH, Stuttgart, Germany, 1985.
- [36] European Directorate for the Quality of Medicine (EDQM), 3.1.4 Polyethylene without additives for containers for parenteral preparations and for ophthalmic preparations, in: European Pharmacopoeia, 7th ed., 2011.
- [37] European Directorate for the Quality of Medicine (EDQM), 3.1.13 Plastic additives, in: European Pharmacopoeia, 7th ed., 2011.
- [38] P. Eyerer, P. Elsner, T. Hirth, Polymer Engineering, Springer Verlag, Berlin, Heidelberg, 2008.
- [39] K.R. Williams, Analysis of Ethylene-Vinyl Acetate Copolymers: A Combined TGA/FTIR Experiment, *J. Chem. Educ.* 71 (1994) A195.
- [40] T. Zuyi, C. Taiwei, On the Applicability of the Langmuir Equation to Estimation of Adsorption Equilibrium Constants on a Powdered Solid from Aqueous Solution, *J. Colloid Interface Sci.* 231 (2000) 8–12.
- [41] S. Sharma, G.P. Agarwal, Interactions of proteins with immobilized metal ions: a comparative analysis using various isotherm models, *Anal. Biochem.* 288 (2001) 126–40.
- [42] R.J. Umpleby, S.C. Baxter, Y. Chen, R.N. Shah, K.D. Shimizu, Characterization of molecularly imprinted polymers with the Langmuir-Freundlich isotherm, *Anal. Chem.* 73 (2001) 4584–91.
- [43] R. Sips, On the Structure of a Catalyst Surface, *J. Chem. Phys.* 16 (1948) 490–495.
- [44] L.K. Koopal, W.H. van Riemsdijk, J.C.M. de Wit, M.F. Benedetti, Analytical Isotherm Equations for Multicomponent Adsorption to Heterogeneous Surfaces, *J. Colloid Interface Sci.* 166 (1994) 51–60.

- [45] Q. Luo, Cooperative Adsorption of Proteins onto Hydroxyapatite, *J. Colloid Interface Sci.* 200 (1998) 104–113.
- [46] I. Lundström, H. Elwing, Simple kinetic models for protein exchange reactions on solid surfaces, *J. Colloid Interface Sci.* 136 (1990) 68–84.
- [47] L.C. Zanetti-Domingues, C.J. Tynan, D.J. Rolfe, D.T. Clarke, M. Martin-Fernandez, Hydrophobic fluorescent probes introduce artifacts into single molecule tracking experiments due to non-specific binding, *PLoS One.* 8 (2013) e74200.
- [48] M.S. Lord, M. Foss, F. Besenbacher, Influence of nanoscale surface topography on protein adsorption and cellular response, *Nano Today.* 5 (2010) 66–78.
- [49] P.E. Scopelliti, A. Borgonovo, M. Indrieri, L. Giorgetti, G. Bongiorno, R. Carbone, et al., The effect of surface nanometre-scale morphology on protein adsorption, *PLoS One.* 5 (2010) e11862.
- [50] K. Rechendorff, M.B. Hovgaard, M. Foss, V.P. Zhdanov, F. Besenbacher, Enhancement of protein adsorption induced by surface roughness, *Langmuir.* 22 (2006) 10885–8.
- [51] P. Elter, R. Lange, U. Beck, Atomic force microscopy studies of the influence of convex and concave nanostructures on the adsorption of fibronectin, *Colloids Surf. B. Biointerfaces.* 89 (2012) 139–46.
- [52] D. Deligianni, Effect of surface roughness of the titanium alloy Ti–6Al–4V on human bone marrow cell response and on protein adsorption, *Biomaterials.* 22 (2001) 1241–1251.
- [53] F.A. Denis, P. Hanarp, D.S. Sutherland, J. Gold, C. Mustin, P.G. Rouxhet, et al., Protein Adsorption on Model Surfaces with Controlled Nanotopography and Chemistry, *Langmuir.* 18 (2002) 819–828.
- [54] K. Grundke, Characterization of Polymer Surfaces by Wetting and Electrokinetic Measurements – Contact Angle, Interfacial Tension, Zeta Potential, in: M. Stamm (Ed.), *Polymer Surfaces and Interfaces*, 1st ed., Springer Verlag, Berlin, Heidelberg, 2008: pp. 103–138.
- [55] D.Y. Kwok, H. Ng, A.W. Neumann, Experimental Study on Contact Angle Patterns: Liquid Surface Tensions Less Than Solid Surface Tensions, *J. Colloid Interface Sci.* 225 (2000) 323–328.
- [56] L. Gao, T.J. McCarthy, Contact angle hysteresis explained, *Langmuir.* 22 (2006) 6234–7.
- [57] G. Wolansky, A. Marmur, Apparent contact angles on rough surfaces: the Wenzel equation revisited, *Colloids Surfaces A Physicochem. Eng. Asp.* 156 (1999) 381–388.
- [58] N. Correia, Estimation of the Surface Tension of a Solid: Application to a Liquid Crystalline Polymer, *J. Colloid Interface Sci.* 189 (1997) 361–369.
- [59] M. Michalski, J. Hardy, B. Saramago, On the Surface Free Energy of PVC/EVA Polymer Blends: Comparison of Different Calculation Methods, *J. Colloid Interface Sci.* 208 (1998) 319–328.

- [60] D.K. Owens, R.C. Wendt, Estimation of the surface free energy of polymers, *J. Appl. Polym. Sci.* 13 (1969) 1741–1747.
- [61] Z.I. Ali, Effect of electron beam irradiation and vinyl acetate content on the physicochemical properties of LDPE/EVA blends, *J. Appl. Polym. Sci.* 104 (2007) 2886–2895.
- [62] C. Devallencourt, S. Marais, J.M. Saiter, M. Labbé, M. Métayer, Study of transport of small molecules through ethylene-co-vinyl acetate copolymers films. Part A: Water molecules, *Polym. Test.* 21 (2002) 253–262.
- [63] I. Uettwiller, D. Dubut, N. Voute, Quantification of protein adsorption onto the surface of single-use flexible containers, *Bioprocess Int.* 4 (2006) Supplement 22–26.
- [64] M. van der Veen, M.C. Stuart, W. Norde, Spreading of proteins and its effect on adsorption and desorption kinetics, *Colloids Surf. B. Biointerfaces.* 54 (2007) 136–42.
- [65] Chih-Hu Ho, Vladimir Hlady, Adsorption of Human Low-Density Lipoprotein onto a Silica-Octadecyldimethylsilyl (C18) Gradient Surface, in: T.A. Horbett, J.L. Brash (Eds.), *Proteins at Interfaces II*, American Chemical Society, Washington, DC, 1995: pp. 371–384.
- [66] J.-Y. Yoon, J.-H. Kim, W.-S. Kim, The relationship of interaction forces in the protein adsorption onto polymeric microspheres, *Colloids Surfaces A Physicochem. Eng. Asp.* 153 (1999) 413–419.
- [67] B.J. Kirby, E.F. Hasselbrink, Zeta potential of microfluidic substrates: 2. Data for polymers, *Electrophoresis.* 25 (2004) 203–13.
- [68] K. Ahrer, A. Jungbauer, Chromatographic and electrophoretic characterization of protein variants, *J. Chromatogr. B. Analyt. Technol. Biomed. Life Sci.* 841 (2006) 110–22.
- [69] F. MacRitchie, The adsorption of proteins at the solid/liquid interface, *J. Colloid Interface Sci.* 38 (1972) 484–488.
- [70] R.J. Marsh, R.A.L. Jones, M. Sferrazza, Adsorption and displacement of a globular protein on hydrophilic and hydrophobic surfaces, *Colloids Surfaces B Biointerfaces.* 23 (2002) 31–42.
- [71] T. Arai, W. Norde, The behavior of some model proteins at solid-liquid interfaces 1. Adsorption from single protein solutions, *Colloids and Surfaces.* 51 (1990) 1–15.
- [72] J.J. Gray, The interaction of proteins with solid surfaces, *Curr. Opin. Struct. Biol.* 14 (2004) 110–5.
- [73] M.E. Wiseman, C.W. Frank, Antibody adsorption and orientation on hydrophobic surfaces., *Langmuir.* 28 (2012) 1765–74.
- [74] J.E. Lee, S.S. Saavedra, Molecular Orientation in Heme Protein Films Adsorbed to Hydrophilic and Hydrophobic Glass Surfaces, *Langmuir.* 12 (1996) 4025–4032.
- [75] J. Ramsden, Puzzles and paradoxes in protein adsorption, *Chem. Soc. Rev.* 24 (1995) 73–78.
- [76] V. Hlady, J. Buijs, Protein adsorption on solid surfaces, *Curr. Opin. Biotechnol.* 7 (1996) 72–7.

- [77] J. Buijs, J.W.T. Lichtenbelt, W. Norde, J. Lyklema, Adsorption of monoclonal IgGs and their F(ab')₂ fragments onto polymeric surfaces, *Colloids Surfaces B Biointerfaces*. 5 (1995) 11–23.
- [78] W. Norde, J. Lyklema, The adsorption of human plasma albumin and bovine pancreas ribonuclease at negatively charged polystyrene surfaces, *J. Colloid Interface Sci.* 66 (1978) 257–265.
- [79] I. Langmuir, The Adsorption of Gases on Plane Surfaces of Glass, Mica and Platinum, *J. Am. Chem. Soc.* 40 (1918) 1361–1403.
- [80] K. Höger, Investigations on Protein Adsorption to Coated Glass Vials, PhD thesis, Ludwig-Maximilians-Universität München, Germany, 2014.
- [81] A. Hawe, W. Friess, Development of HSA-free formulations for a hydrophobic cytokine with improved stability, *Eur. J. Pharm. Biopharm.* 68 (2008) 169–82.
- [82] J. Revilla, Adsorption of Bovine Serum Albumin onto Polystyrene Latex Particles Bearing Saccharidic Moieties, *J. Colloid Interface Sci.* 180 (1996) 405–412.
- [83] J.S. Bee, D. Chiu, S. Sawicki, J.L. Stevenson, K. Chatterjee, E. Freund, et al., Monoclonal antibody interactions with micro- and nanoparticles: adsorption, aggregation, and accelerated stress studies, *J. Pharm. Sci.* 98 (2009) 3218–38.
- [84] M. Duncan, Influence of surfactants upon protein/peptide adsorption to glass and polypropylene, *Int. J. Pharm.* 120 (1995) 179–188.
- [85] M. Hoehne, F. Samuel, A. Dong, C. Wurth, H.-C. Mahler, J.F. Carpenter, et al., Adsorption of monoclonal antibodies to glass microparticles, *J. Pharm. Sci.* 100 (2011) 123–32.
- [86] B.M. Chan, J.L. Brash, Adsorption of fibrinogen on glass: reversibility aspects, *J. Colloid Interface Sci.* 82 (1981) 217–225.
- [87] H.J. van Enkevort, D.V. Dass, A.G. Langdon, The adsorption of bovine serum albumin at the stainless-steel/aqueous solution interface, *J. Colloid Interface Sci.* 98 (1984) 138–143.
- [88] P. Van Dulm, W. Norde, The adsorption of human plasma albumin on solid surfaces, with special attention to the kinetic aspects, *J. Colloid Interface Sci.* 91 (1983) 248–255.
- [89] M. Duncan, M. Gilbert, J. Lee, Development and Comparison of Experimental Assays to Study Protein/Peptide Adsorption onto Surfaces, *J. Colloid Interface Sci.* 165 (1994) 341–345.
- [90] R. Baffi, G. Dolch, R. Garnick, Y.F. Huang, B. Mar, D. Matsuhira, et al., A total organic carbon analysis method for validating cleaning between products in biopharmaceutical manufacturing, *J. Parenter. Sci. Technol.* 45 (1991) 13–9.
- [91] G. Liu, V.S.J. Craig, Improved cleaning of hydrophilic protein-coated surfaces using the combination of Nanobubbles and SDS, *ACS Appl. Mater. Interfaces*. 1 (2009) 481–7.
- [92] S.R. Mulzer, J.L. Brash, Analysis of proteins adsorbed to glass from human plasma using immunoblotting methods, *J. Biomater. Sci. Polym. Ed.* 1 (1989) 173–182.

- [93] A. Herrig, M. Janke, J. Austermann, V. Gerke, A. Janshoff, C. Steinem, Cooperative adsorption of ezrin on PIP2-containing membranes, *Biochemistry*. 45 (2006) 13025–34.
- [94] D. Pellenc, R.A. Bennett, R.J. Green, M. Sperrin, P.A. Mulheran, New insights on growth mechanisms of protein clusters at surfaces: an AFM and simulation study, *Langmuir*. 24 (2008) 9648–55.
- [95] P.A. Mulheran, D. Pellenc, R.A. Bennett, R.J. Green, M. Sperrin, Mechanisms and dynamics of protein clustering on a solid surface, *Phys. Rev. Lett.* 100 (2008) 068102.
- [96] D.T. Kim, H.W. Blanch, C.J. Radke, Direct Imaging of Lysozyme Adsorption onto Mica by Atomic Force Microscopy, *Langmuir*. 18 (2002) 5841–5850.
- [97] R. Ishiguro, Y. Yokoyama, H. Maeda, A. Shimamura, K. Kameyama, K. Hiramatsu, Modes of conformational changes of proteins adsorbed on a planar hydrophobic polymer surface reflecting their adsorption behaviors, *J. Colloid Interface Sci.* 290 (2005) 91–101.
- [98] M.. Soderquist, A.. Walton, Structural changes in proteins adsorbed on polymer surfaces, *J. Colloid Interface Sci.* 75 (1980) 386–397.
- [99] B.M.. Chan, J.L. Brash, Conformational change in fibrinogen desorbed from glass surface, *J. Colloid Interface Sci.* 84 (1981) 263–265.
- [100] W. Norde, J.P. Favier, Structure of adsorbed and desorbed proteins, *Colloids and Surfaces*. 64 (1992) 87–93.
- [101] M. Shomali, A. Freitag, J. Engert, M. Siedler, Z. Kaymakcalan, G. Winter, et al., Antibody responses in mice to particles formed from adsorption of a murine monoclonal antibody onto glass microparticles, *J. Pharm. Sci.* 103 (2014) 78–89.
- [102] M.M.C. Van Beers, F. Gilli, H. Schellekens, T.W. Randolph, W. Jiskoot, Immunogenicity of recombinant human interferon beta interacting with particles of glass, metal, and polystyrene., *J. Pharm. Sci.* 101 (2012) 187–99.

CHAPTER III

STUDYING PROTEIN ADSORPTION WITH QUARTZ CRYSTAL MICROBALANCE (QCM)

ABSTRACT

Adsorption of a model antibody (IgG) to model surfaces made from EVA and PE polymers was studied in situ using QCM measurements. In this setup, spin-coated polymer surfaces on QCM chips should mimic typical contact layers of single-use bioprocess bags. Depending on pH and ionic strength, adsorbed amounts of IgG were in the range of 7 to 10 mg/m². Applying the Sauerbrey equation was assumed to be valid since formed IgG layers in most cases were rigid. Furthermore, calculated adsorbed amounts were confirmed by independent measurements using HP-SEC quantification after IgG desorption. With the help of $\Delta\Gamma$ vs. Δf plots, three distinct phases during the adsorption process were identified for most formulation conditions. Rigid attachment was assumed during the first phase, followed by fast adsorption of more loosely bound protein in a second step and a subsequent, final rigidification phase. The adsorption process was found to be mainly governed by electrostatic interactions, therefore variations in pH and ionic strength led to slightly modified adsorption profiles. The three nonionic surfactants polysorbate 20, polysorbate 80, and poloxamer 188 were able to reduce adsorption to the EVA surface only during co-incubation. In conclusion, QCM studies with model surfaces helped to gain a deeper understanding of the adsorption process but cannot replace adsorption studies with real surfaces encountered during drug product manufacturing, since adsorbed amounts from HP-SEC (see previous chapter) and QCM analysis differed substantially.

Parts of the following chapter are intended for publication.

Data on mAb adsorption to PE surfaces at pH 2, 6 and 10 was collected by Stephanie Marlene Burisch during her Master thesis project entitled "IgG adsorption to single-use bioprocess bags with ULDPE contact layer" (2014).

8 INTRODUCTION

8.1 Methods for Studying Protein Adsorption in Situ

Apart from simply quantifying protein adsorption, deeper insights into adsorption kinetics foster a better understanding of this omnipresent phenomenon. There is a variety of methods, especially with spectroscopic background, that enable the observation of protein adsorption *in situ* and in a time-dependent manner. In the following section, the most commonly used methods including possible advantages and shortcomings are shortly introduced.

During ellipsometry studies, changes in the phase and amplitude of polarized monochromatic light are measured after reflection from a surface on which a thin, homogeneous film is built due to adsorption. Changes are recorded for both the parallel and perpendicular polarized light components. From these changes, the refractive index of the film as well as its thickness is calculated via mathematical fitting. This method can only be applied to light-reflecting surfaces and films that do not adsorb light to a measurable extent, otherwise the complex refractive index of the film must be known or estimated [1]. Examples for ellipsometry studies that monitor protein adsorption to solid surfaces in a timely manner include the work of McArthur *et al.* [2] with Cu-Al films, Svensson and Arnebrandt's studies on antibody adsorption to polystyrene surfaces [3], and experiments by Giacomelli and coworkers on albumin adsorption to titanium oxide electrodes [4].

Infrared spectroscopy can be applied to protein films on solid supports in the form of infrared reflection-adsorption spectroscopy (IRRAS) or as total internal reflection fluorescence (TIRF) measurements. IRRAS is a highly sensitive method that measures changes in polarized, infrared light in reflectance mode with high incidence angles. In analogy to ellipsometry, it is mainly applicable to highly-reflecting surfaces like metals, but also the adsorption at the air-water interface is widely studied with this technique [5]. IRRAS can give additional information on the orientation of molecules adsorbed on these surfaces [1]. Omanovic and colleagues, for example, employed polarization-modulation IRRAS analysis for monitoring fibrinogen adsorption kinetics to stainless steel [6] and also albumin to gold [7]. In a typical TIRF setup, the light beam incidents from the outside and is totally reflected at the solid-liquid interface. An evanescent wave penetrates into the liquid phase and surface-associated protein is excited [8]. For quantitative evaluation of the emitted fluorescence intensities, rather complex calibration procedures have to be developed [9]. Most often fluorescently-labeled molecules are employed during TIRF studies, but also the intrinsic fluorescence of proteins can be exploited [10]. One critical factor here is the penetration depth of the evanescent wave. It should be long enough to capture the entire adsorption layer, but short enough to reduce unwanted signal contributions from the bulk solution [11]. In literature, time-resolved TIRF studies are reported amongst others by Buijs and Hlady for human growth hormone and lysozyme adsorption on clean and modified silica [12] and by Daly *et al.* for lysozyme adsorption to silica [13].

The most often used technique is surface plasmon resonance (SPR). In SPR, a light beam passes a glass prism and undergoes total internal reflection at the interface to a metal (typically gold) coating. An evanescent wave passes through the metal film and excites plasmons on the outer side of the film. Excitation occurs at a specific angle of incidence only and causes a reduction in the intensity of the reflected light. The incidence angle changes if protein binds due to a change in the dielectric properties, and thus the refractive index dependent on the thickness of the adsorbing protein layer [14]. Most often, simply the change in SPR angle is reported since a correlation with the amount of

adsorbed mass needs specific calibration [15]. Studying adsorption to other materials than metals is feasible with very thin film coatings on top of the metal surface. However, such thin coatings might not be achievable with polymers [10]. Using SPR; real-time microscale bioadhesion events were monitored by Aldred *et al.* [16] and Green *et al.* analyzed three plasma proteins for their adsorption behavior on the sensor's silver surface and on a model polystyrene film [14].

Likewise, the interaction of an evanescent field generated by diffracted laser light with deposited molecules is measured by optical waveguide lightmode spectroscopy (OWLS). This rather new method is claimed to have intrinsic sensitivity superior to SPR. However, due to the limited propagation of the evanescent wave of only 100 to 200 nm, very thin coatings are necessary, too. A major benefit results from the possibility of determining the thickness as well as the refractive index of the adsorbed layer. Assumptions about this latter parameter are necessary for other optical methods like SPR and ellipsometry and can lead to uncertainties in the final results [17]. Calonder and coworkers extensively employed OWLS to study the history dependence of fibronectin and cytochrome c adsorption kinetics with multistep experiments on Si(Ti)O₂ [18,19].

Studies with a quartz crystal microbalance (QCM) rely on the analysis of the propagation properties of acoustic waves as measuring principle. Acoustic waves are generated by a piezoelectric sensor and enable the observation of adsorption events as well as changes in the viscoelastic properties of the surrounding medium and the adsorbed layer [20]. Since this method is independent of the optical properties of the surface under investigation, adsorption events on a variety of coatings can be investigated [21]. Although the thin film requirement needs to be equally fulfilled for a correct modelling of QCM data, limitations for rigid coatings are considered not as strict as for SPR or OWLS. This method was therefore chosen for the *in situ* and real-time adsorption monitoring of a model therapeutic antibody to polymer surfaces in this study. Surfaces coated with polyethylene (PE) and ethylene vinyl acetate (EVA) were produced as surrogates for typical fluid contact layers of single-use bioprocess bags.

All herein mentioned methods are strictly applicable to homogeneous layers only. However, this might not always hold true for adsorbed protein. Analysis of the lateral distribution of adsorbed molecules is achievable with atomic force microscopy (AFM). However, AFM measurements require very smooth adsorbent surfaces like mica or gold. Moreover, this method suffers from limitations for real-time measurements as well as from possible artifacts arising from the mechanical interference of the AFM tip with the adsorption process and the adsorbed layer [22,23].

8.2 Adsorption Studies with Quartz Crystal Microbalance (QCM)

QCM devices employ an AT-cut quartz crystal (cut angle of 35.25° with respect to the quartz's optical axis) sandwiched between two gold electrodes as sensor. The cutting of quartz in this specific direction relative to its crystallographic axes results in so-called thickness-shear mode oscillations when applying alternating voltage via the gold electrodes. The anti-parallel movement of both sensor surfaces results in acoustic waves that propagate perpendicular to the surface into the bulk solution. The resonance frequency of the sensor depends on its mass, a dependence which is given by the Sauerbrey equation. A QCM in this sense acts as a microweighing device only. By including a second information, namely dissipation, information on the viscoelastic properties of the adsorbed layer can be gained. Instruments that include a recording of dissipation signals are often referred to as QCM-D devices. For QCM-D analysis, the driving voltage is intermittently switched off and from the decay curve of the oscillation both the resonance frequency f and the energy dissipation D are calculated

[21]. In this study, the equivalent parameter ‘damping’ was evaluated. The damping signal is the corresponding bandwidth Γ of the resonance peak in the spectrum obtained during impedance analysis. Bandwidth Γ and dissipation D are proportional to each other ($D = 2\Gamma/f$) [24]. There are studies that report resistance values R , which are also proportional to the other two parameters and can thus be interpreted in a similar way [20].

Possible signal changes that are encountered during QCM measurements are depicted in Figure III-24. It has to be kept in mind that the frequency shift is influenced by changes in the adsorbed mass as well as by changes in the density and viscosity of the surrounding medium or the adsorbed layer. Hence, care needs to be taken during quantitative evaluation of frequency shifts. The damping signal reflects changes in the viscoelastic properties only and gives valuable additional information that is not accessible with the other spectroscopic methods mentioned above.

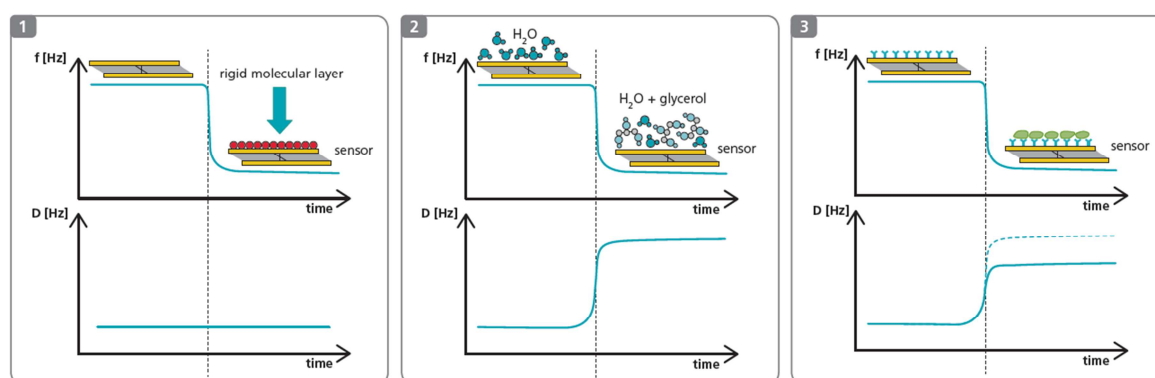


Figure III-24: Measurement signals obtained during QCM studies. (1) Upon attachment of a thin and rigid layer, a frequency shift is recorded whereas the damping signal D does not change. (2) A purely viscous change in the surrounding medium results in comparable frequency and damping shifts. (3) A viscoelastic layer leads to frequency as well as damping shifts, although damping shifts are reduced in this case. Graphics are taken from 3T analytik brochure [25].

As mentioned above, QCM benefits from the flexibility in the choice of substrate material. In principle, any material that can be coated or deposited onto the sensor in the form of a sufficiently thin layer (nm to μm range) can be employed [21]. Sensor modifications can be achieved by spin-coating, sputtering, evaporation, and casting procedures. In consequence, QCM sensors can be widely employed, e.g. as biosensors, for the estimation of affinity constants, for biocompatibility testing, and for studying cell adhesion processes. Possible applications are reviewed in detail by Dixon [21], Marx [26], as well as Speight & Cooper [27]. The QCM technique is increasingly used to study protein adsorption to polymer surfaces. The studies reported in literature mainly focus on biopolymers, synthetic polymers with biomedical applications, molecular imprinted polymers and polymer brushes, but not on polymers used in bioprocess materials [27].

It is the aim of this study to gain deeper insights into the adsorption process of a therapeutic monoclonal antibody (mAb) to PE and EVA surfaces that are common contact materials of single-use bags. In the previous chapter, protein adsorption to these surfaces was characterized quantitatively via desorption and subsequent HP-SEC quantification. This QCM study aims not only at quantification of the protein on PE and EVA films but also at the evaluation of the adsorption reversibility and of the time-dependent viscoelastic properties of the formed protein layer. Formulation pH and ionic strength were varied in order to get a more detailed understanding of the contributions from

electrostatic interactions on the adsorption process. Furthermore, the capability of three nonionic surfactants (polysorbate 20, polysorbate 80, poloxamer 188) to reduce protein adsorption in sequential and co-incubation mode was evaluated. Finally, adsorbed amounts on polymer-coated QCM chips are critically compared to adsorbed amounts on real bag surfaces as presented in the previous chapter for assessing the suitability of QCM as an orthogonal method.

9 MATERIALS AND METHODS

9.1 Materials

9.1.1 Chemicals

NaCl, Na₂HPO₄, and NaH₂PO₄ were obtained from VWR International (Darmstadt, Germany). NaOH (1 M), HCl (1 M) and sodium dodecyl sulfate (SDS) were obtained from Sigma-Aldrich (Taufkirchen, Germany). Polysorbate (PS) 20 and 80 as well as trichloroethylene were purchased from Merck KGaA (Darmstadt, Germany), Poloxamer 188 (Pol 188) was from BASF (Ludwigshafen, Germany). Tetrahydrofurane (THF) was obtained from J.T. Baker (Deventer, Netherlands). Highly purified water used for buffer preparation was obtained from an arium[®] pro DI Ultrapure Water System (Sartoris Stedim Biotech GmbH, Goettingen, Germany) or a USF ELGA PURELAB Plus UV/UF purification system (ELGA LabWater, Celle, Germany). Buffer filtration (volumes ≥ 500 mL) was performed with pressurized nitrogen and 0.2 μm cellulose acetate filters (47 mm, Sartorius Stedim Biotech GmbH).

9.1.2 Model Antibody

A 33.4 mg/mL IgG1 antibody (148 kDa) drug substance solution in 20 mM histidine buffer (pH 5.4) was kindly donated by Roche GmbH (Penzberg, Germany).

9.1.3 Polymers for QCM chip coating

Ethylene vinyl acetate (EVA) granules of the type Elvax 3190A were kindly donated by DuPont Packaging & Industrial Polymers (Neu-Isenburg, Germany). This EVA material with a vinyl acetate (VA) content of 25 % should mimic the EVA surface of the previously tested Sartorius Flexboy[®] bags (see Chapter II). As a model for the ULDPE surfaces of Sartorius Flexel[®] and Millipore PureFlex[™] multilayer bags, bags made from pure PE were purchased (Stomacher[®], VWR, Darmstadt, Germany). The identity and purity of the PE bag was confirmed via ATR-IR microscopy as described in Chapter II (see Figure III-25).

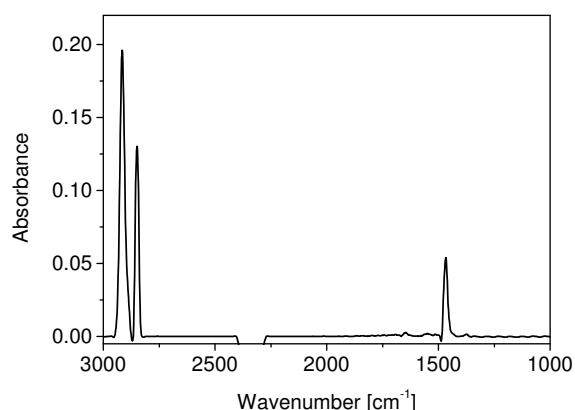


Figure III-25: IR spectrum of the PE Stomacher[®] bag.

9.2 Methods

9.2.1 QCM Chip Coating

Gold-covered quartz sensors mounted on a thin polymer sheet were obtained from 3T Analytik (3T GmbH & Co. KG, Tuttlingen, Germany). The crystals were 8.5 mm in diameter. The area exposed to liquid was 38 mm², the active electrode area is stated to be 19.6 mm² [25].

EVA was dissolved in THF at 5 mg/mL under stirring and heating to approximately 50°C. For creating a homogenous EVA layer, 10 x 8 µl aliquots of the EVA solution were added to the crystal sensor while rotating in a SCI 20 spin coater with a customized sample stage (Schaefer Technologie GmbH, Langen, Germany) at 100 rpm. Pieces of the PE bag (0.5 g) were heated in 20 mL THF under stirring at 50°C. The PE coating was established by spin-coating 10 x 10 µL aliquots of the supernatant of this mixture on a QCM chip. After every measurement, the QCM chip surface was cleaned with trichloroethylene solution by gently patting the surface with a commercially available cotton swab. A new coating was produced prior to every measurement. Before coating and before insertion into the QCM device, the coated chip was cleaned and dried using filtered (Acro 50, 0.2 µm PTFE, Pall Corporation, Port Washington, USA), pressurized air.

9.2.2 Microscopy

Coating homogeneity was monitored by default via light microscopy (Keyence VHX-500F, Neu-lsenburg, Germany) at 30x magnification. Morphology was visualized at higher resolution using a Keyence VK-X210 3D Laser Scanning Microscope with a 20x objective.

9.2.3 Sample Preparation

For obtaining 20 mM histidine buffers with varying pH and ionic strength (IS), pH adjustments were conducted with 1 M NaOH and 1 M HCl. Ionic strength was set to either 100 or 300 mM via the addition of adequate amounts of NaCl. The calculation of the corresponding amounts of salt is described in detail by Mathes [28]. The spread sheet template was adapted to the histidine buffer system with pK_{a1} = 1.8, pK_{a2} = 6.0 and pK_{a3} = 9.3 as given by Lieberman, Marks and Peet [29]. IgG stock solution was diluted using the corresponding buffer to a final sample concentration of 2 mg/mL. Experiments with surfactants (PS 20, PS 80 and Pol 188) were performed at pH 6 without any addition of sodium chloride and at a constant surfactant concentration of 0.02 % (w/V). The pH of all samples was checked using a Mettler Toledo MP220 pH meter (Mettler Toledo, Greifensee, Switzerland). Calibration with purchased standard buffers of pH 2.0 and 7.0 was performed prior to every use. Finally, all samples were filtered using a 0.2 µm PES syringe filter (VWR, ID of 25 mm). Protein concentration was verified by UV absorption at 280 nm using a Nanodrop Micro-Volume UV-Vis spectrometer (Nano Drop 2000, Thermo Scientific, Wilmington, USA), applying an extinction coefficient of 1.51 cm²/mg.

9.2.4 QCM Measurements

QCM measurements were performed at 25°C with a qCell T from 3T Analytik (Tuttlingen, Germany) connected to an Ismatec peristaltic pump operated at a flow rate of 100 µL/min. The system was controlled using qGraph software. Before starting the actual experiment, the coated QCM chip was pre-equilibrated in air and subsequently in highly-purified water. The sequence of a typical QCM experiment is shown in Figure III-26. The influence of pH and ionic strength on IgG adsorption was

studied in triplicates. Buffer rinsing was performed with the corresponding blank buffer that matched pH and ionic strength of the IgG sample. The desorption buffer was composed of 10 mM phosphate with 145 mM NaCl and 0.05 % SDS. Each solution was allowed to stay in contact with the crystal until a stable baseline in frequency (± 1 Hz within 10 minutes) and damping (± 10 Hz within 10 minutes) was reached. Equilibration with buffer was performed in flow mode. IgG samples equilibrated statically after the introduction of a limited sample volume of 290 μ L. Care was taken not to introduce any air into the system upon changing samples. The formation of air bubbles within the measuring cell was further reduced by degassing all samples in an exsiccator connected to a vacuum pump (Laboport, KNF Neuberger GmbH, Freiburg, Germany) prior to use.

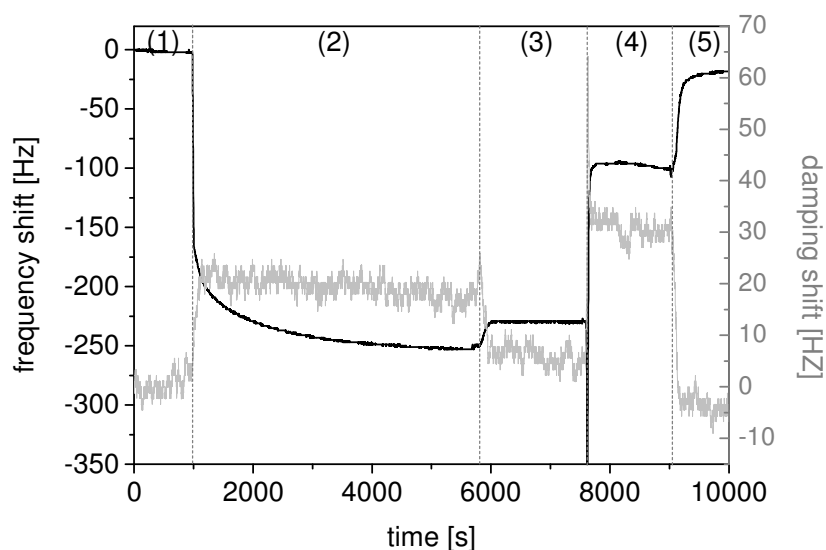


Figure III-26: Frequency and damping shifts as a function of time for a typical QCM experiment. The different steps include: 1 - buffer rinsing, 2 - incubation with IgG, 3 - buffer rinsing, 4 - desorption with buffer containing 0.05 % SDS, 5 - buffer rinsing.

The sample sequence applied for studying the influence of surfactants on IgG adsorption is displayed in Table III-12. Injection of a limited volume of 290 μ L for all samples containing surfactant and / or IgG was followed by static incubation. For this study, QCM measurements were performed in duplicates.

Table III-12: Sample sequence for QCM studies with surfactants.

Sequence	Rinsing	Incubation I	Rinsing	Incubation II	Rinsing
#1	buffer	surfactant (0.02%)	buffer	IgG (2 mg/mL)	buffer
#2	buffer	IgG (2 mg/mL)	buffer	surfactant (0.02%)	buffer
#3	buffer	IgG (2 mg/mL) + surfactant (0.02%)			buffer

9.2.5 Calculations

The adsorbed amount was calculated from the frequency shift during adsorption by applying the Sauerbrey equation [30]. The presence of a thin, homogeneous, and rigidly adsorbed layer was assumed, as the Sauerbrey equation is valid for such systems only [21].

$$\Delta f = \frac{2f_0^2}{A\sqrt{\rho\mu}} \times \Delta m$$

- Δf : frequency shift [Hz]
 f_0 : resonant frequency of the crystal (about 10 MHz) [25]
 A : active electrode area (0.196 cm²) [25]
 ρ : density of quartz (2.648 g/cm³) [31]
 μ : shear modulus of quartz (2.947 × 10¹¹ g/cm·s²) [31]
 Δm : adsorbed mass [g]

By combining the constant terms, the adsorbed mass was directly calculated using the instrument specific crystal sensitivity constant C :

$$\Delta m = C \times \Delta f$$

with $C = 0.86$ ng/Hz [25] and Δf being the frequency shift between incubation step (1) and (3) as shown in Figure III-26. The amount of IgG that was desorbed upon rinsing with the SDS containing buffer was calculated from the frequency shift between step (3) and (5). The adsorbed amount per unit area was obtained by normalization to the active electrode area.

Layer thickness h of the coating as well as adsorbed IgG and surfactant layers was calculated as follows:

$$h = \frac{C \times \Delta f}{A \times \rho}$$

with Δf being the change in frequency upon coating after equilibration in air for the determination of the coating thickness or the frequency shift between the two buffer rinsing steps before and after incubation with IgG (step (1) and (3) as described in Figure III-26) or surfactant (rinsing before and after incubation I in sequence #1, as described in Table III-12). The value for ρ was chosen accordingly (see Table III-13).

Table III-13: Densities of the different layer materials used for the calculation of layer thickness.

Layer material	Density ρ [g/cm ³]	Reference
EVA coating	0.95	DuPont™ Elvax® 3190 Product Data Sheet [32]
PE coating	Approx. 0.9	Sepe 2012 [33]
IgG	1.35	Fischer <i>et al.</i> 2004 [34]
Polysorbate 20	1.1	Merck Millipore Product Information [35]
Polysorbate 80	1.07	Merck Millipore Product Information [35]
Poloxamer 188	1.06	BASF Product Information [36]

Reversibility [%] of IgG adsorption was calculated from the frequency shifts upon incubation with IgG and the subsequent rinsing step [37]:

$$\text{reversibility} = \frac{\Delta f (\text{step } (3) - \text{step } (2))}{\Delta f (\text{step } (1) - \text{step } (2))} \times 100\%$$

Viscoelastic properties of the adsorbed layer were evaluated with the obtained damping signals Γ [20]:

$$\frac{\Delta\Gamma}{\Delta f} = \frac{\Delta\Gamma (\text{step } (3) - \text{step}(1))}{\Delta f(\text{step}(1) - \text{step}(3))}$$

The higher the value for $\Delta\Gamma/\Delta f$, the more viscous is the adsorbed layer. If only the viscosity of the sample changes and adsorption events do not occur, e.g. when filling the dry chamber with water, this quotient is maximal. A value of zero indicates the formation of a completely elastic layer with rigidly attached molecules.

9.2.6 IgG Size Determination with Dynamic Light Scattering (DLS)

IgG size determination was performed by dynamic light scattering using the Zetasizer Nano-ZS (Malvern Instruments Ltd., Herrenberg, Germany). The undiluted, freshly filtrated (0.02 μm , PES) samples (IgG at 2 mg/mL in 20 mM histidine buffer pH 2 / 6 / 10 with 100 mM IS) were measured in disposable Plastibrand semi-micro PMMA cuvettes (Brand GmbH, Wertheim, Germany) at a backward scatter of 173° at 25°C and with water as dispersant. Positioning, attenuation selection and measurement duration as well as number of sub runs for the three performed measurements per sample were optimized automatically for each run by the Zetasizer Software 6.32. Z-average and polydispersity index (PDI) were calculated from the correlation function applying the 'General purpose (normal resolution)' analysis model.

9.2.7 Viscosity measurements

The viscosities of both the IgG and surfactant incubation solutions were determined using a m-VROC viscometer (RheoSense, San Ramon, CA, USA). Measurements were performed with sample volumes of 150 μL and a flow rate of 150 $\mu\text{L}/\text{min}$ at 20°C.

9.2.8 HP-SEC Quantification of IgG Adsorbed to the QCM Chip Surface

EVA-coated QCM chips were incubated with IgG (pH 2 / 6 / 10, 100 mM IS) in the qCell T device as described above. After the second buffer rinsing step (step (3) in Figure III-26), the QCM chip with adsorbed IgG was removed from the flow cell and replaced by a cleaning insert. After thoroughly rinsing the whole QCM system with desorption buffer containing 0.05 % SDS, the previously incubated QCM chip was transferred into the measuring chamber again. IgG adsorbed to the QCM chip surface was desorbed by introducing 80 μL of the desorption buffer into the measuring chamber. As soon as a stable frequency signal was achieved, the desorption solution was pumped backwards and collected in a sample tube (Eppendorf GmbH, Hamburg, Germany). Two further rinsing steps with 20 μL desorption buffer each were performed and these fractions were added to the collected sample. The amount of desorbed IgG in the sample was quantified via HP-SEC on an Agilent 1200 device (Agilent Technologies GmbH, Boeblingen, Germany) with fluorescence detection (excitation at 279 nm, emission at 336 nm). A TSK Gel G3000 SWXL column with a SEC guard column was used. The mobile phase was composed of 0.05 % SDS in 10 mM phosphate buffer pH 7.2 with 145 mM NaCl. The flow rate was 0.7 mL/min. The injection volume was 40 μL . A five-point calibration

curve was included for quantification with concentrations of 0.05, 0.025, 0.005, 0.0025, and 0.001 mg/mL. All chromatograms were integrated manually using ChemStation software.

9.2.9 HP-SEC Quantification of IgG Adsorbed to Bag Pieces In the Presence of Surfactant

As QCM is not able to differentiate between mass contributions from different types of molecules, the total amount of IgG adsorbed to Flexboy® bag pieces after consecutive incubation, pre-incubation or co-incubation with surfactants as described in Table III-12 was quantified using HP-SEC. Pieces of 1.2 cm width and 2.2 cm length were cut out of a Flexboy® bag (Sartorius Stedim Biotech SA, Aubagne, France). The outer faces of two pieces were mounted together using double-sided adhesive tape (tesa® Verlegebond, Ref. 05681-00018, Beiersdorf, Hamburg, Germany). Care was taken not to touch the inner surface of the bag at any time. Each piece was transferred into a flat base tube (VWR International, Darmstadt, Germany). The dimensions of the bag pieces were chosen so that they fitted exactly into the tube. Each bag piece was incubated with 3 mL of the appropriate incubation solution ('Incubation I' in Table III-12) at room temperature for four hours (n=3). Subsequently, incubated bag pieces were rinsed five times with 3 mL of 20 mM histidine buffer pH 6. Therefore, tubes were centrifuged upside down using short spins of up to 1000 rpm between each washing step in order to remove excessive liquid. 3 mL of the second incubation solution ('Incubation II' in Table III-12) were added and removed after four hours by the mentioned washing procedure. After cutting off the bag piece edges, each sample was transferred into a fresh tube and 2.8 mL of desorption medium (10 mM phosphate buffer with 145 mM NaCl and 0.05 % SDS, pH 7.2) was added. After desorption at room temperature for at least two hours, aliquots from the supernatant were transferred into HPLC glass vials (VWR, Darmstadt, Germany) and the IgG content was quantified via HP-SEC with the above mentioned system. In this case, injection volume was 300 µL and the calibration curve encompassed samples with concentrations of 0.01, 0.005, 0.001, 0.0005, 0.0002 and 0.0001 mg/mL of IgG in desorption medium. To calculate the correct adsorbed amount per square meter bag surface, the measures of each incubated bag piece were calipered and the corresponding surface area was determined.

9.2.10 Statistics

Unless otherwise stated, results are presented as mean values with standard deviations (n ≥ 2). F-tests (equality of variances) were conducted with p = 0.95. Significance testing was performed via the t-test function in Microsoft Excel 2010. Significance levels are indicated by asterisks: p < 0.05 (*), p < 0.01 (**), and p < 0.001 (***). Statistics are depicted in the figures only for differences discussed in the text.

10 RESULTS

10.1 QCM Chip Coating Development and Morphology

Light microscopy was used as standard method to verify chip surface coverage and coating homogeneity. Figure III-27a shows the pure gold surface of a QCM chip. After coating with EVA, the surface appeared slightly shiny (Figure III-27b), whereas the PE coating was clearly visible as opaque layer (Figure III-27c). A new coating was produced prior to every measurement.

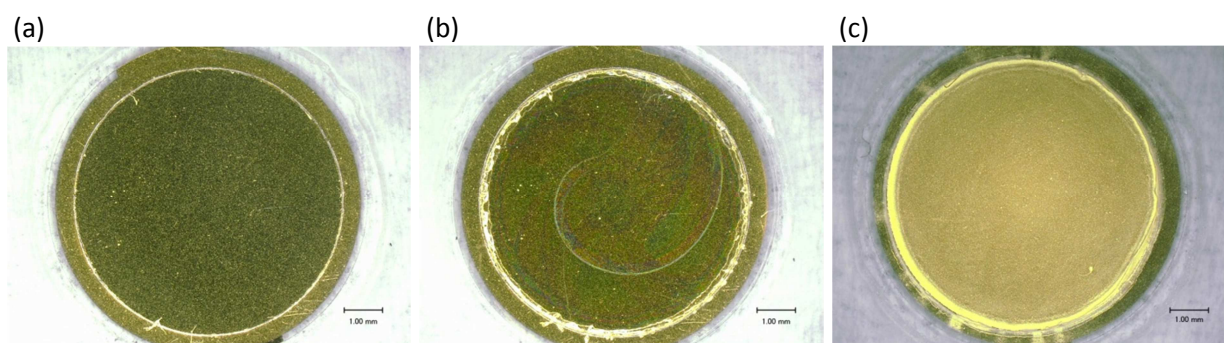


Figure III-27: Light microscopy pictures of QCM chips. (a) Uncoated, (b) with EVA coating, and (c) with PE coating.

Surface morphology of the coating was investigated in more detail using 3D laser scanning microscopy (Figure III-28). The QCM chip surface itself was completely smooth apart from scratches that were introduced by the cleaning technique over time. The EVA coating in Figure III-28b revealed structural features that arose from the coating process. The less smooth morphology of the PE coating is depicted in Figure III-28c.

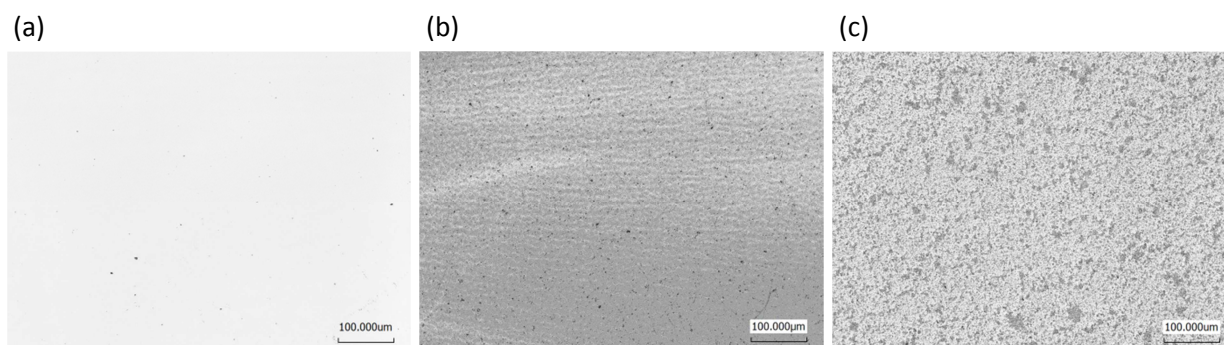


Figure III-28: 3D laser scanning micrographs of QCM chips. (a) Uncoated, (b) with EVA coating, and (c) with PE coating.

The frequency shift upon coating was recorded prior to every measurement as an indicator for the thickness of the applied coating (Table III-14). On average, EVA coatings were 252 nm thick, whereas PE coating mean thickness was 37 nm. Coating thicknesses varied strongly between experiments.

Coating thicknesses were calculated with the Sauerbrey equation assuming a rigid coating. For EVA, the average $\Delta\Gamma/\Delta f$ quotient of 0.041 ± 0.036 ($n=34$) confirms coating rigidity. The quotient could not be calculated for all prepared coatings due to casual drifts in the damping signal. For PE, in most cases a negative shift in the damping signal after coating was recorded. Therefore, $\Delta\Gamma/\Delta f$ values could not be evaluated. Höök *et al.* ascribe negative shifts in the dissipation signal to interfacial friction phenomena between the overlayer (in our case the PE coating) and the surrounding liquid [38]. Applying the Sauerbrey equation might thus underestimate the actual coating thickness since the

viscoelastic properties of the PE coating layer are unclear. Both coatings were found to be stable upon contact with water, buffer, and SDS desorption buffer since resonant frequencies were stable during rinsing with these solutions (data not shown).

Table III-14: Frequency shifts [Hz] upon coating and corresponding coating thicknesses [nm]. Calculations were performed applying the Sauerbrey equation. 43 EVA coatings and 44 PE coating were evaluated.

Coating material		Minimum	Maximum	Mean value
EVA	Frequency shift [Hz]	2724	12504	5465
	Coating thickness [nm]	126	578	252
PE	Frequency shift [Hz]	140	2178	758
	Coating thickness [nm]	6	106	37

10.2 QCM Method Development

The robustness of the QCM method with specific focus on variations in EVA coating thickness was tested with a 2 mg/mL IgG incubation solution of pH 6 (20 mM histidine, 100 mM IS) and flow mode incubation (Table III-15). Independent of the applied coating thickness both tested QCM chips gave rather identical frequency shifts after equilibration with IgG solution. The overall mean frequency shift was 258 Hz with a standard deviation of only 8 Hz. This represents a relative variability of $\pm 3.2\%$. The variabilities for the three runs performed with the same chip were in the same range (RSD of 3.3 %).

Table III-15: Influence of QCM chip number and EVA coating thickness on QCM results obtained during flow mode incubation (2 mg/mL IgG, 20 mM histidine, pH 6.0, 100 mM IS).

Chip No.	Frequency shift due to coating [Hz]	Coating thickness [nm]	Frequency shift due to IgG adsorption [Hz]
5	11590	535	-257
5	6534	302	-271
5	3198	148	-255
2	3732	172	-247
2	6354	293	-256
2	14178	655	-264

The QCM method was developed as an orthogonal analytical technique for the previously presented adsorption studies with HP-SEC quantification (see Chapter II). Therefore, the final experimental parameters were adapted in a way that mimicked the incubation procedure with bag pieces best. Table III-16 lists exposed polymer surface, incubation volume, and incubation mode for the setup described in the previous chapter. Given a defined QCM chip surface area, the incubation volume was chosen accordingly to result in the same surface area to sample volume ratio. Similarly, incubation with protein solution was performed statically. After introducing the incubation solution to the measuring chamber, the pump was stopped and the sample was equilibrated until frequency and damping signals were stable. In contrast, rinsing of the QCM chip was performed in flow injection mode.

Table III-16: Experimental parameters for adsorption studies with HP-SEC and QCM quantification.

Method	Polymer surface exposed to incubation solution	Volume of incubation solution	Incubation mode
HP-SEC	528 mm ² (2 x 12 mm x 22 mm)	3.0 mL	static
QCM	38 mm ²	216 µL + dead volume (74 µL)	static

10.3 Influence of pH on IgG Adsorption

QCM measurements were applied to study the influence of different formulation pH values on IgG adsorption. IgG concentration in the incubation solution was constantly set to 2 mg/mL in 20 mM histidine buffer, ionic strength was 100 mM.

10.3.1 Adsorbed Amount

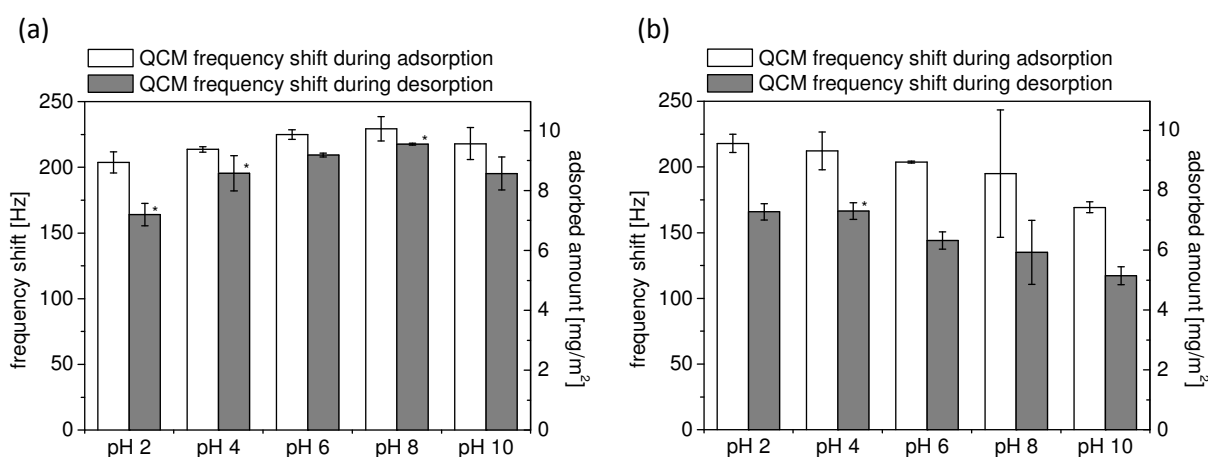


Figure III-29: Frequency shifts (n=3, *: n=2) upon IgG adsorption (2 mg/mL IgG, 20 mM histidine, 100 mM IS) and desorption with SDS for (a) EVA and (b) PE. Corresponding adsorbed amounts were calculated using the Sauerbrey equation.

In contrast to HP-SEC measurements, QCM can measure frequency shifts directly during adsorption. Figure III-29 depicts frequency changes resulting from IgG adsorption as well as subsequent desorption with SDS.

For EVA, frequency shifts during adsorption ranged from 204 Hz at pH 2 to 229 Hz at pH 8. Applying the Sauerbrey equation, this corresponds to adsorbed amounts of 8.9 mg/m² to 10.1 mg/m². For a homogeneous IgG layer (density of 1.35 g/cm³), this results in a layer thickness of 6.6 nm to 7.5 nm. The frequency shift during desorption showed a stronger pH dependency. At pH 2, 80.5 % of adsorbed IgG was desorbed upon rinsing with SDS. For all other pH values, the fraction that could be desorbed was 90 % or higher. The highest desorbed amount was 94.8 % at pH 8.

Using PE, the highest adsorbed amount was found for pH 2 with a frequency shift of 218 Hz. At pH 10, the frequency shift was 169 Hz and thus significantly lower (p < 0.001). Adsorbed amounts at pH 4, 6 and 8 lay in-between these values with frequency shifts between 212 and 195 Hz. For pH values > 6, adsorption to PE was in the range of 7.4 to 8.9 mg/m² and was thus slightly less than adsorption to EVA. Adsorbed layer thicknesses were between 5.5 and 7.1 nm. The overall desorption

efficiency of SDS on PE was reduced in comparison to EVA. Desorption was lowest for pH 8 (68.9 %), and highest for pH 4 (78.4 %).

10.3.2 Adsorption Kinetics

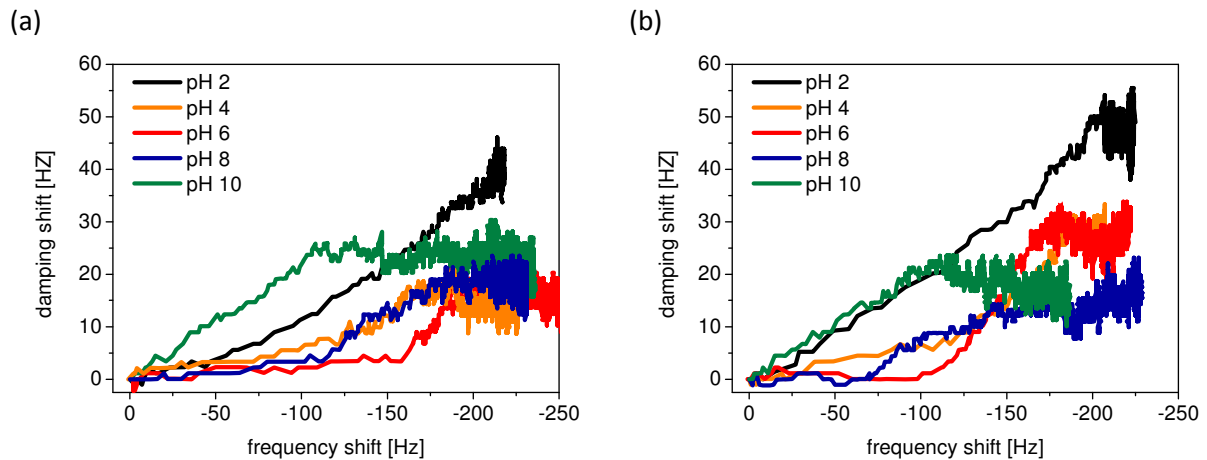


Figure III-30: Representative $\Delta\Gamma$ vs. Δf plots for formulations (2 mg/mL IgG, 20 mM histidine, 100 mM IS) with different pH values for (a) EVA and (b) PE.

Kinetics during adsorption can be monitored with $\Delta\Gamma$ vs. Δf plots. Figure III-30 shows representative plots for the time frame from IgG injection into the measuring cell until signal equilibration. Depending on the pH value of the formulation, one, two, or three phases with different slopes can be defined. For both surfaces, these observations are comparable. For pH 2, the $\Delta\Gamma$ vs. Δf plot consists of only one phase showing a linear and rather steep increase. For pH 10, two phases can be identified. An initial, steep increase is followed by a plateau phase, which starts after a frequency shift of approximately 100 Hz. For pH values of 4, 6, and 8, three segments can be distinguished. Initially, the slope is close to zero. After a short, steep increase, the graph then approaches a plateau after a frequency shift of around 175 Hz. In all cases, this plateau phase was reached within two minutes after IgG introduction to the measuring cell. The overall times until equilibrium are depicted in Figure III-31. At pH 2, signals equilibrated within 20 minutes. For all other pH values, equilibration took more than 40 minutes. For the EVA surface, equilibration time was longest at pH 10 with 80 minutes. For PE, the maximum equilibration time of 70 minutes was found at pH 6.

Reversibility (Figure III-32) was defined as the percentage of IgG that was desorbed upon rinsing with blank buffer. For the EVA surface, reversibility was in the range of 3 to 10 % for all tested pH values. For the PE surface, lowest reversibility values of 1 and 4 % were found at pH 2 and 10, respectively. At pH 8, reversibility was 17 % and therefore maximal.

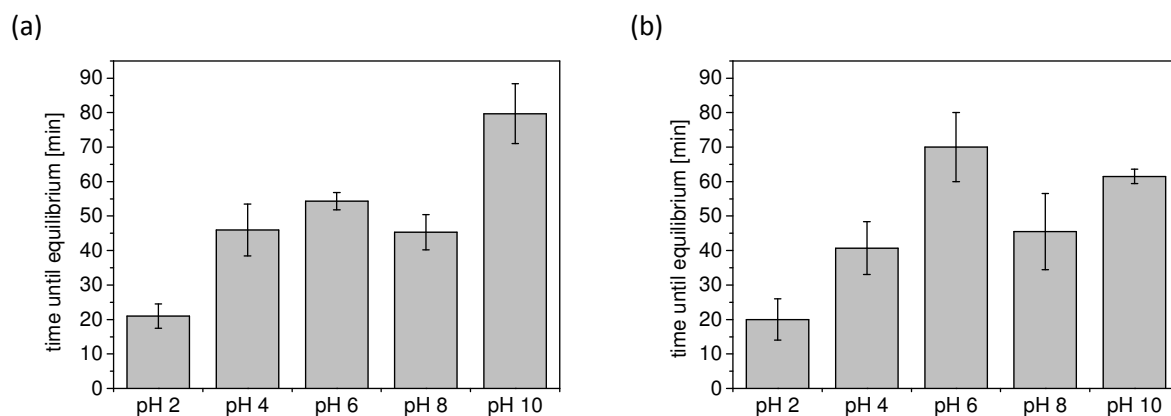


Figure III-31: Time until equilibrium for formulations (2 mg/mL IgG, 20 mM histidine, 100 mM IS) with different pH values on (a) EVA and (b) PE coatings.

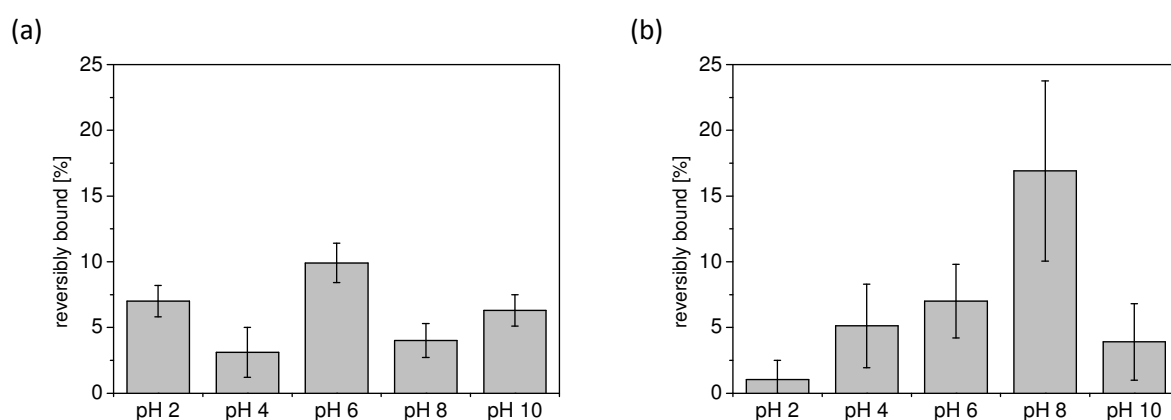


Figure III-32: Percentage of reversibly bound IgG (2 mg/mL IgG, 20 mM histidine, 100 mM IS) in dependency of formulation pH for (a) EVA and (b) PE.

10.3.3 Viscoelastic Properties of the Adsorbed IgG Layer

The quotient of damping and frequency shift after buffer rinsing is an indicator for the viscoelastic behavior of the irreversibly adsorbed protein layer (Figure III-33). $\Delta\Gamma/\Delta f$ values of zero describe the completely elastic behavior of a rigidly adsorbed layer. The maximum value of 0.75 to 0.8 was obtained when introducing liquid into the flow cell and characterizes a completely viscous behavior. Water as well as buffer components do not adsorb to the QCM chip, the observed changes in damping and frequency can thus be attributed to a change in viscosity only. The lower the $\Delta\Gamma/\Delta f$ value, the more rigid is the adsorbed layer. For most pH values, a rather small $\Delta\Gamma/\Delta f$ quotient was calculated. For EVA, a minimum value of 0.02 was determined at pH 6, whereas for PE, this value was lowest at pH 8 and 10 ($\Delta\Gamma/\Delta f = 0.03$). At pH 2, this value was significantly increased (0.11 for EVA and 0.12 for PE) and points towards a more viscoelastic behavior of the formed IgG layer.

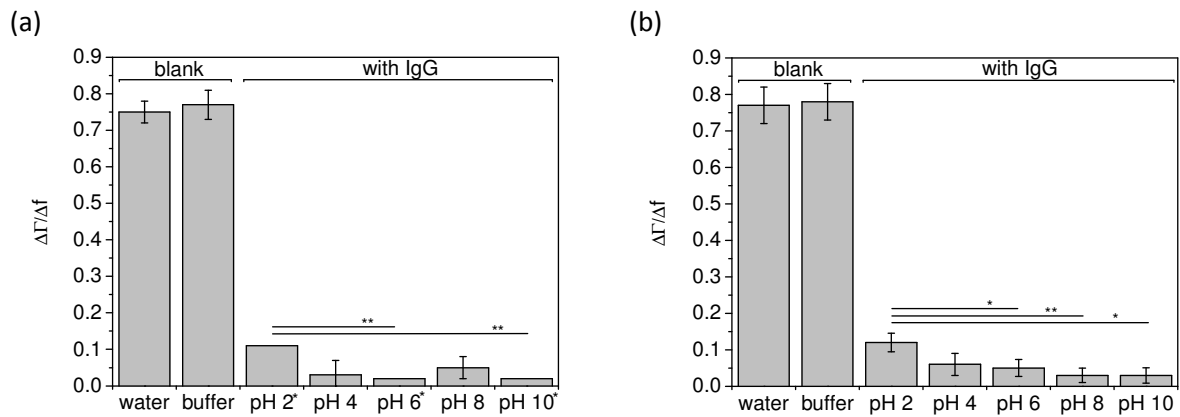


Figure III-33: $\Delta\Gamma/\Delta f$ ratios ($n=3$, $^*n=2$) of adsorbed IgG layers on (a) EVA and (b) PE for formulations (2 mg/mL IgG, 20 mM histidine, 100 mM IS) with different pH values as well as for water and various blank histidine buffers ($n=39$ for water / $n=42$ for buffer on EVA, $n=23$ for water and buffer on PE).

10.3.4 Influence of pH on IgG Size Distribution

In order to address the observed differences in viscoelastic behavior of IgG layers formed at pH 2, the hydrodynamic diameter of freshly filtrated IgG samples of different pH values was determined by DLS (Figure III-34). For pH 6 and 10, Z-average values were 11.03 ± 0.01 nm and 10.97 ± 0.12 nm, respectively. An increased Z-average of 14.34 ± 0.09 nm was measured at pH 2. Pdl values were 0.072 ± 0.008 for pH 2, 0.038 ± 0.005 for pH 6 and 0.046 ± 0.005 for pH 10.

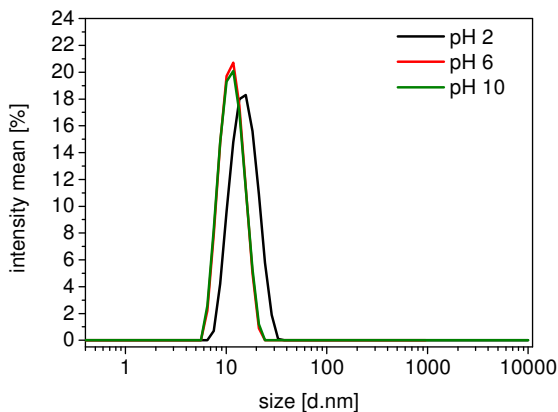


Figure III-34: DLS size distributions of IgG incubation solutions (2 mg/mL IgG, 20 mM histidine, 100 mM IS) of different pH values.

10.4 Influence of Ionic Strength on IgG Adsorption

In the following section, the influence of varying the ionic strength (IS) on IgG adsorption was addressed. In all cases, IgG was formulated at 2 mg/mL in 20 mM histidine buffer pH 6.0. Ionic strength was adjusted via the addition of sodium chloride. Assuming that zwitterions do not contribute to the overall ionic strength of a solution, ionic strength of formulations without additional sodium chloride is supposed to be approximately 10 mM.

10.4.1 Adsorbed Amount

In Figure III-35, frequency shifts upon IgG adsorption and corresponding adsorbed amounts are shown for different ionic strength values. For EVA, the adsorbed amount increased significantly upon addition of sodium chloride ad 100 mM ionic strength ($p < 0.001$). With higher ionic strength, there was no further change in the adsorbed amount. The amount of IgG adsorbed to PE was also slightly increased upon addition of salt, but the effect was not significant.

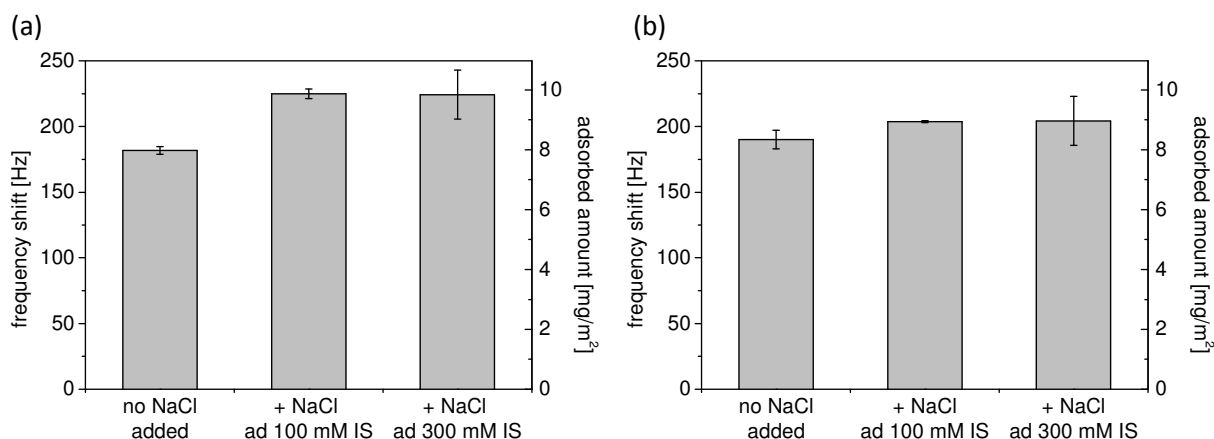


Figure III-35: Frequency shifts upon IgG adsorption (2 mg/mL IgG, 20 mM histidine, pH 6.0) in dependency of ionic strength for (a) EVA and (b) PE.

10.4.2 Adsorption Kinetics and Viscoelastic Properties

The influence of ionic strength on the adsorption kinetics is shown in Figure III-36. For EVA, all three graphs essentially overlap and reveal the three-phasic behavior described above. Upon adsorption of the formulation with 300 mM ionic strength to PE, a biphasic behavior comparable to the one at pH 10 is observed. Kinetics of IgG adsorption to PE was comparable for the formulations with 10 mM and 100 mM ionic strength.

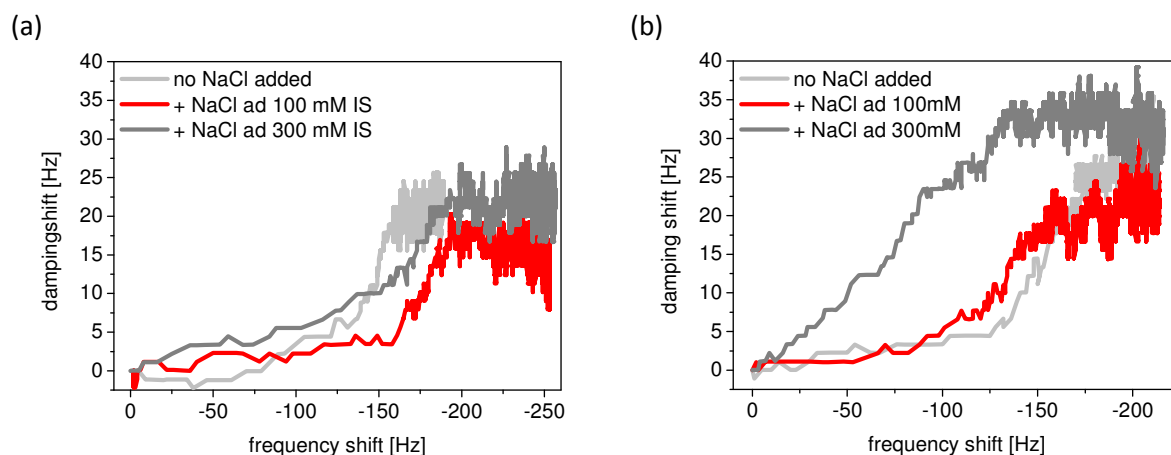


Figure III-36: Representative $\Delta\Gamma$ vs. Δf plots for formulations (2 mg/mL IgG, 20 mM histidine, pH 6.0) with different ionic strength for (a) EVA and (b) PE.

With increasing ionic strength, equilibration times on both surfaces increased stepwise from around 40 minutes up to 80 minutes (Figure III-37). Reversibility of adsorption was lowest for the formulation with lowest ionic strength (Figure III-38). On EVA, IgG formulated at 100 mM ionic strength adsorbed with highest reversibility of 10%. On PE, reversibility was highest at 300 mM ionic

strength with 12 %, but overall variability in the results did not lead to any significant effects. All IgG layers formed were rather rigid, as indicated by the low $\Delta\Gamma/\Delta f$ ratios in the range of 0.01 to 0.05 (Figure III-39).

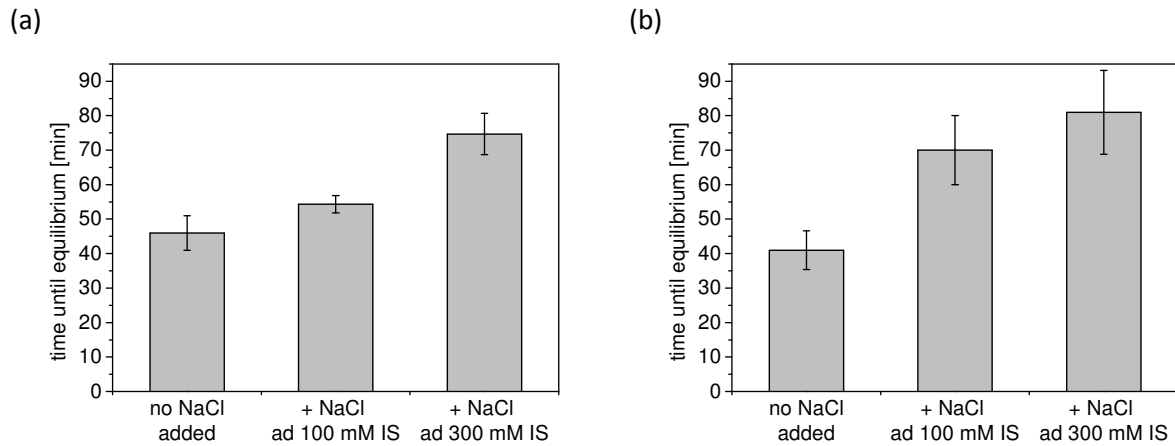


Figure III-37: Time until equilibrium for formulations (2 mg/mL IgG, 20 mM histidine, pH 6.0) with different ionic strength for (a) EVA and (b) PE.

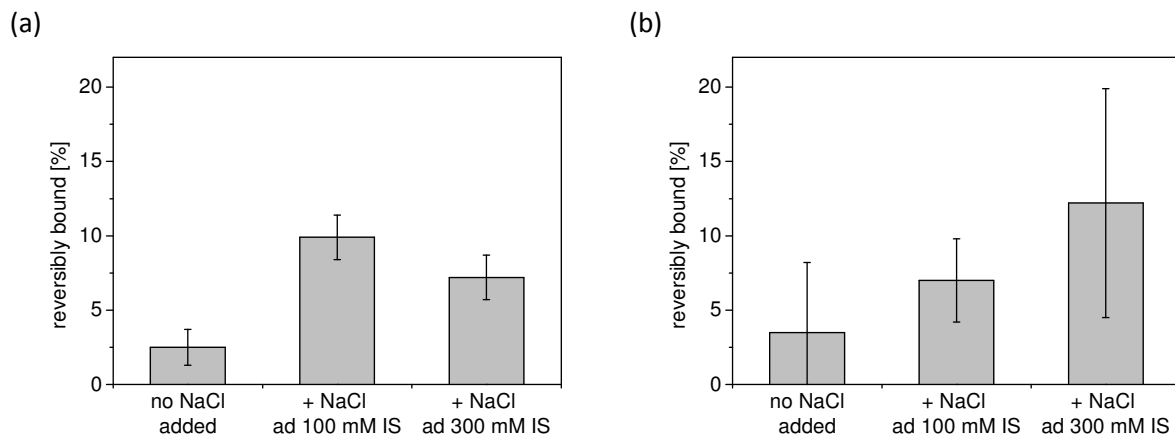


Figure III-38: Percentage of reversibly bound IgG for formulations (2 mg/mL IgG, 20 mM histidine, pH 6.0) with different ionic strength for (a) EVA and (b) PE.

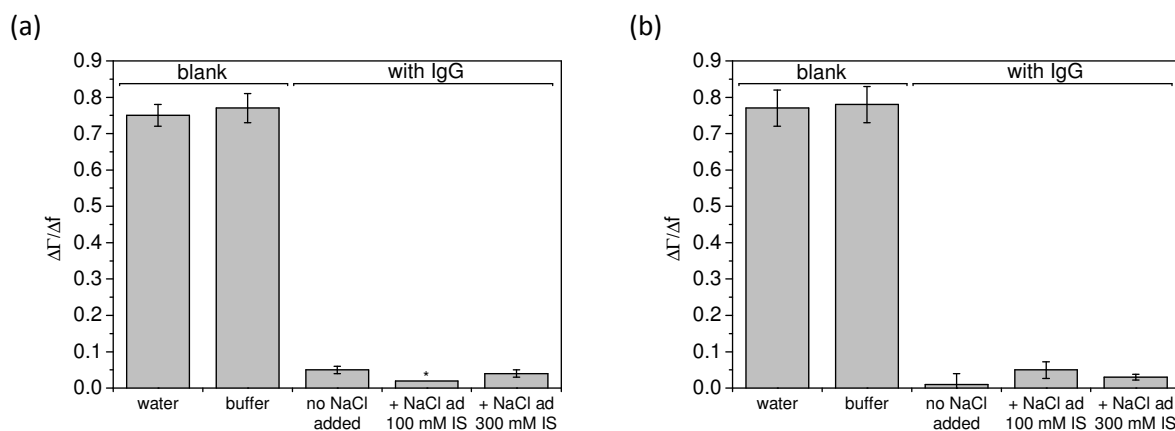


Figure III-39: $\Delta\Gamma/\Delta f$ ratios (n=3, *:n=2) of adsorbed IgG layers on (a) EVA and (b) PE for formulations (2 mg/mL IgG, 20 mM histidine, pH 6.0) with different ionic strength as well as for water and various blank histidine buffers (n=39 for water / n=42 for buffer on EVA, n=23 for water and buffer on PE).

10.5 Influence of Non-Ionic Surfactants on IgG Adsorption to EVA surfaces

10.5.1 Influence of Three Different Surfactants on Adsorption

The influence of the three non-ionic surfactants polysorbate 20 (PS 20), polysorbate 80 (PS 80) and poloxamer 188 (Pol 188) on IgG adsorption was tested with QCM runs applying different incubation schemes (see Table III-12). Sequential incubation of EVA surfaces with surfactant and IgG (and the other way around) as well as concomitant incubation with both components was performed. Frequency changes as an indicator for changes in the adsorbed mass were recorded for every single incubation step (Figure III-40).

Adsorption of PS 20 resulted in a frequency shift of 109 Hz after 92 minutes equilibration time. Subsequent incubation with IgG led to a minor frequency shift of only 11 Hz and fast equilibration within 6 minutes. Similar to previous experiments, adsorption of IgG on the freshly prepared EVA surface was completed within 42 minutes and induced a frequency shift of 179 Hz. The following incubation step with PS 20 took 23 minutes until equilibration and led to an additional frequency shift of 69 Hz. Upon concomitant incubation, the overall frequency shift was only 82 Hz and thus less than for the individual components. Moreover, QCM signals equilibrated very quickly within only 17 minutes.

For PS 80, similar observations were made although adsorption of the surfactant itself resulted in higher frequency shifts of around 200 Hz and longer equilibration times of up to 120 minutes. Therefore, the overall reduction in adsorbed mass upon co-incubation was even more obvious. Equilibration during incubation with the surfactant after precedent IgG adsorption took 93 minutes and thus significantly longer than for PS 20.

Adsorption of Pol 188 shifted the resonant frequency to a similar extent as PS 20, but occurred much faster (within 6 minutes). When incubating pre-adsorbed IgG with Pol 188, a comparable small frequency shift of 27 Hz was recorded after only 4 minutes equilibration time. The frequency shift as well as the equilibration time induced by co-incubation was in the same range as for Pol 188 adsorption alone.

Reversibility values for surfactant adsorption and co-adsorption with IgG are given in Table III-17. The amount of reversibly adsorbed mass is obviously increased in co-incubation mode. Reversibility is calculated from frequency changes between incubation solution and blank buffer and thus contributions from viscosity differences between those two media have to be considered. Viscosities of IgG / surfactant mixtures were consistently lower than viscosities of the pure surfactant solutions (Table III-17). Hence, viscosity effects did not account for the strong increase in reversibility upon co-adsorption.

Table III-17: Adsorption reversibility (n=2) and viscosities of incubation solutions containing surfactant only and surfactant plus IgG (2 mg/mL IgG, 0.02 % surfactant, 20 mM histidine, pH 6.0, no NaCl added).

Surfactant	Reversibility [%] upon adsorption of		Viscosity [mPa·s] of	
	surfactant solution	surfactant + IgG	surfactant solution	surfactant + IgG
PS 20	7.7 ± 0.5	28.6 ± 5.4	1.333	1.125
PS 80	2.2 ± 6.0	26.7 ± 0.2	1.466	1.398
Pol 188	18.1 ± 6.7	25.6 ± 1.9	1.287	1.139

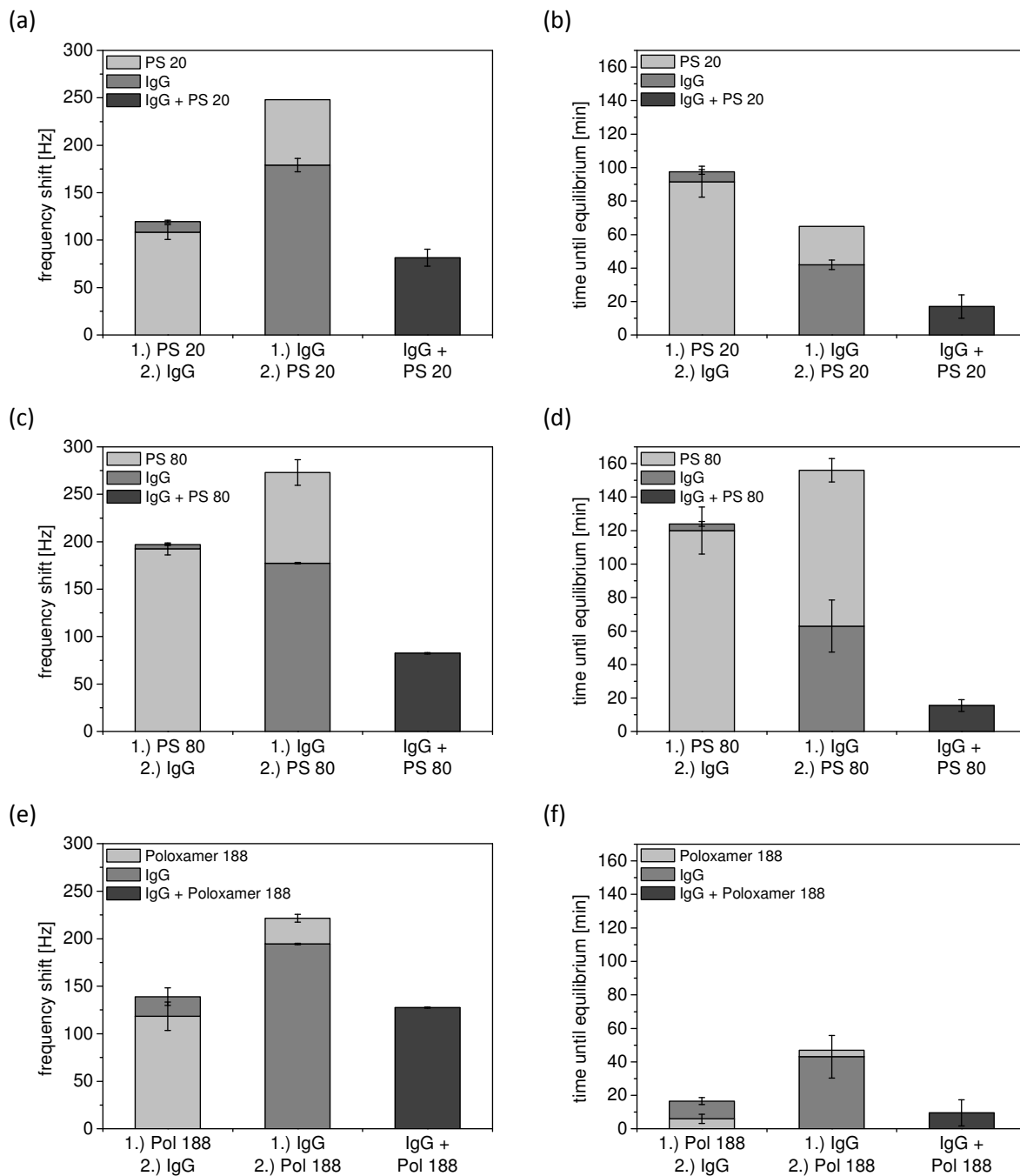


Figure III-40: Frequency change and time until equilibrium for subsequent and concomitant incubation of EVA-coated QCM chips with surfactant and IgG (2 mg/mL IgG, 0.02 % surfactant, 20 mM histidine, pH 6.0, no NaCl added). Frequency changes for single incubation steps are displayed in differently shaded bars. Frequency changes for subsequent adsorption steps are shown in stacked mode. Results are displayed for (a+b) PS 20, (c+d) PS 80, and (e+f) Pol 188 (n=2).

The damping shifts obtained for separate as well as co-incubation of surfactants and IgG are shown in Figure III-41. IgG adsorption resulted in rather small damping shifts. For PS 20 almost no damping shift occurred. For the other two surfactants, PS 80 and Pol 188, adsorption led to high damping shifts with considerable variability. For IgG / PS mixtures, damping shifts could not be evaluated due to signal drifts. For the IgG / Pol 188 mixture, damping was shifted by 8 Hz due to adsorption.

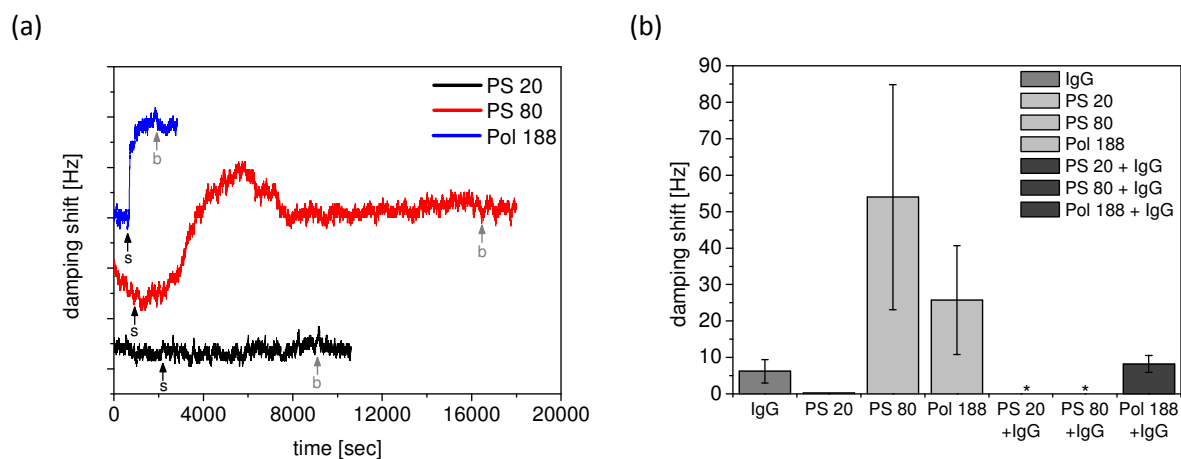


Figure III-41: (a) Damping shifts induced by adsorption of surfactants only. Arrows indicate the introduction of surfactant solution ("s") and blank buffer ("b") to the measuring cell. (b) Damping shifts during adsorption of IgG, surfactants, and IgG / surfactant mixtures (2 mg/mL IgG, 0.02 % surfactant, 20 mM histidine, pH 6.0, no NaCl added). *Negative values due to drifts in damping signal.

10.5.2 HP-SEC Determination of the Amount of Adsorbed IgG

QCM is able to detect minimal changes in mass due to adsorption, but cannot tell the mass contributions by different adsorbing species. Therefore, the different incubation schemes were applied to Flexboy® bag pieces and the amount of adsorbed protein was determined via desorption with SDS and subsequent HP-SEC quantification as described in Chapter II. The results are depicted in Figure III-42. For incubation mode #1 (surfactant followed by IgG), IgG amounts close to the IgG control were found. Only with Pol 188, the adsorbed IgG amount was significantly reduced ($p < 0.01$). Using incubation mode #2 (IgG followed by surfactant), markedly less adsorbed IgG was found in presence of both polysorbate types. For Pol 188, incubation mode #2 resulted in comparable adsorbed amounts of protein as incubation mode #1. After co-incubation of IgG and surfactant (incubation mode #3), the level of desorbed IgG was below the detection limit (= signal from lowest standard concentration of 0.1 $\mu\text{g/mL}$ in calibration curve).

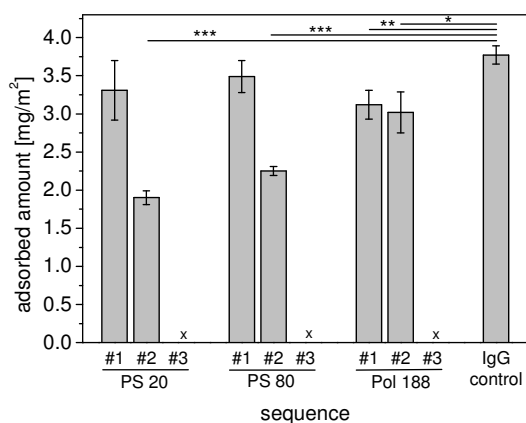


Figure III-42: Influence of surfactants (0.02 %) on the adsorbed amount of IgG on Flexboy® bag pieces after applying different incubation modes. IgG control: Incubation with IgG (2 mg/mL IgG, 20 mM histidine, pH 6.0, no NaCl added) only. x: < LOQ of 0.76 mg/m^2 .

10.5.3 Influence of PS 80 Concentration

The influence of PS 80 concentration on adsorption was assessed with PS 80 concentrations of 0.001 %, 0.02 %, and 0.2 %. For comparison, frequency shifts, reversibility values, equilibration times, and $\Delta\Gamma/\Delta f$ ratios for adsorption of IgG or surfactant only are also included in Figure III-43.

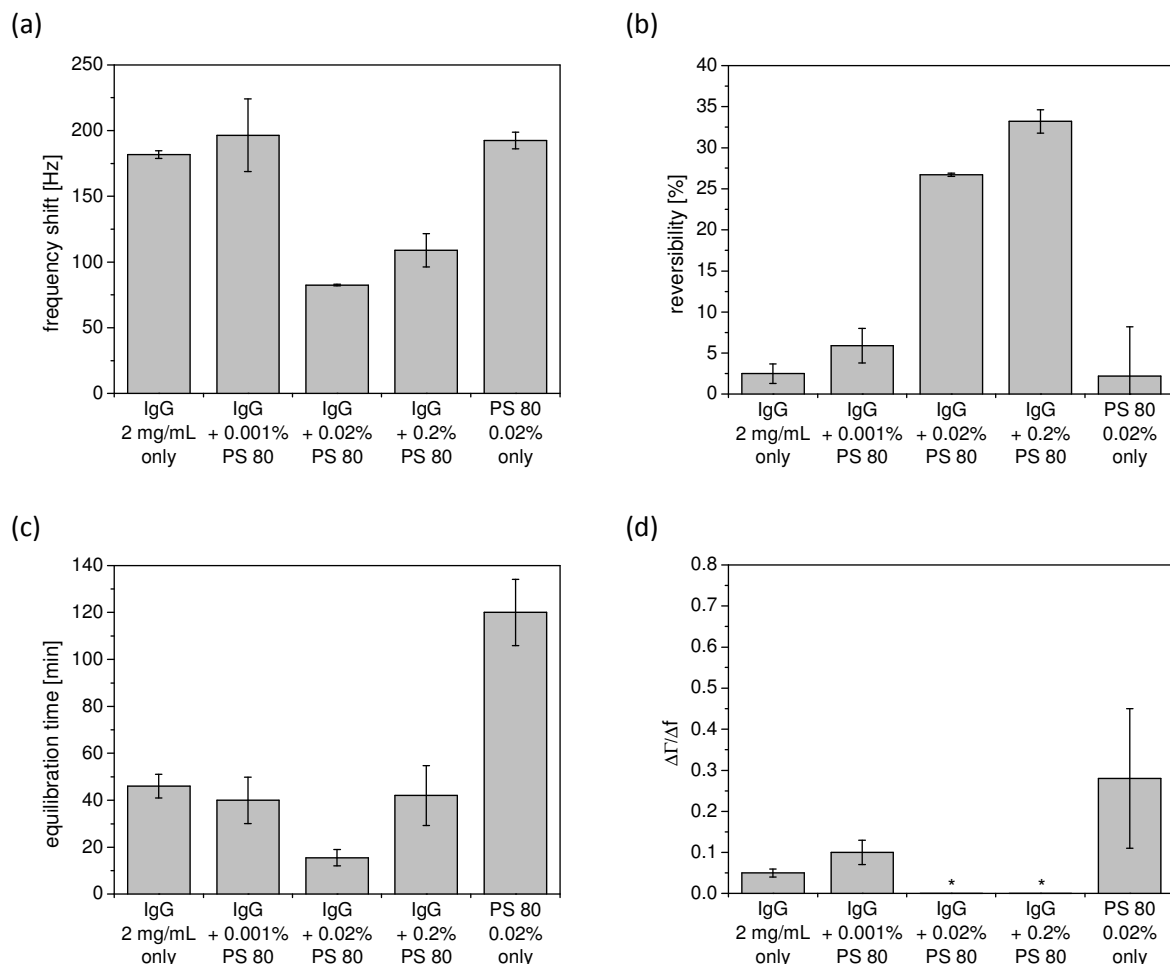


Figure III-43: Influence of PS 80 concentration on IgG adsorption upon co-incubation (2 mg/mL IgG, 20 mM histidine, pH 6.0, no NaCl added). (a) Frequency shifts, (b) reversibility, (c) equilibration time, and (d) rigidity in the form of $\Delta\Gamma/\Delta f$ ratios (n=2). *Negative values due to drifts in damping signal.

As already mentioned above, the frequency shift and equilibration time upon co-incubating with IgG and surfactant at a concentration of 0.02 % were clearly reduced in comparison to incubation with the two components individually. A PS 80 concentration of 0.001 % resulted in frequency shifts, equilibration time, and reversibility close to that of the IgG solution without added surfactant. The higher PS 80 concentration of 0.2 % also reduced mass adsorption significantly. Reversibility was observed to be highest for the mixtures with PS 80 concentrations of 0.02 and 0.2 %.

10.6 Verification of QCM Results with HP-SEC Quantification

With the help of the Sauerbrey equation, adsorbed amounts can be calculated from measured frequency shifts. In order to verify this assumption, adsorbed amounts obtained from such calculations were compared to the amount of IgG that was found after SDS desorption from the QCM chip. This was tested for pH 2, pH 6, and pH 10 with 100 mM ionic strength and EVA-coated QCM chips. Figure III-44 shows that both methods led to comparable results.

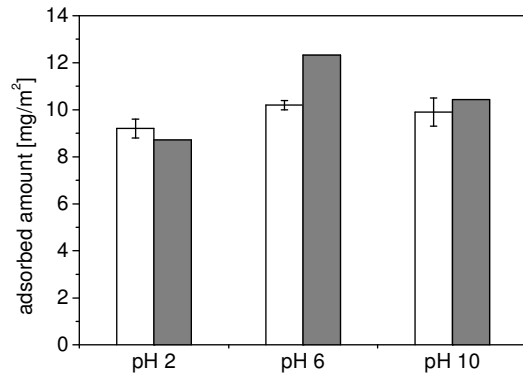


Figure III-44: Results for IgG amounts adsorbed on EVA-coated QCM chips (2 mg/mL IgG, 20 mM histidine, 100 mM IS) obtained from QCM frequency shifts (white bars, n=3) and via IgG desorption from the QCM chip and subsequent HP-SEC quantification (grey bars, n=1).

11 DISCUSSION

11.1 Implementation of QCM Measurements for Adsorption Studies with Single-Use Bag Polymer Surfaces

QCM crystals can be modified with many different kinds of materials and thus implemented as sensors in various applications [26,27]. PE and EVA are typical contact layer materials of single-use bioprocess bags [39]. Simple spin-coating of QCM chips with PE or EVA solutions allowed for the production of homogeneous polymer layers. Although the coating thickness varied significantly from experiment to experiment, complete chip surface coverage could be assumed in any case. Independent of the employed QCM chip as well as the achieved coating thickness, reproducible frequency shifts for IgG adsorption were obtained. A QCM model for studying protein adsorption to the bioprocess materials PE and EVA was thus successfully established.

11.2 Quantification of Protein Adsorption with QCM

The QCM frequency shifts upon incubation with IgG provide a direct measurement of the amount of adsorbed protein. Assuming a rigid IgG layer, the Sauerbrey equation was applied for calculating the adsorbed amount per unit area from the frequency shift provided in Hertz. The influence of pH and ionic strength on protein adsorption to both polymer surfaces was rather small. For the EVA coating, the adsorption maximum with approx. 10 mg/m^2 was found at pH 8, which is close to the protein's IEP. Adsorption maxima are often claimed to be found at the IEP due to the protein's overall neutral charge at this pH value. Thus reduced lateral repulsion forces between adsorbed protein molecules enable denser packing of molecules on the surface [11]. At pH 2, adsorption to EVA was slightly reduced to 8.9 mg/m^2 . At this pH value, both protein molecules and polymer layer are positively charged. At pH 10 the adsorbed amount of 9.6 mg/m^2 was close to the adsorption maximum despite likewise electrostatically repulsive forces between the now both negatively charged interaction partners. On the PE surface, the adsorbed amount decreased slightly but steadily with increasing pH value. Once again, this trend could not be explained with the expected electrostatic interactions between adsorbing protein and polymer surface. As a result of the polymer's zero point of charge at around 3.5, maximal electrostatic attraction and thus maximal adsorbed amount would have been anticipated between pH 4 and 8 in both cases. Oom *et al.* did not find the expected strong decrease in mAb adsorption to silicon dioxide and polystyrene-coated QCM chips at lower pH values. At pH 6, the amounts adsorbed to PS without any added surfactants were found to be 7.1 mg/m^2 and 12.5 mg/m^2 for two antibodies with lower and higher hydrophobicity, respectively [40]. Our results for IgG adsorption to PE and EVA surfaces were in a similar range and thus significantly higher than the maximum adsorbed amount of 5.5 mg/m^2 expected for monolayer adsorption [41]. Calculated IgG layer thicknesses of 5.5 to 7.5 nm exclude a completely flat-on orientation of adsorbed antibodies when assuming typical IgG dimensions of $10 \times 14 \times 5 \text{ nm}$ [42]. Instead, an end-on orientation with incomplete surface coverage in the range of 0.547 as given by the jamming limit of the random sequential adsorption model [43] might be assumed. An incomplete layer of randomly distributed IgG molecules that extend into the bulk solution by 10 nm in end-on orientation would give an apparent thickness of 5.5 nm for a homogeneous, evenly distributed layer. Alternatively, the formation of more than one layer of IgG has to be taken into account. Wiseman and Frank discuss adlayer formation at IgG bulk concentrations above $100 \text{ }\mu\text{g/mL}$ [44].

The influence of ionic strength on the amount of adsorbed IgG can be explained by the charge shielding effect of salt ions. With increasing ionic strength, lateral repulsive forces between individual IgG molecules are increasingly shielded. This allows a denser packing of protein molecules on the adsorbent. This effect was observed for both polymer surfaces, but more pronounced with the more hydrophilic EVA coating. An optimum in charge shielding was already achieved at an ionic strength of 100 mM as the adsorbed amount of IgG was not further increased at ionic strength values of 300 mM. Dixit *et al.* studied adsorption of an Fc-fusion protein on silicone oil-coated QCM sensors and found that an increased ionic strength of 150 mM was sufficient to neutralize any charge effects. The observed pH dependency at 10 mM ionic strength was thus leveled off and adsorbed amounts in the pH range from 3 to 9 all were around 4-5 mg/m² [31]. Interestingly, in a QCM study by Höök *et al.* the ferritin amount adsorbed on a methyl-thiolated gold surface strongly increased with increasing ionic strength, despite the hydrophobic character of the QCM chip coating. However, above a salt concentration of 50 mM adsorbed amounts remained relatively constant. Similar observations with pure gold surfaces led to the conclusion that the differences obtained with varying ionic strength are dominated by protein-protein rather than protein-surface interactions. Apart from a denser packing of protein molecules due to a reduction of repulsive forces upon salt addition, cluster formation in the bulk and subsequent adsorption of these pre-formed clusters is discussed [38].

The application of the Sauerbrey equation for a quantitative determination of protein adsorption is limited to rigidly adsorbed layers only. In the case of a viscoelastic layer, viscous coupling to the surrounding fluid reduces the totally measured frequency shift. The Sauerbrey equation thus underestimates the adsorbed mass – this is often referred to as the ‘missing mass effect’ [45]. The more complex Voigt model accounts for these viscoelastic contributions and includes density, viscosity, and shear elasticity of the adsorbed layer in its equations [46]. However, as these values are commonly not known for protein layers, they have to be estimated and / or fitted by measuring frequency shifts at various overtones [47,48]. For example, density is assumed to be between 1.0 and 1.35 mg/m³, depending on the water content of the adsorbed layer [40]. However, this assumption introduces uncertainties that might be comparable to the error encountered with the Sauerbrey approximation. In many cases, the Sauerbrey equation was found to result in adsorbed amounts that were close to values calculated with the Voigt model. Oom *et al.* state a difference of only 2-5 % between calculations with the Sauerbrey and the Voigt model for mAb adsorption to various surfaces like polystyrene and teflon [40]. Likewise, Kim and coworkers report very good agreement between both calculation methods for β -lactoglobulin adsorption to polyethersulfone surfaces for protein concentrations up to 10 mg/mL. Only at higher concentrations of 20 mg/mL, the Voigt mass was about 50 % higher than the Sauerbrey mass due to an observed increase in dissipation [48]. Dixit *et al.* also justified calculations with the Sauerbrey equation by assuming rigidly adsorbed Fc-fusion protein layers on silicone oil-coated surfaces [31]. Applying the Sauerbrey equation for close approximations to real adsorbed masses was thus also considered valid for the present study.

During the quantitative interpretation of QCM data, another aspect has to be considered. The QCM frequency shift is not specific for the mass of adsorbed protein, but likewise includes contributions from entrapped or adsorbed water and salt molecules [49,50]. According to Lubarsky *et al.*, the amount of water within the adsorbed protein film may be up to 90 %, depending on the protein and the type of surface under investigation [47,49]. Caruso *et al.* measured 2.3 times more adsorbed mass in the liquid phase than after drying when studying ferritin adsorption to gold surfaces. For IgG, a factor of 1.8 is reported [51]. However, mass contribution from associated water molecules strongly depends on surface coverage. At high surface coverage, the contribution from surrounding

water to frequency changes is postulated to be disproportionately low [24]. This might also apply for the present study since adsorption experiments were conducted at rather high IgG incubation concentrations and thus saturation conditions (see Chapter II). Additionally, studies by Ouberai *et al.* indicate a generally decreased hydration of 'soft' proteins when adsorbed on hydrophobic surfaces [52]. This might hold true for the combination of the 'soft' protein IgG and nonpolar polymer surfaces like EVA and PE as well. Cross-validation of the adsorbed amounts calculated with the Sauerbrey equation was performed by desorbing IgG from the EVA-coated QCM chip and analyzing the IgG content in the desorption medium. HP-SEC quantification data confirmed the QCM results and once again confirms the applicability of the Sauerbrey assumption for the present study. The amount of water incorporated in the adsorbed IgG layers did not seem to significantly affect the adsorbed mass measured with QCM.

11.3 Insights into Adsorption Kinetics

Adsorption kinetics are commonly analyzed in the form of $\Delta\Gamma/\Delta R/\Delta D$ vs. Δt plots [38,48,53–57]. For pH values of 4, 6, and 8, a three-stage adsorption process on both studied surfaces was observed. In such a plot, a slope close to zero represents the formation of rigid and densely adsorbed layers, whereas a steeper slope indicates that a soft and water-rich film is formed [56]. The first phase during adsorption was characterized by a slope of zero and thus the formation of a rigid IgG layer. The steep increase during the second phase is indicative of the attachment of loosely bound protein. This loosely bound fraction might adsorb to unoccupied areas in-between already attached molecules or as a second layer on top of the first one [40,57]. Possibly, a change in antibody orientation from rigidly attached, flat-on oriented antibodies towards more loosely bound, end-on oriented molecules is induced by increasing surface coverage [44]. During the subsequent plateau phase, rigidification of the previously formed layer as it becomes more closely packed is anticipated [38]. Alternatively, the formation of an additional, rigid layer might be the reason for this third phase [55]. The slope of the initial adsorption phase seems to be dominated by the prevailing electrostatic forces between protein and surface: At pH 6, both interaction partners were oppositely charged and thus electrostatically attracted each other. At this pH value, the initial phase with zero slope was most pronounced. At pH 4 and 8, either the surface or the protein were close to their ZPC (approx. 3.5) or IEP (approx. 8.5), respectively. Therefore, electrostatic attraction was diminished and the initial phase was shorter and / or the slope was slightly higher than for adsorption at pH 6. At pH 2 and 10, both protein and surface bear charge of the same sign. Electrostatic repulsive forces resulted in an initial steep adsorption phase indicative for the formation of soft IgG films. At pH 10 subsequent rigidification occurred, whereas at pH 2 hardly any plateau phase was observed. Rigidification was the most dominant step during equilibration and this phase was typically reached within the first minutes. Equilibration times for formulations with pH 2 were the shortest, whereas the pronounced rigidification phase for pH 10 on the EVA surface led to prolonged adsorption times. It is assumed that rigidification is also achieved via structural rearrangements [58].

Variations in ionic strength at pH 6 hardly affected adsorption kinetics for IgG adsorption to EVA. $\Delta\Gamma$ vs. Δf plots for the formulation with 300 mM ionic strength revealed a slightly higher initial slope and a less sharp transition between the first and second adsorption phase, possibly due to a shielding of attractive forces between protein and surface. However, choosing an ionic strength of 300 mM for IgG adsorption to the less charged PE surface was sufficient to eliminate effects from electrostatic attraction during the first adsorption phase. Adsorption was thus reduced to a biphasic process with a steep initial slope, comparable to the plots for formulations with pH 10. At the same time,

equilibration times extended with increasing ionic strength. According to the described observations for $\Delta\Gamma$ vs. Δf plots, this effect was more pronounced with the PE surface. Although the effect of ionic strength on the adsorbed amount on both surfaces was limited, a clear influence on adsorption kinetics and especially equilibration times was thus determined. A hampering of adsorption at higher ionic strength for oppositely charged surfaces as in the case of pH 6 was expected [11].

Doliška *et al.* also report a three-phasic process for fibrinogen adsorption to polyethylene terephthalate surfaces, but in their studies slopes of the first and third phase were steeper than during the second phase [56]. For the adsorption of protein A to Au and Ti surfaces, Marxer *et al.* describe two phases in corresponding ΔD vs. Δf plots. The authors ascribe each phase to the formation of a separate protein layer. Comparable to our studies, fast initial adsorption events were followed by the formation of more rigid adlayers [55]. Similarly, from their studies on β -lactoglobulin adsorption to PES surfaces Kim *et al.* conclude that after an initial, rapid stage, conformational changes might occur in the following plateau phase [48]. Wiseman and Frank interpreted their QCM data for mAb adsorption on a hydrophobic model surface as a two-step process: Initially, antibodies attach rigidly to the surface in a flat-on orientation, but with increasing surface coverage mAb rearrange into a vertical, end-on orientation with looser mechanical coupling to the surface [44].

In this context, the three-stage cooperativity model deduced by Luo and Andrade from their studies on protein adsorption to hydroxyapatite shall be discussed [59]. In most cases, Hill plots from isotherm data of four proteins (lysozyme, BSA, lactoferrin, and transferrin) resulted in S-shaped graphs. The three obtained slopes refer to the cooperativity of adsorption at that specific stage. Values > 1 indicate positive cooperativity, whereas values < 1 represent negative cooperativity. Cooperativity values for the three different phases typically ranked as follows: $3 > 1 > 2$. Interestingly, Hill plots of isotherm adsorption data from Chapter II follow these observations (Figure III-45).

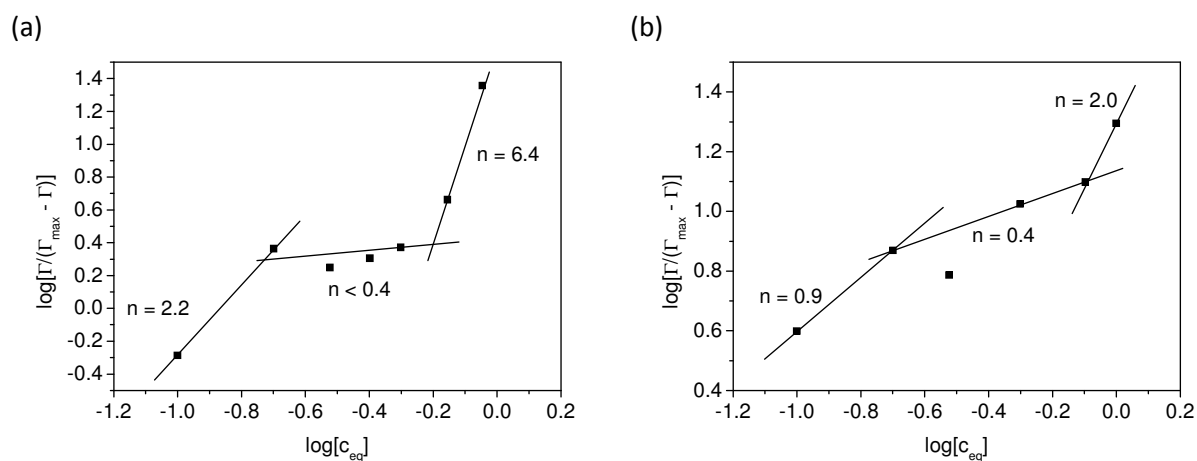


Figure III-45: Hill plots of IgG adsorption (concentrations from 0 to 1 mg/mL, pH 5.4, in 20 mM histidine buffer without further additives) for (a) Flexboy® (EVA) and (b) Flexel® (ULDPE) bag. Data is taken from Chapter II.

When relating increasing equilibration concentrations with increasing surface coverage and thus increasing frequency shifts during QCM measurements, the interpretation of protein adsorption as described by Luo and Andrade can be applied to the three stages observed in $\Delta\Gamma$ vs. Δf plots. The initial phase is thus characterized by strong cooperativity between protein molecules and the surface due to electrostatic attraction. This is followed by a rather short transition phase with low and even negative cooperativity and thus loose attachment of protein molecules. Finally, the third stage

indicates very high cooperativity due to lateral interactions between individual protein molecules and finally results in the formation of a densely adsorbed layer.

Nevertheless, a certain fraction of protein molecules can still be rather loosely and thus reversibly associated with the adsorbed layer. Reversibility in most cases was found to be below 10%. Exceptions of rather high reversibility values were obtained for IgG adsorption on PE of up to 17% at pH 8 and 100 mM ionic strength and of around 12% at pH 6 and 300 mM ionic strength. At both formulation conditions and especially in combination with the completely nonpolar PE surface, electrostatic interactions are reduced since pH 8 is close to the protein's IEP and high ionic strength leads to the discussed charge shielding effect. The lack of electrostatic attraction to the surface might be the reason for this increase in adsorption reversibility. Reversibility in general is inversely related to the ability of the protein molecules to adapt to the surface [52] and can thus be expected to be low for 'soft' proteins like IgG [8,11]. Reversibility values of around 10% were also found in other studies. Felsovalyi *et al.* observed reversibility of up to 8.5% for lysozyme adsorption on silica [60] and Dixit *et al.* state reversibility values of less than 10% for Fc-fusion proteins on silicone oil surfaces [31]. Kim *et al.* measured up to 15% reversibility for β -lactoglobulin adsorbed to PES at 20 mg/mL with a tendency for increased reversibility at higher protein concentrations. Reversibility is calculated from frequency shifts between IgG solution and blank buffer and can thus be biased due to viscosity differences of the two media. In consequence, the already rather low reversibility values might still be slightly overestimated.

11.4 Viscoelastic Properties of Adsorbed IgG Layers

Due to the above described rigidification process during IgG adsorption and $\Delta\Gamma/\Delta f$ values of less than 0.1, protein layers obtained for pH values ≥ 4 were assumed to be rigid in nature. The critical $\Delta\Gamma/\Delta f$ value of 0.1 for rigid layers is a more concrete interpretation of the requirement $\Delta\Gamma \ll \Delta f$ by Reviakine and coworkers [24]. Depending on the parameter utilized and the applied QCM system, various limits can be found in literature. Muramatsu *et al.* defined the reliable range for the Sauerbrey equation for values up to $\Delta R/\Delta f = 0.01$ [53], and Doliška *et al.* applied a threshold of $\Delta D/\Delta f < 0.1 \times 10^{-6} \text{ Hz}^{-1}$ [56].

IgG layers formed at pH 2 were significantly softer than most other layers. This is deduced from $\Delta\Gamma/\Delta f$ values of > 0.1 and the rather short plateau phase observed in $\Delta\Gamma$ vs. Δf plots. Oom *et al.* also describe an increased softness of IgG layers when adsorbed at lower pH values. Increased hydration and a possibly more unfolded structure are claimed to be the reason for this behavior [40]. However, from DLS results at pH 2 the prevalence of IgG dimers instead of monomers is concluded and thus a completely different adsorption mechanism has to be assumed. The tendency of IgG molecules to form dimers and trimers at acidic pH and in the presence of salt was extensively studied by Arosio *et al.* [61,62]. Reported hydrodynamic radii for IgG monomer and dimer of 6 nm and 7.3 nm, respectively, correlate well with Z-average values of 11 nm at pH 6 / 10 and 14.3 nm at pH 2 obtained for IgG formulations in the present study. Other than IgG monomers, most likely these IgG dimers attach to the surface at an acidic pH of 2. It is anticipated that dimers cannot interact with the surface to the same extent as the monomer species. Each IgG molecule already interacts with a second molecule within the formed dimer; therefore hardly any further interactions with the adsorbent can be established. In this context, especially exposed hydrophobic patches that would be the most important surface interaction sites might be already covered by the second IgG molecule. Moreover, the adsorbing dimer species forms a thicker, but less dense packed layer due to its

increased size. In consequence, more water can be entrapped between adsorbed dimers. Together with the lacking rigidification step, this results in an overall softer IgG layer.

11.5 Influence of Surfactants on IgG Adsorption

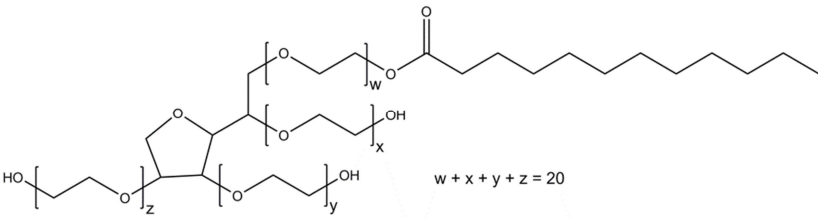
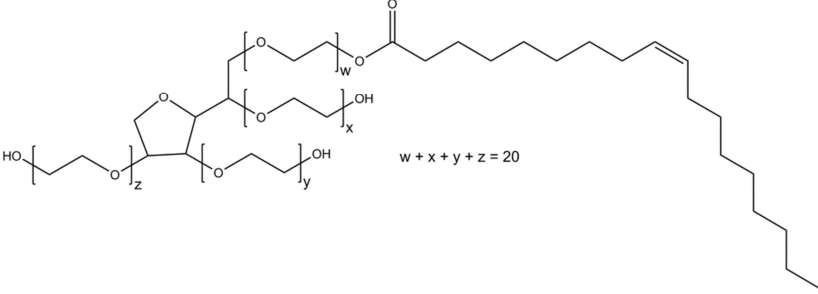
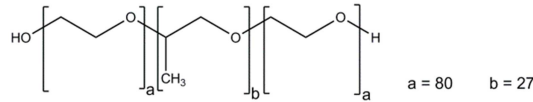
Nonionic surfactants like polysorbate 20 (PS 20), polysorbate 80 (PS 80), and poloxamer 188 (Pol 188) are commonly used formulation excipients that can stabilize protein drugs via a reduction of interfacial destabilization events [63,64]. Like proteins, surfactants are amphiphatic molecules with relatively large hydrophobic moieties and thus are supposed to readily adsorb to interfaces. In the following section, the adsorption behavior of surfactants alone as well as in combination with the model IgG on EVA surfaces is discussed.

11.5.1 Adsorption Behavior of Surfactants

The highest adsorbed amount of 8.4 mg/m^2 was measured for PS 80 which corresponds to a layer thickness of 7.9 nm. Adsorbed amounts for PS 20 and Pol 188 were in a comparable range with 4.8 mg/m^2 (4.3 nm) and 5.2 mg/m^2 (4.9 nm), respectively (see Figure III-40 after step 1 of incubation mode #1). As indicated by a lower HLB value and the longer hydrocarbon chain, PS 80 is more hydrophobic than the other two surfactants (see Table III-18) which might be the reason for the higher adsorbed amounts. Molecular weights of PS 20 and 80 are comparable, thus for PS 80 a more dense packing of the surfactant molecules with a decreased footprint on the EVA surface can be assumed. In consequence, the surfactant molecules are more extended towards the bulk solution, giving rise to a higher adsorption layer thickness and also to more pronounced damping shifts during adsorption. In contrast to the rather soft PS 80 layer, PS 20 layers were found to be rigidly attached to the surface, as damping shifts were close to zero and even below the values obtained for IgG layers. Adsorbed Pol 188 was found to result in layers with rather high viscoelasticity, too.

Adsorption times for PS 80 were approx. 2 hours and thus remarkable long. Together with the observed overshooting effect in the damping signal, this might point towards the occurrence of structural reorganizations during surface filling [63]. The equilibrium time for Pol 188 was less than 10 minutes and thus approx. ten times faster than adsorption equilibration for PS 20 and PS 80. This might be due to the relatively few poloxamer molecules that actually adsorbed on the surface. Although total adsorbed amounts were comparable to PS 20, six times more PS 20 molecules adsorbed per unit area in comparison to Pol 188 due to the large difference in molecular weight. Adsorption of fewer molecules might simply be completed in a shorter period of time. The reduced amount of adsorbing molecules might arise from the bulky structure of individual poloxamer molecules together with the lack of reorientation, from a reduced affinity for the hydrophobic surface based on the higher hydrophilicity of poloxamer, or from the limited availability of adsorbing molecules. Equal incubation concentrations for all surfactants were chosen in the form of mass concentrations (w/V) rather than molar concentrations. For Pol 188, this could have resulted in non-saturation conditions. Although there is no consensus about the true CMC of Pol 188 [65], a concentration of 0.02 % (w/V) is supposed to be below this value.

Table III-18: Properties of employed surfactants.

Surfactant type and chemical structure	CMC	HLB
PS 20  $w + x + y + z = 20$ MW = 1228 g/mol	$59 \mu\text{M}^{\text{a}}$ / 0.007 %	16.7 ^a
PS 80  $w + x + y + z = 20$ MW = 1310 g/mol	$12 \mu\text{M}^{\text{a}}$ / 0.0016 %	15 ^a
Pol 188  $a = 80 \quad b = 27$ MW = 8400 g/mol	$40 \mu\text{M}^{\text{c}}$ / 0.03 %	> 24 ^b

^a from Merck Millipore product information, available online at <http://www.merckmillipore.com>, accessed January 5, 2015.

^b from BASF product information, available online at <http://worldaccount.basf.com>, accessed January 5, 2015.

^c from Sigma-Aldrich product information, available online at <http://www.sigmaaldrich.com>, accessed January 5, 2015.

Not all results are consistent with observations described in literature. The specific surface under investigation as well as the quality, concentration, and formulation of the surfactant might have a significant impact on the adsorption behavior. For PS 20 (0.06 mM) adsorbed on PS, Shen *et al.* measured a layer thickness of only 1.4 nm using SPR. They also observed a dense PS 20 layer, which is anticipated to be the result of a fast initial adsorption phase followed by a slower reorganization step at high surface coverage [66]. Dixit *et al.* studied adsorption of surfactants to a silicone oil surface using QCM and found significantly less adsorbed protein. Pol 188 (0.035 %) adsorbed to the highest extent with 3.8 mg/m², PS 20 and PS 80 (both at 0.02 %) adsorbed with only 2.2 mg/m² and 2.5 mg/m², respectively. Comparable increases in resistance and thus similar viscoelasticity for all surfactant layers are stated [67].

11.5.2 Sequential Adsorption and Co-Adsorption of IgG and Surfactants

From the negligible frequency shift during IgG incubation after pre-incubation with surfactant, the existence of a protein-resistant surfactant layer on the chip surface might be assumed. However, the true composition of the adsorbed layer after the second incubation step cannot be concluded from frequency shifts alone. When IgG incubation is followed by surfactant adsorption, the additional frequency shifts point towards surfactant attachment on top of or in-between the IgG layer. Dixit *et al.* also describe this process and attribute the smaller frequency shift upon subsequent Pol 188 incubation to the inability of the larger poloxamer molecules to permeate all the available vacancies in the pre-existing protein layer [67]. Additionally, at least partial replacement of IgG molecules on the surface by surfactant molecules is also expected. For complete IgG replacement, final frequency shifts comparable to frequency shifts obtained for pure surfactant adsorption would have been expected.

Interestingly, for polysorbate / IgG co-incubation, frequency shifts were less than for adsorption of the individual compounds, thus neither a complete surfactant nor a saturated IgG layer was formed. The remarkable increase in adsorption reversibility that could not be ascribed to viscosity effects might point towards the formation and reversible attachment of a mix of protein and surfactant molecules [40,64]. Binding of polysorbates to IgG was shown to be negligible [68,69] and also other authors deny the formation of protein-polysorbate complexes [70]. Instead, the smaller, faster diffusing surfactant molecules are likely to pre-occupy the hydrophobic surface [67], but might not be able to reorganize into a dense layer due to subsequently arriving IgG molecules. In return, IgG molecules possibly cannot spread and rigidly attach on the surface due to the presence of surfactants and thus reversibility is increased. The reduced equilibration times for polysorbate / IgG mixtures may thus be explained by the generally reduced amount of adsorbed mass and the lacking reorganization process of polysorbate molecules or by an acceleration of surfactant adsorption by the protein as described by Lee *et al.* [64]. In their review, these authors claim that proteins may reduce the major entropic barrier for surfactant movement from micelles to the interface. Alternatively, the enthalpy of activation might be reduced by a destabilized surfactant self-association. Corresponding experimental data gives evidence that this theory seems to hold true for polysorbate but not poloxamer adsorption to the air-water interface [71]. For Pol 188 / IgG co-adsorption, frequency shifts and equilibration times were similar to the values obtained for poloxamer adsorption alone. This indicates that the layer formed during co-incubation was mainly composed of Pol 188 and that the presence of protein did not influence the poloxamer adsorption rate. Dixit *et al.* were able to deduce the relative composition of layers formed during co-incubation from the extent of damping shifts [67,72]. From our data on damping shifts, no clear conclusion can be drawn about the presence of IgG and / or surfactant in co-adsorbed layers. Only the damping shift for Pol 188 / IgG co-incubation could be evaluated. Since this value was between the damping shifts received for adsorption of pure IgG and pure surfactant, also a mixed layer might have been formed.

Quantification of the final amount of IgG on the EVA surface via desorption and HP-SEC analysis after the above described sequential and co-adsorption steps brings us to partially revise the theory about the formation of a protein-resistant surfactant coating. IgG molecules were able to replace most of the adsorbed surfactant molecules since adsorbed IgG amounts after incubation mode #1 were close to the IgG control value. Pre-adsorbed IgG molecules were only partly replaced by surfactants in a subsequent incubation step. In this context, polysorbate 20 was most effective and replaced about 50 % of adsorbed IgG, whereas Pol 188 desorbed only 20 %. For co-incubated samples, adsorbed IgG amounts were below the detection limit. However, due to the rather high detection limit up to 20 % of IgG found in the control might still be present on the surface after co-incubation.

Replacement of pre-adsorbed proteins by surfactants is reported in several studies [73–76]. Desorption from the surface can be either mediated by the formation of surfactant-protein complexes and subsequent solubilization or by comparably stronger surfactant-surface interactions. The extent of protein displacement was found to depend on the properties of the protein, the surfactant, and the surface. In this context, rather low effectivity is attributed to nonionic surfactants [64]. Replacement of pre-adsorbed surfactant by proteins, however, was less expected. Many authors report the formation of a protein-resistant surfactant layer that effectively inhibits subsequent protein adsorption [66,67,76,77]. Only for very hydrophilic surfaces different observations were made. Joshi and McGuire found that pre-coating silica surfaces with PS 80 did not reduce lysozyme adsorption [76]. Also, Kim *et al.* report displacement of Pol 188 as well as PS 20 and 80 from silica-titania surfaces during subsequent lysozyme and GCSF incubation. The ability of pre-

adsorbed surfactant to inhibit protein adsorption thus strongly depends on the affinity of the surfactant and the protein for the specific surface. The affinity of the tested surfactants to the EVA surface under investigations was apparently not sufficient for efficient protein adsorption reduction when applied successively. Only during co-incubation, surfactants were able to effectively reduce protein adsorption.

11.5.3 Importance of Surfactant Concentration

Varying the PS 80 concentration demonstrated that a surfactant concentration above the CMC is needed for effectively inhibiting protein adsorption during co-incubation. The adsorption profile for the IgG formulation with a PS 80 concentration of 0.001 % strongly resembled the one for the IgG formulation without surfactant. An increased PS 80 concentration of 0.02 or 0.2 % led to clearly reduced frequency shifts and higher reversibility, probably due to the above discussed adsorption mechanism during co-incubation. Similar observations are described in literature. Zhang and Ferrari found that albumin adsorption reduction to silicon surfaces by PS 20 was most effective at concentrations close to the CMC [78]. Joshi and McGuire describe an increase in reduction of lysozyme adsorption to silica with increasing PS 80 concentrations of up to 80 ppm (≈ 0.008 % (w/V)) [76]. In contrast, Mollmann *et al.* showed that insulin displacement from a hydrophobic silane-modified quartz was effective for PS 80 concentrations from 0.001 % upwards [75]. Likewise, Kapp *et al.* report that already a PS 80 concentration of half the CMC was effective in reducing mAb adsorption to hydrophobically modified surfaces, but a concentration of two times CMC was necessary to achieve a reduction in mAb adsorption of up to 90 % [77].

11.6 Comparison of Results Obtained with Real Bag Surfaces and Casted Polymer Films

In the previous chapter, IgG adsorption to real bag surfaces was measured by desorbing IgG with SDS and subsequently analyzing the IgG content via HP-SEC with fluorescence detection. Table III-19 comparatively lists the adsorbed amounts obtained with this method for QCM chips with the casted EVA surface and for real Flexboy® bag pieces. It is obvious that for the model surface three to four times more adsorbed protein mass was found than for the real bag surface. However, trends with regards to the observed pH dependency of adsorption were similar.

Table III-19: Adsorbed amounts [mg/m^2] obtained with the desorption / HP-SEC method for EVA-coated QCM chips and the real bag surface (results from Chapter II) for IgG formulations (2 mg/mL IgG, 20 mM histidine, 100 mM IS) of different pH values.

pH	From desorption of EVA-coated QCM chip (n=1)	From desorption of Flexboy® bag piece (n=3)	Deviation by factor
2	8.7	2.3 ± 0.2	3.8
6	12.3	4.6 ± 0.7	2.7
10	10.4	2.9 ± 0.1	3.6

The adsorbed protein amounts obtained with the real bag pieces were in the range of monolayer coverage. In contrast, results from QCM chips pointed towards the formation of IgG multilayers. The observed differences trace back to the disparity between the real bag surface and the model surface. The model surface was produced via polymer dissolution in an organic solvent und subsequent spin-

coating. Real bag surfaces are manufactured by extruding melted polymer granules. The contact with organic solvents during the preparation of QCM model surfaces might have a significant impact on film properties. A thorough control of surface characteristics like contact angles, surface free energy, and residual solvent content during future studies is thus highly recommended for future studies. Moreover, surface morphology of both films as analyzed via 3D laser scanning microscopy revealed distinct differences. This divergence in surface roughness can also affect the extent of protein adsorption considerably [79,80].

12 SUMMARY AND OUTLOOK

During the course of this study, spin-coated polymer surfaces were employed as model surfaces for single-use bioprocess bags during QCM adsorption studies. It was thus possible to gain insights into the adsorption mechanism of therapeutic proteins on process materials like EVA and PE. Frequency shifts from QCM experiment were translated into adsorbed mass per unit area by applying the Sauerbrey equation. This approach was found to be valid since the model IgG adsorbed rigidly to the sensor surface and contributions from water associated with the adsorbed layer seemed to be negligible. Adsorbed IgG amounts were in the range of 7 to 10 mg/m², which clearly exceeds monolayer coverage. The influence of pH on the adsorbed amounts was rather small. Increasing adsorbed masses and equilibration times with increasing ionic strength could be attributed to the charge shielding effect of salt ions. For most formulations a three-stage adsorption process was identified in the corresponding $\Delta\Gamma$ vs. Δf plots. During the first phase, rigid attachment was most likely governed by electrostatic attractive forces between protein and surface. The second phase was characterized by rather loose adsorption of additional molecules, possibly in a second layer. Finally, positive cooperativity in the form of lateral interactions between protein molecules is supposed to be responsible for rigidification of the adsorbed layer in the third phase. Consequently, most final IgG layers revealed a low $\Delta\Gamma/\Delta f$ ratio, which indicates low viscoelasticity. An exception to that observation was IgG layer formation at pH 2. In this case, a completely different adsorption mechanism, namely adsorption of IgG dimers that hardly undergo conformational changes on the surface, is anticipated. The influence of the three nonionic surfactants PS 20, PS 80, and Pol 188 on IgG adsorption was studied in sequential and co-adsorption mode. The three surfactants clearly varied in adsorption behavior, with more pronounced differences between the polysorbate types and poloxamer. However, all three surfactants were effective in reducing adsorption only during co-incubation. For PS 80, it was exemplarily shown that a surfactant concentration above the CMC seems to be necessary for significantly affecting protein adsorption. A comparison of adsorption data from the previous chapter (HP-SEC quantification after protein desorption from real bag surfaces) with the results obtained from QCM chip desorption revealed deviations in the adsorbed amounts by a factor of 3 to 4. This divergence is traced back to differences in polarity and roughness of the QCM model surface and the real bag film. However, the combination of real bag films with QCM as an orthogonal method was found to be useful, e.g. for the elucidation of the adsorption layer composition in the presence of surfactants. Cross-checking the reliability of quantitative QCM results with an additional, independent method like AFM [47,48,51,81], SPR [49,51,81,82], TIRF [77], dual polarization interferometry [52], OWLS [50], or ellipsometry [49] is recommended. In conclusion, QCM studies with model surfaces helped to gain a deeper understanding of the adsorption process but cannot replace adsorption studies with real surfaces encountered during drug product manufacturing.

13 ABBREVIATIONS

A	active electrode area
AFM	atomic force microscopy
ATR-IR	attenuated total reflection infrared
C	crystal sensitivity constant
CMC	critical micelle concentration
D	dissipation
DLS	dynamic light scattering
EVA	ethylene vinyl acetate
f	frequency
HCl	hydrochlorid acid
HLB	hydrophilic-lipophilic balance
HP-SEC	high performance size exclusion chromatography
ID	inner diameter
IgG	immunoglobulin G
IRAS	infrared reflection adsorption spectroscopy
IS	ionic strength
mAb	monoclonal antibody
MW	mean value
NaCl	sodium chloride
NaOH	sodium hydroxide
OWLS	optical waveguide lightmode spectroscopy
PDI	polydispersity index
PE	polyethylene
PES	polyethersulfone
Pol	Ploxamer
PS	polystyrene
QCM	quartz crystal microbalance
R	resistance
rpm	revolutions per minute
RSD	relative standard deviation
s	standard deviation
SDS	sodium dodecyl sulfate
SPR	surface plasmon resonance
THF	tetrahydrofurane
TIRF	internal reflection fluorescence
ULDPE	ultra-low density polyethylene
VA	vinyl acetate
Γ	damping
Δm	mass
μ :	shear modulus of quartz
ρ :	density of quartz

14 REFERENCES

- [1] P. Tengvall, I. Lundström, B. Liedberg, Protein adsorption studies on model organic surfaces: an ellipsometric and infrared spectroscopic approach., *Biomaterials*. 19 (1998) 407–22.
- [2] M.A. McArthur, T.M. Byrne, R.J. Sanderson, G.P. Rockwell, L.B. Lohstreter, Z. Bai, et al., An in situ study of protein adsorption on combinatorial Cu-Al films using spectroscopic ellipsometry., *Colloids Surf. B. Biointerfaces*. 81 (2010) 58–66.
- [3] O. Svensson, T. Arnebrant, Antibody-antigen interaction on polystyrene: An in situ ellipsometric study., *J. Colloid Interface Sci.* 368 (2012) 533–9.
- [4] C. Giacomelli, M. Esplandiú, P. Ortiz, M. Avena, De Pauli CP, Ellipsometric Study of Bovine Serum Albumin Adsorbed onto Ti/TiO(2) Electrodes., *J. Colloid Interface Sci.* 218 (1999) 404–411.
- [5] J.M. Ruso, Á. Piñeiro, eds., *Proteins in Solution and at Interfaces: Methods and Applications in Biotechnology and Materials Science*, John Wiley & Sons, Hoboken, New Jersey, USA, 2013.
- [6] M.-J. Desroches, S. Omanovic, Adsorption of fibrinogen on a biomedical-grade stainless steel 316LVM surface: a PM-IRRAS study of the adsorption thermodynamics, kinetics and secondary structure changes., *Phys. Chem. Chem. Phys.* 10 (2008) 2502–12.
- [7] M. Dargahi, S. Omanovic, A comparative PM-IRRAS and ellipsometry study of the adsorptive behaviour of bovine serum albumin on a gold surface., *Colloids Surf. B. Biointerfaces*. 116 (2014) 383–8.
- [8] K. Nakanishi, T. Sakiyama, K. Imamura, On the adsorption of proteins on solid surfaces, a common but very complicated phenomenon, *J. Biosci. Bioeng.* 91 (2001) 233–44.
- [9] B.K. Lok, Y.L. Cheng, C.R. Robertson, Total internal reflection fluorescence: A technique for examining interactions of macromolecules with solid surfaces, *J. Colloid Interface Sci.* 91 (1983) 87–103.
- [10] K.E. Sapsford, F.S. Ligler, Real-time analysis of protein adsorption to a variety of thin films., *Biosens. Bioelectron.* 19 (2004) 1045–55.
- [11] M. Rabe, D. Verdes, S. Seeger, Understanding protein adsorption phenomena at solid surfaces, *Adv. Colloid Interface Sci.* 162 (2011) 87–106.
- [12] J. Buijs, V. Hlady, Adsorption Kinetics, Conformation, and Mobility of the Growth Hormone and Lysozyme on Solid Surfaces, Studied with TIRF, *J. Colloid Interface Sci.* 190 (1997) 171–81.
- [13] S.M. Daly, T.M. Przybycien, R.D. Tilton, Coverage-Dependent Orientation of Lysozyme Adsorbed on Silica, *Langmuir*. 19 (2003) 3848–3857.
- [14] R. Green, J. Davies, M. Davies, C. Roberts, S. Tendler, Surface plasmon resonance for real time in situ analysis of protein adsorption to polymer surfaces, *Biomaterials*. 18 (1997) 405–413.

- [15] L.S. Jung, C.T. Campbell, T.M. Chinowsky, M.N. Mar, S.S. Yee, Quantitative Interpretation of the Response of Surface Plasmon Resonance Sensors to Adsorbed Films, *Langmuir*. 14 (1998) 5636–5648.
- [16] N. Aldred, T. Ekblad, O. Andersson, B. Liedberg, A.S. Clare, Real-time quantification of microscale bioadhesion events in situ using imaging surface plasmon resonance (iSPR)., *ACS Appl. Mater. Interfaces*. 3 (2011) 2085–91.
- [17] J. Vörös, J.J. Ramsden, G. Csúcs, I. Szendro, S.M. De Paul, M. Textor, et al., Optical grating coupler biosensors., *Biomaterials*. 23 (2002) 3699–710.
- [18] C. Calonder, Y. Tie, P.R. Van Tassel, History dependence of protein adsorption kinetics., *Proc. Natl. Acad. Sci. U. S. A.* 98 (2001) 10664–9.
- [19] Y. Tie, C. Calonder, P.R. Van Tassel, Protein adsorption: kinetics and history dependence., *J. Colloid Interface Sci.* 268 (2003) 1–11.
- [20] G.N.M. Ferreira, A.-C. da-Silva, B. Tomé, Acoustic wave biosensors: physical models and biological applications of quartz crystal microbalance., *Trends Biotechnol.* 27 (2009) 689–97.
- [21] M.C. Dixon, Quartz crystal microbalance with dissipation monitoring: enabling real-time characterization of biological materials and their interactions., *J. Biomol. Tech.* 19 (2008) 151–8.
- [22] P. Schön, M. Görlich, M.J.J. Coenen, H. a Heus, S. Speller, Nonspecific protein adsorption at the single molecule level studied by atomic force microscopy, *Langmuir*. 23 (2007) 9921–3.
- [23] D.T. Kim, H.W. Blanch, C.J. Radke, Direct Imaging of Lysozyme Adsorption onto Mica by Atomic Force Microscopy, *Langmuir*. 18 (2002) 5841–5850.
- [24] I. Reviakine, D. Johannsmann, R.P. Richter, Hearing what you cannot see and visualizing what you hear: interpreting quartz crystal microbalance data from solvated interfaces., *Anal. Chem.* 83 (2011) 8838–48.
- [25] 3T analytik qCell / qCell T product brochure. Available online at: http://www.3t-analytik.de/sites/default/files/Prospekt_qCell_T_120913_web.pdf (accessed January 5, 2015).
- [26] K.A. Marx, Quartz crystal microbalance: a useful tool for studying thin polymer films and complex biomolecular systems at the solution-surface interface, *Biomacromolecules*. 4 (2003) 1099–120.
- [27] R.E. Speight, M.A. Cooper, A survey of the 2010 quartz crystal microbalance literature, *J. Mol. Recognit.* 25 (2012) 451–73.
- [28] J.M. Mathes, Protein Adsorption to Vial Surfaces – Quantification, Structural and Mechanistic Studies, Cuvillier Verlag, Göttingen, Germany, 2010.
- [29] M. Lieberman, A. Marks, A. Peet, Marks’ Basic Medical Biochemistry, 4th ed., Lippincott Williams & Wilkins, Philadelphia, PA, 2013.
- [30] G. Sauerbrey, Verwendung von Schwingquarzen zur Wägung dünner Schichten und zur Mikrowägung, *Zeitschrift Für Phys.* 155 (1959) 206–222.

- [31] N. Dixit, K.M. Maloney, D.S. Kalonia, Application of quartz crystal microbalance to study the impact of pH and ionic strength on protein-silicone oil interactions, *Int. J. Pharm.* 412 (2011) 20–7.
- [32] DuPont™ Elvax® 3190 Product Data Sheet. Available online at: http://www.dupont.com/content/dam/assets/products-and-services/packaging-materials-solutions/assets/elvax_3190.pdf (accessed February 29, 2012).
- [33] M. Sepe, Density & Molecular Weight in Polyethylene, *Plast. Technol.* (2012). Available online at: <http://www.ptonline.com/columns/density-molecular-weight-in-polyethylene> (accessed January 5, 2015).
- [34] H. Fischer, I. Polikarpov, A.F. Craievich, Average protein density is a molecular-weight-dependent function, *Protein Sci.* 13 (2004) 2825–8.
- [35] Merck Millipore Product Information. Available online at: <http://www.merckmillipore.com> (accessed January 5, 2015).
- [36] BASF Product Information. Available online at: <http://worldaccount.basf.com> (accessed January 5, 2015).
- [37] J.L. Jordan, E.J. Fernandez, QCM-D sensitivity to protein adsorption reversibility., *Biotechnol. Bioeng.* 101 (2008) 837–42.
- [38] F. Höök, M. Rodahl, P. Brzezinski, B. Kasemo, Measurements Using the Quartz Crystal Microbalance Technique of Ferritin Monolayers on Methyl-Thiolated Gold: Dependence of Energy Dissipation and Saturation Coverage on Salt Concentration., *J. Colloid Interface Sci.* 208 (1998) 63–67.
- [39] S. Vanhamel, C. Masy, Production of Disposable Bags: A Manufacturer’s Report, in: R. Eibl, D. Eibl (Eds.), *Single-Use Technology in Biopharmaceutical Manufacture*, John Wiley & Sons, Inc., Hoboken, New Jersey, USA, 2011: pp. 113–134.
- [40] A. Oom, M. Poggi, J. Wikström, M. Sukumar, Surface interactions of monoclonal antibodies characterized by quartz crystal microbalance with dissipation: Impact of hydrophobicity and protein self-interactions, *J. Pharm. Sci.* (2011).
- [41] J. Buijs, J.W.T. Lichtenbelt, W. Norde, J. Lyklema, Adsorption of monoclonal IgGs and their F(ab’)₂ fragments onto polymeric surfaces, *Colloids Surfaces B Biointerfaces.* 5 (1995) 11–23.
- [42] F. Caruso, E. Rodda, D.N. Furlong, Orientational aspects of antibody immobilization and immunological activity on quartz crystal microbalance electrodes, *J. Colloid Interface Sci.* 178 (1996) 104–115.
- [43] J.L. Brash, T.A. Horbett, Proteins at Interfaces: An Overview, in: T.A. Horbett, J.L. Brash (Eds.), *Proteins at Interfaces II - Fundamentals and Applications*, American Chemical Society, Washington, DC, 1995: pp. 1–23.
- [44] M.E. Wiseman, C.W. Frank, Antibody adsorption and orientation on hydrophobic surfaces., *Langmuir.* 28 (2012) 1765–74.

- [45] M. V Voinova, M. Jonson, B. Kasemo, Missing mass effect in biosensor's QCM applications., *Biosens. Bioelectron.* 17 (2002) 835–41.
- [46] M. V Voinova, M. Rodahl, M. Jonson, B. Kasemo, Viscoelastic Acoustic Response of Layered Polymer Films at Fluid-Solid Interfaces: Continuum Mechanics Approach, *Phys. Scr.* 59 (1999) 391–396.
- [47] G. V Lubarsky, M.R. Davidson, R.H. Bradley, Hydration-dehydration of adsorbed protein films studied by AFM and QCM-D., *Biosens. Bioelectron.* 22 (2007) 1275–81.
- [48] J.T. Kim, N. Weber, G.H. Shin, Q. Huang, S.X. Liu, The study of beta-lactoglobulin adsorption on polyethersulfone thin film surface using QCM-D and AFM., *J. Food Sci.* 72 (2007) E214–21.
- [49] F. Höök, B. Kasemo, T. Nylander, C. Fant, K. Sott, H. Elwing, Variations in coupled water, viscoelastic properties, and film thickness of a Mefp-1 protein film during adsorption and cross-linking: a quartz crystal microbalance with dissipation monitoring, ellipsometry, and surface plasmon resonance study., *Anal. Chem.* 73 (2001) 5796–804.
- [50] J. Vörös, The density and refractive index of adsorbing protein layers., *Biophys. J.* 87 (2004) 553–61.
- [51] F. Caruso, D. Furlong, P. Kingshott, Characterization of Ferritin Adsorption onto Gold, *J. Colloid Interface Sci.* 186 (1997) 129–40.
- [52] M.M. Ouberai, K. Xu, M.E. Welland, Effect of the interplay between protein and surface on the properties of adsorbed protein layers., *Biomaterials.* 35 (2014) 6157–63.
- [53] H. Muramatsu, A. Egawa, T. Ataka, Reliability of correlation between mass change and resonant frequency change for a viscoelastic-film-coated quartz crystal, *J. Electroanal. Chem.* 388 (1995) 89–92.
- [54] J. Novais, N. Titchener-Hooker, M. Hoare, Economic comparison between conventional and disposables-based technology for the production of biopharmaceuticals, *Biotechnol. Bioeng.* 75 (2001) 143–153.
- [55] C. Galli Marxer, M. Collaud Coen, L. Schlapbach, Study of adsorption and viscoelastic properties of proteins with a quartz crystal microbalance by measuring the oscillation amplitude., *J. Colloid Interface Sci.* 261 (2003) 291–8.
- [56] A. Doliška, V. Ribitsch, K. Stana Kleinschek, S. Strnad, Viscoelastic properties of fibrinogen adsorbed onto poly(ethylene terephthalate) surfaces by QCM-D., *Carbohydr. Polym.* 93 (2013) 246–55.
- [57] F. Höök, M. Rodahl, B. Kasemo, P. Brzezinski, Structural changes in hemoglobin during adsorption to solid surfaces: effects of pH, ionic strength, and ligand binding., *Proc. Natl. Acad. Sci. U. S. A.* 95 (1998) 12271–6.
- [58] M. Rankl, T. Ruckstuhl, M. Rabe, G.R.J. Artus, A. Walser, S. Seeger, Conformational reorientation of immunoglobulin G during nonspecific interaction with surfaces., *Chemphyschem.* 7 (2006) 837–46.

- [59] Q. Luo, Cooperative Adsorption of Proteins onto Hydroxyapatite, *J. Colloid Interface Sci.* 200 (1998) 104–113.
- [60] F. Felsovalyi, P. Mangiagalli, C. Bureau, S.K. Kumar, S. Banta, Reversibility of the adsorption of lysozyme on silica, *Langmuir*. 27 (2011) 11873–82.
- [61] P. Arosio, G. Barolo, T. Müller-Späth, H. Wu, M. Morbidelli, Aggregation stability of a monoclonal antibody during downstream processing., *Pharm. Res.* 28 (2011) 1884–94.
- [62] P. Arosio, S. Rima, M. Morbidelli, Aggregation mechanism of an IgG2 and two IgG1 monoclonal antibodies at low pH: from oligomers to larger aggregates., *Pharm. Res.* 30 (2013) 641–54.
- [63] B.A. Kerwin, Polysorbates 20 and 80 used in the formulation of protein biotherapeutics: structure and degradation pathways., *J. Pharm. Sci.* 97 (2008) 2924–35.
- [64] H.J. Lee, A. McAuley, K.F. Schilke, J. McGuire, Molecular origins of surfactant-mediated stabilization of protein drugs., *Adv. Drug Deliv. Rev.* 63 (2011) 1160–71.
- [65] A. V. Kabanov, I.R. Nazarova, I. V. Astafieva, E. V. Batrakova, V.Y. Alakhov, A.A. Yaroslavov, et al., Micelle Formation and Solubilization of Fluorescent Probes in Poly(oxyethylene-b-oxypropylene-b-oxyethylene) Solutions, *Macromolecules*. 28 (1995) 2303–2314.
- [66] L. Shen, A. Guo, X. Zhu, Tween surfactants: Adsorption, self-organization, and protein resistance, *Surf. Sci.* 605 (2011) 494–499.
- [67] N. Dixit, K.M. Maloney, D.S. Kalonia, Protein-silicone oil interactions: comparative effect of nonionic surfactants on the interfacial behavior of a fusion protein, *Pharm. Res.* 30 (2013) 1848–59.
- [68] P. Garidel, C. Hoffmann, A. Blume, A thermodynamic analysis of the binding interaction between polysorbate 20 and 80 with human serum albumins and immunoglobulins: a contribution to understand colloidal protein stabilisation., *Biophys. Chem.* 143 (2009) 70–8.
- [69] P. Garidel, A. Blume, M. Wagner, Prediction of colloidal stability of high concentration protein formulations., *Pharm. Dev. Technol.* 20 (2015) 367–74.
- [70] H.L. Kim, A. McAuley, B. Livesay, W.D. Gray, J. McGuire, Modulation of protein adsorption by poloxamer 188 in relation to polysorbates 80 and 20 at solid surfaces., *J. Pharm. Sci.* 103 (2014) 1043–9.
- [71] H.L. Kim, A. McAuley, J. McGuire, Protein effects on surfactant adsorption suggest the dominant mode of surfactant-mediated stabilization of protein., *J. Pharm. Sci.* 103 (2014) 1337–45.
- [72] N. Dixit, K.M. Maloney, D.S. Kalonia, The effect of Tween^(®) 20 on silicone oil-fusion protein interactions, *Int. J. Pharm.* 429 (2012) 158–67.
- [73] M. Feng, A.B. Morales, A. Poot, T. Beugeling, A. Bantjes, Effects of Tween 20 on the desorption of proteins from polymer surfaces., *J. Biomater. Sci. Polym. Ed.* 7 (1995) 415–24.

- [74] R.J. Marsh, R.A.L. Jones, M. Sferrazza, Adsorption and displacement of a globular protein on hydrophilic and hydrophobic surfaces, *Colloids Surfaces B Biointerfaces*. 23 (2002) 31–42.
- [75] S.H. Mollmann, U. Elofsson, J.T. Bukrinsky, S. Frokjaer, Displacement of adsorbed insulin by Tween 80 monitored using total internal reflection fluorescence and ellipsometry., *Pharm. Res.* 22 (2005) 1931–41.
- [76] O. Joshi, J. McGuire, Adsorption behavior of lysozyme and Tween 80 at hydrophilic and hydrophobic silica-water interfaces., *Appl. Biochem. Biotechnol.* 152 (2009) 235–48.
- [77] S.J. Kapp, I. Larsson, M. Van De Weert, M. Cárdenas, L. Jorgensen, Competitive adsorption of monoclonal antibodies and nonionic surfactants at solid hydrophobic surfaces., *J. Pharm. Sci.* 104 (2015) 593–601.
- [78] M. Zhang, M. Ferrari, Reduction of albumin adsorption onto silicon surfaces by Tween 20., *Biotechnol. Bioeng.* 56 (1997) 618–25.
- [79] P.E. Scopelliti, A. Borgonovo, M. Indrieri, L. Giorgetti, G. Bongiorno, R. Carbone, et al., The effect of surface nanometre-scale morphology on protein adsorption, *PLoS One*. 5 (2010) e11862.
- [80] C. Galli, M. Collaud Coen, R. Hauert, V.L. Katanaev, P. Gröning, L. Schlapbach, Creation of nanostructures to study the topographical dependency of protein adsorption, *Colloids Surfaces B Biointerfaces*. 26 (2002) 255–267.
- [81] C. Zhou, J.-M. Friedt, A. Angelova, K.-H. Choi, W. Laureyn, F. Frederix, et al., Human immunoglobulin adsorption investigated by means of quartz crystal microbalance dissipation, atomic force microscopy, surface acoustic wave, and surface plasmon resonance techniques., *Langmuir*. 20 (2004) 5870–8.
- [82] Y. Luan, D. Li, Y. Wang, X. Liu, J.L. Brash, H. Chen, 125I-radiolabeling, surface plasmon resonance, and quartz crystal microbalance with dissipation: three tools to compare protein adsorption on surfaces of different wettability., *Langmuir*. 30 (2014) 1029–35.

PARTICLE SHEDDING FROM SILICONE TUBING UPON PERISTALTIC PUMPING

ABSTRACT

In a typical manufacturing setup for biopharmaceutical drug products, the fill and dosing pump is placed after the final sterile filtration unit in order to ensure adequate dispensing accuracy and avoid backpressure peaks. Given the sensitivity of protein molecules, peristaltic pumps are often preferred over piston pumps. However, particles may be shed from the silicone tubing employed. In this study, particle shedding and a potential turbidity increase during peristaltic pumping of water and buffer were investigated using three types of commercially available silicone tubing used in pharmaceutical fill & finish. In the recirculates, mainly particles of around 200 nm size next to a very small fraction of particles in the lower micrometer size range were found. Using 3D laser scanning microscopy, surface roughness of the inner tubing surface was found to be a determining factor for particle shedding from silicone tubing. As the propensity towards particle shedding varied between tubing types and also cannot be concluded from manufacturer's specifications, individual testing with the presented methods is recommended during tubing qualification. Choosing low abrasive tubing can help to further minimize the very low particle counts to be expected in pharmaceutical drug products.

Parts of this chapter are published as:

Particle Shedding from Peristaltic Pump Tubing in Biopharmaceutical Drug Product Manufacturing

Verena Saller, Julia Matilainen, Ulla Grauschopf, Karoline Bechtold-Peters, Hanns-Christian Mahler, Wolfgang Friess

Journal of Pharmaceutical Sciences, DOI 10.1002/jps.24357

© 2015 Wiley Periodicals, Inc. and the American Pharmacists Association

1 INTRODUCTION

The design of a suitable drug product (DP) manufacturing process is essential for biopharmaceutical DP quality. Due to the sensitivity of protein molecules, decisions should be taken with care [1,2]. For fill & finish processes, several types of pumps are generally employed, including rotary piston pumps, rolling diaphragm pumps, peristaltic pumps, and time-pressure fillers. Given the fact that pumping to dispense into units occurs after the sterile filter in order to avoid backpressure peaks and to ensure adequate dispensing accuracy, generated particles may directly end up in the final drug product units [1,3,4]. The European and US pharmacopeia require parenteral drug products to be essentially/practically free from visible particles. Additionally, subvisible particle counts have to be below harmonized thresholds (not more than (NMT) 6000 particles $\geq 10 \mu\text{m}$ and NMT 600 particles $\geq 25 \mu\text{m}$ per container) [5]. Therefore, drug products are carefully monitored for visible as well as subvisible particles, also in frame of continuous discussions about immunogenicity caused by protein particles [1,6–9]. Non-proteinaceous particles might pose a risk to patients due to capillary occlusion, although controlled studies on this subject are not available [10].

To date, several studies indicate that the use of rotary piston pumps might increase the risk of particle formation in protein-based DP solution [1,3,6]. Upon filling, the protein possibly acts as lubricant and is exposed to significant forces [1]. In consequence, the formation of protein particles is frequently encountered. Moreover, stainless steel particles can be shed from the pump head [6]. In contrast, stress on the proteins exercised upon filling with peristaltic pumps has been shown to be minimal [2,11,12] and the use of peristaltic pumps has not led to a significant increase in particle counts and turbidity [3]. Another main benefit of filling with a peristaltic pump is the fact that the DP solution only comes into contact with the inner surface of the disposable tubing. This greatly diminishes the risk for cross-contaminations [13] and the need for cleaning validation of these components. Downsides of peristaltic pumps include the lower dosing accuracy in comparison with piston pumps.

For fill & finish operations with a peristaltic pump, platinum-cured silicone tubing is the material of choice as it releases less leachables than peroxide-cured silicone or tubing made from other plasticizer containing materials [14]. Concerns about extractables and leachables from these materials are generally low, given that additives for silicone tubing usually only involve fillers like fumed silica but not plasticizers. Moreover, silicone tubing exhibits excellent long-term durability, can be sterilized, is highly flexible, and therefore, is well-suited for usage in peristaltic pumps [15]. Nevertheless, potential drawbacks might result from enhanced particle spallation from the tubing material due to the mechanical stress exerted within the peristaltic pump. Presently, particle shedding and tubing wear have mainly been investigated in the context of medical use [16–23], as silicone tubing is employed i.e. during haemodialysis and in cardiopulmonary bypass operations [24]. Silicone tubing was shown to be more prone for particle shedding as compared to tubing made from polyvinyl chloride and polytetrafluoroethylene composites [25]. Despite these findings, silicone tubing remains the standard material for operation in peristaltic pumps due to the above mentioned advantages.

A study that characterizes particle shedding from different kinds of silicone tubing used during biopharmaceutical drug product manufacturing is still lacking. We close this gap by presenting a comprehensive data set on the amount of shed particles, particle characteristics, and tubing wear of three different commercially available silicone tubing types. Influences of tubing pre-treatment,

pumping time, recirculation medium (Wfl and a surfactant-containing placebo solution), and possible batch-to-batch variations were considered. Furthermore, the influences of tubing inner diameter (ID), pump head type, and an additional post-curing step during tubing production on particle shedding were investigated. Surface characterization with 3D laser scanning microscopy of all tested tubing types was employed to identify the root cause for the observed differences in particle shedding. In addition, the impact of pumping cycles on the mechanical properties of the different tubing sets was studied. As experiments were performed under recirculating conditions, particle counts of this study were extrapolated to production conditions during fill & finish of a biopharmaceutical DP. Studying the influence of shed particles on the stability of a biopharmaceutical DP or interactions with protein was beyond the scope of this study, but is addressed in a follow-up study (see Chapter V).

2 MATERIALS AND METHODS

2.1 Materials

Water for injection (Wfi) was produced via distillation (Muldestor Modell SE, Wagner + Munz, München, Germany) from deionized water. Placebo pH 6.0 containing 10 mM L-histidine monohydrochlorid monohydrate and 10 mM L-histidine (Ajinomoto Europe S.A.S, Louvain-la-Neuve, Belgium), 200 mM sucrose (Sigma-Aldrich Chemie GmbH, Steinheim, Germany) and 0.02 % polysorbate 20 (Croda GmbH, Nettetal, Germany) was prepared with highly purified water (purification system arium pro with Sartopore 2 150 0.2 µm filter capsule from Sartorius AG, Göttingen, Germany). After filtration (0.2 µm, cellulose acetate, Sartorius) the buffer was stored at 2 - 8°C until further use.

Three different types of commercially available silicone tubing (A, B, and C) were tested (see Table IV-20). Tubing sets employed in recirculation experiments consisted of two 30 cm long pieces for location within the pump head connected to 100 cm long tubing pieces via polypropylene Y-connectors (Kartell, purchased from VWR International GmbH, Darmstadt, Germany). Sets were used either untreated, washed (washing cycles with highly purified water of 80°C, drying with filtered air at 110°C), washed and sterilized (30 minutes at 126°C and 2 bar) or CIP/SIP/DIP treated (washing cycles with highly purified water of 80°C, sterilization for 30 minutes at 131°C and 3 bar, drying with sterile nitrogen at room temperature). This material processing was performed in analogy to production conditions and parameters. Unless otherwise stated, tubing was used as received from the manufacturer (=untreated).

Table IV-20: Tubing specifications as given by the manufacturers.

Tubing Type	Tubing A		Tubing B		Tubing C	
Type	pt-cured		pt-cured, post-cured		pt-cured	
ID (mm)	6.0	1.6	6.0	1.6	6.4	1.6
Wall thickness (mm)	2.1	1.6	2.1	1.6	1.6	1.6
Hardness (Shore A)	55 - 65		60 ± 5 / 57 - 65*		50 (15 sec)	
Specific gravity	1.09 - 1.15		1.12 - 1.16		1.14	
Tear B / tear strength / tear resistance (ppi)	≥ 150		85 - 171		185	
Ultimate tensile strength (psi)	≥ 900		943 - 1885		1293	
Elongation at break (%)	≥ 300		300 - 650		719	

* Specifications for second generation tubing B

2.2 Methods

2.2.1 Online-Turbidity Monitoring

Pumping cycles were performed under a laminar flow cabinet to avoid external particle contamination. Tubing sets (6 mm ID) were flushed with 4 L of highly purified water and 1 L of Wfi prior to the recirculation experiment using a laboratory vacuum pump (LABOPORT, KNF Neuberger GmbH, Freiburg, Germany). Flush volumes were based on initial experiments (data not shown). The low-pressure flow-through cuvette set (HACH LANGE GmbH, Düsseldorf, Germany) as well as the

outer surfaces of the ends of the tubing set were rinsed with highly purified water and Wfl until the rinsing fluid was visually free from particles. Online-turbidity monitoring was performed with 250 mL of Wfl or placebo in recirculation over 24 h with the setup shown in Figure IV-46. The operation parameters of the Flexicon PD12 peristaltic pump (Watson-Marlow Flexicon, Ringsted, Denmark) were based on previous experiments (data not shown) and set as follows: dispensing mode, 180 rpm, acceleration of 60, starting filling volume of 5.0 mL. As occlusion pressure is known to have an impact on particle shedding [16,17,19], this parameter was kept at factory settings resulting in an occlusion pressure of 1.1 bar (tubing A) or 1.3 bar (tubing B and C) upon operation in air (accuracy class 2.5 manometer from WIKA Alexander Wiegand SE & Co. KG, Klingenberg, Germany). For the smaller tubing ID of 1.6 mm the pressure was approx. 3 bar. In continuous mode, these settings resulted in a flow rate of 23 mL/s for 6.0 mm ID and 2 mL/s for 1.6 mm ID. Online-turbidity monitoring was carried out with a HACH 2100AN turbidimeter connected to a computer using HachLink 2000 V.2.9 alpha software. The operation mode of the turbidimeter included activated ratio function, auto range function and signal averaging (n=15). Data points were collected every 60 seconds. Turbidimeter functionality was confirmed with turbidity standards (< 0.15 NTU stray light standard, 0-2 / 0-20 / 0-200 / 0-2000 NTU Gelex Secondary Standards from HACH; max. deviation of $\pm 5\%$ in comparison to precedent measurement) prior to every experiment. Different pre-treatments of each tubing type were investigated with n=2.

For tubing with 1.6 mm ID the starting filling volume was 50 mL and was adjusted during the course of the experiment. For pre-rinsing, 0.5 L of highly purified water and 0.5 L of Wfl were pumped through the tubing set with the Flexicon pump in continuous operation mode.

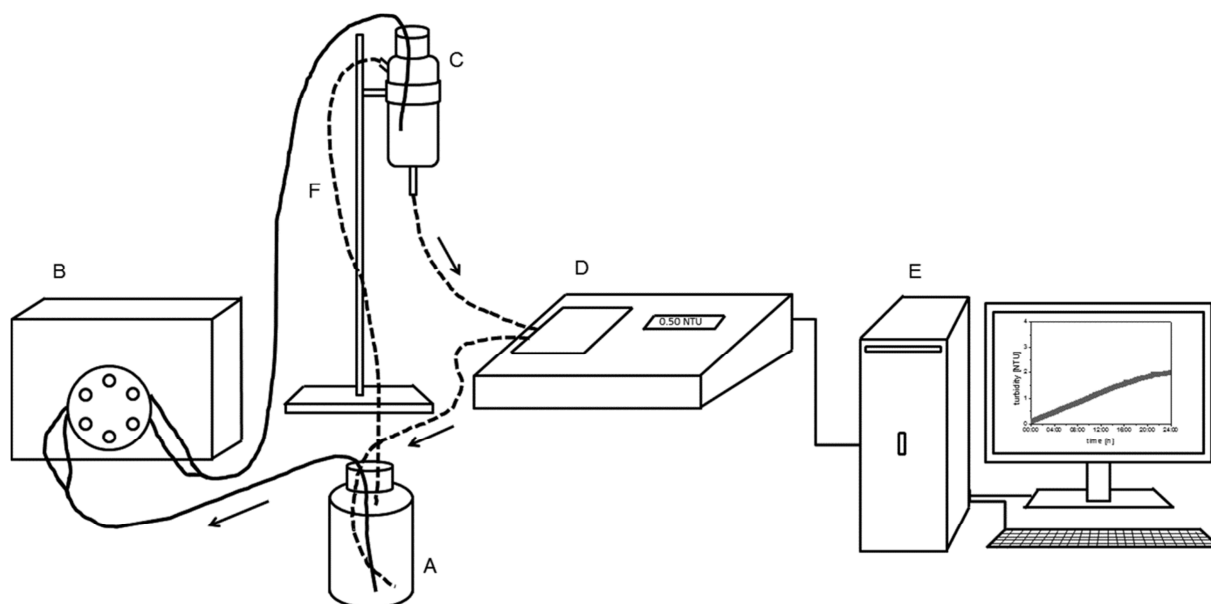


Figure IV-46: Experimental setup for online-turbidity monitoring experiments. A – recirculation reservoir containing 250 mL of Wfl or placebo, B – peristaltic pump, C – reservoir levelling off volume and pressure variations, D – turbidimeter with flow-through cuvette, E – computer for data acquisition, F – flow path in case of mismatch between pumped volume and volume flowing through turbidimeter due to hydrostatic pressure. Black solid line: tubing set under investigation, black dashed line: Tygon® R-3603 tubing as part of HACH flow-through cuvette set.

2.2.2 Determination of Pump Rate

A stop watch and a measuring cylinder (250 mL for 6.0 mm ID, 50 mL for 1.6 mm ID) were used to determine the pump rate of each tubing set over approx. 10 seconds before and after the 24 h pumping cycle (n=5).

2.2.3 Dynamic light scattering (DLS)

Particle characterization in the nanometer range was performed by dynamic light scattering using the Zetasizer Nano-ZS (Malvern Instruments Ltd., Herrenberg, Germany). The undiluted, neither filtered nor centrifuged samples were measured in disposable Plastibrand semi-micro PMMA cuvettes (Brand GmbH, Wertheim, Germany) at a backward scatter of 173° after 20 seconds equilibration time at 25°C and with water as dispersant (viscosity of 0.8872 cP). Positioning, attenuation selection and measurement duration as well as number of sub runs for the three performed measurements per sample were optimized automatically for each run by the Zetasizer Software 6.32. Z-average and polydispersity index (Pdl) were calculated applying the 'General purpose (normal resolution)' analysis model.

The ζ -potential of the particles was measured with the same instrument. An aliquot of 800 μ L of the final recirculate was analyzed in disposable folded capillary cells (Malvern) with three measurements of 10 to 30 sub runs each at a voltage of 50 V. ζ -potentials were derived from electrophoretic mobility data applying the monomodal analysis model and Smoluchowski theory.

In order to analyze the ζ -potential over a range of pH values, ζ -potential measurements with the Zetasizer Nano ZS were performed as described above and combined with pH titration performed by a connected MPT-2 autotitrator (Malvern). 9.0 mL of Wfl recirculate were filled into a polypropylene sample tube (Sarstedt AG & Co., Nümbrecht, Germany) equipped with a stirring bar. 0.1 M NaOH and HCl were employed for titration from pH 10 to 2 in pH steps of 0.5 with a target pH tolerance of 0.1. Pump speed was set to 80% and stirrer speed was 30%. The sample was recirculated between repeat measurements (n=3).

2.2.4 Light Obscuration (LO)

The final recirculate was analyzed for particles in the micrometer range by light obscuration (in analogy to USP 788 and Ph Eur 2.9.19 requirements) with a SVSS-C instrument (PAMAS, Partikelmess- und Analysesysteme GmbH, Rutesheim, Germany) within three days after the pumping cycle. After a pre-run volume of 0.5 mL, each sample was analyzed in triplicates of 0.3 mL at a filling and emptying rate of 10 mL/min. Size channels from 1 to 60 μ m were auto-scaled logarithmically. Before each run, the system was rinsed with at least 5 mL of highly purified water. Data was collected using PAMAS PMA Program V 2.1.2.0.

2.2.5 Analysis of Particle Morphology

Using the micro-flow imaging (MFI) system DPA4100 from Brightwell Technologies Inc. (Ottawa, Canada) equipped with a high-resolution 100 μ l flow cell and the MFI™ View Application Software, particle morphology was investigated. Pre-run volumes of 0.3 mL and sample volumes of 0.65 mL were drawn through the flow cell by a peristaltic pump at a flow rate of 0.1 mL/min. Prior to each sample run, the system was rinsed with highly purified water to provide a clean baseline and to optimize illumination.

Additionally, particle morphology was visualized using a FlowCAM VS-I instrument (Fluid Imaging Technologies, Yarmouth, Maine, USA) equipped with a 20x objective and a FC 50 FlowCell. The system was controlled by Visual Spreadsheet software v3.1.10. Prior to each run, the system was rinsed with 1 mL highly purified water at a flow rate of 0.5 mL/min. After a pre-run volume of 0.5 mL, 0.5 mL of the undiluted sample was analyzed at a flow rate of 0.07 mL/min in the AutoImage Mode at a camera rate of 20 frames per second.

2.2.6 Fourier-Transform-Infrared-Spectroscopy (FTIR)

10 mL of Wfl recirculate from tubing C were centrifuged (Megafuge 1.0R, Thermo Scientific) for 60 min at 4000 rpm, the supernatant was decanted and the pellet was air-dried. 500 μ L of n-heptane (Sigma-Aldrich) were added. After two days at RT the pellet had turned transparent and the supernatant was analyzed by FTIR. A Bruker Tensor 27 FTIR spectrometer (Bruker Optics, Ettlingen, Germany) with a BIO ATR II measuring cell was used. The detector was cooled with liquid nitrogen and the beam path was purged with nitrogen. Each spectrum was recorded in 64 scans between 400 to 4000 cm^{-1} with a resolution of 4 cm^{-1} and a corresponding blank spectrum was subtracted. Moreover, water and atmospheric compensation as well as vector normalization were performed with the Opus software version 6.5.

2.2.7 Nanoparticle Tracking Analysis (NTA)

For NTA measurements shortened pumping cycles of only 2 h (2880 fillings à 5.0 mL) with a reduced recirculation volume of 70 mL of Wfl or placebo were carried out. Pumping cycle time was decreased in order to enable prompt characterization of all samples within one analysis run. Turbidity of the final recirculates was measured with a Lange Nephla turbidimeter in triplicates in pre-rinsed glass cuvettes with flat bottom. Scattered light of a $\lambda = 860$ nm laser is detected at an angle of 90° and the result is given in FNU (Formazine nephelometric units). This turbidimeter requires a sample volume of only 1.5 mL and was therefore preferred in this experiment. Nanoparticle tracking analysis was performed with a NanoSight LM20 system with PL 20/0 objective using NTA2.2 software (NanoSight Ltd., Salisbury, UK). The measuring cell was cleaned with particle-free water (filtered through a 0.02 μ m filter, Anotop 2, Whatman) and flushed with 1 mL of sample prior to analysis (n=3). Shutter (ca. 700) and gain (ca. 300) as well as focus were adjusted manually for each sample. Capture duration was set to 60 seconds and measurements were performed at RT. Wfl recirculates from tubing A were diluted 1:10 with particle-free water prior to analysis, all other recirculates were not diluted. Analysis was performed with background extraction, a minimum track length of 10 and a minimum expected particle size of 100 nm. Detection threshold (ca. 5) and blur (mostly 9x9) were adjusted manually for each video.

2.2.8 Scanning Electron Microscopy (SEM)

Tubing wear was visualized with scanning electron microscopy using a Jeol JSM-6500F instrument (Jeol Ltd., Tokyo, Japan) with Inca Software (Oxford instruments, Oxfordshire, UK). Tubing pieces were fixed with conductive silver on aluminum stubs (both from Plano GmbH, Wetzlar, Germany) and were sputtered with carbon. SEM micrographs were collected at a magnification of 90x and an accelerating voltage of 5.0 kV.

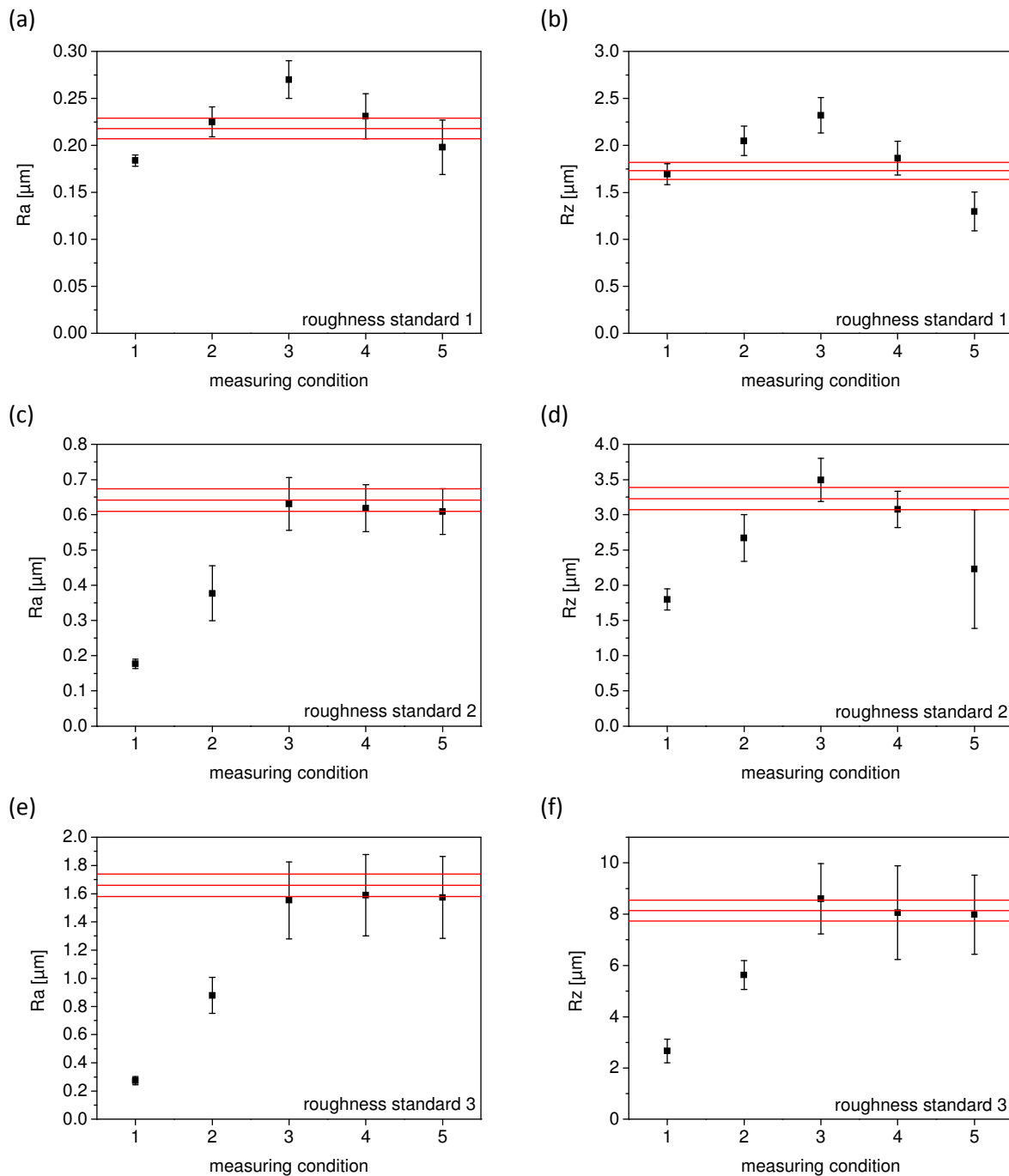


Figure IV-47: Evaluation of three roughness standards (HALLE Präzisions-Kalibriernormale GmbH) for the appropriate selection of cutoff values. Cutoff value combinations (= measuring conditions 1 to 5) for λ_c and λ_s were chosen according to DIN EN ISO 4288:1998 and DIN EN ISO 3274:1998. Cutoff values λ_c in mm / λ_s in μm for the five different measuring conditions are 1) 0.08 / 2.5, 2) 0.25 / 2.5, 3) 0.8 / 2.5, 4) 2.5 / 8, 5) 8 / 25. Red lines indicate the mean as well as maximum and minimum values stated by the DKD calibration.

2.2.9 3D Laser Scanning Microscopy

Surface roughness of inner tubing walls was visualized using the 3D laser scanning microscope Keyence VK-X210 with a CF Plan 20x objective (Keyence GmbH, Neu-Isenburg, Germany). Using a scalpel, tubing pieces were cut into thin strips and placed under the microscope with horizontal flow direction. For every sample micrographs were captured with VK Viewer software in 'Easy Mode' at eight different sections. For used tubing all of these analyzed areas had been located inside the pump head during pumping cycles. The roughness parameters arithmetic mean roughness R_a and maximum

height R_z were calculated according to the JIS standard B0601:2001 in the multi-line roughness mode with VK Analyzer Plus software version 3.3.0.0 from an average of $2n+1$ horizontal lines with $n=30$ and 10 (5 for ID of 1.6 mm) skipped lines in-between. Tubing curvature was corrected via the 'correct tilt – sec curved surf. (auto)' function. Appropriate cutoff values for λ_c (high-pass filtering) and λ_s (low-pass filtering) were evaluated using a KNT 4058/03 set of three roughness standards from HALLE Präzisions-Kalibriernormale GmbH (Edemissen, Germany). Cutoff values of $\lambda_c = 2.5$ mm and $\lambda_s = 8$ μm were applied since these settings provided the best results for the roughness standards (see Figure IV-47).

2.2.10 Evaluation of a Second Type of Pump Head

Sets of 1.6 mm ID tubing were employed in 2 h pumping cycles with 20 mL of Wfl or placebo as recirculate without online-turbidity monitoring. The different geometries of the two investigated pump heads from Flexicon and Optima (Optima pharma GmbH, Schwäbisch Hall, Germany) are shown in Figure IV-48. In order to mimic the pump settings chosen for the default Flexicon pump, the parameters for the Optima pump were adjusted as follows: 1.5 sec filling time, 1.0 sec cycle time, and start / end filling ramp of 30 %. The filling volume was set to 1.65 mL in order to achieve a filling speed of 180 rpm. In order to achieve comparable recirculates, pumping cycles with 0.7 mL filling volume were performed with the Flexicon pump. All other parameters for the Flexicon pump were set as described above (2.2.1). Settings on both pump types corresponded to 24 fillings per minute and a total filling number of 2880. Sample turbidity was analyzed with the Dr. Lange Nephla turbidimeter ($n=2$) with a 90° turn of the glass cuvette between measurements.

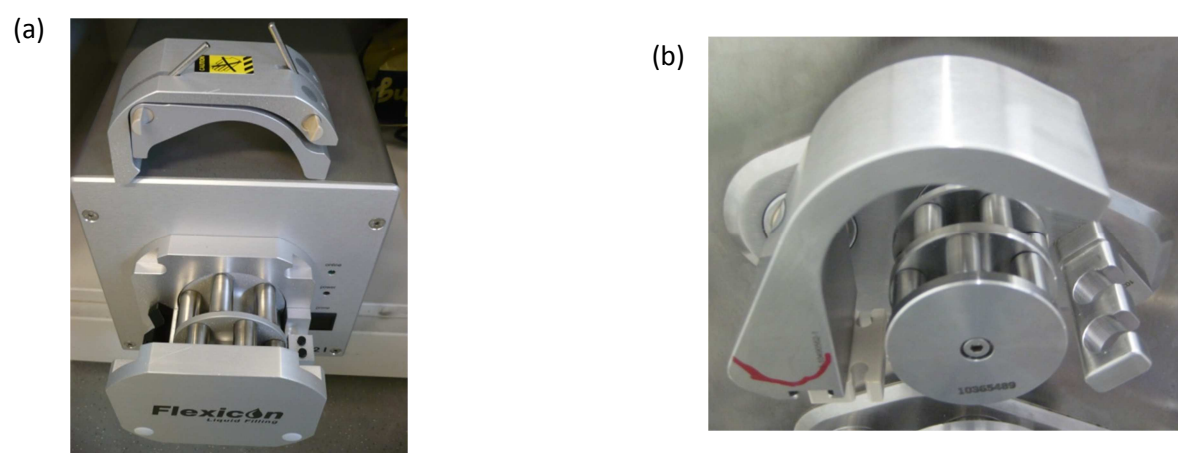


Figure IV-48: Employed pump heads. (a) Flexicon PD12I pump head, (b) Optima pump head.

2.2.11 Simulated Post-Curing Process

Post-curing of tubing sets was simulated by 4 h incubation at 200°C in a drying cabinet (Binder GmbH, Tuttlingen, Germany).

2.2.12 Determination of Mechanical Properties

The mechanical strength of the tubing material was analyzed with a Texture Analyser (TA.XT plus, Stable Micro Systems, Godalming, UK). As test probe, a cylinder with a diameter of 12.7 mm was used. The indentation force at an indentation depth of 5 mm for 6 mm ID / 1 mm for 1.6 mm ID tubing was measured ($n=3$ for areas outside the pump head, $n=5$ for areas within the pump head). Pre-test speed was set to 1.0 mm/s and test speed was 2.0 mm/s.

2.2.13 Thermogravimetric Analysis (TGA)

20 to 30 mg of cut tubing pieces (ID 6.0 mm) were placed on an aluminum crucible of the TGA instrument (TGA 2950 CE, TA Instruments GmbH, Alzenau, Germany). The temperature program included an equilibration step at 30°C, followed by an increase in temperature up to 200°C with 10°C/min. The mass loss during a holding time of 240 minutes at 200°C was evaluated. Subsequently, the temperature was further increased to 300°C with 10°C/min. Since the aluminum crucible showed a minor weight increase during the equilibration step at 200°C, measurement results were corrected for this blank value.

2.2.14 Statistics

Measurement results are reported as mean values with standard deviation (SD). F-tests (equality of variances) were conducted with $p=0.95$. Significance testing was performed via the t-test function in Microsoft Excel 2010. Significance levels are indicated by asterisks: $p < 0.05$ (*), $p < 0.01$ (**), and $p < 0.001$ (***)

3 RESULTS

3.1 Online-Turbidity Monitoring

In order to study the extent of particle shedding from silicone tubing, the setup described in Figure IV-46 was employed. During the course of the experiment, the recirculate repeatedly passed the peristaltic pump with the tubing under investigation as well as the flow-through cuvette inside the turbidimeter.

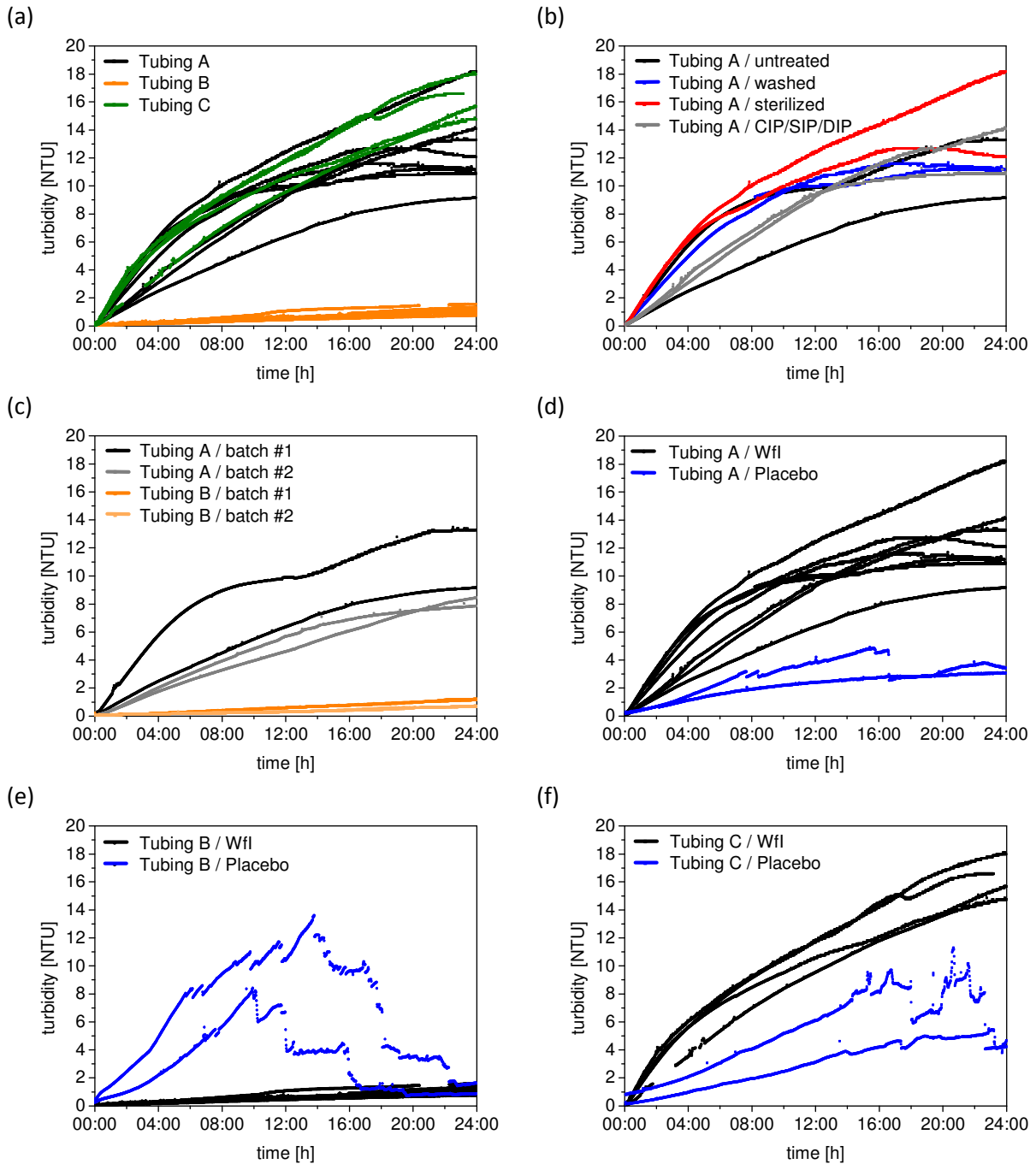


Figure IV-49: Online-turbidity monitoring graphs from 24 h pumping cycles with (a) different tubing A, B and C, (b) differently treated sets of tubing A, (c) different batches of tubing A and B, all with Wfl in recirculation. Online turbidity monitoring graphs obtained for pumping of placebo in comparison to Wfl are shown in (d-f).

Figure IV-49a shows the obtained turbidity profiles for 24 h pumping cycles with Wfl in recirculation. Solutions that were recirculated with tubing A and C showed highly increased turbidity endpoint values of up to 18 NTU. After a steep increase during the first hours, the profiles flattened or even reached a plateau during the second half of the experiment. In contrast, recirculates of tubing B showed only a minor and almost linear increase over the test period and turbidity endpoints reached a maximum of 1.6 NTU. Turbidity graphs from pumping cycles with tubing A showed considerable variation concerning the starting slope of the curve, the onset of the plateau and the turbidity endpoints. As shown in Figure IV-49b, differences could not be ascribed to the pre-treatment of the tubing sets, which included several washing and sterilization procedures. Moreover, for tubing A and B a second batch of untreated tubing was tested. Considering the overall variations between different runs, turbidity increase (see Figure IV-49c), LO particle counts, and DLS particle characteristics (data not shown) of the Wfl recirculate did not significantly differ between the two batches. During online-turbidity monitoring experiments with a surfactant-containing placebo buffer steep increases and sudden drops in turbidity were observed, especially with tubing B and C (see Figure IV-49d-f). In these experiments, air bubbles visibly accumulated in the flow-through cuvette. The formation of these air bubbles and their sudden release from the cuvette wall caused these excursions. For tubing A and B, turbidity endpoints of the air bubble free placebo recirculates were consistently lower than the ones obtained with Wfl. With tubing B, comparably low turbidity endpoints were measured upon recirculation of placebo and Wfl.

3.2 Particle Characterization

Recirculates were qualitatively analyzed for particles in the nanometer range using DLS. For WFI, Z-average values of around 200 nm were obtained, independent of tubing type and tubing pre-treatment (Figure IV-50a). The narrow size distribution was reflected by a rather low polydispersity index (Pdl) below 0.2. The size distribution was mostly monomodal, only in a few cases a second rather small micrometer particle fraction was observed (Figure IV-50c). This second fraction in DLS occurred randomly. NTA measurements also suggested a monomodal size distribution in the nanometer range with a peak at approximately 180 nm.

In recirculated placebo solution, Z-average and Pdl values were higher (Figure IV-50b) due to a multimodal size distribution (Figure IV-50d). Apart from the shed particle fraction, additional peaks at around 1 nm and 10 nm were detected, arising from the high sucrose concentration [26] and the existence of polysorbate micelles in the placebo buffer. The particle fraction in the micrometer range occurred more frequently in placebo recirculates. As the shed particle fraction was observed to be smaller for tubing B, Z-average and Pdl values for tubing B recirculates were more heavily impacted by the additional peaks present in placebo. With NTA, only the particle fraction with a diameter of a few hundred nanometers was detected, since the measurable size range of this technique is between 30 and 1000 nm [5,27].

In conclusion, the nanometer particle fraction was the most predominant particle fraction in all samples. Table IV-21 shows turbidity values and corresponding NTA counts for nanometer-sized particles for recirculates from tubing A and B. In analogy to turbidity values, NTA counts were less for recirculates from tubing B (2.0 to 2.4×10^8 particles/mL in Wfl) than from tubing A (5×10^9 particles/mL in Wfl). For tubing A recirculates, NTA counts were slightly decreased when using placebo (3×10^9 particles/mL). For tubing B recirculates, only a minor difference between Wfl and placebo particle counts (around 1.7×10^8 particles/mL in placebo) was noted. It needs to be

mentioned that NTA particle counts have to be interpreted in a more semi-quantitative way due to the significant imprecision inherent to this technique [27].

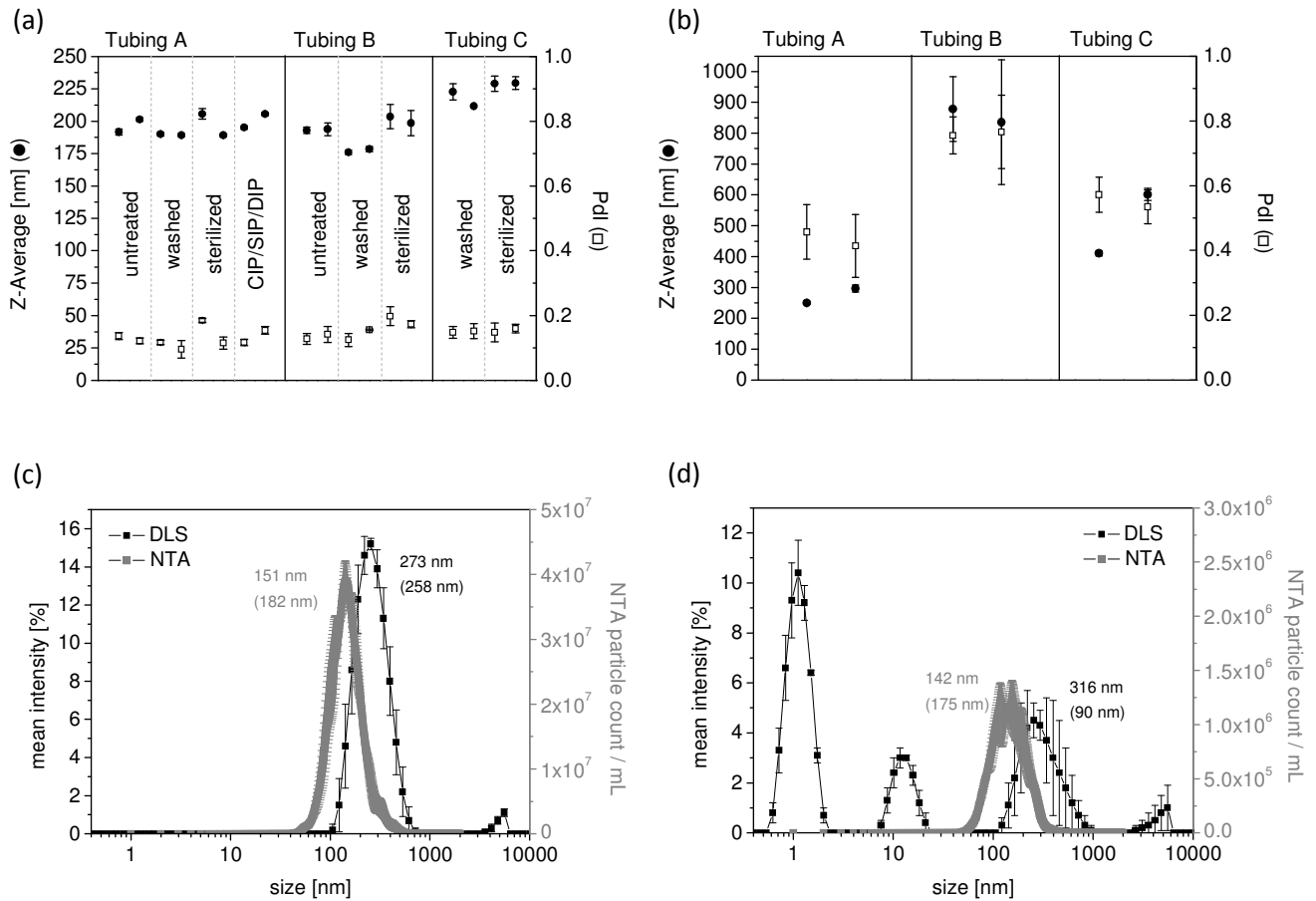


Figure IV-50: Results from DLS and NTA analysis. Pdl and Z-average of (a) Wfl and (b) placebo recirculates after 24 h pumping cycles. Different pre-treatments were tested with Wfl as recirculate (a), for placebo studies (b) untreated tubing sets were employed. Values are depicted as replicates (n=2) for every pre-treatment. The lower panel shows representative particle size distributions as analyzed by DLS (peak maximum (Z-average)) and NTA (mode (mean) value) for (c) a Wfl recirculate of tubing A and (d) a placebo recirculate of tubing B after 2 h pumping cycles.

Table IV-21: NTA particle counts and measured turbidity endpoints after 2 h pumping cycles.

Sample description			Turbidity [FNU]	NTA particle count [$\times 10^6$ / mL]
Blank	Wfl		0.2 ± 0.0	5 ± 2
	Placebo		0.2 ± 0.0	132 ± 27
Tubing A	Wfl	#1	5.5 ± 0.1	4953 ± 176
		#2	5.7 ± 0.0	4703 ± 449
	Placebo	#1	2.6 ± 0.0	2647 ± 566
		#2	2.7 ± 0.0	2877 ± 337
Tubing B	Wfl	#1	0.4 ± 0.0	201 ± 28
		#2	0.3 ± 0.0	237 ± 40
	Placebo	#1	0.2 ± 0.0	169 ± 45
		#2	0.3 ± 0.0	176 ± 15

Table IV-22 depicts subvisible particle counts ≥ 2 , ≥ 5 , ≥ 10 , and ≥ 25 μm from light obscuration (LO) measurements. Particle counts for recirculated Wfl were between 300 and 1,000 particles ≥ 2 μm per mL with few exceptions. No clear influence of tubing type or pre-treatment on LO particle counts was observed. Particle counts in recirculated placebo ranged from around 1,300 particles ≥ 2 μm per mL for tubing A up to nearly 7,000 particles ≥ 2 μm per mL for tubing B. This difference in subvisible particle counts between Wfl and placebo is in accordance with the more frequent appearance of the second species of larger particles in DLS measurements of placebo recirculates. Only few subvisible particles ≥ 10 μm (NMT 51 particles / mL for Wfl and NMT 258 particles / mL for placebo) and ≥ 25 μm (NMT 13 particles / mL for Wfl and NMT 34 particles / mL for placebo) were found. The recirculated solutions did not contain particulates that were macroscopically visible to the naked eye.

Table IV-22: Particle counts of recirculated Wfl and placebo after 24 h pumping cycles as obtained from light obscuration data (tubing ID of 6 mm).

Tubing type	Recirculating solution	Tubing pre-treatment		Particle counts / mL				
				≥ 2 μm	≥ 5 μm	≥ 10 μm	≥ 25 μm	
A	<i>Wfl</i>	<i>untreated</i>	#1	1104	267	19	0	
			#2	954	226	18	0	
		<i>washed</i>	#1	1332	322	51	13	
			#2	919	248	26	0	
		<i>sterilized</i>	#1	2427	392	39	1	
			#2	830	216	14	0	
		<i>CIP/SIP/DIP</i>	#1	264	49	6	1	
			#2	2199	338	28	0	
	<i>Placebo</i>	<i>washed</i>	#1	1354	124	32	3	
		<i>sterilized</i>	#2	2106	422	109	17	
B	<i>Wfl</i>	<i>untreated</i>	#1	467	138	17	1	
			#2	358	92	18	2	
		<i>washed</i>	#1	684	150	18	1	
			#2	841	206	24	6	
		<i>sterilized</i>	#1	617	144	24	2	
			#2	500	129	26	2	
		<i>Placebo</i>	<i>washed</i>	#1	5681	431	69	16
			<i>sterilized</i>	#2	6823	1538	258	8
	C	<i>Wfl</i>	<i>Washed</i>	#1	644	168	22	6
				#2	457	81	21	9
<i>sterilized</i>			#1	791	209	19	1	
			#2	952	183	37	10	
<i>placebo</i>		<i>untreated</i>	#1	2681	414	113	14	
			#2	2469	512	192	34	

The ζ -potential of shed particles was found to be around -30 mV in Wfi and around -3 mV in placebo (Table IV-23). These values indicate a rather low colloidal stability of shed particles. This is well in line with the observation that subvisible particle counts $\geq 1 \mu\text{m}$ in Wfi increased substantially between day 5 and 14 upon quiescent storage of fresh recirculates (see Figure IV-51a). The attenuated ζ -potential in placebo most likely enhanced particle agglomeration. This most probably led to the frequently higher numbers of micrometer-sized particles in recirculated placebo (see Table IV-22), which coincides with decreased turbidity and NTA counts in placebo as compared to WFI (see Table IV-21). However, characteristics of the nanometer-sized particles in Wfi did not change over storage time (see Figure IV-51b).

Table IV-23: Zeta-potential (mV) of particles in recirculated solutions from 2 h pumping cycles.

Tubing type	Recirculated Wfi	Recirculated placebo
A	-34.5 \pm 0.9	-4.6 \pm 0.6
	-29.8 \pm 1.5	-4.4 \pm 0.4
B	-28.1 \pm 1.2	-3.3 \pm 1.2
	-26.0 \pm 1.0	-1.7 \pm 1.2

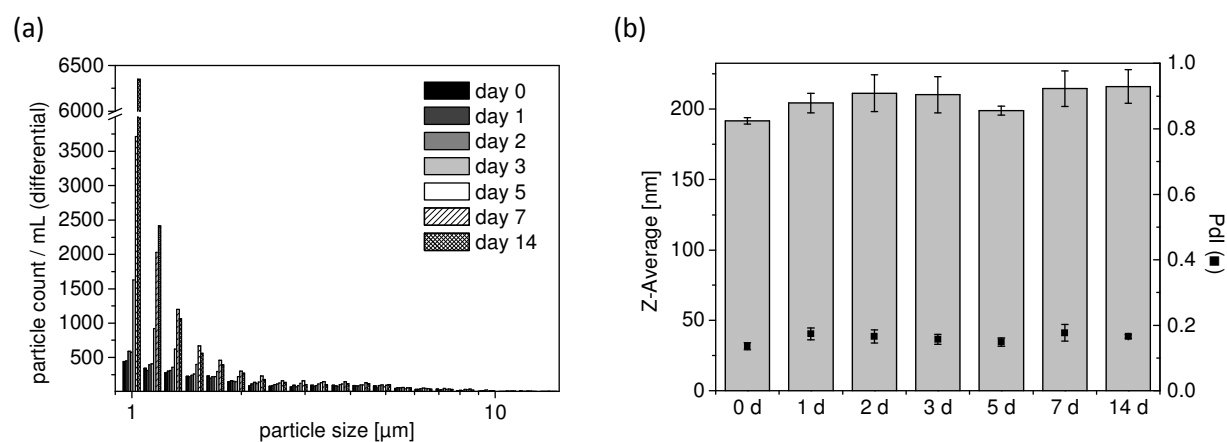


Figure IV-51: Evolution of particle characteristics of a Wfi recirculate of tubing A upon storage at 2-8°C. (a) Differential particle counts $\geq 1 \mu\text{m}$ as determined with LO analysis. (b) Z-Average (bars) and Pdl values (black squares) obtained from DLS analysis.

Recirculated solution from tubing A ($n=6$, received from differently pre-treated tubing sets) were additionally investigated for particle morphology with MFI. Representative scatter plots and particle images for one sample are exemplarily shown in Figure IV-52a-c. The object intensity mean value of 786.0 ± 5.2 pointed to translucent particles. The maximal object intensity mean value was automatically set to 870 due to contrast adjustment and relates to the saturated background. The average aspect ratio of 0.82 ± 0.02 indicated rather spherical particles. As the employed MFI system has limitation in image resolution,[28] the FlowCAM instrument VS-I was additionally used for morphological characterization. The FlowCAM pictures confirmed the spherical morphology (Figure IV-52d). For particles $\geq 2 \mu\text{m}$ a bright center within a dark edge area becomes noticeable, which is typical for transparent particles.

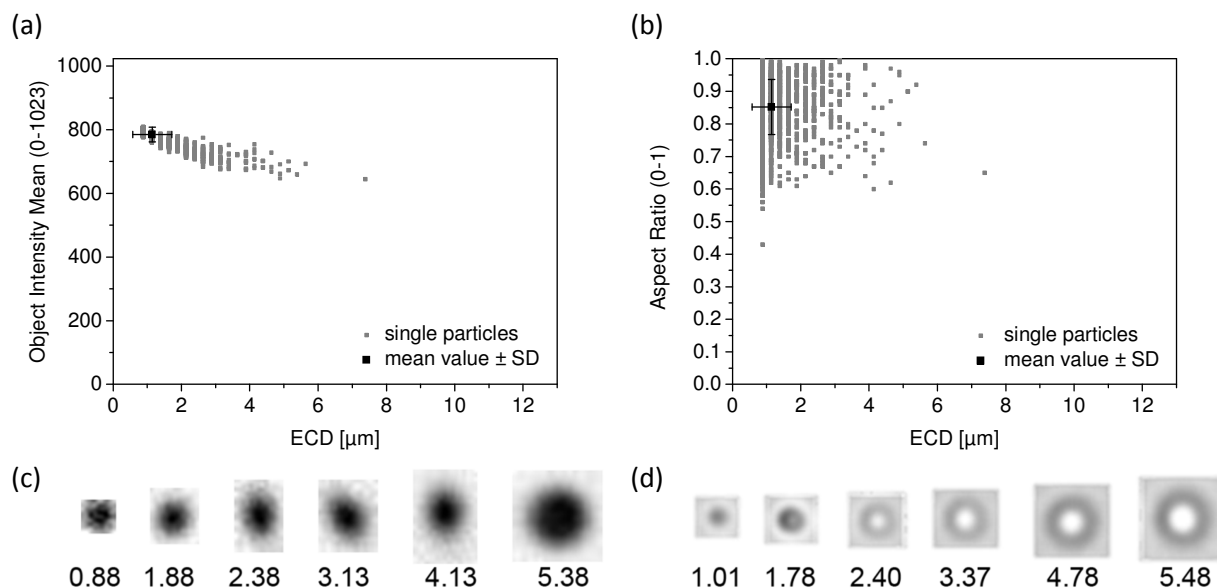


Figure IV-52: Particle morphology. (a) Object intensity mean and (b) aspect ratio as calculated from MFI analysis of a 24 h Wfl recirculate from tubing A. (c) Representative MFI pictures of analyzed particles with varying equivalent circular diameter (ECD given in μm). (d) FlowCAM pictures of particles with varying equivalent spherical diameter (ESD given in μm).

Shed particles revealed the chemical characteristics of polydimethylsiloxane material [29]. The FT-IR spectrum of the dissolved fraction of shed particles (Figure IV-53a) showed a peak at 1260 cm^{-1} arising from symmetric deformation vibrations of methyl groups, and peaks at 1097 and 1018 cm^{-1} which can be attributed to Si-O-Si valence stretching vibrations. The small peak at 1412 cm^{-1} points towards asymmetric deformation vibrations of the methyl group [30,31]. A broadening of the peak at around 1100 cm^{-1} in comparison to the corresponding silicone oil peak is typical for a strongly cross-linked silicone polymer [32]. Figure IV-53b shows the ζ -potential of particles in Wfl in dependence of the pH value. Interestingly, the variation of the ζ -potential with pH follows exactly the same distribution as described by Gu and Li for silicone oil droplets in water [33]: at acidic pH, the ζ -potential was around 20 mV, whereas at basic pH it was approximately -80 mV. The zero point of charge was located near pH 5.

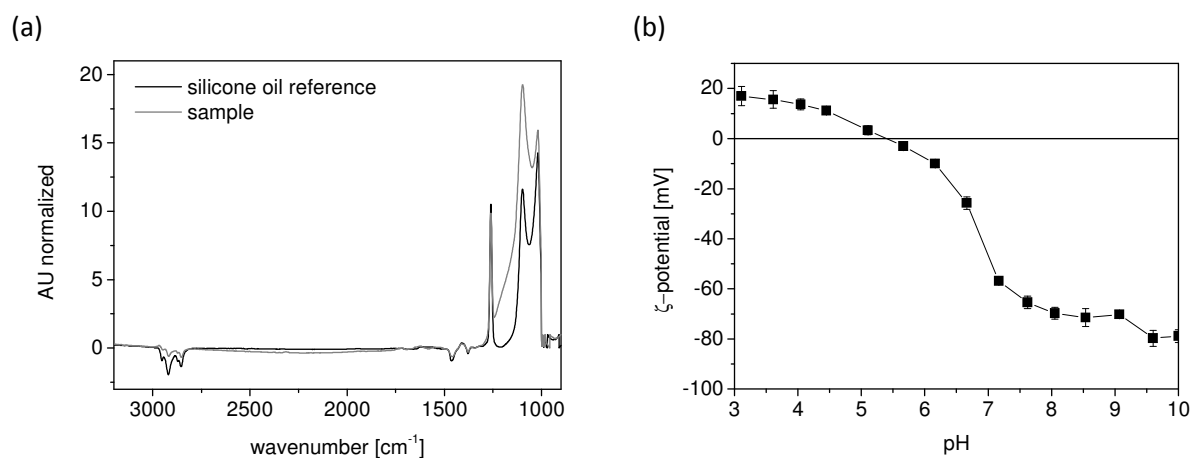


Figure IV-53: (a) FT-IR spectra of shed particles dissolved in n-heptane. (b) ζ -potential of particles suspended in water as a function of pH value.

3.3 Tubing Wear

Investigation of tubing wear led to the conclusion that the particles found in the recirculated solution must indeed originate from the tubing itself, more precisely from the part of the tubing that was located inside the pump head during pumping cycles. In Figure IV-54, scanning electron micrographs are shown for tubing A, B and C before and after pumping cycles with Wfl. The inner surface of unused tubing showed platelet-like structures for all three tubing types. After the 24 h pumping cycles, the morphology remained unchanged for tubing parts outside the pump head. In contrast, tubing parts that were located inside the pump head exhibited a smoothed morphology without any platelet-like structures. At the exit from the pump head, particle deposition was visible with Wfl as a recirculate. These depositions most likely reflect clusters of shed subvisible and/or submicron particles or may represent larger visible particles that did not even reach the recirculation reservoir after generation in the pump head. Cluster formation is suggested due to the stickiness of the particles that was observed during different sample preparation procedures. For example, recirculate filtration eventually led to clogged filter membranes covered by a smooth, continuous layer. Likewise, recirculate centrifugation resulted in a compact pellet that was not re-dispersible.

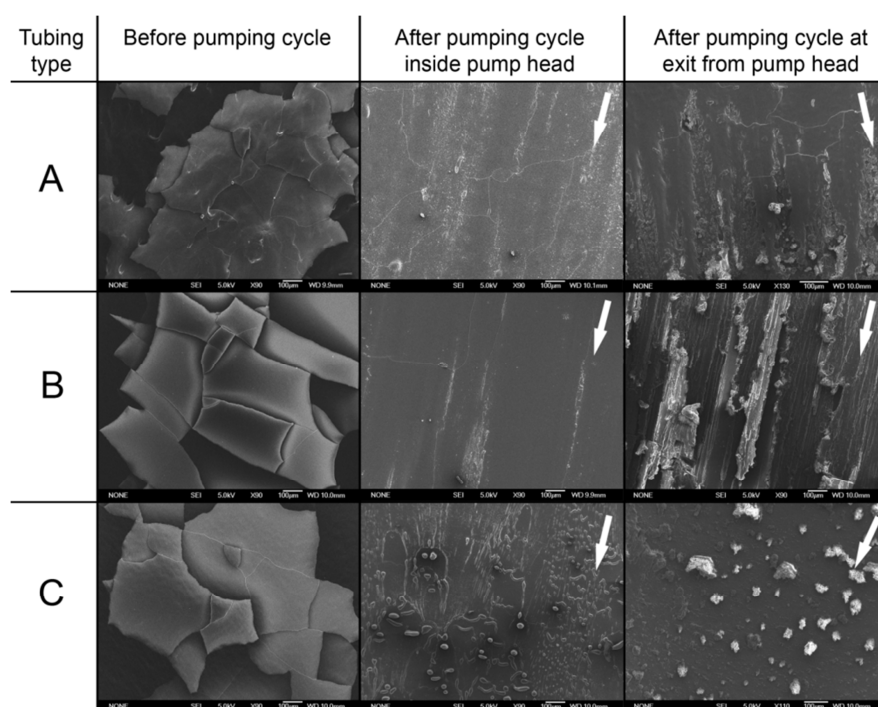


Figure IV-54: Characterization of tubing wear on tubing inner surfaces with SEM after 24 h pumping cycles with Wfl. Arrows indicate flow direction during pumping. The depicted area per micrograph is 1067 μm x 1333 μm .

Furthermore, tubing surface morphology was visualized using a 3D laser scanning microscope. Other than with SEM, where surfaces of unused pieces of all three tubing types appeared similar, 3D laser scanning microscopy elucidated distinct differences in surface roughness of tubing A, B and C (Figure IV-55). For tubing A and C the inner tubing surface was smoothed after 2 h and this effect was even more pronounced after 24 h of pumping. Pumping cycles with tubing B resulted on the one hand in a rather smooth surface (Figure IV-55iii+iv) and on the other hand in regions with plaques (Figure IV-55i+ii). Most likely, this plaque formation was a consequence of the above described tendency for particle deposition. Apart from smoothed tubing surfaces, 3D laser scanning

micrographs revealed an increased number of indentations for tubing A and C upon recirculation of placebo. Recirculation of placebo with tubing B resulted in a smooth surface without any indentations or plaques. The existence of plaques or indentations was determined via profile analysis in the microscope software (see Figure IV-56).

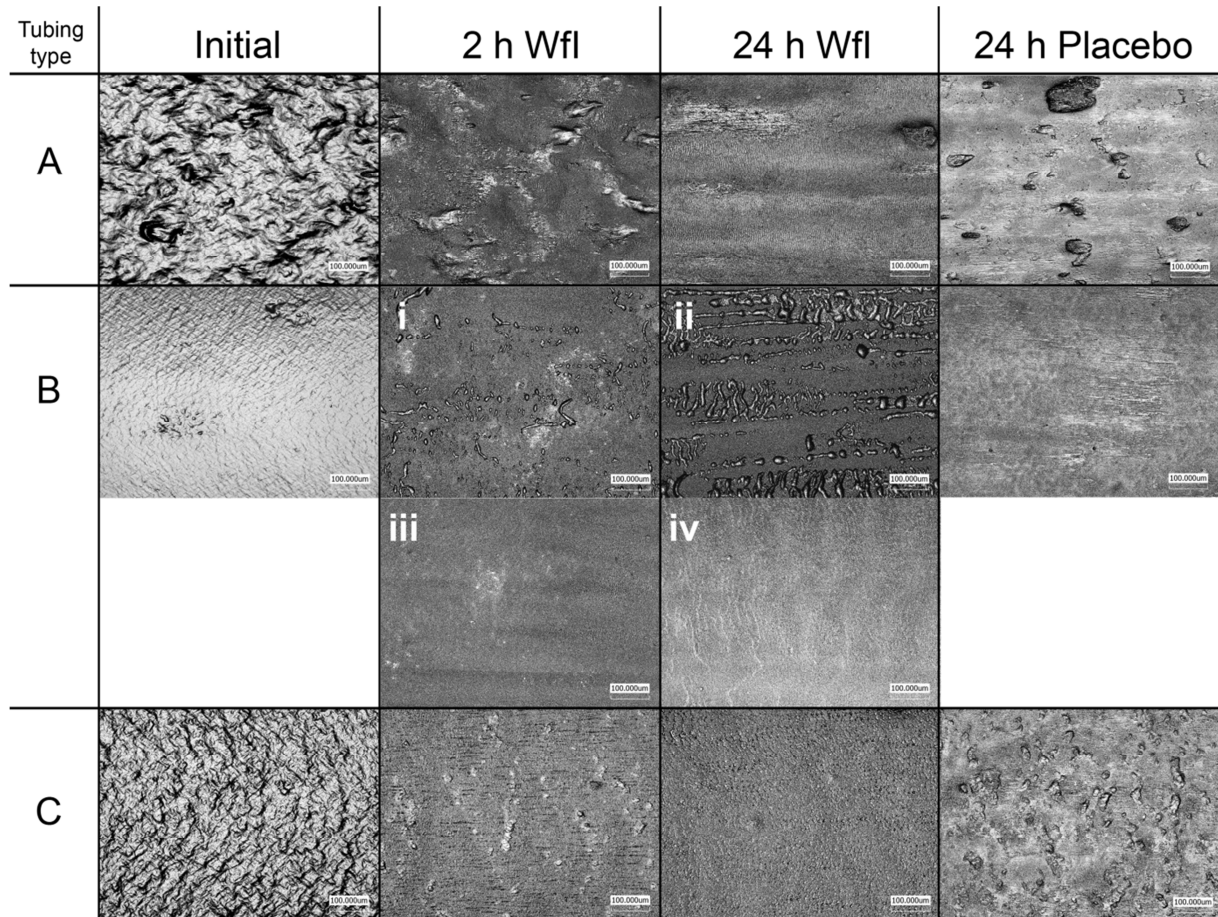


Figure IV-55: Characterization of surface morphology of tubing inner surfaces in dependence on pumping time with 3D laser scanning microscopy. For microscopy tubing pieces were oriented horizontally with direction of flow from left to right. The depicted area per micrograph is 534 μm x 712 μm .

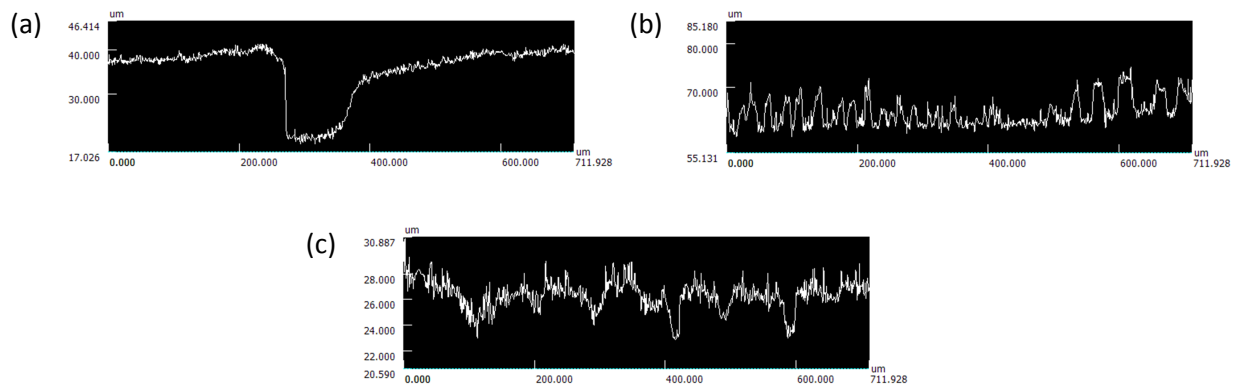


Figure IV-56: Exemplified profiles of micrographs from Figure IV-55 showing the existence of plaques or indentations. (a) Tubing A, 24 h placebo – (b) tubing B, 24 h Wfl – (c) tubing C, 24 h placebo.

Surface roughness of the three tested tubing types was evaluated via the calculation of R_a and R_z values. With the help of roughness standards, the correct settings for the cut-off values were determined prior to roughness evaluation (see Figure IV-47). The cut-off values as recommended by DIN standards [34,35] were not applicable in this case due to the limited scanning area of $712 \mu\text{m} \times 534 \mu\text{m}$. Figure IV-57 depicts the R values for tubing A, B and C over pumping time obtained from areas that were located within the pump head during the applied pumping cycle. R values of unused tubing substantiated the visual impression from the micrographs shown in Figure IV-55. Unused tubing A exhibited the highest surface roughness with a R_a value of $3.95 \pm 0.41 \mu\text{m}$ and a R_z value of $29.7 \pm 3.8 \mu\text{m}$. In comparison, values for tubing B with $0.41 \pm 0.05 \mu\text{m}$ for R_a and $3.0 \pm 0.2 \mu\text{m}$ for R_z were significantly lower and confirmed the smoother appearance in the micrographs. Tubing C revealed a rather moderate surface roughness as indicated by a R_a value of $1.15 \pm 0.08 \mu\text{m}$ and a value of $8.7 \pm 1.3 \mu\text{m}$ for R_z . With increasing pumping time, R_a and R_z values of all tubing types approached a similar end value of about $0.6 \mu\text{m}$ and $5 \mu\text{m}$, respectively. Moreover, the increased relative standard deviations for R values after 2 and 24 h pumping reflected the observed heterogeneity in the form of indentations and plaques on the tubing surface. For example, the relative standard deviation for R_a of tubing A increased from initially 10 % up to 50 % after 24 h.

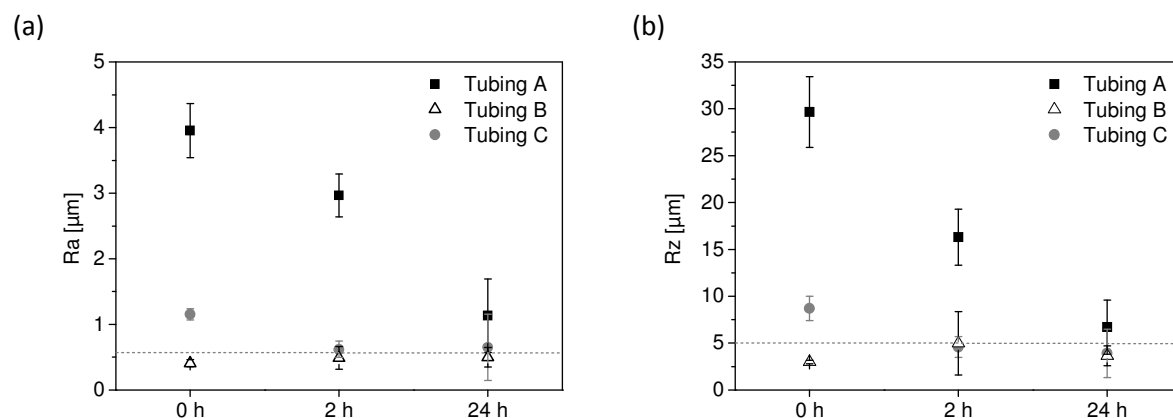


Figure IV-57: (a) R_a and (b) R_z values calculated from 3D laser scanning microscopy of untreated tubing surfaces (0 h) and after 2 and 24 h pumping cycles with Wfl.

3.4 Influence of Tubing ID

Particle shedding from tubing with an ID of 1.6 mm was studied in analogy to the 6 mm ID tubing but with Wfl as recirculate only. Figure IV-58a shows the turbidity profiles for the three different tubing types A, B, and C obtained during online monitoring of 24 h pumping cycles. Final turbidity values of tubing A recirculates varied between 2.6 and 5.9 NTU, recirculates from tubing B showed end values of around 2 NTU, and using tubing C led to turbidity end values of 6 to 7.4 NTU. The two different starting profiles obtained for tubing A were due to the different tubing batches that were used for the preparation of the tubing sets (see paragraph 3.5). Intermittences of the turbidity profiles were due to errors during data transfer to the computer. Influences of the tubing pre-treatment on the turbidity profiles as well as the particle characteristics were not observed for any tubing type. DLS analysis for all recirculates led to Z-average values between 160 and 200 nm with a Pdl between 0.1 and 0.2 (Figure IV-58b). Particle counts in the micrometer range as obtained by LO analysis (see Table IV-24) did not differ significantly for all samples and were less than 1000 particles $\geq 2 \mu\text{m}/\text{mL}$ with few exceptions only. Rather limited amounts of subvisible particles $\geq 10 \mu\text{m}$ (NMT 135 particles / mL) and $\geq 25 \mu\text{m}$ (NMT 42 particles / mL) were found.

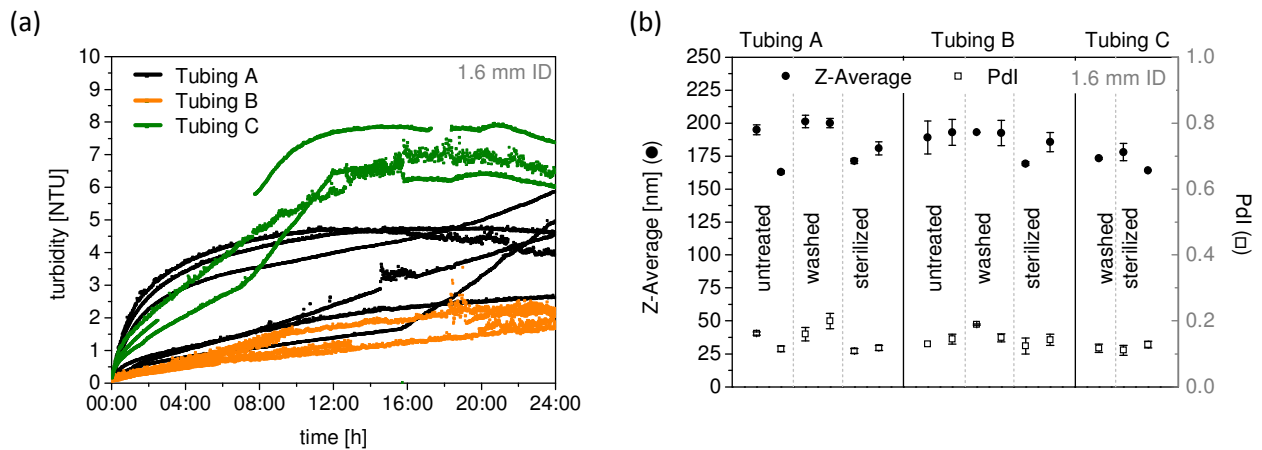


Figure IV-58: Characterization of particle shedding from tubing with an ID of 1.6 mm. (a) Online-turbidity monitoring over 24 h pumping cycles, (b) results from particle characterization of recirculates with DLS.

Table IV-24: Particle counts (LO analysis) of 24 h Wfl recirculates from tubing with an ID of 1.6 mm.

Tubing type	Tubing pre-treatment		Particle counts / mL			
			$\geq 2 \mu\text{m}$	$\geq 5 \mu\text{m}$	$\geq 10 \mu\text{m}$	$\geq 25 \mu\text{m}$
A	<i>untreated</i>	#1	490	141	17	1
		#2	457	153	22	3
	<i>washed</i>	#1	3333	859	130	13
		#2	9888	1836	135	1
	<i>sterilized</i>	#1	430	120	27	1
		#2	1139	242	24	0
B	<i>untreated</i>	#1	290	76	13	1
		#2	373	92	22	3
	<i>washed</i>	#1	998	183	36	4
		#2	714	151	22	6
	<i>sterilized</i>	#1	406	112	21	0
		#2	502	118	9	0
C	<i>washed</i>	#1	466	152	62	42
	<i>sterilized</i>	#1	503	132	24	2
		#2	393	86	17	1

Initially, the tubing surface morphology of the three tubing types differed substantially (Figure IV-59). All three surfaces exhibited regular variations in surface height. These height differences were most pronounced on the surface of tubing A, whereas tubing B showed more frequent but less distinct height changes. This is reflected in the corresponding roughness values (Figure IV-60), which were highest for tubing A ($R_a = 3.31 \pm 0.52 \mu\text{m}$, $R_z = 21.4 \pm 3.3 \mu\text{m}$), lowest for tubing B ($R_a = 0.55 \pm 0.04 \mu\text{m}$, $R_z = 3.8 \pm 0.3 \mu\text{m}$), and in-between for tubing C ($R_a = 1.52 \pm 0.29 \mu\text{m}$, $R_z = 10.1 \pm 2.0 \mu\text{m}$). After 2 h of pumping, surface roughness values of tubing A already decreased slightly, whereas roughness values of tubing B was unchanged. After 24 h, 3D laser scanning

microscopy revealed very smooth surfaces but especially for tubing A and B also areas with distinct irregularities in the form of plaques and indentations. The observed heterogeneities gave rise to R_a and R_z values of around 1-2 μm and 7-10 μm , respectively, that significantly varied depending on the investigated spot on the tubing surface (RSDs of up to 97 % for tubing B). In comparison to the initial surface roughness, mean R_a and R_z values after 24 h pumping time were thus decreased for tubing A, increased for tubing B, and rather unchanged for tubing C.

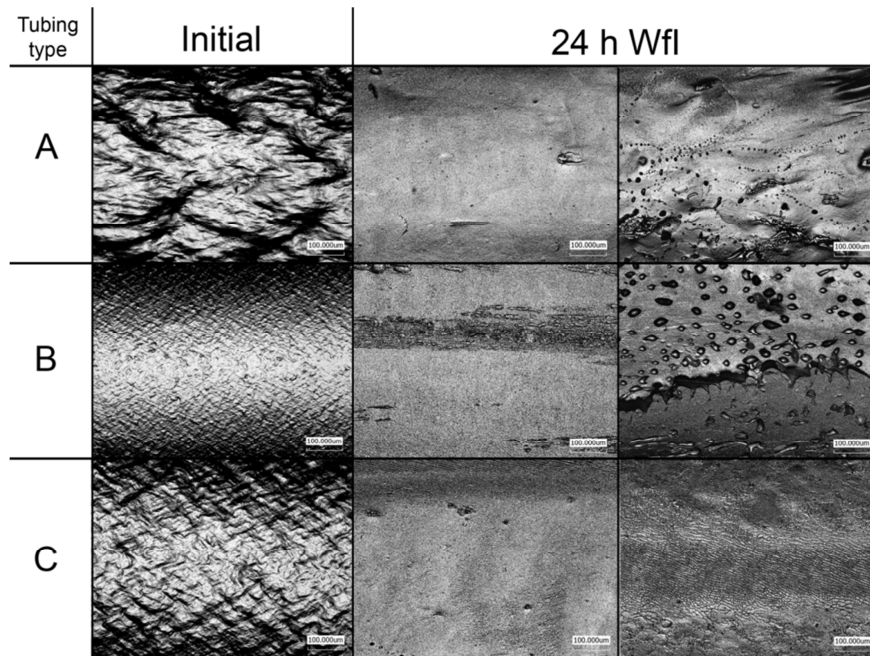


Figure IV-59: Morphology of surface roughness (tubing ID of 1.6 mm) initially and after 24 h pumping cycles with Wfl, analyzed with 3D laser scanning microscopy.

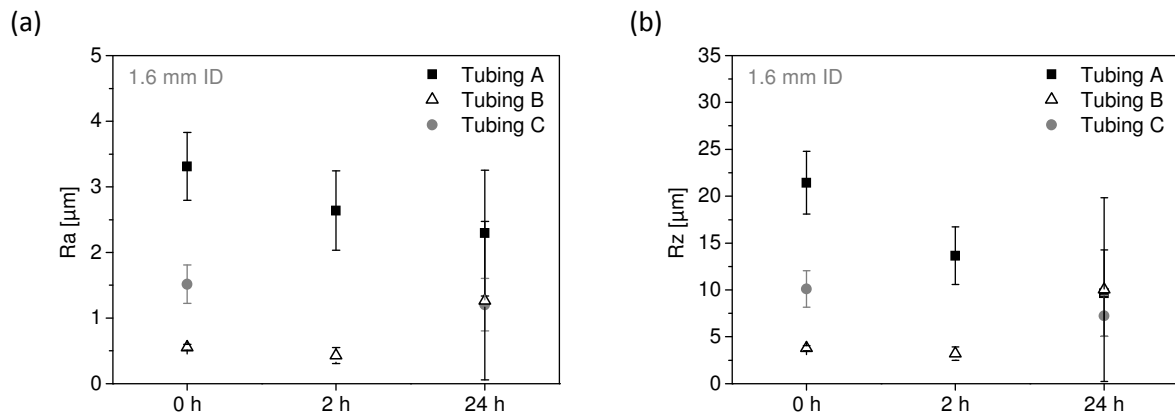


Figure IV-60: Evolution of surface roughness values (a) R_a and (b) R_z of tubing with an ID of 1.6 mm over pumping time using Wfl as recirculate.

3.5 Influence of Tubing Batch

In order to account for batch-to-batch differences, at least a second batch of tubing A (6.0 and 1.6 mm ID) and B (6.0 mm) was analyzed via online-turbidity monitoring (Figure IV-61). Moreover, the recirculates were characterized for particles in the nano- and micrometer range and the decrease in flow rate was determined (Table IV-25). Although the corresponding data for tubing A with ID 1.6 mm was already presented in section 3.4, it is included again for better comparison.

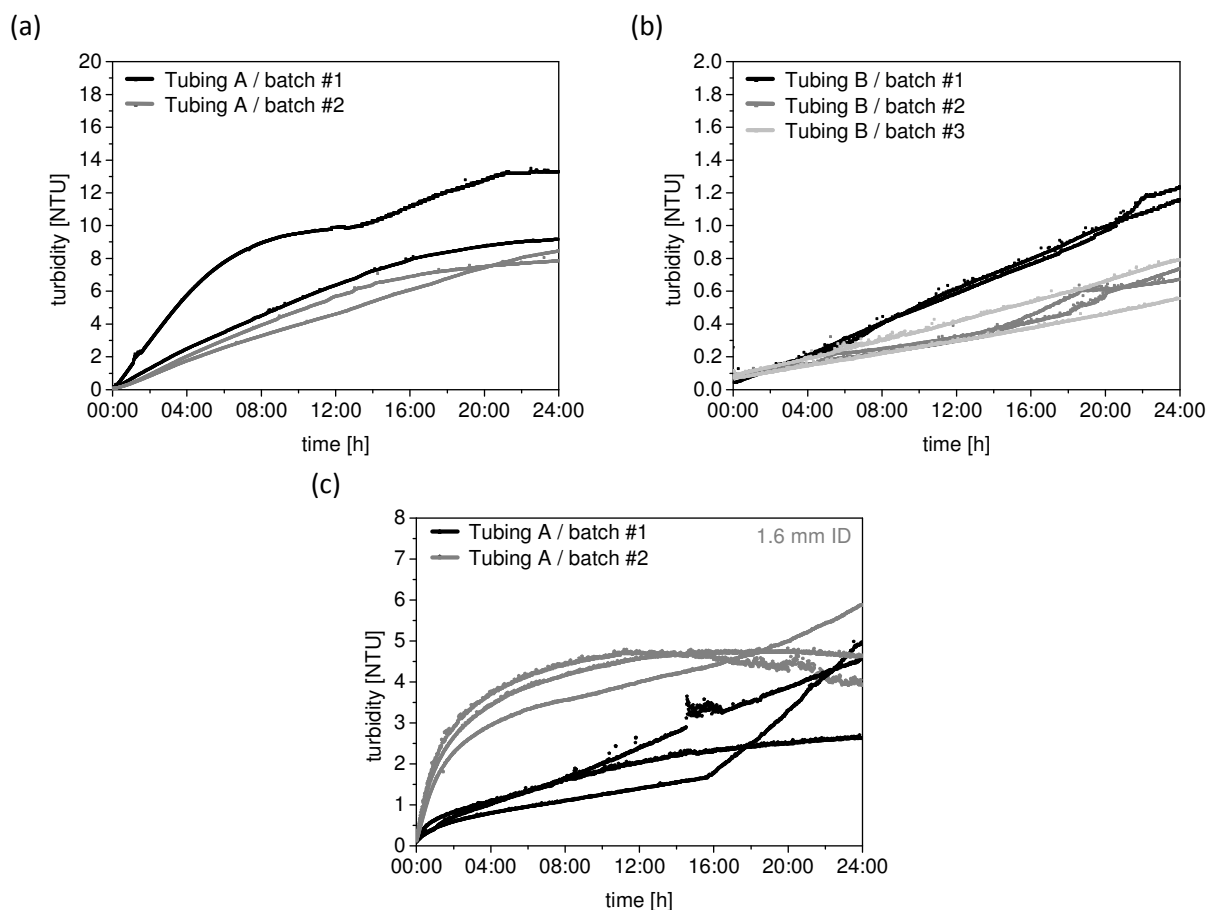


Figure IV-61: Online-turbidity monitoring of different batches of (a) tubing A with 6.0 mm ID, (b) tubing B with 6.0 mm ID, and (c) tubing A with 1.6 mm ID. Please note the differences in scale of the y-axis.

For the second batch of tubing A (6.0 mm ID), slightly lower turbidity end values than for the first batch were obtained (Figure IV-61a). Considering the overall quite high variability between different runs with the same tubing type (see Figure IV-49b), this effect is rather small. The same conclusion applies for the marginal differences in particles counts $\geq 2 \mu\text{m}$. DLS results and flow rate decreases were comparable for both tubing batches (see Table IV-25). All three batches of tubing B (6.0 mm ID) led to turbidity end values below 1.2 NTU (see Figure IV-61b). Turbidity profiles for batch #2 and #3 were very similar and ended at around 0.7 NTU. Particle characteristics in the nano- and micrometer range as well as flow rate changes after pumping were comparable for all three tested batches. It needs to be mentioned that the manufacturer of tubing B announced a production change while this study was performed. Batch #3 is part of this new generation of tubing B made with the same raw materials and extrusion equipment, but with a more optimized mixing ratio of its compounds. This change does not seem to have altered the anyway low propensity of tubing B to shed particles. However, the modified composition led to 35 % higher indentation forces for this batch (see Figure IV-62). Flow rate decreases for all 6 mm ID tubings investigated ranged between 1.7 and 6.1 % (see details in section 3.6).

The turbidity profiles for different batches of tubing A with an ID of 1.6 mm revealed distinct differences, especially with regards to the initial slope. Batch #1 tubing sets showed a steady, but limited increase in turbidity over pumping time, whereas sets from batch #2 led to a rather steep turbidity increase initially with a plateau phase afterwards (see Figure IV-61c). Z-Average and Pdl values for particles obtained from batch #2 tended to be lower than from batch #1. No significant effect of the used batch on particle counts $\geq 2 \mu\text{m}$ could be deduced. Hardly any changes in flow

rates before and after the pumping cycle were measured for batch #2, whereas for batch #1 flow rates decreased by 3 % on average. Initial pump rates for batch #2 were 7 % higher than for batch #1 (see section 3.6). The indentation force for batch #2 was 22 % lower than for batch #1 (Figure IV-62).

Table IV-25: Comparison of particle characteristics of recirculates as well as flow rate variations obtained from different tubing batches.

Tubing type	batch	run	Particle counts ≥ 2 μm/mL (LO)	DLS		Decrease in flow rate [%]
				Z-Average [nm]	Pdi	
A 6 mm ID	1	#1	1104 ± 55	201.3 ± 1.4	0.122 ± 0.009	-2.2
		#2	954 ± 62	195.0 ± 1.0	0.193 ± 0.009	-1.7
	2	#1	763 ± 23	197.3 ± 0.8	0.108 ± 0.019	-2.2
		#2	787 ± 90	191.5 ± 0.5	0.100 ± 0.019	-3.5
B 6 mm ID	1	#1	467 ± 67	193.0 ± 2.5	0.128 ± 0.017	-4.5
		#2	358 ± 46	193.8 ± 4.9	0.142 ± 0.025	-5.3
	2	#1	1046 ± 51	196.2 ± 5.5	0.199 ± 0.028	-4.9
		#2	361 ± 17	198.9 ± 7.2	0.181 ± 0.046	-6.1
	3	#1	308 ± 31	198.0 ± 3.2	0.228 ± 0.046	-4.0
		#2	188 ± 28	194.3 ± 5.3	0.159 ± 0.030	-3.8
A 1.6 mm ID	1	#1	490 ± 51	195.0 ± 3.8	0.162 ± 0.005	-2.9
		#2	3333 ± 75	201.2 ± 4.8	0.160 ± 0.009	-2.5
		#3	9888 ± 282*	200.0 ± 3.5	0.200 ± 0.023	-3.4
	2	#1	457 ± 40	162.9 ± 1.2	0.115 ± 0.009	±0.0
		#2	430 ± 20	171.3 ± 2.1	0.109 ± 0.007	-1.9
		#3	1139 ± 54	180.9 ± 4.9	0.118 ± 0.008	±0.0

*Flow via flow path F as shown in Figure IV-46 was observed towards the end of this run. It is assumed that flow via flow path F correlates with the increased slope in the turbidity profile Figure IV-61 starting at approx. 16 h pumping time and likewise might have resulted in comparably high particle counts.

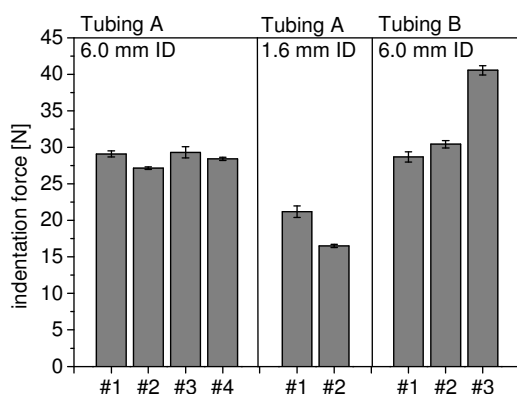


Figure IV-62: Indentation forces for different tubing batches.

Initial surface roughness values of several batches of tubing A and B (ID of 6.0 mm) were comparable within one tubing type, however were differing by a factor of 10 on average between tubing A and B (Figure IV-63). The evolution of surface roughness over time was confirmed for a second batch of tubing A and B, as well as for tubing sets from pumping cycles with placebo (Figure IV-64).

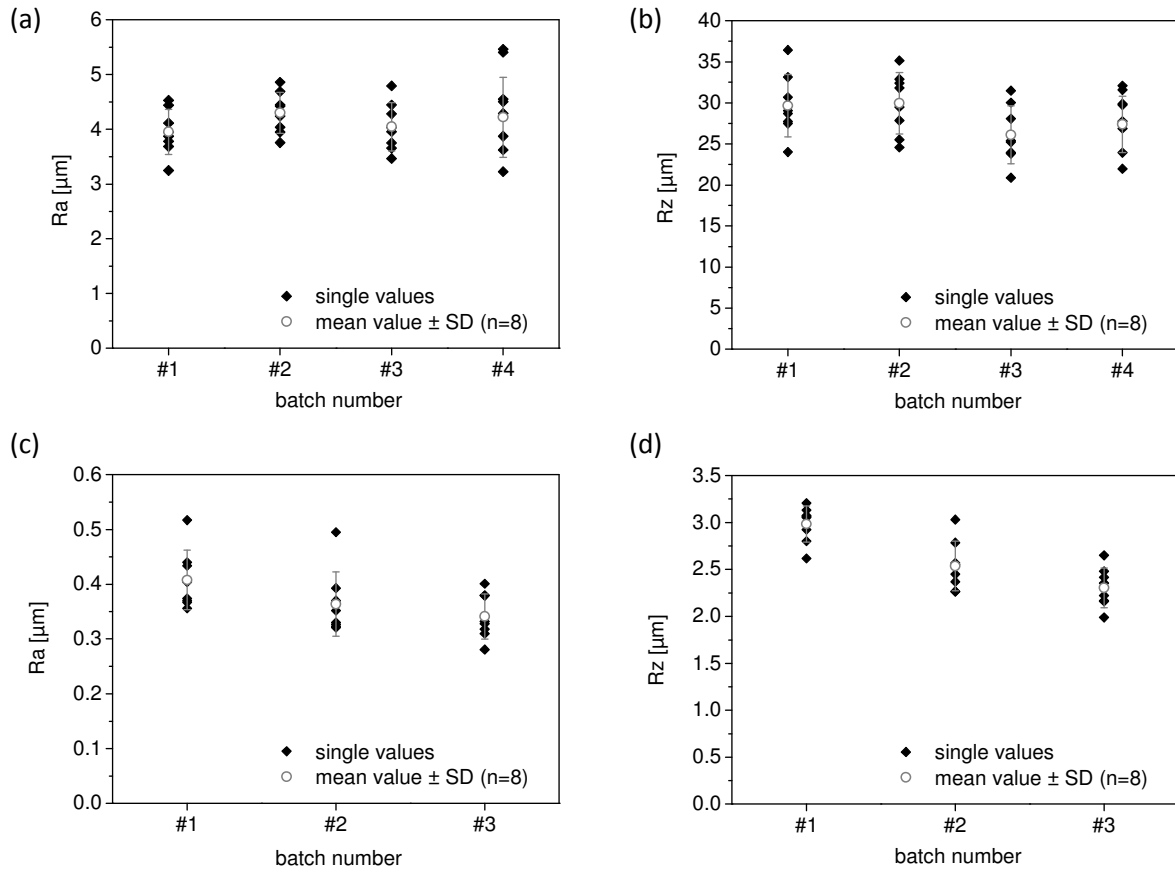


Figure IV-63: Surface roughness values R_a and R_z of different batches of tubing A (a+b) and B (c+d) (6.0 mm).

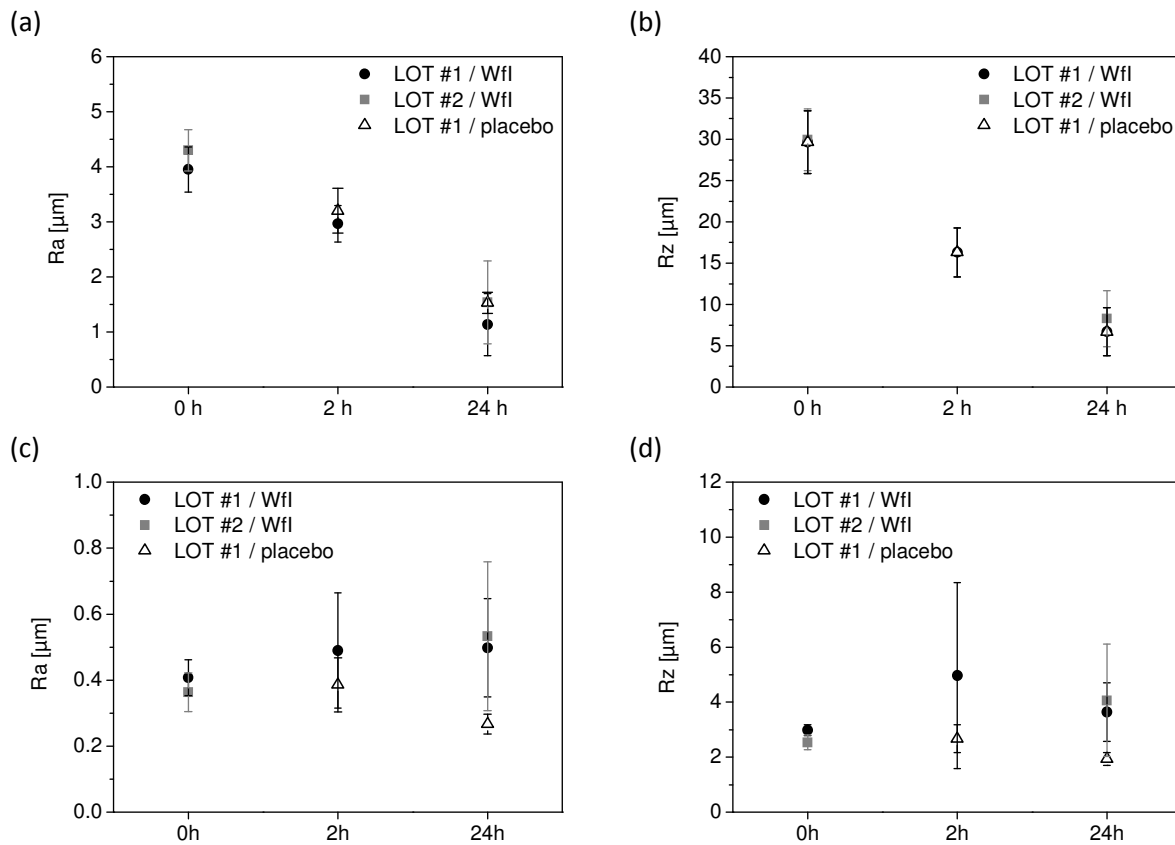


Figure IV-64: Evolution of surface roughness over time in dependency of batch and recirculating medium for tubing A (a+b) and B (c+d) (6.0 mm ID).

3.6 Effect of Pumping on Mechanical Properties of Tubing

Pump rates of tubing sets were determined prior and after pumping cycles (Figure IV-65) as a measure for the deformation of the tubing lumen due to the mechanical stress exerted by the peristaltic pump.

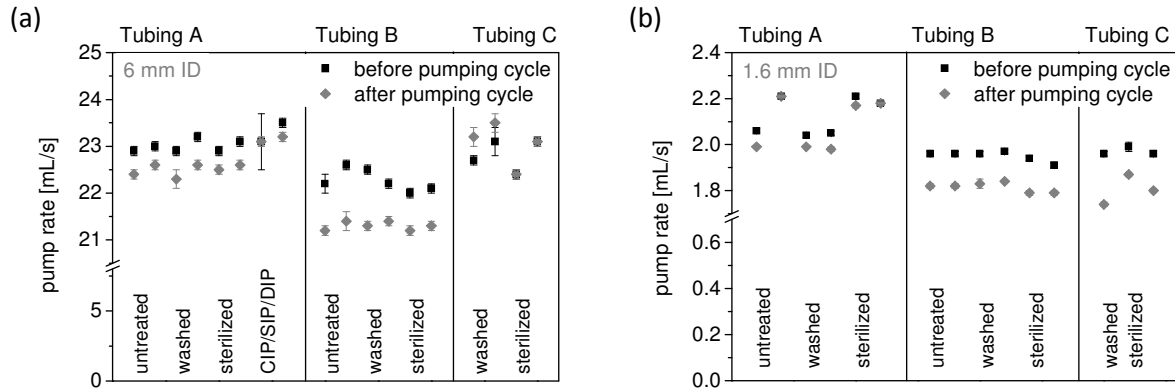


Figure IV-65: Pump rates before and after pumping cycles for tubing with (a) 6 mm and (b) 1.6 mm ID.

All tubing sets apart from tubing C (6 mm ID) showed a clear decrease in pump rate after the pumping cycle. In contrast to this, for 1.6 mm ID tubing, this decrease in percent as listed in Table IV-26 was highest for tubing C, followed by tubing B and lowest for tubing A. Big differences in initial pump rate and decrease were seen between the two batches of tubing A with 1.6 mm ID (see also section 3.5).

Table IV-26: Change (%) in pump rates after 24 h pumping cycles with Wfl, calculated as mean values with standard deviations from the pump rates shown in Figure IV-65.

Tubing type	6 mm ID	1.6 mm ID
A	-1.8 ± 0.9	-2.9 ± 0.5 / -0.6 ± 1.1*
B	-4.5 ± 0.9	-7.0 ± 0.5
C	+1.0 ± 1.2	-8.5 ± 2.6

*: Pump rate deviations for the two different batches used

Indentation forces were recorded as a second measure for the mechanical stress that the rollers within the pump head exert on the tubing (Figure IV-66). For all tubing types and IDs, indentation forces were clearly reduced after the pumping cycles on areas located within the pump head. Reductions in indentation forces were between 22 to 27 % for tubing with an ID of 6 mm (A: -23.5 %, B: -27.3 %, C: -21.8 %), and even up to 40 % for the smaller tubing ID of 1.6 mm (A: -39.8 %, B: -31.6 %, C: -34.3 %). Already after 2 h of pumping, indentation forces for all tubing types were decreased by approx. 20 %.

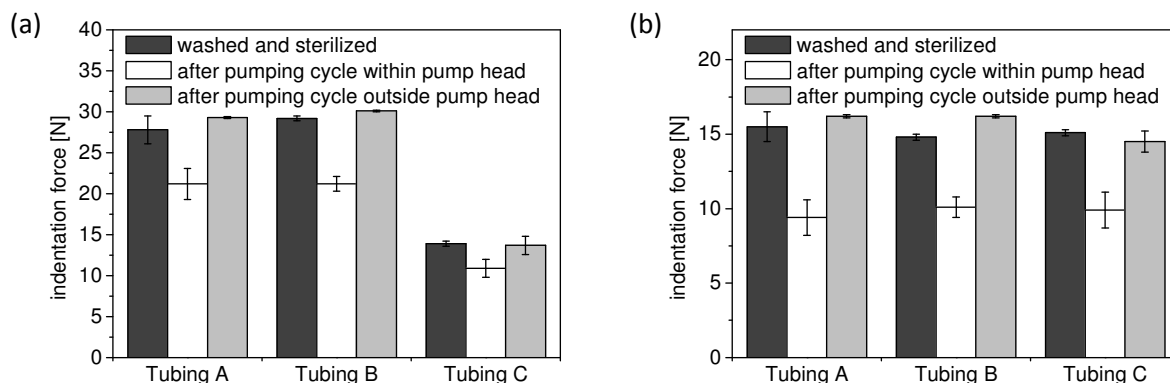


Figure IV-66: Indentation forces measured for tubing sets with an ID of (a) 6 mm and (b) 1.6 mm, before and after 24 h pumping cycles with Wfl.

3.7 Influence of Pump Head

The influence of a different pump on particle shedding from tubing A and B with an ID of 1.6 mm was studied via 2 h recirculation experiments employing Wfl and placebo buffer as recirculation media. This comparative study included turbidity, DLS and LO analysis of the obtained recirculates. Moreover, particle deposition at the exit from the pump head as already described in Figure IV-54 was evaluated via visual and microscopic inspection.

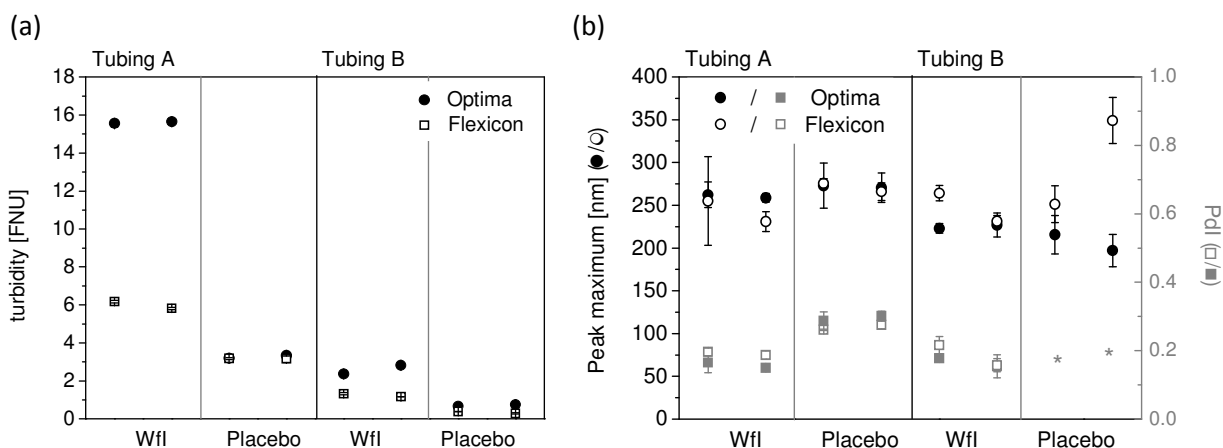


Figure IV-67: Comparison of the two pump heads Flexicon and Optima in terms of (a) turbidity and (b) DLS characteristics of the obtained recirculates. (*PDI not shown, multimodal size distribution due to additional micelles and sucrose peak resulted in highly increased values that are not meaningful in this context.)

Turbidity values confirmed previously described trends since turbidity values of recirculates from tubing A were generally higher than those from tubing B and also generally higher when pumping Wfl instead of placebo (Figure IV-67a). Upon recirculation of Wfl with the Optima pump, the turbidity increase was by a factor of 2.7 / 2 (tubing A / B) higher compared to the turbidity increase resulting with the Flexicon pump. Turbidity values of placebo recirculates were similar. No differences in the size distribution of shed nanoparticles could be deduced (Figure IV-67b). Particle counts in the micrometer range were higher for Optima than for Flexicon recirculates (Table IV-27). Correspondingly, particle deposition on the inner tubing surface was more often observed upon operation in the Optima pump, especially with Wfl as recirculate (Table IV-28).

Table IV-27: Particle counts from LO analysis of recirculates produced with two different pump heads.

Pump head	Tubing type	Recirculating solution		Particle counts / mL			
				$\geq 2 \mu\text{m}$	$\geq 5 \mu\text{m}$	$\geq 10 \mu\text{m}$	$\geq 25 \mu\text{m}$
Optima	A	Wfl	#1	12322	1287	242	29
			#2	8606	1489	232	33
		Placebo	#1	6358	1520	408	134
			#2	6174	1379	367	119
	B	Wfl	#1	6140	1030	136	23
			#2	3940	881	171	40
		Placebo	#1	3564	584	211	101
			#2	3416	536	213	112
Flexicon	A	Wfl	#1	4560	968	192	23
			#2	4119	702	126	16
		Placebo	#1	1988	540	122	42
			#2	2278	594	156	47
	B	Wfl	#1	1099	244	40	3
			#2	704	182	16	1
		Placebo	#1	2823	631	159	37
			#2	1906	1046	409	128

Table IV-28: Evaluation of particle deposition on the inner tubing surface after the pumping cycle.

Tubing type	Recirculating solution		Optima	Flexicon
A	Wfl	#1	++	-
		#2	++	-
	Placebo	#1	-	-
		#2	-	-/+
B	Wfl	#1	+/-	-
		#2	+	-
	Placebo	#1	-	-
		#2	-	-

- : no particle depositions visible

+/- : particle deposition observed in only one of two flanks

+ : minor particle deposition observed in both flanks

++ : major particle deposition observed in both flanks

A smoothed inner surface after pumping was observed for all studied tubing sets (Figure IV-68). Surfaces of tubing B generally appeared smoother, but apart from that tubing morphologies were comparable and independent of the used pump head. This observation is reflected in the corresponding roughness values (Figure IV-69). Mean R values of tubing B were slightly less reduced when using the Optima pump for recirculation. However, due to the rather high standard variations resulting from surface heterogeneity, this effect was not significant.

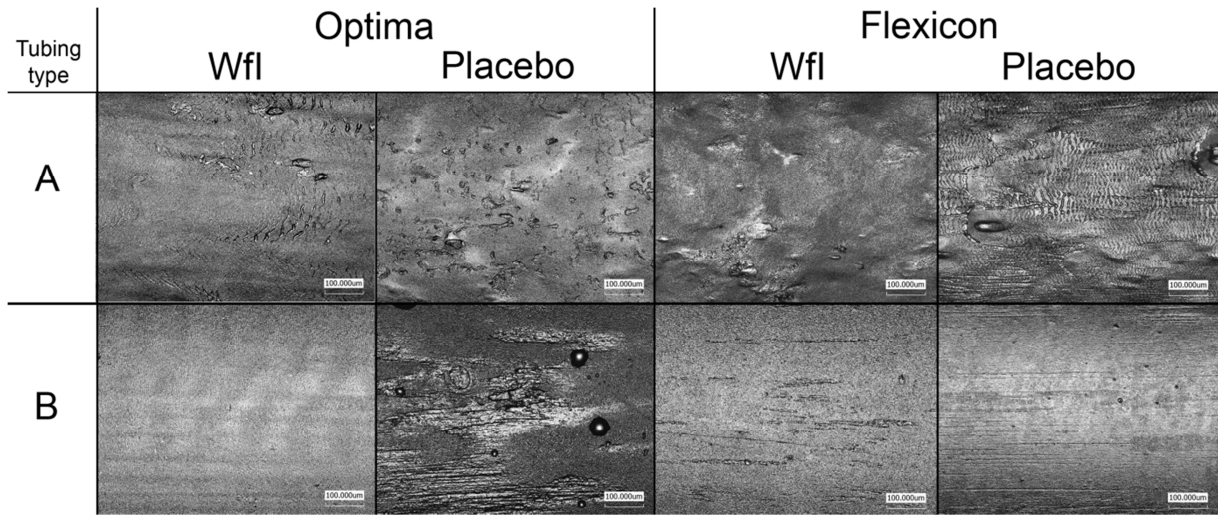


Figure IV-68: 3D laser scanning micrographs of the inner tubing surface on areas located inside the pump head during pumping cycles (2 h).

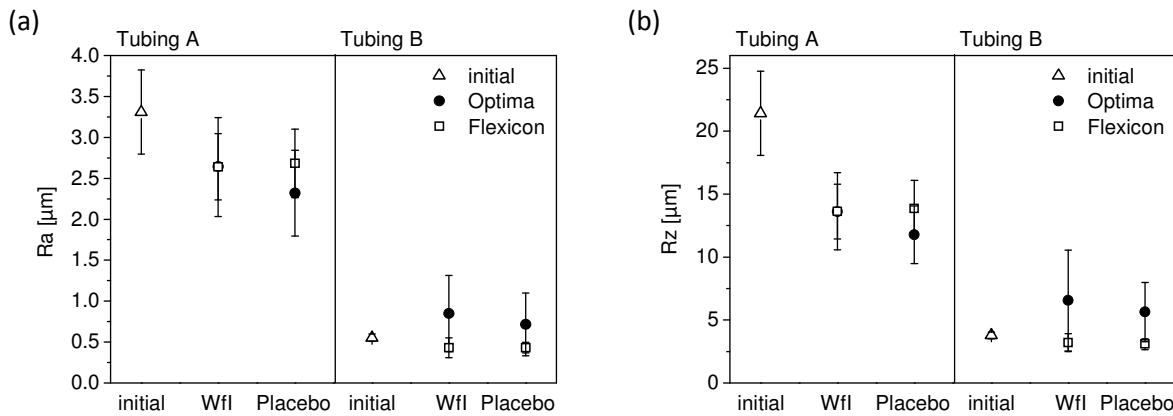


Figure IV-69: Roughness values (a) R_a and (b) R_z of the inner tubing surfaces shown in Figure IV-68 in comparison to initial surface roughness before pumping.

As a measure for the mechanical stress that the different pump heads exerted on the tubing, mechanical stiffness in percent was determined as the relative indentation force on areas that were located within the pump head in comparison to areas outside the pump head (Figure IV-70). The mechanical stiffness of all samples was decreased by at least 20 % after 2 h of pumping. Only for tubing A with WFI as recirculating medium, significant differences ($p < 0.05$) were found for the impact of the two pump heads on the mechanical properties of the tubing material.

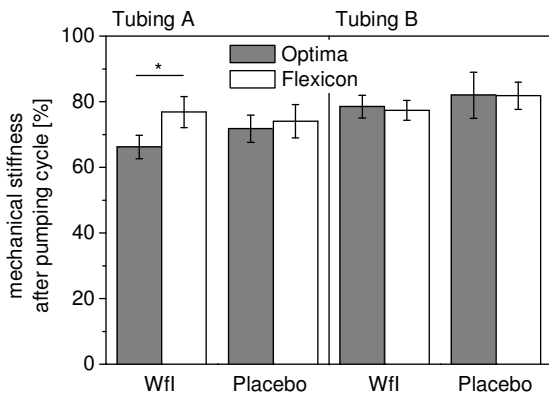


Figure IV-70: Remaining mechanical stiffness of the different tubing sets after the 2 h pumping cycle.

3.8 Influence of Post-Curing

Only the manufacturing process of tubing B includes a post-curing step. Therefore, the impact of such a post-curing step was further investigated with tubing of 6.0 mm ID, especially with regards to particle shedding. The manufacturer of tubing B claims that post-curing for 4 h at 200°C with high air throughput ensures a reduced amount of volatile residues and optimized physical properties by completing crosslinking. Post-curing was simulated in a heating oven without the possibility for continuous air throughput. The performance of post-cured tubing sets in terms of particle shedding, mass loss during heating, as well as mechanical properties was compared to tubing sets that did not receive this additional treatment.

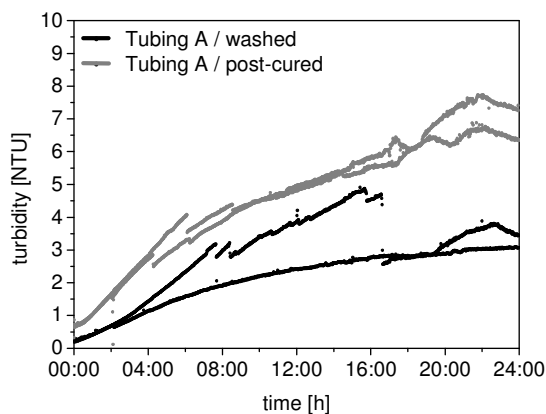


Figure IV-71: Turbidity monitoring graphs of recirculation experiments with placebo buffer and two differently treated sets of tubing A (6.0 mm ID).

Online-turbidity monitoring demonstrated slightly higher turbidity values for the post-cured tubing set (Figure IV-71). However, these differences seem to be well within the overall variability in turbidity profiles obtained for tubing A (see Figure IV-49d). Depending on the tubing type, TGA analysis revealed mass losses during equilibration for 4 h at 200°C of 0.1 to 0.6 %. Mass losses were minimally reduced after the applied post-curing treatment and the obtainable mass losses seemed to recover with prolonged storage time. For data interpretation, the precision of the TGA instrument of 0.1 % needs to be considered. Indentation forces increased by less than 1 N and were thus largely unaffected by the simulated post-curing step.

4 DISCUSSION

Online-monitoring of turbidity with recirculating Wfl turned out to be highly valuable for characterizing the extent of particle shedding from silicone tubing upon peristaltic pumping. With surfactant-containing placebo solution, the obtained online-turbidity monitoring graphs were less valuable due to excursions caused by the entrapment of air bubbles within the measuring cell. The observed slight variability in turbidity profiles between different runs with the same tubing type may be due to variations in the manual mounting of the tubing sets within the pump head and in particle deposition at the pump head end. Washing cycles as well as sterilization of the tubing material at temperatures up to 131°C, as applied during typical CIP/SIP/DIP cycles, did not impact the extent of particle shedding. This is well in line with the fact that silicones are thermally stable due to a shielding of the polar backbone by methyl groups and therefore can be operated at temperatures up to 215°C [14]. High temperatures may instead enhance the extraction of low molecular weight species [36]. However, the determination of extractable levels was not within the scope of this study.

Shedding mainly resulted in particles of around 200 nm in size. With both DLS and NTA, a narrow monomodal size distribution was identified in recirculated Wfl (Pdl of about 0.2). Particle characteristics were independent of tubing type and pre-treatment. The number of nanometer-sized particles as assessed with NTA varied between different tubing types. Wfl recirculated with tubing A contained about 20 to 25 times more nanometer-sized particles than Wfl recirculated with tubing B. Additional excipient peaks in DLS measurements of recirculated placebo solutions lead to higher variability in Z-average and Pdl values. These parameters are therefore considered as less meaningful for the interpretation of particle characteristics in recirculated placebo. The main particle fraction of 200 nm was also observed in recirculated placebo. It is anticipated that particle shedding will result in similar particle characteristics when using e.g. protein solution.

It is assumed that this nanometer-sized particle fraction was the primary form of particle spallation from silicone tubing and that these particles formed the obtained micrometer-sized particles. This hypothesis of agglomeration and subsequent fusion of shed nanoparticles is supported by the observed particle stickiness and the increase in particle counts of around 1 μm after several days of quiescent storage of fresh recirculates (see Figure IV-51). The change in particle size distribution due to colloidal instability seemed to be more pronounced in placebo buffer. The effect corresponds to the less negative ζ -potential of the particles in buffer compared to Wfl. Accordingly, the numbers of micrometer-sized particles in recirculated placebo tended to be higher than particle counts in recirculated Wfl. The morphology of the micrometer-sized particles as assessed with MFI strongly resembled those of silicone oil droplets apart from slightly brighter edges [9,37,38]. FT-IR characterization of the particles after redissolution in heptane demonstrated spectral features that are typical for silicone polymer materials, and also the pH-dependent ζ -potential profile in Wfl indicated that the particles consist of polydimethylsiloxane. For clarification, it needs to be pointed out that the particles consisted of silicone elastomer and not silicone oil, a fact that is simply deducible from the rather high relative density of the particles.

Barron *et al.* reported that the majority of shed particles in their studies was smaller than 16 μm in diameter [19] and in line with their findings, we also observed only few particles larger than 10 μm . Therefore, it is unlikely that the pharmacopeial requirements for subvisible particle counts $\geq 10 \mu\text{m}$ and $\geq 25 \mu\text{m}$ could be compromised by particle shedding from silicone tubing [5]. However, it is nevertheless desirable to keep any particulates in the final product to a minimum. Overall, particles shed from silicone tubing upon operation in a peristaltic pump should be considered as one possible

source of particle contamination, although to a rather limited extent. For the interpretation of our data, it has to be kept in mind that particle counts presented here resulted from recirculation experiments. Hence, the number of shed particles accumulated in a limited volume of recirculation medium. From our particle count data after 2 h pumping time, we estimated the number of particles deriving from the particle shedding and to be expected in a final DP. This extrapolation translated into a very low particle burden for both the micrometer and nanometer range for the final DP (Table IV-29) close to blank level. For several reasons, this calculation is only an approximation. Firstly, NTA counts are a rather semi-quantitative estimate of nanometer-size particle numbers. Secondly, a more diluted particle suspension as obtained after filling without recirculation might lower the possibility for particle agglomeration and the formation of micrometer-sized particles.

Still, in order to obtain a DP with optimal quality, unwanted particle contamination should be avoided and choosing low abrasive tubing contributes to this ubiquitous pharmaceutical claim.

Table IV-29: Expected particles to be found in a filled product due to tubing shedding during production conditions calculated from the 2 h recirculation experiments.

	Number of (shed) particles			
	< 1 μm in 10^6 particles / mL (NTA)		$\geq 2 \mu\text{m}$ / mL (LO)	
	<i>recirculating conditions^a</i>	<i>production conditions^b</i>	<i>recirculating conditions^a</i>	<i>production conditions^b</i>
Tubing A / Wfl	4953 \pm 176	24 \pm 0.9	719 \pm 59	3 \pm 0
Tubing A / placebo	2646 \pm 566	12 \pm 2.8	340 \pm 34	1 \pm 0
Tubing B / Wfl	201 \pm 28	1 \pm 0.1	277 \pm 38	1 \pm 0
Tubing B / placebo	169 \pm 45	0.2 \pm 0.3	652 \pm 22	3 \pm 0

^a Experimental data was not corrected for blank values. Blank values measured with NTA / LO in particles per mL were $5 \pm 2 \times 10^6 / 3 \pm 0$ for Wfl and $132 \pm 27 \times 10^6 / 107 \pm 13$ for placebo.

^b During experiments, 70 mL of recirculation medium was employed with a total of 2880 fills of 5 mL each. This resulted in a pumped volume of 14,400 L meaning that every milliliter of the recirculate passed the pump 206 times. The particle counts obtained from experimental conditions as stated in the table were divided by this factor after blank value subtraction in order to give the stated number of additional particles to be expected in the filled drug product.

Wear of the inner surface of tubing after pumping cycles was noticed in earlier studies with medical background. Kim and Yoon found grooves with SEM and phase contrast microscopy [22]. Kurusz also described grooves located at the points of maximum flexure within the tubing material [21]. Such grooves seem to be a natural consequence of the occlusion pressure applied by the pump head and were visible inside all tubing sets of this study as well. On the inner surface of unused tubing, Dewan *et al.* noted adherent particles that were not seen after use of the tubing within a pump [20]. In our case, the tubings were free of pre-existing particle contamination. Instead, spallation and smoothening of the surface as reported by Kurusz [21] drives particle formation during pumping. The ongoing particle shedding was proven by the alteration in morphology of the inner tubing walls after pumping as depicted with SEM and 3D laser scanning microscopy.

Distinct differences in surface morphology were found to be responsible for the different extent of particle shedding from the three analyzed tubing types. In SEM micrographs, all unused tubing revealed a similar platelet-like structure, which might be a result of the extrusion process during tubing production. In contrast, 3D laser scanning microscopy clearly depicted the diversity of the three tubing types in terms of surface texture, thus making this analytical tool an exquisite method for tubing surface characterization. Factors with possible influence on surface texture are extrusion equipment and the composition and features of the extrusion mixture. Surface characteristics cannot

be concluded from the specifications given by the manufacturers who only provide mechanical features like hardness / Shore A, specific gravity, Tear B / tear strength / tear resistance, ultimate tensile strength, and elongation at break. Therefore, analysis of the surface morphology of tubing by the customer can be a helpful additional characterization technique, especially when new tubings are considered, evaluated, and qualified for DP manufacturing. Surface roughness was found to be specific for each tubing type and rather independent of the investigated batches.

With the applied 3D laser scanning microscopy, surface morphology could not only be visualized but also put in numbers via the roughness parameters R_a and R_z . The obtained values were lowest for tubing B and correlated with the lowest extent of particle spallation. It is therefore concluded that the number of shed particles can be minimized by choosing tubing with low R values. Although surface morphology of tubing B changed over pumping time, R values shifted only marginally. The minimally increased R values after 2 and 24 h if WFI was pumped were due to the observed plaque formation via particle deposition. Upon pumping of placebo, such depositions did not occur and R values remained constant (see Figure IV-64c+d). It is assumed that the contained surfactant helped to keep shed particles suspended. In contrast, the higher surface roughness values of unused tubing A and C decreased with increasing pumping time. After 24 hours, roughness values of all three tested tubing types approached the same low R_a and R_z values of approximately $0.6\ \mu\text{m}$ and $5\ \mu\text{m}$, respectively. Similarly, during pumping cycles with online monitoring, turbidity graphs for tubing A and C flattened after several hours and approached a plateau. This indicates that particle shedding due to surface ablation is more pronounced at the start of pumping and diminishes once a certain smoothness of the surface is achieved.

In conclusion, 3D laser scanning microscopy was found to be a valuable and effective tool for surface roughness determination of tubing material. This is the first study that successfully implemented this surface characterization method with regards to biopharmaceutical DP processing materials. The correct cut-off values for the evaluation of the roughness parameters R_a and R_z can be obtained via roughness standards.

For smaller tubing with an ID of 1.6 mm, previous observations in terms of particle characteristics in the recirculates as well as the rank order of initial tubing surface roughness were confirmed. However, endpoint turbidity values were slightly increased for tubing C in comparison to tubing A, and the overall higher increase in turbidity compared to tubing B was less pronounced than with tubing of 6 mm ID. Generally, endpoint turbidity values of recirculates obtained from tubing with an ID of 1.6 mm were lower than those from 6 mm ID tubing. A reduced extent of particle shedding seems to be a logical consequence of the smaller inner tubing surface that is available for particle spallation. After 24 h pumping cycles, surface roughness likewise tended to decrease. Not only smooth areas but also pronounced heterogeneities, especially for tubing B, were microscopically visible on the inner tubing surface. Roughness values after 24 h of pumping were thus slightly higher and more diverse than for the 6 mm ID tubing. Thus smaller tubing appears to be more susceptible to the mechanical stress exerted by the pump. After 24 h, not only surface erosion but possibly also destructive events already started leading to more frequent heterogeneities on the tubing surface.

For tubing with an ID of 6 mm, different batches resulted in a comparable extent of particle shedding. In contrast, the two different batches of tubing A with an ID of 1.6 mm led to distinct variations in turbidity profile, indentation force, and also flow rate reduction. The stiffer batch #1 led to a minor, but steady turbidity increase over time and the lower flow rate of 2.05 mL/min was decreased by 2.8 % on average after the pumping cycle. Indentation forces for batch #2 were lower,

turbidity profiles were characterized by a steep initial increase with a subsequent plateau, and the higher flow rate of 2.2 mg/mL remained unchanged after pumping. According to Colas *et al.*, batch to batch variations appear greater with smaller tubing IDs since smaller defects in the polymer material seem to be more critical here [14].

Differences in indentation forces were also observed for batch #3 of tubing B with 6.0 mm ID, but this did not have a measurable effect on particle shedding. The announced production change regarding the relative composition of the extrusion mixture might encompass an increase in the amount of used fillers like silicon dioxide. This compound leads to higher mechanical strength via interactions with the silicone elastomer molecules [29].

All in all, the mechanical properties of tubings were not found to be the determining factor for particle shedding. Tubing with both high and low propensity towards particle spallation showed comparable mechanical properties initially (A vs. B) as well as rather identical decreases in stiffness after the pumping cycle. Flow rates after pumping were decreased by 2 to 8 % in most cases due to a flattening of the tubing lumen [14]. Such decreases are to be expected and compensated by automatic adjustments of pump settings over the course of the filling process. The lumen deformation and the loss in stiffness demonstrate the strong mechanical stress that the tubing experiences within the pump head. Therefore, silicone tubing is limited in its operation time. However, typically forming part of a disposable concept, the silicone tubing is replaced after each and every filling process anyway.

When it comes to the mechanical stress that is exerted on the tubing material, the choice of a suitable pump head is of utmost importance. Indeed, operating tubing A and B with the Optima pump led to higher turbidity values of WFI recirculates, increased numbers of micrometer-sized particles, and a more frequent occurrence of particle depositions in the tubing lumen. Surface roughness as well as mechanical stiffness of tubing sets after the pumping cycle was comparable for both tested pumps. For different pump heads, the use of a different kind of tubing might thus be recommended.

Initially, it was anticipated that the post-curing step that is included in the manufacturing of tubing B might be responsible for the differences in particle shedding. Post-curing refers to a 4 h curing step at 200°C with high air throughput which is applied after tubing extrusion. The performed TGA analysis resembles the testing for volatile matter of silicone tubing as described by the European Pharmacopeia [39]. Up to 2 % of volatile matter is accepted for platinum-cured silicone tubing, only 0.5 % is acceptable for peroxide-cured tubing. Platinum-cured silicone polymer is produced in the presence of cyclic siloxanes as process aids. These volatile compounds are claimed to remain in the tubing with concentrations of 0.5 to 2 % (w/w), if post-curing is not performed. However, even before the simulated post-curing step mass loss for none of the tested samples was above 0.6 %. Mass losses were slightly reduced after post-curing, but tended to recover upon storage. Consequently, post-curing was not found to have a sustainable lasting effect on mass loss. Likewise, the claimed increase in mechanical strength after a post-curing step could not be confirmed. Post-curing might affect physical properties only if applied directly after the tubing production process. An impact on particle shedding was not observed in our study, but post-curing indeed might improve tubing quality with regards to extractables and leachables. Particle shedding, however, seems to be predominantly influenced by the surface roughness of the tubing.

5 SUMMARY AND CONCLUSION

Particle shedding from silicone tubing upon operation in a peristaltic pump during DP processing cannot be completely avoided but can be minimized. The amount of shed (nano)particles to be expected during production conditions was calculated to be below any detection limit. Nevertheless, when choosing tubing with low surface roughness values – as this parameter was found to correlate with particle shedding – particle shedding can further be minimized.

The use of a new surface analytical technique like surface roughness measurements with 3D laser scanning microscopy can be employed to assess the particle shedding propensity of tubing types with otherwise comparable material characteristics. Pumping cycle experiments, e.g. with online-turbidity monitoring, can be a useful tool to directly evaluate particle shedding and to support evaluation of tubing for biopharmaceutical DP manufacturing. The possible impact of external particle contaminations from tubing shedding on protein stability in the final drug product is addressed in the next chapter.

6 ABBREVIATIONS

CIP/SIP/DIP	cleaning-in-place / sterilization-in-place / drying-in-place
DKD	Deutscher Kalibrierdienst
DLS	dynamic light scattering
DP	drug product
ECD	equivalent circular diameter
ESD	equivalent spherical diameter
FNU	Formazine nephelometric units
ID	inner diameter
JIS	Japan Industrial Standard
λ_c	cutoff wavelength for high-pass filtering
λ_s	cutoff wavelength for low-pass filtering
LO	light obscuration
MFI	micro-flow imaging
NMT	not more than
NTA	nanoparticle tracking analysis
NTU	nephelometric turbidity unit
PdI	polydispersity index
R_a	arithmetic mean roughness
rpm	revolutions per minute
RSD	relative standard deviation
RT	room temperature
R_z	maximum height
SD	standard deviation
SEM	scanning electron microscopy
TGA	thermogravimetric analysis
Wfi	water for injection

7 REFERENCES

- [1] M.E.M. Cromwell, E. Hilario, F. Jacobson, Protein aggregation and bioprocessing., *AAPS J.* 8 (2006) E572–579.
- [2] C.R. Thomas, D. Geer, Effects of shear on proteins in solution., *Biotechnol. Lett.* 33 (2011) 443–456.
- [3] A. Nayak, J. Colandene, V. Bradford, M. Perkins, Characterization of subvisible particle formation during the filling pump operation of a monoclonal antibody solution, *J. Pharm. Sci.* 100 (2011) 4198–4204.
- [4] T.W. Randolph, J.F. Carpenter, Engineering challenges of protein formulations, *AIChE J.* 53 (2007) 1902–1907.
- [5] S. Zöls, R. Tantipolphan, M. Wiggenghorn, G. Winter, W. Jiskoot, W. Friess, et al., Particles in therapeutic protein formulations, Part 1: overview of analytical methods., *J Pharm Sci.* 101 (2012) 914–935.
- [6] A.K. Tyagi, T.W. Randolph, A. Dong, K.M. Maloney, C. Hitscherich, J.F. Carpenter, IgG particle formation during filling pump operation: a case study of heterogeneous nucleation on stainless steel nanoparticles., *J. Pharm. Sci.* 98 (2009) 94–104.
- [7] J.S. Bee, D. Chiu, S. Sawicki, J.L. Stevenson, K. Chatterjee, E. Freund, et al., Monoclonal antibody interactions with micro- and nanoparticles: adsorption, aggregation, and accelerated stress studies, *J. Pharm. Sci.* 98 (2009) 3218–38.
- [8] J.F. Carpenter, T.W. Randolph, W. Jiskoot, D.J.A. Crommelin, C.R. Middaugh, G. Winter, et al., Overlooking subvisible particles in therapeutic protein products: gaps that may compromise product quality., *J. Pharm. Sci.* 98 (2009) 1201–5.
- [9] S.K. Singh, N. Afonina, M. Awwad, K. Bechtold-Peters, J.T. Blue, D. Chou, et al., An industry perspective on the monitoring of subvisible particles as a quality attribute for protein therapeutics., *J. Pharm. Sci.* 99 (2010) 3302–21.
- [10] L. Doessegger, H.-C. Mahler, P. Szczesny, H. Rockstroh, G. Kallmeyer, A. Langenkamp, et al., The potential clinical relevance of visible particles in parenteral drugs., *J. Pharm. Sci.* 101 (2012) 2635–44.
- [11] U.J. Bausch, Impact of Filling Processes on Protein Solutions, PhD thesis, Universität Basel, Switzerland, 2008.
- [12] S.N. Denking, Modelle zur Simulation des Abfüllprozesses biologisch-pharmazeutischer Arzneimittel, PhD thesis, Rheinische Friedrich-Wilhelms-Universität Bonn, Germany, 2010.
- [13] W.G. Whitford, Single-Use Systems As Principal Components in Bioproduction, *Bioprocess Int.* 8 (2010) 34–42.
- [14] A. Colas, R. Malczewski, K. Ulman, Silicone tubing for pharmaceutical processing, *PharmaChem.* (2004) 30–36.

-
- [15] A. Colas, J. Curtis, Silicone biomaterials: history and chemistry, in: B.D. Ratner, A.S. Hoffman, F.J. Schoen, J.E. Lemons (Eds.), *Biomaterials Science: An Introduction to Materials in Medicine*, 2nd ed., Elsevier Academic Press, San Diego, USA, 2004: pp. 80–86.
- [16] J. Bommer, E. Pernicka, J. Kessler, E. Ritz, Reduction of silicone particle release during haemodialysis., *Proc. Eur. Dial. Transplant Assoc. Eur. Ren. Assoc.* 21 (1985) 287–90.
- [17] J.C. Briceño, T.M. Runge, Tubing spallation in extracorporeal circuits. An in vitro study using an electronic particle counter., *Int. J. Artif. Organs.* 15 (1992) 222–8.
- [18] A.S. Leong, D.W. Gove, Pathological findings in silicone spallation in vitro studies., *Pathology.* 15 (1983) 189–92.
- [19] D. Barron, S. Harbottle, N.A. Hoenich, A.R. Morley, D. Appleton, J.F. McCabe, Particle Spallation Induced by Blood Pumps in Hemodialysis Tubing Sets, *Artif. Organs.* 10 (1986) 226–235.
- [20] P.A. Dewan, A.J. Owen, P.J. Ashwood, J. Terlet, R.W. Byard, An in vitro study of silicone migration from intravenous fluid tubing, *Pediatr. Surg. Int.* 12 (1996) 49–53.
- [21] M. Kurusz, Roller pump induced tubing wear: another argument in favor of arterial line filtration, *JECT.* (1980) 49–59.
- [22] W.G. Kim, C.J. Yoon, Roller pump induced tubing wear of polyvinylchloride and silicone rubber tubing: phase contrast and scanning electron microscopic studies., *Artif. Organs.* 22 (1998) 892–7.
- [23] A.S. Leong, A.P. Disney, D.W. Gove, Spallation and migration of silicone from blood-pump tubing in patients on hemodialysis., *N. Engl. J. Med.* 306 (1982) 135–40.
- [24] J. Curtis, A. Colas, Medical Applications of Silicones, in: B.D. Ratner, A.S. Hoffman, F.J. Schoen, J.E. Lemons (Eds.), *Biomaterials Science: An Introduction to Materials in Medicine*, 2nd ed., Elsevier Academic Press, San Diego, USA, 2004: pp. 697–707.
- [25] S.M. Bahal, J.M. Romansky, Spalling and sorption of tubing for peristaltic pumps., *Pharm. Dev. Technol.* 7 (2002) 317–23.
- [26] M. Kaszuba, D. McKnight, M.T. Connah, F.K. McNeil-Watson, U. Nobbmann, Measuring sub nanometre sizes using dynamic light scattering, *J. Nanoparticle Res.* 10 (2007) 823–829.
- [27] V. Filipe, A. Hawe, W. Jiskoot, Critical evaluation of Nanoparticle Tracking Analysis (NTA) by NanoSight for the measurement of nanoparticles and protein aggregates., *Pharm. Res.* 27 (2010) 796–810.
- [28] S. Zölls, D. Weinbuch, M. Wiggernhorn, G. Winter, W. Friess, W. Jiskoot, et al., Flow imaging microscopy for protein particle analysis - a comparative evaluation of four different analytical instruments, *AAPS J.* 15 (2013) 1200–11.
- [29] R. Rößler, 3.1.9 Silicon-Elastomer für Verschlüsse und Schläuche, in: *Arzneibuch-Kommentar*, Wissenschaftliche Verlagsgesellschaft Stuttgart / Govi-Verlag, Pharmazeutischer Verlag GmbH, Eschborn, 2004.

- [30] A.J.J. O'Lenick, Chapter 24: Methods in Silicone Chemistry, in: Angela C. Kozlowski (Ed.), *Silicones for Personal Care*, 2nd ed., Allured Publishing Corporation, Carol Stream, USA, 2008: pp. 371–386.
- [31] G. Peinhardt, *Simeticon* (Monographie), in: *Arzneibuch-Kommentar*, Wissenschaftliche Verlagsgesellschaft Stuttgart / Govi-Verlag, Pharmazeutischer Verlag GmbH, Eschborn, 2014.
- [32] T. Mundry, *Einbrennsilikonisierung bei pharmazeutischen Glaspackmitteln - Analytische Studien eines Produktionsprozesses*, PhD thesis, Humboldt-Universität Berlin, Germany, 1999.
- [33] Y. Gu, D. Li, The zeta-Potential of Silicone Oil Droplets Dispersed in Aqueous Solutions., *J. Colloid Interface Sci.* 206 (1998) 346–349.
- [34] DIN EN ISO 3274:1998. Geometrische Produktspezifikationen (GPS) - Oberflächenbeschaffenheit: Tastschnittverfahren - Nenneigenschaften von Tastschnittgeräten (ISO 3274:1996).
- [35] DIN EN ISO 4288:1998. Geometrische Produktspezifikation (GPS) - Oberflächenbeschaffenheit: Tastschnittverfahren - Regeln und Verfahren für die Beurteilung der Oberflächenbeschaffenheit (ISO 4288:1996).
- [36] E. Gautriaud, K. Stafford, J. Adamchuk, M.W. Simon, D.L. Ou, Effect of Sterilization on the Mechanical Properties of Silicone Rubbers. Available online at: <http://www.biopharm.saint-gobain.com/en/products/WhitePapers/White Paper - Effect 2D2876.pdf> (accessed December 1, 2014).
- [37] R. Strehl, V. Rombach-Riegraf, M. Diez, K. Egodage, M. Bluemel, M. Jeschke, et al., Discrimination Between Silicone Oil Droplets and Protein Aggregates in Biopharmaceuticals: A Novel Multiparametric Image Filter for Sub-visible Particles in Microflow Imaging Analysis., *Pharm. Res.* 29 (2011) 594–602.
- [38] D.K. Sharma, D. King, P. Oma, C. Merchant, Micro-flow imaging: flow microscopy applied to sub-visible particulate analysis in protein formulations., *AAPS J.* 12 (2010) 455–64.
- [39] European Directorate for the Quality of Medicine (EDQM), 3.1.9 Silicon-Elastomer für Verschlüsse und Schläuche, in: *European Pharmacopoeia*, 8th ed., 2014: pp. 541–542.

INFLUENCE OF PARTICLE SHEDDING FROM SILICONE TUBING ON ANTIBODY STABILITY

ABSTRACT

Rotary piston pumps but also peristaltic pumps that are commonly employed during fill & finish operations of a biopharmaceutical drug may shed particles into the final product. It was the aim of this study to elucidate the potential influence of silicone particles shed from peristaltic pump tubing on the stability of a drug product. Therefore, two formulated antibodies were spiked with two realistic, but worst-case levels of particles and a 6-month accelerated stability study at 2-8°, 25°, and 40°C was conducted. Both mAbs revealed instabilities in terms of protein aggregation and fragmentation in SEC analysis. These instabilities were independent of the presence and the amount of spiked-in particles. Monitoring of turbidity, subvisible, and visible particles did not uncover any additional mAb particle formation. An increase in MFI particle counts for one the mAb formulations containing shed particles could be attributed to the limited colloidal stability of shed particles in this composition as indicated by a similar increase in placebo. In conclusion, shed silicone particles from peristaltic pump tubing are assumed to not impair DP stability.

The following chapter is intended for publication.

1 INTRODUCTION

The use of peristaltic pumps in fill & finish operations of a biopharmaceutical drug product (DP) complies with the emerging disposables concept. Furthermore, this type of pump is often preferred over rotary piston pumps, especially for the filling of shear-sensitive therapeutic proteins [1]. It was shown that the formation of proteinaceous particles is enhanced in rotary piston pumps [2]. Additionally, rotary piston pumps may shed stainless-steel particles that also end up in the final product [3]. However, previous studies revealed that silicone tubing operated in a peristaltic pump may also lead to particle shedding, although to a rather limited extent [4].

Several studies indicate that (external) particle contamination might induce protein instability by acting as aggregation seed and / or adsorption interface [5]. Bee *et al.* [6] tested the influence of micro- and nanoparticles made from various potential processing materials like glass, iron(III)oxide, silica, alumina, titania, cellulose, and stainless steel on the aggregation behavior of a monoclonal antibody (IgG1) and found that the addition of stainless steel microparticles caused mAb aggregation. However, the number of spiked-in particles was about 10^6 times higher than expected for an actual product. Tyagi and coworkers [3] focused on the influence of stainless steel nanoparticles shed from rotary piston pumps on the stability of an IgG and propose that these particles serve as heterogeneous nuclei for the formation of protein microparticles. But not only pumps can be a source for shed particles. In a study by Liu *et al.* [7], filters were identified as processing units that can introduce foreign micro- and nanoparticles to a DP solution. Increased particle formation during agitation of keratinocyte growth factor 2 solutions after filtration with polyether sulfone membranes was observed. More often, the impact of silicone oil droplets on the stability of therapeutic proteins was investigated. Silicone oil droplets in a formulation can originate from siliconized stoppers or syringe barrels. In this context, Thirumangalathu *et al.* [8] conducted an “accelerated degradation” study by adding 1.5 % (w/v) silicone oil to a model antibody with subsequent isothermal storage. Only upon agitation with at least 350 rpm, mAb aggregation was observed. Aggregation could be completely inhibited by the presence of 0.1 % (w/v) polysorbate 20. Similarly, Jones *et al.* [9] observed silicone oil induced aggregation of four proteins with various molecular weights and isoelectric points in the presence of 0.5 % (w/v) silicone oil under gentle horizontal shaking in a multi-well plate. Distinct conformational changes or alterations in the thermal stability of the proteins were not detected. In contrast, Britt *et al.* [10] found a significantly perturbed tertiary structure for three model antibodies when adsorbed to silicone oil droplets. However, aggregation or precipitation of the antibodies was not observed. Correspondingly, Li *et al.* [11] did not see abatacept aggregation in the presence of silicone oil when stored at RT. Only at 40°C a slight increase in aggregate levels occurred, which could be prevented by adding polysorbate 80.

Depending on the chosen experimental setup including storage mode (agitated, non-agitated), storage temperature, type of particles spiked-in as well as their spiking level and of course the chosen model protein, instabilities in the presence of added particles might occur. The possible influence of particles shed from silicone tubing during peristaltic pumping on the stability of two IgGs was assessed in this study. After particle preparation via placebo buffer recirculation, particles were characterized and spiked to the mAb formulations at worst-case, but realistic spiking levels. A 6-months stability study with quiescent storage at 2-8°, 25°, and 40°C was conducted and protein aggregates, turbidity, as well as visible and subvisible particles were monitored. The mAb formulations used in this study were representative for standard protein formulations used in clinical trials and on the market, including stabilizers such as sugar and surfactants.

2 MATERIALS AND METHODS

2.1 Materials

2.1.1 Chemicals

Histidine, histidine-hydrochloride monohydrate as well as methionine were purchased from Ajinomoto (Louvain-la-Neuve, Belgium), sucrose and trehalose were from Ferro Pfanstiehl (Waukegan, IL, USA). Polysorbate 20 was obtained from Croda GmbH (Nettetal, Germany), Poloxamer 188 was received from BASF (Ludwigshafen, Germany). HP-SEC buffer compounds included KH_2PO_4 (Sigma-Aldrich, St. Louis, MO, USA), KH_2PO_4 and KCl (both from Acros Organics, Thermo Fisher Scientific, Geel, Belgium).

2.1.2 Silicone Tubing

The employed platinum-cured silicone tubing with an ID of 6.0 mm is commercially available (type A as described in previous chapters). Tubing sets were prepared and rinsed as described earlier [4] and subsequently autoclaved at 121°C and 2 bar for 15 minutes.

2.1.3 Model Antibodies

The monoclonal IgG1 antibody solutions mAb1 at 25 mg/mL and mAb2 at 150 mg/mL were filtered using 0.22 μm Sterivex™-GV filters in combination with a Sterivex™-HV 0.45 μm pre-filter unit (Millipore, Billerica, Massachusetts, USA) prior to use. mAb1 was formulated in 20 mM histidine buffer at pH 5.5 with 240 mM sucrose, 10 mM methionine, and 0.02 % PS 20. The mAb2 formulation contained 20 mM histidine buffer pH 5.5 with 200 mM trehalose and 0.04 % Poloxamer 188. Placebo buffers were prepared using deionised water and sterile filtrated using Stericups (0.22 μm PVDF, Millipore).

2.1.4 Packaging Material

Samples were stored in 6 mL colorless glass vials (Schott AG, Mainz, Germany). Filled vials were closed with teflon-coated serum stoppers (Daikyo Seiko, Ltd., Tokyo, Japan) and crimped using aluminum caps with PP-cap (Helvoet Pharma Deutschland GmbH, Karlsbad, Germany).

2.2 Methods

2.2.1 Preparation of Recirculates

Recirculates containing particles shed from peristaltic silicone tubing were prepared as described earlier [4]. Autoclaved tubing sets were operated in a Flexicon PD 12 peristaltic pump. 100 mL of the respective placebo buffer were recirculated for 2 h in dispense mode (2800 fillings à 5 mL). Every aliquot of placebo buffer thus passed the pump 140 times (concentration factor = $2800 \cdot 5 \text{ mL} / 100 \text{ mL} = 140$) and recirculates represent a 140x concentrated particle suspension in comparison to non-recirculating conditions during actual filling.

2.2.2 Sample Preparation and Stability Study

Sample preparation was performed under a laminar flow cabinet. Both mAbs were spiked with the corresponding recirculates at two spiking levels (140:1 and 280:1). The “high” spiking level of 140:1

represents a 1x concentrated particle suspension obtained by diluting the 140x concentrated recirculate. This particle level is expected for drug product units that are filled during the first hours of the filling cycle. An earlier study revealed a flattening of turbidity monitoring graphs with increasing recirculation time (after approx. 8 hours) indicating that with time of use less additional particles are worn away from the tubing [4]. Therefore, the “low” spiking level of 280:1 was chosen due to the reduced extent of particle shedding expected for these later time points during the filling process. The concentration of shed particles in the “high” spiking level samples was thus twice as high as for the “low” spiking level samples. Control solutions included antibody formulations spiked with placebo buffer (140:1, ‘IgG blank’) and placebos spiked with recirculate (140:1, ‘Particle blank’). All solutions were prepared in glass beakers and homogenized via gentle rotation for 30 seconds. Aliquots of 2.4 mL were filled into 6R glass vials using 25 mL Eppendorf biopur Combitips (Eppendorf AG, Hamburg, Germany) and stored upright at 2-8°C, 25°C, and 40°C for up to 6 months without applying agitation.

2.2.3 Visual Inspection

Visual inspection was carried out under a polarized light inspection device (Optima pharma GmbH, Schwäbisch Hall, Germany) as well as with the semi-automatic inspection device Seidenader V90-T (Seidenader Maschinenbau GmbH, Markt Schwaben, Germany) with automated container spin at 20 % rotation speed.

2.2.4 Turbidity

Under a laminar flow cabinet, 2 mL sample aliquots were transferred into round glass cuvettes. Turbidity in FTU was measured using a HACH 2100AN turbidimeter (HACH LANGE GmbH, Düsseldorf, Germany).

2.2.5 Subvisible Particle Analysis

Subvisible particle analysis was performed via light obscuration (LO) with a HIAC/Royco Model 9703+ particle counter (Beckman Coulter Life Sciences, Brea, CA, USA). Particle counts for three aliquots of 0.4 mL were determined. Results are given as average values from run two and three.

Additionally, subvisible particles were characterized using micro-flow imaging (MFI) with a DPA4200 Flow Microscope from Brightwell Technologies Inc. (Ottawa, Canada). Illumination optimization was performed with particle-free water or filtered mAb formulation (0.22 µm Millex®-GV, Millipore) in the case of particle blank samples or samples containing mAb, respectively. The purge volume was 0.20 mL and the analyzed sample volume was set to 0.60 mL at a flow rate of 0.17 mL/min (set point 3). Two vials per sample were pooled and analyzed in triplicates. Results are given as mean values with standard deviations. Only particles > 5 µm in size were considered for morphological evaluation.

Performance of both instruments was checked with commercially available 5 µm particle size and count standards (Thermo Fisher Scientific Inc., Waltham, MA, USA) prior to every use.

2.2.6 High Performance Size Exclusion Chromatography (HP-SEC)

The relative amount of monomer, aggregates, and fragments was determined with HP-SEC with a TSKgel G3000SWXL column (Tosoh Bioscience GmbH, Stuttgart, Germany) operated in a Waters 2695 Alliance Separations Module (Waters Corporation, Milford, MA, USA) with UV detection at 280 nm. Samples were diluted to a protein concentration of 10.0 mg/mL using the corresponding placebo

buffer. The mobile phase consisted of 200 mM potassium phosphate buffer pH 7.0 with 250 mM potassium chloride. Injection volume was 15 μ L and flow rate was set to 0.5 mL/min. The autosampler was cooled to 5°C, whereas the column oven temperature was 25°C.

2.2.7 Dynamic Light Scattering (DLS)

Particle characterization in the nanometer range was performed by dynamic light scattering using the Zetasizer Nano-ZS (Malvern Instruments Ltd., Herrenberg, Germany). The undiluted, neither filtered nor centrifuged samples were measured in disposable Plastibrand semi-micro PMMA cuvettes (Brand GmbH, Wertheim, Germany) at a backward scatter of 173° after 20 seconds equilibration time at 25°C and with water as dispersant (viscosity of 0.8872 mPa·s). Positioning, attenuation selection and measurement duration as well as number of sub runs for the three performed measurements per sample were optimized automatically for each run by the Zetasizer Software 6.32. Z-average and polydispersity index (Pdl) were calculated applying the 'General purpose (normal resolution)' analysis model.

2.2.8 Nanoparticle Tracking Analysis (NTA)

Nanoparticle tracking analysis was performed with a NanoSight LM20 system with a 488 nm laser and NS200 camera type using NTA software version 2.3 (NanoSight Ltd., Salisbury, UK). The measuring cell was cleaned with particle-free water (filtered through a 0.02 μ m filter, Anotop 2, Whatman) and flushed with 1 mL of sample prior to analysis (n=3). Shutter (ca. 900 for formulation 1, ca. 500 for formulation 2) and gain (ca. 260 for formulation 1, ca. 330 for formulation 2) as well as focus were adjusted manually for each recirculate and the same settings were applied to the corresponding placebo blanks. Capture duration was set to 60 seconds and measurements were performed at RT. Analysis of undiluted samples was performed with background extraction, a minimum track length of 10 and an automatically set minimum expected particle size. Detection threshold was set to 10 and blur was chosen to be 5x5 after manual optimization.

2.2.9 Leachable Analysis via GC-MS

After stir bar sorptive extraction ("Twister", Gerstel GmbH & Co. KG, Mülheim an der Ruhr, Germany) for 60 minutes at 800 rpm, leachables analysis after thermal desorption (Gerstel TDS 3) was carried out on an Agilent 6890 gas chromatograph equipped with a DB-1MS column (J&W Scientific, Folsom, CA, USA). An Agilent 5975 mass spectrometer was used as detector (Agilent Technologies GmbH, Boeblingen, Germany). For quantification purposes, the two reference substances tetrahydrofurfuryl methacrylate and di-pentyl-phthalate were used as internal standards.

2.2.10 3D Laser Scanning Microscopy

Surface roughness of inner tubing walls was visualized using the 3D laser scanning microscope Keyence VK-X210 with a CF Plan 20x objective (Keyence GmbH, Neu-Isenburg, Germany). With a scalpel, tubing pieces were cut into thin strips and placed under the microscope with horizontal flow direction. For every sample, micrographs were captured with VK Viewer software in 'Easy Mode' at eight different sections. All of the analyzed areas of used tubing had been located inside the pump head during the pumping cycle. The roughness parameters arithmetic mean roughness R_a and maximum height R_z were calculated according to the JIS standard B0601:2001 in the multi-line roughness mode with VK Analyzer Plus software version 3.3.0.0 from an average of $2n+1$ horizontal lines with $n=30$ and 10 skipped lines in-between. Tubing curvature was corrected via the 'correct tilt

– sec curved surf. (auto)' function. Cutoff values of $\lambda_c = 2.5 \text{ mm}$ and $\lambda_s = 8 \text{ }\mu\text{m}$ were applied. Roughness values are stated as mean values (n=8) with standard deviations.

3 RESULTS

3.1 Recirculate Characterization

3.1.1 Particle Characterization

Using LO and MFI, the number of particles in the micrometer range of the recirculates was analyzed (Table V-30). The particle counts $\geq 2 \text{ }\mu\text{m}$ obtained with LO were below 100 for both recirculates and blanks. For placebo 1 no significant increase in the number of micrometer-sized particles after recirculation was observed. A trend to a slight increase of the number of particles in the 2 to 10 μm range after recirculation could be identified for placebo 2. Clearly more particles could be identified with MFI. After recirculation, a ten- and fivefold increase in particle counts $\geq 1 \text{ }\mu\text{m}$ was measured for placebo 1 and 2, respectively. The increase of the number of particles became less pronounced with larger size. MFI pictures did not reveal a well-defined morphology of the particles (Figure V-72). Rather blurry pictures were obtained due to the small size of the particles; a spherical and rather transparent morphology can be anticipated.

Table V-30: Subvisible particle counts per mL of recirculates and corresponding blanks.

Method	Size range	Placebo 1		Placebo 2	
		Recirculate	Blank	Recirculate	Blank
LO (#/mL)	$\geq 2 \text{ }\mu\text{m}$	82 ± 31	61 ± 68	55 ± 12	10 ± 11
	$\geq 5 \text{ }\mu\text{m}$	14 ± 0	14 ± 18	9 ± 3	2 ± 2
	$\geq 10 \text{ }\mu\text{m}$	3 ± 2	1 ± 2	0 ± 1	0 ± 1
	$\geq 25 \text{ }\mu\text{m}$	0 ± 0	0 ± 0	0 ± 0	0 ± 1
MFI (#/mL)	$\geq 1 \text{ }\mu\text{m}$	2456 ± 672	243 ± 102	2751 ± 383	567 ± 132
	$\geq 2 \text{ }\mu\text{m}$	484 ± 224	69 ± 27	297 ± 66	104 ± 12
	$\geq 5 \text{ }\mu\text{m}$	93 ± 52	12 ± 6	30 ± 14	19 ± 7
	$\geq 10 \text{ }\mu\text{m}$	23 ± 23	1 ± 1	4 ± 3	7 ± 2
	$\geq 25 \text{ }\mu\text{m}$	3 ± 3	0 ± 0	0 ± 0	0 ± 0

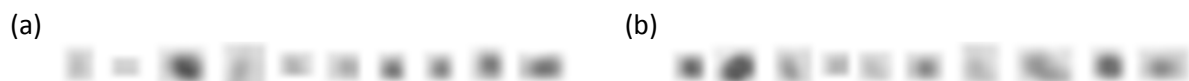
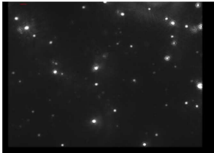



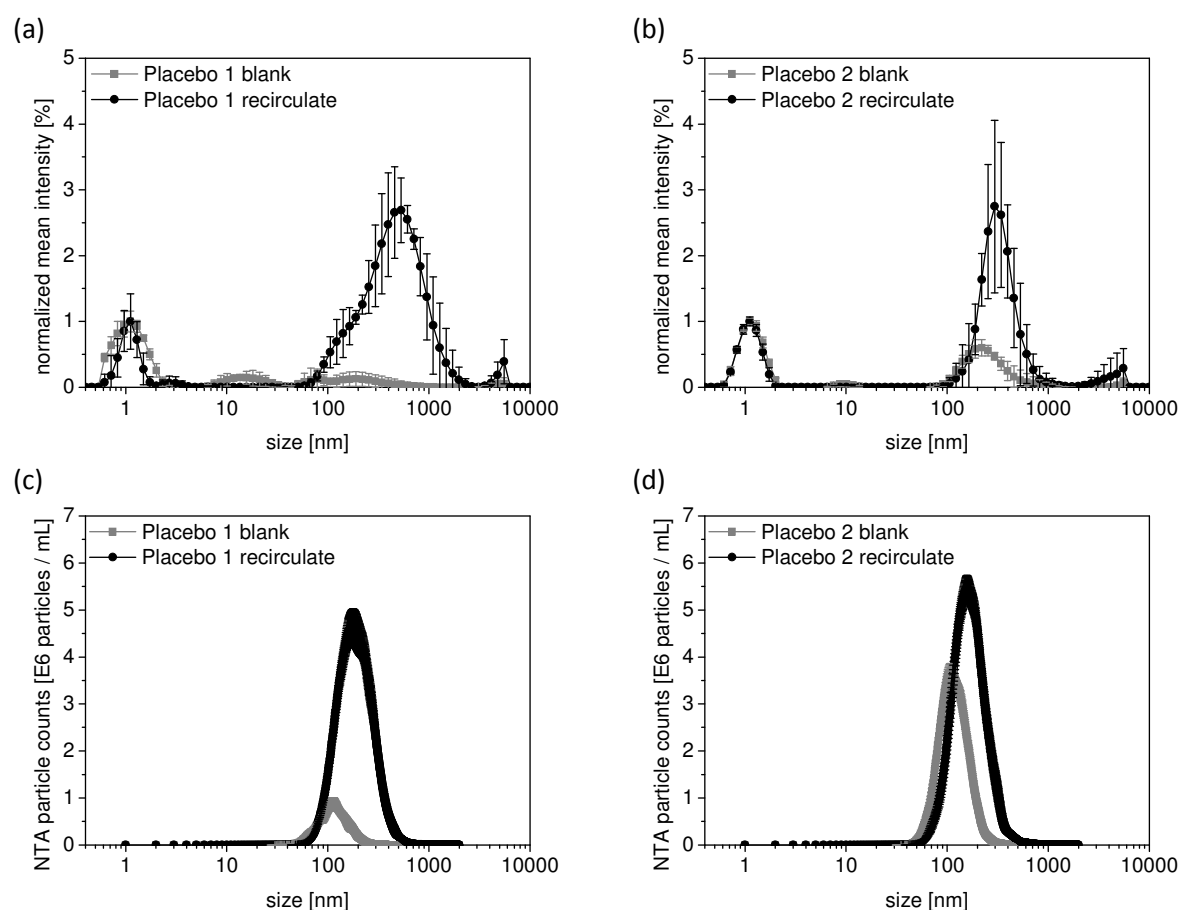


Figure V-72: Morphology of particles in recirculates of (a) placebo 1 and (b) placebo 2. Zoom: 700%.

Table V-31: Turbidity, DLS and NTA characteristics of recirculates and corresponding blanks.

Method / Parameter		Placebo 1		Placebo 2	
		Recirculate	Blank	Recirculate	Blank
Turbidity (FNU)		1.13 ± 0.05	0.112 ± 0.038	0.631 ± 0.013	0.097 ± 0.007
DLS	Z-Average (nm)	302.2 ± 19.4	63.9 ± 84.3	245.0 ± 30.8	58.5 ± 54.3
	PdI	0.563 ± 0.031	0.303 ± 0.102	0.645 ± 0.203	0.546 ± 0.310
NTA	Counts/mL	9.41 ± 0.37 E8	0.80 ± 0.06 E8	8.74 ± 0.27 E8	3.60 ± 0.06 E8
Representative image from analyzed video					
Mean (nm)		235 ± 5.2	134 ± 5.5	205 ± 6.3	135 ± 2.9
Mode (nm)		183 ± 9.0	114 ± 6.7	165 ± 9.4	117 ± 6.0


Figure V-73: Particle size distributions of recirculates and corresponding blanks obtained with DLS (a+b) and NTA (c+d).

Turbidity values as an indicator for the amount of shed particles after recirculation were increased by a factor of 10 and 6.5 for placebo 1 and 2, respectively (Table V-31). Evaluation of DLS data via Z-average and PdI values added limited value to the characterization of the recirculates due to excipient peaks that were already present in the corresponding placebos [12,13]. From the size distribution graphs (Figure V-73a+b), the appearance of a distinct peak at around 300 to 500 nm

became obvious after recirculation. Likewise, NTA size distribution graphs revealed an increased peak at around 200 nm after recirculation (Figure V-73c+d) and also particle counts in the nanometer range were strongly increased in comparison to the particle counts for the placebo blanks (Table V-31). Final NTA particle counts of both recirculates were comparable, however, the increase in particle counts in comparison to the blanks was more pronounced for placebo 1 (12-fold) than for placebo 2 (2.4-fold).

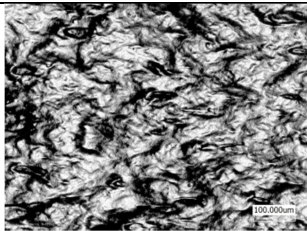
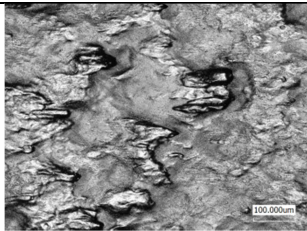
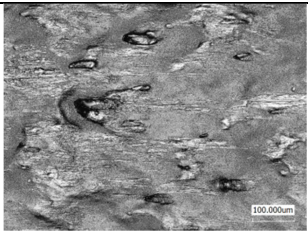
3.1.2 Leachables Analysis

Since leachables also might have a negative effect on the stability of the two antibodies, the amount of possibly present leachables in the recirculates was measured using GC-MS. In both recirculates only one compound, namely 1,2-diacetin, was found at a concentration of 0.06 ppm, close to the reporting threshold of 0.05 ppm. At a leachable concentration of 0.05 ppm, the daily uptake would have to be more than 30 mL in order to exceed the maximally allowed default value of 1.5 µg per day (derived from the ICH M7 Guideline [14]). Due to the applied spiking procedure, the actual leachable level in the samples designed for stability testing was further reduced by a factor of 140 or even 280.

3.1.3 Surface Roughness of Tubing

Tubing surface roughness was evaluated as a proof for the ongoing shedding of particles from the inner tubing wall. After pumping, tubing morphology appeared smoother than initially and the roughness values R_a and R_z were decreased (Table V-32).

Table V-32: Evaluation of surface roughness of used tubing sets before and after the pumping cycle.

Parameter	Initial	After pumping of placebo 1	After pumping of placebo 2
Morphology			
R_a [µm]	3.88 ± 0.33	3.31 ± 0.44	3.36 ± 0.45
R_z [µm]	28.3 ± 4.5	20.0 ± 3.0	19.1 ± 2.2

3.2 Stability Data

The above described recirculates were spiked to the antibody formulations at two different levels. As control, the 'IgG blank' samples contained mAb solution spiked with placebo blank, whereas the 'Particle blank' samples represented a 1:140 dilution of recirculates with the corresponding placebo blank.

3.2.1 Monomer Content

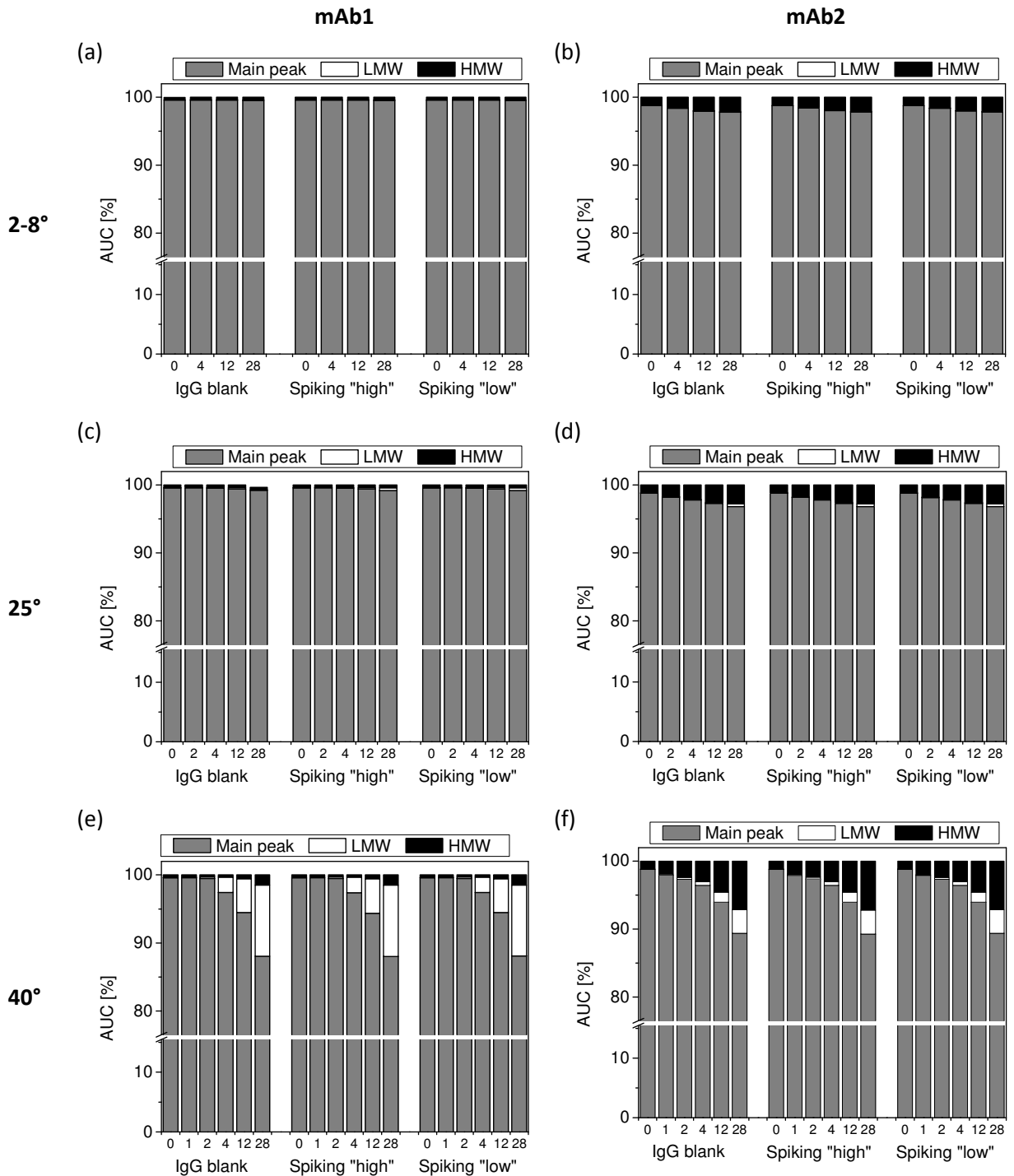


Figure V-74: HP-SEC stability data on monomer (=main peak, including not separated LMW1 fraction in the case of mAb2), fragment (LMW=low molecular weight species) and aggregate (HMW=high molecular weight species) content of mAb1 and mAb2 samples stored at 2-8°, 25° and 40°C.

With both mAbs, the main peak area representing monomer markedly decreased over 28 weeks of storage at 40°C. Samples of mAb1 elicited only minor instability upon storage at 25°C, whereas at 2-8°C storage the monomer content did not change. In contrast, mAb2 samples revealed distinct decreases in the monomer content already during storage at 2-8° and 25°C. The decrease in monomer content was comparable for all samples of each specific mAb and therefore independent of the presence and the amount of spiked-in particles.

Representative SEC chromatograms are shown in Figure V-75. For mAb1, a small shoulder at the longer retention time flank of the main peak arose during storage at 25°C and also a second fragment peak at 20 minutes retention time evolved. Storage at 40°C led to significantly higher fragment peaks. The peak at 13.5 minutes arising from mAb aggregates was only slightly increased after storage at 40°C. The main peak content for mAb2 includes the signal from the first fragment peak as a shoulder of the monomer peak. Only after 28 weeks at 40°C, this first LMW fraction formed a discrete peak. Other than for mAb1, the aggregation peak of mAb2 at around 13 minutes retention time substantially increased during storage at 25° and 40°C.

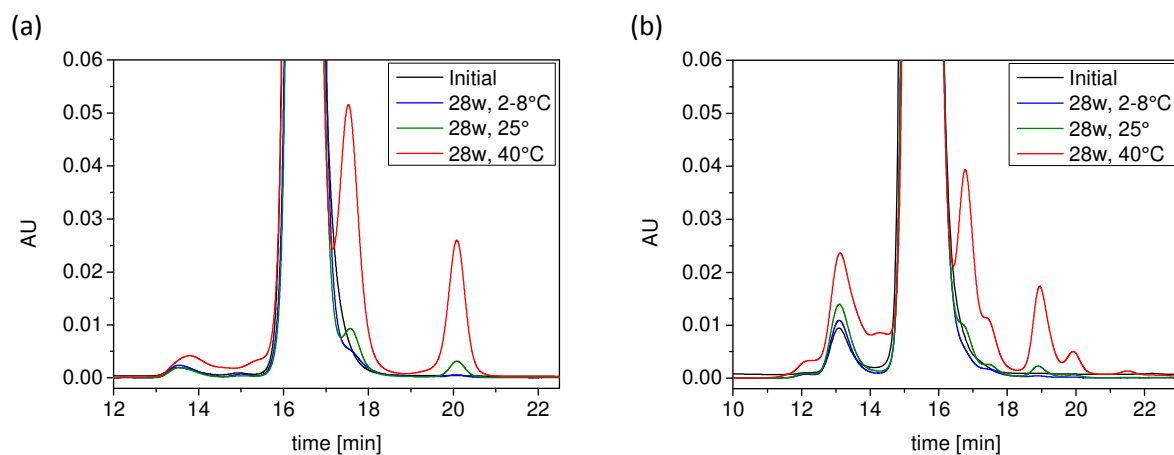


Figure V-75: Representative HP-SEC chromatograms for IgG blank samples of (a) mAb1 and (b) mAb2. Corresponding chromatograms for the two spiking levels „high“ and “low” were identical.

3.2.2 Turbidity Data

Turbidity was monitored as an indicator for particle formation (Figure V-76). For mAb1 samples (25 mg/mL protein), all turbidity values were around 4 FTU. For the higher concentrated mAb2 formulations (150 mg/mL) values of around 5 FTU were obtained. Only for mAb2 samples stored at 40°C a slight tendency towards increasing turbidity values with increasing storage time might be anticipated. Turbidity of the ‘particle blank’ samples that did not contain any protein was below 0.2 FTU in any case.

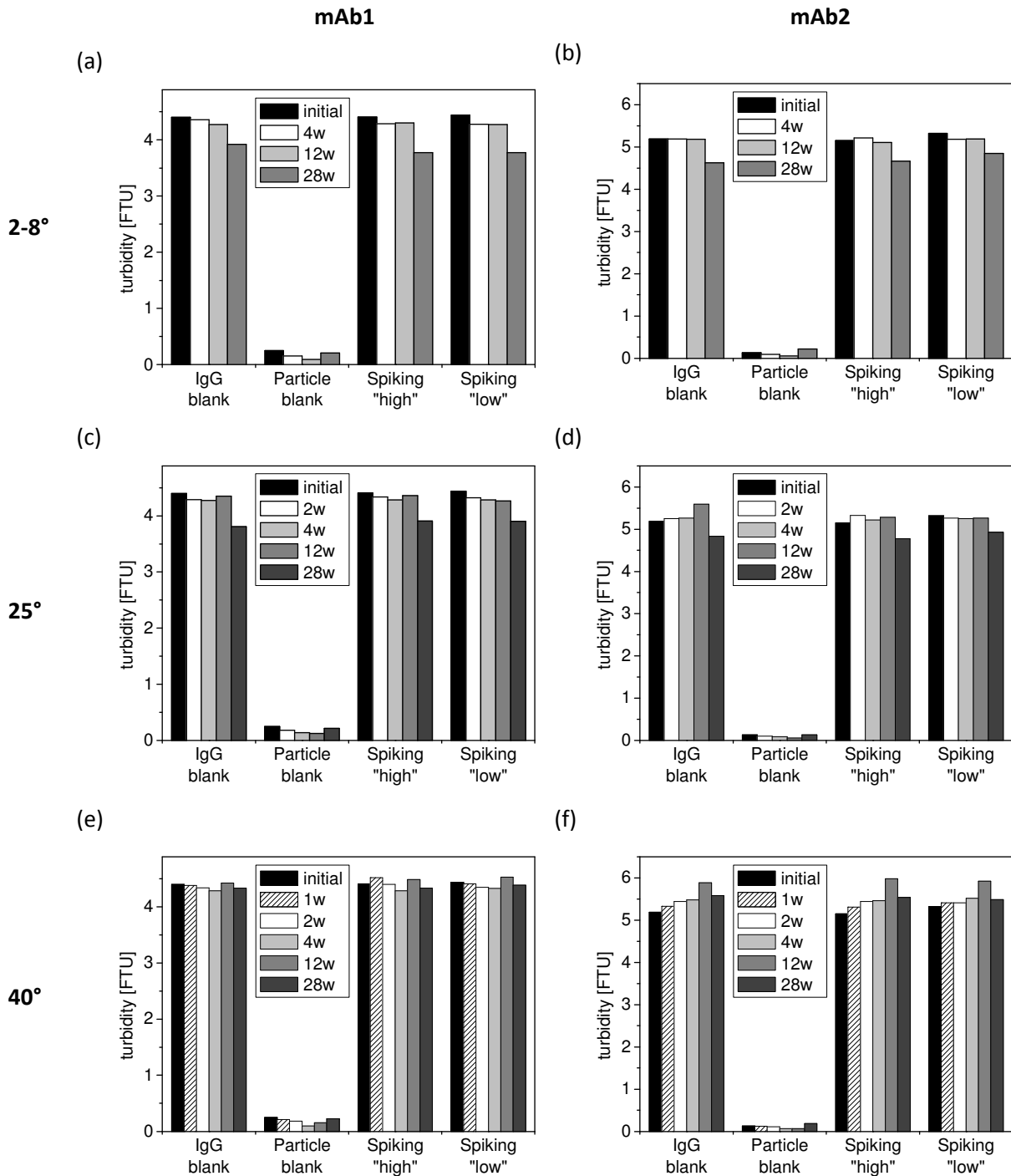


Figure V-76: Turbidity data obtained for mAb1 and mAb2 samples stored at 2-8°, 25° and 40°C.

3.2.3 Subvisible Particle Levels

Particle counts $\geq 2 \mu\text{m}$ per mL obtained with light obscuration were below 1,000 for mAb1 samples and on average below 400 for mAb2 samples. Considering the overall variations in particle counts, particle counts were found to stay constant over the maximum storage time of 28 weeks (Table V-33 and Table V-34 in the Appendix). Clear changes in the LO particle size distributions over storage time could not be identified (Figure V-77).

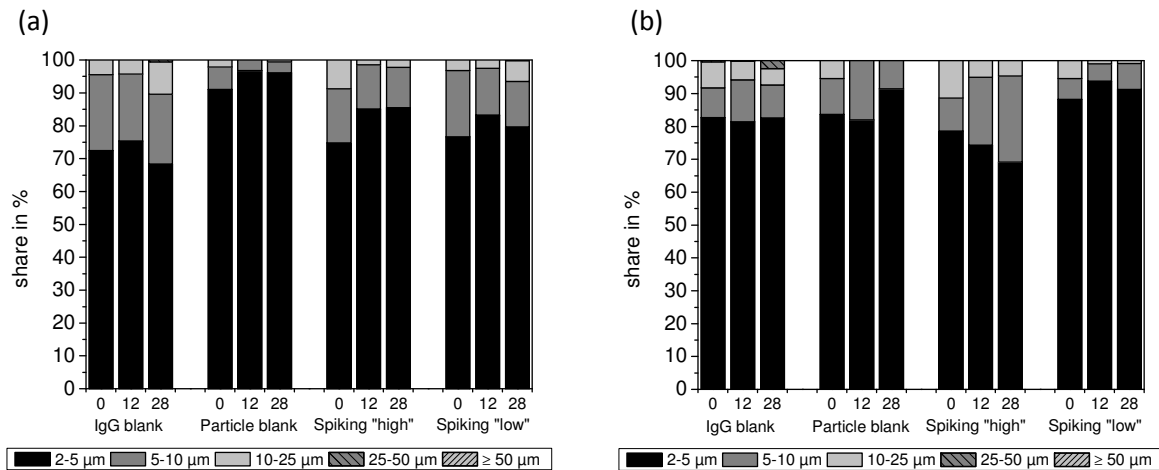


Figure V-77: Particle size distributions for (a) mAb1 and (b) mAb2 samples obtained with LO analysis.

Interestingly, MFI analysis revealed a substantial increase in particle counts after 12 weeks storage at 40°C for all mAb1 samples containing spiked-in silicone particles (Figure V-78a). The highest increase was recorded for the 'Particle blank' sample that did not contain any IgG. After 12 weeks storage at 40°C , particle counts for the 'Particle blank' were around 25,000 particles/mL and remained at that level until the 28 weeks analysis time point. For comparison, analysis of mAb1 placebo after 12 weeks storage at 40°C resulted in low particle counts $\geq 1 \mu\text{m}$ of 1252 ± 43 per mL. The MFI particle count increases thus have to be attributed to the silicone particles themselves. For all protein containing samples, particle counts after 28 weeks were slightly decreased in comparison to the 12 weeks data. This might be a consequence of the suggested shift in the MFI particle size distribution towards larger particles (Figure V-78c).

Particle counts of mAb2 samples (Figure V-78b) were around 2,000 particles/mL for the IgG blank, the particle blank and the "high" spiking level protein sample. The slightly higher particle counts of around 4,000 to 6,000 particles per mL for the "low" spiking level samples seem contradictory. In any case, MFI particle counts as well as particle size distributions (Figure V-78d) for mAb2 samples were comparable at all time points. The particle count for mAb2 placebo stored at 40°C for 12 weeks was 250 ± 111 particles $\geq 1 \mu\text{m}/\text{mL}$.

Since in most cases more than 95 % of all particles detected during MFI analysis were in the range of 1 to $5 \mu\text{m}$, a representative morphological evaluation was hardly achievable. However, for mAb1 samples containing spiked-in particles mostly spherical and transparent particles were found (Figure V-78e). The 'IgG blank' of mAb2 contained big and clearly identifiable protein aggregates (Figure V-78f, upper row). In samples with spiked-in particles also a small fraction of spherical, transparent particles was found (Figure V-78f, lower row).

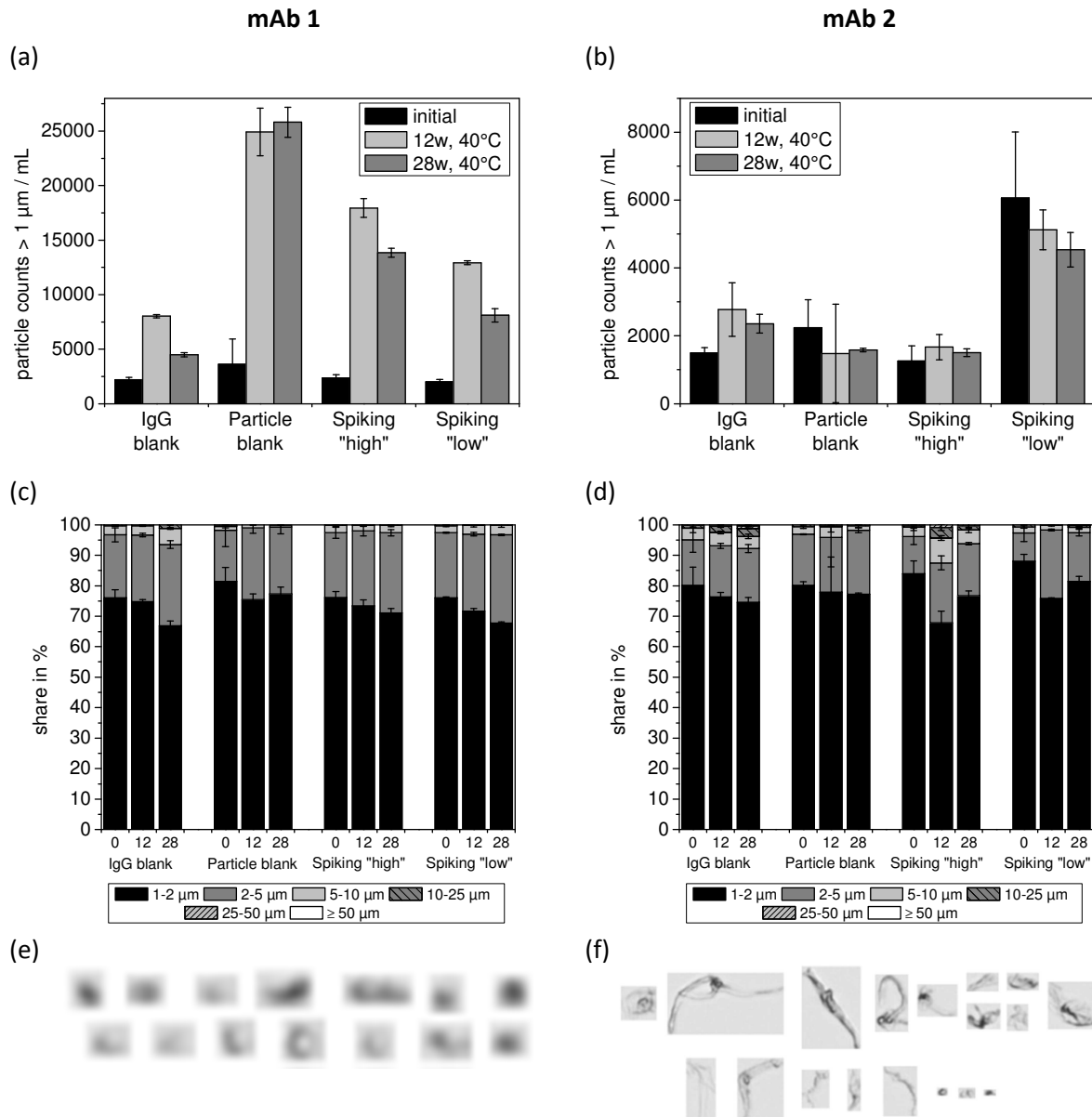


Figure V-78: MFI stability data for storage at 40°C. Particle counts, particle size distributions and representative MFI pictures (28w) for (a+c+e) mAb1 and (b+d+f) mAb2 samples. The zoom factor for the MFI pictures in (e) is 700% and 150% in (f).

3.2.4 Visual Inspection

All samples were found to be practically free of particles (0 to 4 particles per container) upon visual inspection with the polarized light inspection device (Optima lamp). From visual inspection with the Seidenader device it was concluded that the number of visible particles did not change over storage time and that all samples were essentially free of particles (Table V-35 in the Appendix).

4 DISCUSSION

Peristaltic pumping of two different placebo formulations using silicone tubing resulted in shed particles of similar characteristics, which correspond to earlier data [4]. The obtained recirculates contained rather few particles in the lower micrometer range. Due to the low resolution of the MFI system in this size range, the possibility for a morphological particle evaluation was limited [15,16]. The predominantly shed particle fraction appeared at around 200 nm in DLS and NTA analysis. The 200 nm signal of shed particles overlapped with contributions arising from sugar impurities [13]. Nonetheless, from the clearly increased 200 nm peak and higher NTA counts as well as turbidity values after recirculation, the generation of shed particles was proved. Likewise, the smoothing of the inner tubing surface after recirculation demonstrated the origin of these particles.

The two spiking levels with 1:140 and 1:280 dilutions of the recirculates were chosen as realistic, but nevertheless worst-case scenarios since the employed tubing was found to shed particles to a relatively high extent (tubing A in reference [4]). The 1:140 dilution represented an extrapolation to realistic fill & finish conditions during which every aliquot of drug product passes the pump only once. The higher dilution of 1:280 should mimic situations encountered at later time points during filling since particle shedding was found to level off over time [4]. Moreover, it is judged representative for particle levels obtained with tubing that is less prone for particle shedding (e.g. tubing B in reference [4]). For the “high” spiking level, 16 particles $\geq 1 \mu\text{m}$ (MFI) and 6.2×10^6 particles in the nanometer range (NTA) were added to every milliliter of mAb1 formulation. For mAb2, the number of added nanometer particles per mL was 3.7×10^6 . This is rather an approximation due to the limited reliability of particle quantification with NTA [17].

Not only added particulates can impair the stability and quality of a biopharmaceutical drug product, but also leachables can add to this effect [5,18–20]. Only one leachable slightly above the reporting threshold of 0.05 ppm was found in the prepared recirculates. Due to the applied spiking procedure, the found leachable was further diluted by the sample preparation. The non-hazardous substance 1,2-diacetin is a glycerol diacetate ester and used as humectant or aroma carrier in the food industry [21]. Destabilizing effects arising from this compound were not expected. In general, the use of platinum-cured silicone tubing is expected to result in low extractable and leachable levels [22]. Nevertheless, Jiang *et al.* quantified the amount of extractables via total organic carbon (TOC) analysis for several disposable assembly components and ranked the TOC amount per extractable surface area highest for the tested platinum-cured silicone tubing [23]. The unique leachables profile of a specific type of silicone tubing can vary depending on the tubing pre-treatment, tubing lot, contact time and mode as well as formulation components [24–27].

The two mAbs differed in stability, but the presence and the amount of spiked-in silicone particles did not affect mAb stability. For mAb1, which was formulated at 25 mg/mL in histidine buffer pH 5.5 including sucrose, methionine, and polysorbate 20, a marked increase in low molecular weight species upon storage at 40°C was observed with SEC analysis. Fragmentation seems to be the main route of degradation for mAb1. The increase in aggregates was minimal. Turbidity (4 to 4.5 FTU), visible and subvisible particle counts $\geq 2 \mu\text{m}$ obtained with HIAC (around 500 particles/mL) of all mAb1 samples stayed constant at all storage temperatures and over the whole storage period of six months. The strong increase in MFI particle counts in samples containing shed silicone particles is attributed to the earlier described colloidal instability of these particles [4]. It is anticipated that the

colloidal instability of the nanometer-sized particles led to particle fusion. The presence of mAb1 seemed to influence the colloidal stability since particle count increases were less for the mAb containing samples than for the 'Particle blank' despite the initially same particle burden. The "low" spiking level samples contained less shed particles and therefore showed a less pronounced increase in particle counts. Ludwig *et al.* also describe possible effects of their model protein lysozyme on the kinetic stability of silicone oil emulsions finally leading to flocculation [28]. In our case, the formation of micrometer-sized particles was reduced instead of increased in the presence of protein. The morphology of these micrometer-sized particles resembled at particles found in the recirculates and thus supports the particle fusion hypothesis. Intrinsic buffer instabilities as root cause could be ruled out since placebo controls did not show any increase in MFI particle counts after 12 weeks storage at 40°C. No further increase in particle counts between 12 and 28 weeks storage was observed. Most likely due to their high transparency, the formed particles were not detectable with LO [29,30]. It is commonly known that MFI is more sensitive and typically detects up to 3 to 10 times more particles than LO [31,32].

For the highly-concentrated mAb2 samples, a strong tendency towards aggregation was observed in SEC, but also fragmentation occurred upon storage at 40°C. Although the trend towards increased turbidity of samples stored at higher temperature was only minor and should not be overestimated, this observation might be traced back to aggregate formation. In any case, turbidity of all mAb2 samples was below 6 FTU and therefore below the turbidity value for the slightly opalescent reference suspension II as stated by the European Pharmacopeia [33]. With MFI, protein aggregates could be identified in mAb2 containing samples. Surprisingly, the number of these micrometer-sized particles remained constant over storage time. Protein aggregation does not necessarily lead to an increase in subvisible particle counts. Depending on the protein and its aggregation mechanism as well as the applied stress, aggregation might rest at the HMW species level in SEC or proceed from a state with soluble oligomers towards bigger, insoluble aggregates that can be detected as particulates [34,35]. There are other cases, however, in which subvisible particles were detected as early signs for protein aggregation before any changes in SEC became measurable [36]. An increase in particle counts was not observed in the 'particle blank' samples either. This might point to a higher colloidal stability of the shed silicone particles in the mAb2 formulation buffer. In general, formulations with high protein concentrations as in the case of mAb2 are considered to show pronounced aggregation even during quiescent storage [37–39]. In any case, the addition of particles shed from silicone tubing during peristaltic pumping did not accelerate or alter the aggregation behavior of mAb2.

5 SUMMARY AND CONCLUSION

In the present study, two model IgG antibodies were spiked with particles shed from silicone tubing during peristaltic pumping. Two realistic particle levels were chosen that actually might be encountered in the final DP after fill & finish. In accordance with previous studies, shedding mainly resulted in particles of around 200 nm in size with a minor particle fraction in the lower micrometer range. During the course of the conducted stability study, both mAbs revealed distinct instabilities in terms of protein aggregation and fragmentation in SEC analysis, especially upon storage at 40°C. However, these instabilities were independent of the presence and the amount of spiked-in particles. The turbidity values as well as the number of subvisible (LO) and visible particles did not change over time. For mAb1, an increase in MFI particle counts was observed for all samples containing shed silicone particles due to their limited colloidal stability in this formulation. In conclusion, DP manufacturers should be aware of the fact that particles shed from silicone tubing can end up in the final product when filled with a peristaltic pump, although they are not detectable with standard release testing methods like LO. Our results indicate that the expected particle burden is very low and does not negatively influence mAb stability. With the presented particle preparation and spiking approach, the susceptibility of other biopharmaceuticals for destabilization by shed silicone particles can be assessed on a case-by-case study.

6 ABBREVIATIONS

DLS	dynamic light scattering
DP	drug product
FTU	formazin turbidity unit
HMW	high molecular weight species
HP-SEC	high-performance size exclusion chromatography
IgG	immunoglobuline G
LMW	low molecular weight species
LO	light obscuration
mAb	monoclonal antibody
MFI	micro-flow imaging
NTA	nanoparticle tracking analysis
ppm	parts per million
R _a	arithmetic mean roughness
rpm	revolutions per minute
R _z	maximum height
w	weeks

7 REFERENCES

- [1] M.E.M. Cromwell, E. Hilario, F. Jacobson, Protein aggregation and bioprocessing., *AAPS J.* 8 (2006) E572–579.
- [2] A. Nayak, J. Colandene, V. Bradford, M. Perkins, Characterization of subvisible particle formation during the filling pump operation of a monoclonal antibody solution, *J. Pharm. Sci.* 100 (2011) 4198–4204.
- [3] A.K. Tyagi, T.W. Randolph, A. Dong, K.M. Maloney, C. Hitscherich, J.F. Carpenter, IgG particle formation during filling pump operation: a case study of heterogeneous nucleation on stainless steel nanoparticles., *J. Pharm. Sci.* 98 (2009) 94–104.
- [4] V. Saller, J. Matilainen, U. Grauschopf, K. Bechtold-Peters, H.-C. Mahler, W. Friess, Particle shedding from peristaltic pump tubing in biopharmaceutical drug product manufacturing., *J. Pharm. Sci.* 104 (2015) 1440–50.
- [5] J.S. Bee, T.W. Randolph, J.F. Carpenter, S.M. Bishop, M.N. Dimitrova, Effects of surfaces and leachables on the stability of biopharmaceuticals., *J. Pharm. Sci.* 100 (2011) 4158–70.
- [6] J.S. Bee, D. Chiu, S. Sawicki, J.L. Stevenson, K. Chatterjee, E. Freund, et al., Monoclonal antibody interactions with micro- and nanoparticles: adsorption, aggregation, and accelerated stress studies, *J. Pharm. Sci.* 98 (2009) 3218–38.
- [7] L. Liu, T.W. Randolph, J.F. Carpenter, Particles shed from syringe filters and their effects on agitation-induced protein aggregation., *J. Pharm. Sci.* 101 (2012) 2952–9.
- [8] R. Thirumangalathu, S. Krishnan, M.S. Ricci, D.N. Brems, T.W. Randolph, J.F. Carpenter, Silicone oil-and agitation-induced aggregation of a monoclonal antibody in aqueous solution, *J. Pharm. Sci.* 98 (2009) 3167–3181.
- [9] L.S. Jones, A. Kaufmann, C.R. Middaugh, Silicone oil induced aggregation of proteins., *J. Pharm. Sci.* 94 (2005) 918–27.
- [10] K.A. Britt, D.K. Schwartz, C. Wurth, H.-C. Mahler, J.F. Carpenter, T.W. Randolph, Excipient effects on humanized monoclonal antibody interactions with silicone oil emulsions., *J. Pharm. Sci.* 101 (2012) 4419–32.
- [11] J. Li, S. Pinnamaneni, Y. Quan, A. Jaiswal, F.I. Andersson, X. Zhang, Mechanistic understanding of protein-silicone oil interactions., *Pharm. Res.* 29 (2012) 1689–97.
- [12] M. Kaszuba, D. McKnight, M.T. Connah, F.K. McNeil-Watson, U. Nobbmann, Measuring sub nanometre sizes using dynamic light scattering, *J. Nanoparticle Res.* 10 (2007) 823–829.
- [13] D. Weinbuch, J.K. Cheung, J. Ketelaars, V. Filipe, A. Hawe, J. den Engelsman, et al., Nanoparticulate Impurities in Pharmaceutical-Grade Sugars and their Interference with Light Scattering-Based Analysis of Protein Formulations., *Pharm. Res.* 32 (2015) 2419–27.
- [14] International Conference on Harmonisation, M7: Assessment and Control of DNA Reactive (Mutagenic) Impurities in Pharmaceuticals to Limit Potential Carcinogenic Risk, (2014).

- [15] S. Zölls, D. Weinbuch, M. Wiggernhorn, G. Winter, W. Friess, W. Jiskoot, et al., Flow imaging microscopy for protein particle analysis - a comparative evaluation of four different analytical instruments, *AAPS J.* 15 (2013) 1200–11.
- [16] S. Zölls, R. Tantipolphan, M. Wiggernhorn, G. Winter, W. Jiskoot, W. Friess, et al., Particles in therapeutic protein formulations, Part 1: overview of analytical methods., *J Pharm Sci.* 101 (2012) 914–935.
- [17] V. Filipe, A. Hawe, W. Jiskoot, Critical evaluation of Nanoparticle Tracking Analysis (NTA) by NanoSight for the measurement of nanoparticles and protein aggregates., *Pharm. Res.* 27 (2010) 796–810.
- [18] M. Huang, T. Horwitz, C. Zweiben, S.K. Singh, Impact of extractables/leachables from filters on stability of protein formulations, *J. Pharm. Sci.* 100 (2011) 4617–4630.
- [19] I. Markovic, Evaluation of safety and quality impact of extractable and leachable substances in therapeutic biologic protein products: a risk-based perspective., *Expert Opin. Drug Saf.* 6 (2007) 487–91.
- [20] D. Bestwick, R. Colton, Extractables and Leachables from Single-Use Disposables, *Bioprocess Int.* (2009) February Supplement p.88–94.
- [21] CHEMIE.DE Information Service GmbH, Diacetin. Available online at: <http://www.chemie.de/lexikon/Diacetin.html> (accessed February 4, 2015).
- [22] A. Colas, R. Malczewski, K. Ulman, Silicone tubing for pharmaceutical processing, *PharmaChem.* (2004) 30–36.
- [23] T. Jiang, S. Kane, J. Chartier, Quantifying and Qualifying Extractable Substances from Components of Disposable Assemblies, *Bioprocess Int.* 5 (2007) S38–44.
- [24] T.-M. Chan, B. Pramanik, R. Aslanian, V. Gullo, M. Patel, B. Cronin, et al., Isolation, structural determination, synthesis and quantitative determination of impurities in Intron-A, leached from a silicone tubing., *J. Pharm. Biomed. Anal.* 49 (2009) 327–32.
- [25] D.R. Jenke, J. Story, R. Lalani, Extractables/leachables from plastic tubing used in product manufacturing., *Int. J. Pharm.* 315 (2006) 75–92.
- [26] J.A. Zimmerman, J.M. Ballard, H. Wang, A. Wu, K.A. Gallagher, Extraction of o-phenylphenol from silicone tubing by a sulfobutylether cyclodextrin formulation, *Int. J. Pharm.* 267 (2003) 113–120.
- [27] M.W.J. den Brok, S.C. van der Schoot, B. Nuijen, M.J.X. Hillebrand, J.H. Beijnen, 2-Hydroxypropyl-beta-cyclodextrin extracts 2-phenylphenol from silicone tubing., *Int. J. Pharm.* 278 (2004) 303–9.
- [28] D.B. Ludwig, J.F. Carpenter, J.-B. Hamel, T.W. Randolph, Protein adsorption and excipient effects on kinetic stability of silicone oil emulsions., *J. Pharm. Sci.* 99 (2010) 1721–33.
- [29] K. Wuchner, J. Büchler, R. Spycher, P. Dalmonte, D.B. Volkin, Development of a microflow digital imaging assay to characterize protein particulates during storage of a high concentration IgG1 monoclonal antibody formulation., *J. Pharm. Sci.* 99 (2010) 3343–61.

- [30] D.K. Sharma, P. Oma, M.J. Pollo, M. Sukumar, Quantification and characterization of subvisible proteinaceous particles in opalescent mAb formulations using micro-flow imaging., *J. Pharm. Sci.* 99 (2010) 2628–42.
- [31] D.K. Sharma, D. King, P. Oma, C. Merchant, Micro-flow imaging: flow microscopy applied to sub-visible particulate analysis in protein formulations., *AAPS J.* 12 (2010) 455–64.
- [32] C.-T. Huang, D. Sharma, P. Oma, R. Krishnamurthy, Quantitation of protein particles in parenteral solutions using micro-flow imaging., *J. Pharm. Sci.* 98 (2009) 3058–71.
- [33] European Directorate for the Quality of Medicine (EDQM), 2.2.1 Clarity and degree of opalescence of liquids, in: *European Pharmacopoeia*, 8th ed., 2014.
- [34] M.C. Manning, D.K. Chou, B.M. Murphy, R.W. Payne, D.S. Katayama, Stability of protein pharmaceuticals: an update., *Pharm. Res.* 27 (2010) 544–75.
- [35] S. Kiese, A. Pappenberger, W. Friess, H.-C. Mahler, Equilibrium studies of protein aggregates and homogeneous nucleation in protein formulation., *J. Pharm. Sci.* 99 (2010) 632–44.
- [36] J.G. Barnard, S. Singh, T.W. Randolph, J.F. Carpenter, Subvisible particle counting provides a sensitive method of detecting and quantifying aggregation of monoclonal antibody caused by freeze-thawing: insights into the roles of particles in the protein aggregation pathway., *J. Pharm. Sci.* 100 (2011) 492–503.
- [37] H.-C. Mahler, W. Friess, U. Grauschopf, S. Kiese, Protein aggregation: pathways, induction factors and analysis., *J. Pharm. Sci.* 98 (2009) 2909–34.
- [38] W. Wang, S. Singh, D.L. Zeng, K. King, S. Nema, Antibody structure, instability, and formulation., *J. Pharm. Sci.* 96 (2007) 1–26.
- [39] S.J. Shire, Z. Shahrokh, J. Liu, Challenges in the development of high protein concentration formulations., *J. Pharm. Sci.* 93 (2004) 1390–402.

8 APPENDIX

Table V-33: Particle counts (LO) for mAb1 samples over storage time.

T [°C]	Sample	Storage Time	Particle counts / mL			
			≥ 2 μm	≥ 5 μm	≥ 10 μm	≥ 25 μm
-	<i>IgG blank</i>	<i>initial</i>	338	93	15	0
	<i>Particle blank</i>		428	38	9	0
	<i>Spiking "high"</i>		218	55	19	0
	<i>Spiking "Low"</i>		403	94	13	0
2-8	<i>IgG blank</i>	<i>4w</i>	485	113	23	0
		<i>12w</i>	106	26	9	0
		<i>28w</i>	641	118	10	0
	<i>Particle blank</i>	<i>4w</i>	381	29	3	0
		<i>12w</i>	795	61	5	0
		<i>28w</i>	533	20	1	0
	<i>Spiking "high"</i>	<i>4w</i>	466	36	4	0
		<i>12w</i>	630	58	8	1
		<i>28w</i>	819	152	14	0
	<i>Spiking "low"</i>	<i>4w</i>	346	28	4	0
		<i>12w</i>	835	115	14	0
		<i>28w</i>	711	161	31	1
25	<i>IgG blank</i>	<i>2w</i>	303	48	9	1
		<i>4w</i>	539	104	18	0
		<i>12w</i>	320	59	14	0
		<i>28w</i>	373	66	14	0
	<i>Particle blank</i>	<i>2w</i>	334	16	0	0
		<i>4w</i>	185	23	1	0
		<i>12w</i>	489	53	5	0
		<i>28w</i>	524	10	0	0
	<i>Spiking "high"</i>	<i>2w</i>	214	38	5	0
		<i>4w</i>	541	86	8	0
		<i>12w</i>	479	59	5	0
		<i>28w</i>	533	49	3	0
<i>Spiking "low"</i>	<i>2w</i>	318	51	5	1	
	<i>4w</i>	358	61	8	0	
	<i>12w</i>	478	65	9	0	
	<i>28w</i>	450	74	14	0	

40	<i>IgG blank</i>	1w	304	43	9	1
		2w	180	36	6	0
		4w	446	129	31	0
		12w	471	116	20	0
		28w	491	155	51	3
	<i>Particle blank</i>	1w	1035	44	9	1
		2w	294	26	8	1
		4w	165	15	0	0
		12w	721	23	0	0
		28w	850	33	5	0
	<i>Spiking "high"</i>	1w	571	55	6	1
		2w	374	35	5	1
		4w	333	41	4	0
		12w	431	64	6	0
		28w	813	118	18	0
	<i>Spiking "low"</i>	1w	388	45	5	0
		2w	415	80	13	0
		4w	501	81	5	0
		12w	514	86	13	0
		28w	664	135	43	1

Table V-34: Particle counts (LO) for mAb2 samples over storage time.

T [°C]	Sample	Storage Time	Particle counts / mL			
			≥ 2 μm	≥ 5 μm	≥ 10 μm	≥ 25 μm
-	<i>IgG blank</i>	<i>initial</i>	231	40	19	1
	<i>Particle blank</i>		55	9	3	0
	<i>Spiking "high"</i>		70	15	8	0
	<i>Spiking "Low"</i>		110	13	6	0
2-8	<i>IgG blank</i>	<i>4w</i>	50	5	1	0
		<i>12w</i>	48	13	4	0
		<i>28w</i>	76	20	8	0
	<i>Particle blank</i>	<i>4w</i>	51	9	1	0
		<i>12w</i>	55	10	3	0
		<i>28w</i>	55	5	1	0
	<i>Spiking "high"</i>	<i>4w</i>	33	13	0	0
		<i>12w</i>	45	26	9	0
		<i>28w</i>	95	29	6	0
	<i>Spiking "low"</i>	<i>4w</i>	190	16	1	0
		<i>12w</i>	201	40	8	0
		<i>28w</i>	184	23	11	1
25	<i>IgG blank</i>	<i>2w</i>	156	24	4	3
		<i>4w</i>	134	11	3	0
		<i>12w</i>	151	23	8	1
		<i>28w</i>	69	9	3	0
	<i>Particle blank</i>	<i>2w</i>	49	11	0	0
		<i>4w</i>	54	14	1	0
		<i>12w</i>	66	15	3	0
		<i>28w</i>	35	6	1	0
	<i>Spiking "high"</i>	<i>2w</i>	186	35	1	0
		<i>4w</i>	175	34	3	0
		<i>12w</i>	109	26	1	0
		<i>28w</i>	255	58	6	0
	<i>Spiking "low"</i>	<i>2w</i>	166	33	8	0
		<i>4w</i>	248	11	0	0
		<i>12w</i>	306	44	14	0
		<i>28w</i>	61	10	4	0
40	<i>IgG blank</i>	<i>1w</i>	101	26	3	0
		<i>2w</i>	199	46	9	1
		<i>4w</i>	266	44	10	1
		<i>12w</i>	564	105	33	1
		<i>28w</i>	121	21	9	3

<i>Particle blank</i>	1w	93	19	3	0
	2w	64	11	3	0
	4w	54	9	0	0
	12w	89	16	0	0
	28w	70	6	0	0
<i>Spiking "high"</i>	1w	90	40	6	0
	2w	145	38	10	0
	4w	90	9	0	0
	12w	296	76	15	0
	28w	214	66	10	0
<i>Spiking "low"</i>	1w	270	23	3	0
	2w	184	45	11	0
	4w	75	13	0	0
	12w	1088	68	11	0
	28w	355	31	3	0

Table V-35: Particle counts obtained via visual inspection with the Seidenader device.

Formulation	Sample	Initial	2-8°C		25°C		40°C	
			12w	28w	12w	28w	12w	28w
mAb1	IgG blank	1-5	> 10	1-5	1-5	1-5	1-5	1-5
	Particle blank	0	> 10	0	0	0	0	1-5
	Spiking „high“	1-5	1-5	1-5	0	1-5	0	1-5
	Spiking „low“	1-5	1-5	1-5	0	0	1-5	0
mAb2	IgG blank	1-5	0	1-5	0	0	0	1-5
	Particle blank	1-5	1-5	1-5	0	1-5	1-5	1-5
	Spiking „high“	0	0	0	0	0	0	0
	Spiking „low“	0	0	1-5	0	0	0	1-5

CHAPTER VI

PRESERVATIVE LOSS FROM SILICONE TUBING DURING FILL & FINISH

ABSTRACT

The high permeability of silicone tubing for gases and volatile substances is widely known and described in literature in the context of preservative losses during filling line down times. This study focuses on the three most commonly used preservatives in protein drugs, benzyl alcohol, phenol, and m-cresol. Concentration losses during static incubation were quantified and interpreted with regards to the potential driving forces for the underlying sorption, diffusion, and desorption steps. Partitioning from the solution into the silicone polymer was identified as the most decisive parameter for the extent of preservative loss. Additionally, the influence of tubing inner diameter, starting concentration as well as silicone tubing type was evaluated. Theoretical calculations assuming equilibrium between solution and tubing inner surface and one-directional diffusion following Fick's first law were used to approximate experimental data. Since significant losses were found already after few minutes, adequate measures must be taken to avoid out of specification (OOS) deviations during filling of preservative-containing protein solutions.

1 INTRODUCTION

Silicone tubing is commonly used for fill & finish processes with a peristaltic pump due to its advantageous mechanical properties. However, silicone rubber is highly permeable for gases and other volatile molecules [1]. As shown by Bahal and Romansky, this characteristic needs to be considered during filling of preservative-containing solutions [2,3]. In their studies, different types of tubing and preservatives were tested and the concentration decrease of preservative solutions was highest when incubated in silicone tubing. Within 24 hours, propylparaben concentrations were reduced by 100% and methylparaben solutions showed losses of around 40% [2]. Similar losses of 30 to 40% were also found for benzoic and sorbic acid as well as for benzyl alcohol. However, sorption did not occur with the ionic substance benzalkonium chloride [3].

Preservatives are used in multi-dose formulations in order to ensure microbial stability. From the numbers presented in Table VI-36 it becomes clear that the overall use of preservatives diminished over the last decades. For protein-based drugs, the most often employed preservatives include benzylalcohol, phenol, and m-cresol. Thiomersal and chlorobutanol can also be found in peptide or protein formulations, but less frequently. Examples for preservative-containing protein drug formulations are Pegasys® from Roche and Sandostatin® from Novartis [4].

Table VI-36: Number and type of marketed parenteral products containing preservatives, adapted from Meyer et al. 2007 [4].

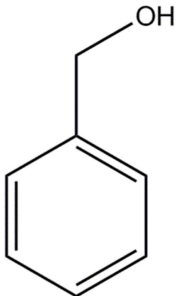
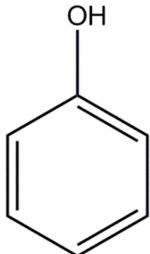
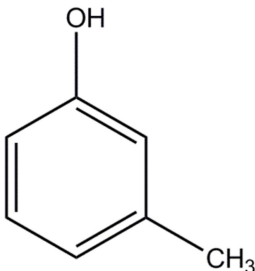
Preservative	Product Type			Frequency of Use		
	Peptide/Protein	Vaccines	Small Molecule	1996	2001	2006
Chlorobutanol	x	-	x	17	13	3
Methylparaben	-	-	x	50	40	9
Propylparaben	-	-	x	40	33	9
Benzyl alcohol	x	-	x	74	69	19
Phenol	x	x	x	48	30	15
Thiomersal	x	x	-	46	20	6
m-Cresol	x	-	-	3	7	11
Phenoxyethanol	-	x	-	3	4	5

A suitable preservative needs to be chosen carefully during formulation development, since a potential effect of the preservative on protein stability cannot be excluded. In this context, Alford *et al.* [5] as well as Zhang and co-workers [6] studied the interactions between benzyl alcohol and recombinant human interleukin-1 receptor antagonist. Hutchings *et al.* [7] found that m-cresol, phenol, benzyl alcohol, phenoxyethanol, as well as chlorobutanol can induce protein aggregation by enhancing partial protein unfolding. In contrast, a positive effect of phenolic preservatives on the self-assembly and thus stability of some insulin analogs was reported [8].

In this study, the three most relevant preservatives for protein formulations, namely benzyl alcohol, phenol, and m-cresol were investigated for their sorption behavior in silicone tubing with two different inner diameters (ID). Previous, unpublished results showed that preservative losses were independent of the presence of a protein drug. Hence, preservative formulations in a placebo buffer

only were employed for this study. With this approach, simple UV measurements could be performed for preservative quantification without any need for further chromatographic separation steps. Formulation parameters like concentration and pH were chosen according to Table VI-37. Since preservative losses are expected to be especially critical during filling line down times, static incubation experiments were performed. It is the aim of this study to quantify losses and also generate a deeper understanding of the underlying mechanism and influencing factors. Therefore, not only the known molecular characteristics of Table VI-37 were used for the interpretation of the obtained data. The three preservatives were additionally characterized for their partitioning, diffusion, and evaporation behavior in conjunction with the silicone polymer matrix and a mathematical model was established.

Table VI-37: Molecular structure and properties of the three investigated preservatives. MW: molecular weight, $\log P_{ow}$: Octanol-water partition coefficient. Typical values for formulation concentration and pH are taken from [4].

Preservative	Structure	MW [g/mol]	$\log P_{ow}$	Typical concentration	pH optimum
Benzyl alcohol		108.14	1.1 [9]	1 %	< 5
Phenol		94.11	1.46 [10]	0.25 – 5 %	< 9
m-Cresol		108.14	1.96 [11]	0.3 %	< 9

2 MATERIALS AND METHODS

2.1 Materials

2.1.1 Chemicals

M-Cresol and benzyl alcohol were purchased from Merck KGaA (Darmstadt, Germany), phenol was obtained from AppliChem (Darmstadt, Germany). NaCl, Na₂HPO₄, and NaH₂PO₄ were supplied by VWR International (Darmstadt, Germany). NaOH (1 M) and HCl (1 M) were obtained from Sigma-Aldrich (Taufkirchen, Germany). Highly purified water used for buffer preparation was taken from an arium® pro DI Ultrapure Water System (Sartorius Stedim Biotech GmbH, Goettingen, Germany) or a USF ELGA PURELAB Plus UV/UF purification system (ELGA LabWater, Celle, Germany). Buffer filtration was performed with pressurized nitrogen and 0.2 µm cellulose acetate filters (47 mm ø, Sartorius Stedim Biotech GmbH).

2.1.2 Silicone Tubing

The two employed platinum-cured silicone tubing types from different manufacturers (type A and B) with an ID of 6.0 mm and 1.6 mm were purchased from Watson-Marlow / Flexicon (Ringsted, Denmark). Wall thicknesses were 2.1 mm and 1.6 mm, respectively.

2.2 Methods

2.2.1 Sample Preparation

The three preservatives were dissolved in 10 mM phosphate buffer containing 145 mM NaCl at the pH and concentration stated in Table VI-38.

Table VI-38: Stock solution formulation and analysis parameters.

Preservative	Concentration	pH	Sampling volume	Dilution for analysis	λ_{\max}
Benzyl alcohol	10 mg/mL (= 1 %)	5	200 µL	1:5	258 nm
Phenol	5.5 mg/mL (= 0.55 %)	7	50 µL	1:20	270 nm
m-Cresol	3.15 mg/mL (= 0.315 %)	7	100 µL	1:10	272 nm

2.2.2 Sorption Experiments

40 cm long pieces of tubing with an ID of 6.0 mm were filled with 10 mL of preservative solution (n=3). For tubing with an ID of 1.6 mm, three 20 cm long pieces per analysis time point were filled with 300 µL. Ends were clamped and the tubing pieces were incubated at RT for 5, 10, 15, 30, 60, 120, 240, and 360 minutes. For the 6.0 mm ID tubing, samples were withdrawn from the filled tube at every analysis time point. The exact volume of the sampling aliquots is given in Table VI-38. 1.6 mm tubing pieces were completely emptied for sampling. Sample aliquots were diluted (Table VI-38) and stored in 2R glass vials (Schott AG, Mainz, Germany) prior to analysis. For phenol and m-cresol samples that were incubated in 1.6 mm tubing for 4 and 6 hours, the dilution factor was reduced to 1:5.

2.2.3 UV Absorption Measurements

200 μL of each diluted sample as well as of each standard concentration (Appendix, Table VI-43) and the corresponding blank buffer were analyzed in triplicates in a 96-well quartz well plate (Hellma Analytics, Müllheim, Germany) for UV absorption with a FLUOstar Omega well-plate reader and Omega software version 1.01 (BMG Labtech GmbH, Ortenberg, Germany). A positioning delay of 0.5 seconds and analysis with 20 flashes per well in 'Absorbance endpoint' mode was applied. Absorption maxima as stated in Table VI-38 were determined from UV absorption scans in the range of 220 to 350 nm. Linear regression fit with the 'average data based on blank corrected' raw data was performed within the MARS Data Analysis Software version 1.01 (BMG Labtech).

2.2.4 Determination of the Partition Coefficient k

Approx. 600 mg of cut silicone tubing pieces were incubated with 2.0 mL of preservative solution in stoppered 10R glass vials (Schott AG, Mainz, Germany). Solutions with concentrations of 1, 2, 4, 6, 8, and 10 mg/mL preservative were employed ($n=3$). For every concentration, a blank glass vial containing preservative solution without any added silicone tubing pieces was prepared. After overnight equilibration, preservative concentrations of the incubation and blank solutions were determined after dilution. From the concentration difference between the blank and the incubation solutions, the sorbed amount of preservative per unit volume of silicone tubing was calculated assuming a specific gravity for silicone tubing of 1.1 as stated by the manufacturer. Preservative concentrations in the silicone were plotted against preservative concentrations in solution. Linear regression analysis (no error weighting, y-intercept of 0) was performed in Origin 8G (OriginLab Corporation, Northampton, MA, USA). The obtained slope represents the partitioning coefficient k .

2.2.5 Determination of the Diffusivity D

Permeation tests with jacketed Franz-type diffusion cells (diameter of 15 mm, volume of 12 mL, Gauer Glas, Püttlingen, Germany) were conducted at 26°C. A cut-open silicone tubing piece (6.0 mm ID, length of 2.5 cm, thickness d of 2.1 mm) was used as membrane. 2.0 mL of a saturated preservative solution (BA: 40 mg/mL, phenol: 80 mg/mL, m-cresol: 20 mg/mL) were employed as donor medium. The exact volume of the corresponding blank buffer in the acceptor compartment was subject to minor variations in the Franz cell geometry and was therefore determined separately for each diffusion cell. Sampling was performed every 15 minutes for up to 4 hours. Using a Hamilton Gastight 1000 μL syringe with 8 cm long stainless steel cannula (Hamilton Company, Bonaduz, Switzerland), approx. 250 μL were withdrawn from the middle of the acceptor compartment. The sampling volume was subsequently replaced by blank buffer. Preservative concentration of the undiluted samples was measured as described above. For every preservative, two sets of experiments with 5 Franz-type diffusion cells each were performed. A plot of absorbance mean value versus time was generated and linear regression analysis (no error weighting) for data points between 90 and 240 minutes incubation time was performed in Origin 8G. The x-intercept was calculated and introduced into the following formula as lag time t :

$$D = \frac{d^2}{6 \times t}$$

2.2.6 Determination of the Evaporation Characteristics

2 cm long, cut-open and weighted tubing pieces were incubated overnight in stoppered 10R glass vials filled with 8 mL of saturated preservative solution (see section 2.2.5). After removal from the incubation solution, the tubing piece was dried from the outside with filtered, pressurized air and placed on a Mettler Toledo AX205 balance (Mettler Toledo, Greifensee, Switzerland). Mass loss over time was automatically monitored via the Balancelink Software version 3.01. Data acquisition was performed every 60 seconds. Data plots show the ratio of actual mass to tubing piece mass (M^∞).

2.2.7 Modelling of Data with Fick's Law of Diffusion

Fick's first law of diffusion describes the amount of substance per unit area and time that diffuses from regions of high concentrations to regions of low concentrations assuming a steady state [12]:

$$J = -D \frac{c_1 - c_2}{d}$$

J : Flux [$\text{g}/(\text{m}^2 \cdot \text{s})$]

D : Diffusivity [m^2/s], experimentally determined

c_1 : concentration of permeant in the medium surrounding the tubing [mg/cm^3]

c_2 : concentration of permeant in the tubing lumen [mg/cm^3]

d : distance [m], in this case tubing wall thickness (2.1×10^{-3} m for tubing ID of 6.0 mm)

Diffusion was presumed to occur in direction of the concentration gradient across the tubing wall only. The concentration c_1 on the outside of the tubing wall was set to zero since the lab and production environment shows high air exchange rates and can be considered a reservoir of infinite volume (=sink conditions). The concentration on the inside of the tubing wall c_2 was calculated as follows:

$$c_2 = k \times c_{lumen}$$

with k being the experimentally determined partition coefficient for the silicone polymer – water system and c_{lumen} being the measured preservative concentration inside the tubing lumen.

Theoretical mass loss from one time point t_n to the next time point t_{n+1} arising from diffusion through the tubing wall was calculated with the following equation:

$$\Delta m_n = J_n \times (t_{n+1} - t_n) \times A$$

whereas A is the contact area per mL of solution. Based on the inner radius of the tubing lumen of $r = 3$ mm, A is given by the following term:

$$A = 2r\pi h$$

$$h = \frac{1 \text{ mL}}{\pi r^2}$$

In total, the theoretical concentration expected for the next analysis time point t_{n+1} by assuming losses due to unhindered steady-state diffusion only is:

$$c_{n+1} = c_n - \frac{\Delta m_n}{1 \text{ mL}}$$

3 RESULTS

3.1 Preservative Loss during Static Incubation in Silicone Tubing

Preservative loss inside the silicone tubing lumen was substantial already during the first minutes of the experiments (Figure VI-79). After five minutes incubation time in tubing with an ID of 6.0 mm, preservative contents were reduced by approx. 3 % in the case of benzyl alcohol and phenol and by 10 % in the case of m-cresol. For tubing with the smaller ID of 1.6 mm, 20 to 40 % preservative were lost within the first five minutes. Over time, preservative losses levelled off. For the 1.6 mm ID tubing, the preservative contents approached zero after six hours. In 6.0 mm ID tubing, the preservative contents remaining after six hours were around 63 % for benzyl alcohol (BA), 53 % for phenol, and 34 % for m-cresol. The same rank order for preservative loss was observed in experiments with 1.6 mm ID tubing. Despite initially overlapping curves, finally less phenol was present than BA. There was no difference in the behavior of the silicone tubings from two different manufacturers.

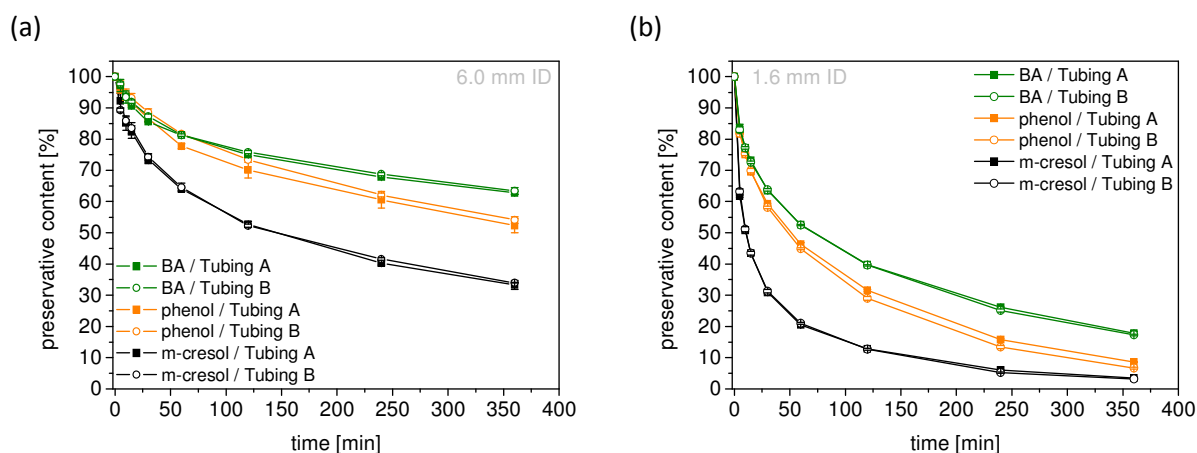


Figure VI-79: Preservative losses in silicone tubing (type A and B) with an ID of (a) 6.0 mm and (b) 1.6 mm.

3.2 Influence of Preservative Concentration

In the previous paragraph, relative preservative losses were compared at different starting concentrations of the preservatives which reflect relevant formulation compositions. In the following, the influence of the starting concentration on the relative loss was investigated for benzyl alcohol and m-cresol at 5.5 mg/mL. For both investigated tubing sizes, relative preservative losses were independent of the actual starting concentration (Figure VI-80). At 5.5 mg/mL, the initial steep slope relates to absolute m-cresol losses of 0.10 and 0.41 mg/mL per minute for an ID of 6.0 and 1.6 mm, respectively (Figure VI-81). For benzyl alcohol and phenol, the initial loss rate was 0.03 and 0.2 mg·mL⁻¹·min⁻¹, respectively. Towards the end of the 6 h incubation period, loss rates decreased to 0.001-0.004 mg·mL⁻¹·min⁻¹ in all cases.

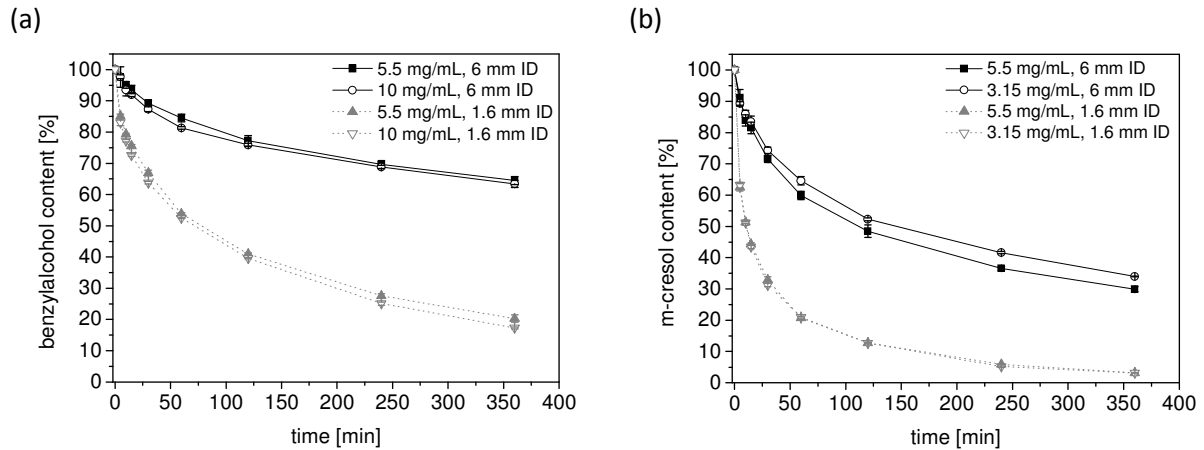


Figure VI-80: Relative preservative loss in tubing A for two differently concentrated incubation solutions of (a) benzyl alcohol and (b) m-cresol.

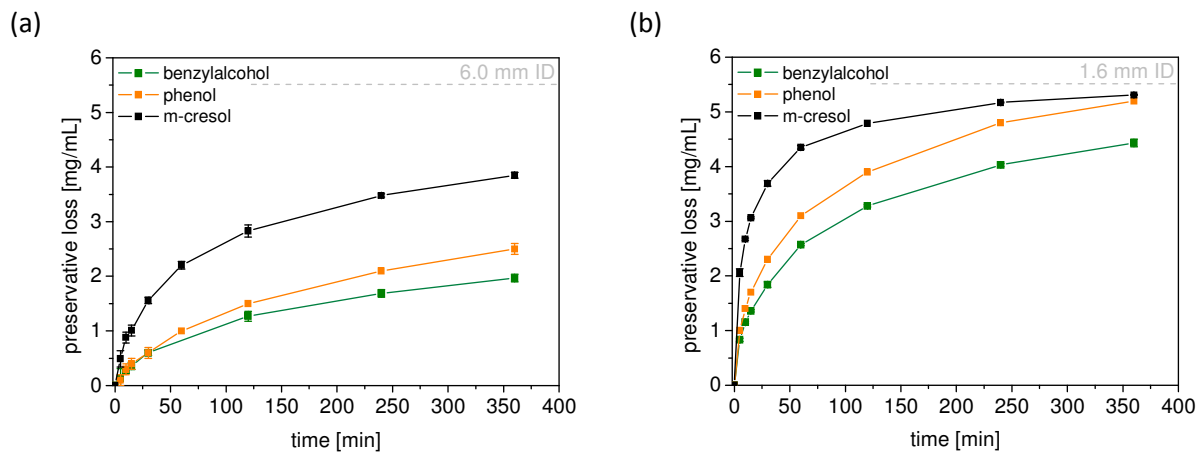


Figure VI-81: Absolute preservative loss over incubation time in silicone tubing B with an ID of (a) 6.0 mm and (b) 1.6 mm. The dotted line represents the maximum loss reflecting starting concentration of 5.5 mg/mL.

3.3 Determination of the Partition Coefficient k

The affinity of the three preservatives for migration into the tubing material was characterized by plotting the preservative concentration in the tubing material against the preservative concentration (w/V) in the supernatant (Figure VI-82). The slope of the linear fit reflects the partition coefficient k . The coefficient of determination was above 0.98 for all three data sets. For better comparison with literature, the logP was calculated (Table VI-39). The rank order of the partition coefficients was $k(\text{m-cresol}) \gg k(\text{benzyl alcohol}) > k(\text{phenol})$. This indicates that the solubility of m-cresol in the silicone matrix was much higher than for the other two preservatives.

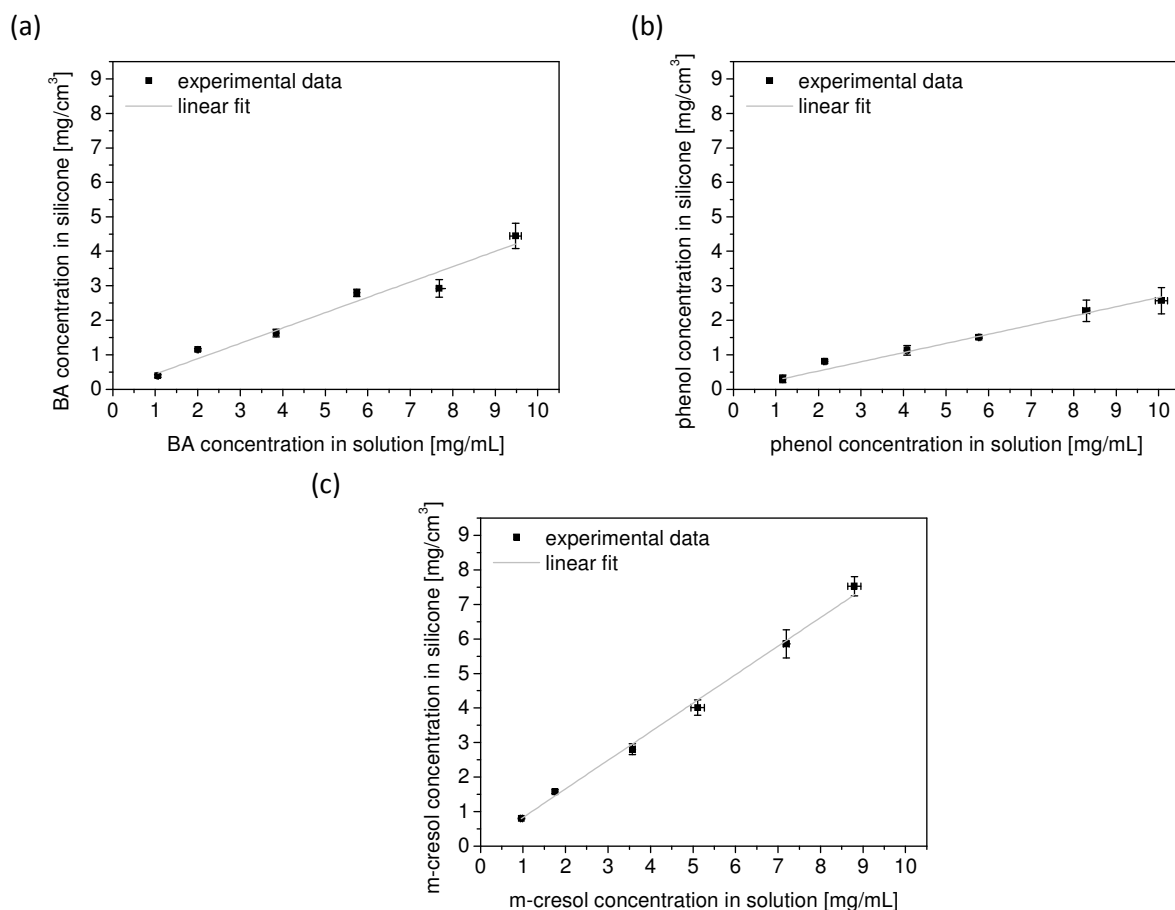


Figure VI-82: Amount of preservative inside the tubing versus the amount of preservative remaining in solution at equilibrium for (a) benzyl alcohol, (b) phenol, and (c) m-cresol. Linear regression analysis was performed for the determination of the partition coefficient (Table VI-39).

Table VI-39: Partition coefficients obtained via linear regression analysis as shown in Figure VI-82.

Parameter	Benzyl alcohol	Phenol	m-Cresol
Slope / partition coefficient k	0.44	0.27	0.83
R^2	0.987	0.994	0.998
Calculated logP (silicone/water)	-0.35	-0.57	-0.08

3.4 Determination of the Diffusivity D

The diffusivity of the three preservatives in the silicone tubing material was determined with a typical Franz cell setup. After a lag time of around 50 minutes, the absorbance and thus the amount of preservative in the acceptor compartment increased linearly (Figure VI-83). From extrapolation of this linear section to the x-intercept, the lag time t was determined and converted into diffusivity values (Table VI-40). Benzyl alcohol and m-cresol revealed comparable lag times of around 54 and 56 minutes and thus similar diffusivity values of 2.3×10^{-10} and 2.2×10^{-10} m^2/s , respectively. Both molecules have an identical molecular weight of 108.14 g/mol. The diffusivity of the smaller molecule phenol was calculated to be 3.0×10^{-10} m^2/s and thus approx. 30% higher.

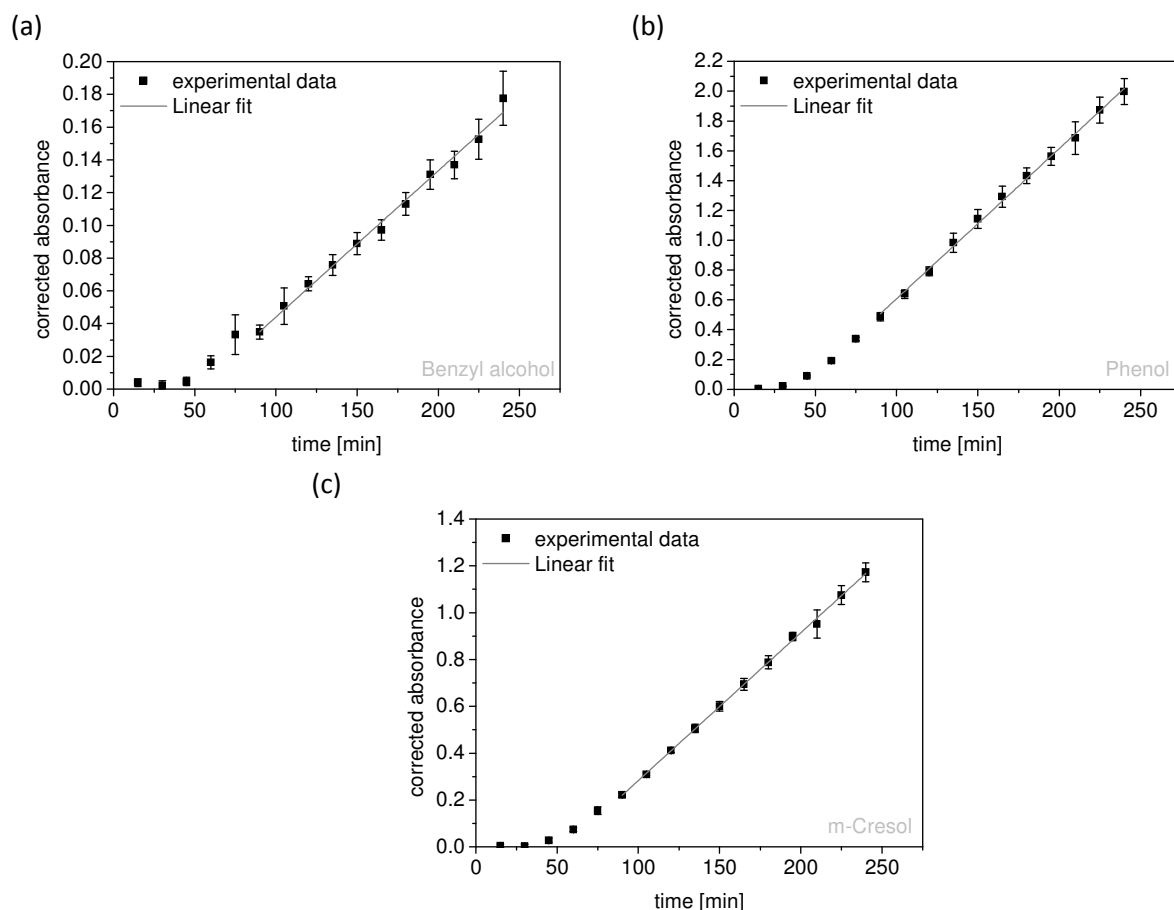


Figure VI-83: Plots of absorbance in the acceptor compartment (corrected for dilution effects during sampling) versus time for (a) benzyl alcohol, (b) phenol, and (c) m-cresol. Extrapolation of the linear part was performed for the determination of lag times t (Table VI-40).

Table VI-40: Lag time t obtained from linear extrapolation of the graphs shown in Figure VI-83 to the x-axis and the corresponding diffusivity values.

Parameter	Benzyl alcohol	Phenol	m-Cresol
Lag time t [min]	54.0	40.4	56.4
Diffusivity D [m ² /s]	2.3E-10	3.0E-10	2.2E-10

3.5 Determination of the Evaporation Characteristics

The propensity of each preservative for evaporation from the tubing surface was characterized by monitoring the time-dependent mass reduction of tubing pieces that were pre-incubated with preservative (Figure VI-84). Incubation in pure water did not lead to any measurable mass uptake. Swelling of the tubing material in water could thus be excluded. The mass uptake was highest for phenol, which was simply due to the higher saturation concentration of phenol that was chosen as incubation concentration. Next to the exact concentration of the incubation solution, also the partition coefficient is decisive for the absolute mass update. The evaporation characteristics are reflected by the rate of the mass decrease. As a numerical measure, the evaporation half-value time was calculated. This value was lowest for phenol with 186 minutes (mean value from $n=2$), indicating the highest evaporation rate. For benzyl alcohol and m-cresol significantly higher $t_{1/2}$ evaporation values of 296 and 377 minutes, respectively, were obtained.

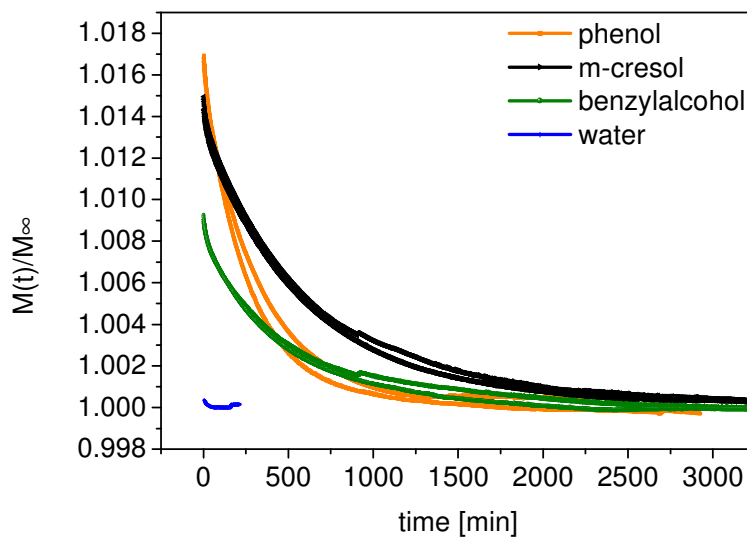


Figure VI-84: Mass loss over time of silicone tubing pieces soaked with preservative (n=2). As a control, silicone tubing was incubated in pure water.

3.6 Modelling of Data with Fick's Law of Diffusion

Fick's first law of diffusion is only applicable to steady state problems and thus not valid for the entire process of preservative loss. In consequence, Fick's equation was used to calculate the flux J through the silicone tubing wall (ID of 6.0 mm) at each specific analysis time point (Table VI-41). This computation is based on the experimental data for comparable starting concentrations of 5.5 mg/mL. The initial flux was found to be highest for m-cresol. Initial flux values for phenol were lowest, but close to those for benzyl alcohol. The flux decreases over time as the concentration gradient diminishes. This decrease in flux rate was most pronounced for m-cresol. Flux values after an incubation time of 6 h were in a similar range for all three preservatives. For tubing with an ID of 1.6 mm, flux rates for the starting concentration of 5.5 mg/mL were 1.3 times higher than for tubing with an ID of 6.0 mm due to the reduced wall thickness of 1.6 mm (Appendix, Table VI-44).

With these flux values, the remaining amount of preservative inside the tubing lumen was estimated for the next analysis time point. A comparison between the experimental data and the theoretically determined concentrations for c_{lumen} is shown in Figure VI-85. During the first hour of the experiment, experimental values were typically lower than theoretical ones. At some point, the theoretical estimation closely matched the experimental data. This was the case at analysis time point $t = 60$ min for benzyl alcohol, and $t = 120$ min for phenol and m-cresol. In the following, the theoretical values underestimated actually measured concentrations significantly. Modeled data for 1.6 mm ID tubing matched experimental values at earlier time points and the divergence at later time points was more pronounced (Appendix, Figure VI-88).

Table VI-41: Calculation of c_2 [mg/mL] and J [g/(m²·s)] for each analysis time point and a tubing ID of 6.0 mm, based on measured preservative concentrations inside the tubing. Experimentally determined partition coefficients k and diffusivities D as presented above were used for the computations. The starting concentration inside the tubing lumen was 5.5 mg/mL for all preservatives.

Analysis time point [min]	Benzyl alcohol		Phenol		m-Cresol	
	c_2	J	c_2	J	c_2	J
0	2.47	0.26	1.48	0.21	4.55	0.50
5	2.41	0.25	1.44	0.21	4.14	0.45
10	2.35	0.25	1.40	0.20	3.81	0.42
15	2.31	0.24	1.38	0.20	3.71	0.41
30	2.21	0.23	1.31	0.19	3.25	0.36
60	2.09	0.22	1.21	0.17	2.72	0.30
120	1.91	0.20	1.08	0.15	2.20	0.24
240	1.72	0.18	0.92	0.13	1.66	0.18
360	1.60	0.17	0.80	0.11	1.36	0.15

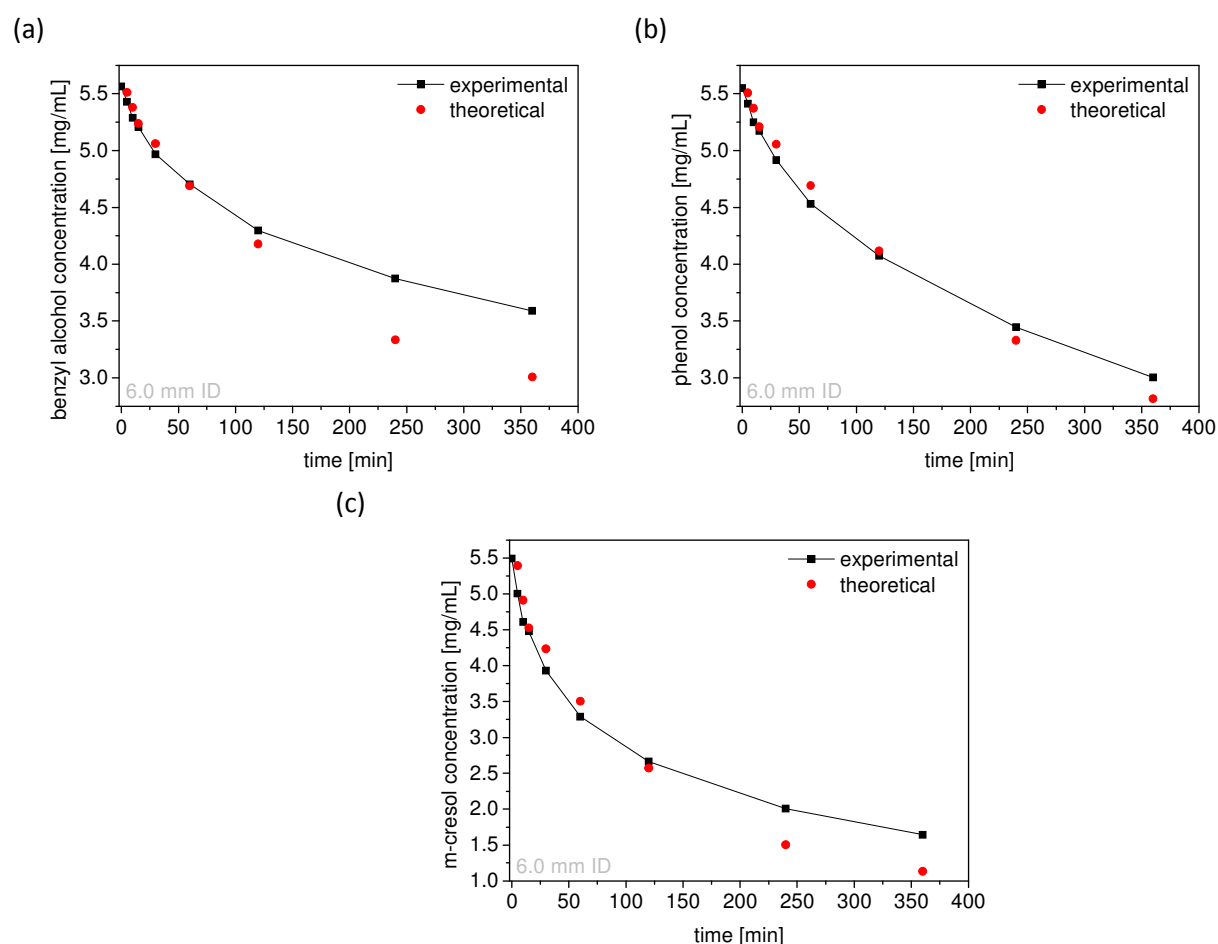


Figure VI-85: Comparison of experimental data for the preservative concentration inside the tubing lumen (ID of 6.0 mm) with theoretically determined values applying Fick's first law of diffusion. Graphs are shown for (a) benzyl alcohol, (b) phenol, and (c) m-cresol.

4 DISCUSSION

The presented data revealed substantial preservative losses inside the lumen of silicone tubing during static incubation. Although losses decreased with increasing incubation time, a plateau was not reached. This indicates that the preservative molecules do not only adsorb on the inside of the silicone tubing or accumulate inside the tubing material, but indeed permeate through the tubing wall and evaporate on the outside. The high permeability of silicone elastomer for gases is described in the commentary of the European Pharmacopoeia [1]. Colas *et al.* also stress the higher permeability of polydimethylsiloxane (PDMS) for low molecular weight species and non-polar substances in comparison to other polymers like polyethylene and polytetrafluoroethylene [13]. Wijman and Baker state that polydimethylsiloxane has long been the most permeable polymer known [14]. This property can be attributed to the low methyl-to-methyl intermolecular interactions between PDMS chains [13], and the high segmental mobility of the Si-O backbone [12,15]. Not only the nature of the polymer, but also the polymer molar mass, the extent of crosslinking, and the presence and amount of fillers [12,16,17] might affect the permeability. Fillers are supposed to reduce the free volume that is available for permeating molecules. The two tested types of silicone tubing might differ in these properties, but the manufacturer's specifications are not meaningful with that respect. However, the preservative loss in this study was independent of the exact type of silicone tubing used.

Although all three tested preservatives were phenolic compounds that in general show higher fluxes than other types of molecules [18], substantial differences in losses were observed. These variations could not be ascribed to the different incubation concentrations since the relative loss over time was shown to be concentration-independent. Bahal and Romansky also found that the actual preservative concentration did not have a significant effect on observed losses [3]. Thus, three molecular characteristics that possibly determine preservative loss were investigated, namely the partition coefficient, the diffusivity, and the evaporation half-life time. These three factors are decisive for the three steps that are involved in the overall process leading to preservative losses. A qualitative summary of the evaluation of these characteristics is provided in Table VI-42. The whole process and its contributing factors are visualized in Figure VI-86.

Table VI-42: Summary of physical processes involved in preservative loss through silicone tubing. The rank order of the values obtained for the different preservatives were evaluated as follows: +++: highest value, ++: medium value, +: lowest value.

Step	Process	Parameter	BA	phenol	m-cresol
1	Partitioning between solution and tubing matrix	Partition coefficient k	++	+	+++
2	Diffusion through tubing matrix	Diffusivity D	+(+)	+++	+
3	Evaporation at air interface on the tubing outside	Evaporation half-life time $t_{1/2}$	++	+++	+
Total	Transport through tubing wall	Loss over time	+	++	+++

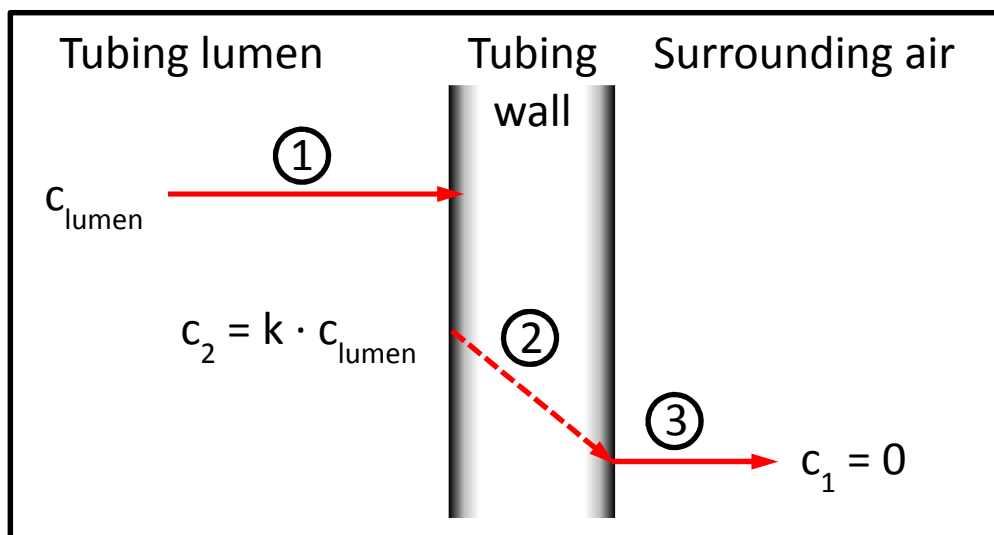


Figure VI-86: Schematic drawing of the three steps that determine preservative loss through silicone tubing. (1) Migration of molecules into the tubing material is characterized by the partition coefficient k . With $k < 1$, this leads to a drop in concentration at the solution-tubing interface. (2) The dotted line represents diffusion of the molecule through the tubing wall. The concentration at the outside of the tubing is assumed to be zero since it is in equilibrium with the surrounding sink conditions. (3) Preservative molecules evaporate from the outside of the tubing wall. c_{lumen} : concentration of the solution inside the tubing, c_2 : concentration in the tubing layer that is in direct contact with the solution, c_1 : concentration in the outermost tubing layer that is in contact with the surrounding air. Modified from Lamer *et al.* 1994 [22].

The partition coefficient describes the solubility of the preservatives inside the silicone elastomer. Interestingly, the rank order was different than expected from $\log P_{ow}$ data given in literature (Table VI-37). Not benzyl alcohol, rather phenol showed the lowest solubility in the silicone material. Most likely the additional methyl group that is present in benzyl alcohol and even fully exposed in the chemical structure of *m*-cresol enhances interactions with the polymer matrix. Apart from partition coefficients, solubility parameters can be used to describe the affinity of a substance to a “solute”. The miscibility of two materials can then be concluded from a comparison of the individual solubility parameters. Amin *et al.* studied sorption of antimicrobial agents in blow-fill-seal packs [19,20] and correlated losses of methylparaben, propylparaben, benzyl alcohol, and chlorbutol in LDPE and PP packaging with calculated solubility parameter distance values.

Diffusivities were clearly influenced by the molecular weight since the smaller molecule phenol exhibited the highest diffusivity of $3.0 \times 10^{-10} \text{ m}^2/\text{s}$. This value is comparable to diffusion coefficients of methanol and acetone in PDMS as determined by Bell *et al.* [21]. Benzyl alcohol and *m*-cresol have the same molecular weight and correspondingly comparable diffusivities were found. The minimally higher value for benzyl alcohol might be a result of a more flattened and elongated molecular structure [12]. Additionally, an inverse relation between diffusion coefficients and solubilities can be stated. As described by Lamer *et al.*, stronger interactions between solvent and solute (=higher solubility) correlate with a stronger retention of diffusing molecules by the polymer matrix (=lower diffusivity) [22]. Although it is argued that the time lag method for the determination of diffusivities may not be suitable for polymers containing fillers [16,17], results appear to be consistent with data obtained by other methods in the case of lightly filled rubbers [23]. Diffusivities are most often evaluated in a concentration-dependent manner [15,24]. However, the herein applied simplification of the model by assuming constant diffusivities seems to be a valid approach for gaining a

comprehensive picture of the underlying processes [25], especially with permeants that swell the polymer only moderately [14].

Comparing evaporation half-life times with vapor pressures reported in literature confirms the high propensity towards evaporation for phenol. The vapor pressure of phenol at 25°C is reported to be 0.35 mmHg [10], whereas literature values for m-cresol and benzyl alcohol are only 0.11 mmHg [11] and 0.094 mmHg [9], respectively. However, Lamer *et al.* suggest that desorption (or vaporization) is often not the rate-limiting step during mass transfer, with sorption and diffusion being more important in this context [22].

Indeed, when relating the markedness of the three influencing parameters with the total loss, the partition coefficient seems to be most decisive. The high losses observed with m-cresol can only arise from the high value of k since the values for the other two factors were both comparably low. Likewise, Lamer *et al.* [22] found that sorption is the mass transfer determining step during pervaporation since the concentration on the inner surface is the driving force for the flux through the membrane. Watson and Payne also stress the greater importance of solubility over that of diffusivity [25]. The studies by Bell *et al.* [21] confirm that a silicone rubber membrane indeed acts as a solubility-controlled barrier.

The importance of the partition coefficient k becomes clear when the calculated values for the flux J are compared among the three preservatives (Table VI-41). The high flux values of m-cresol mostly arise from the high partition coefficient and the subsequently high concentration on the inner side of the tubing wall. The prediction of losses for the next analysis time point based on these flux values showed quite good agreement with experimental data. Underestimation of losses during the first one to two hours might be attributed to the additional losses that occur due to ongoing partitioning of the preservative into the silicone tubing wall. A break-even point is achieved after one to two hours, depending on the type of preservative, and indicates that a steady-state is achieved. The concentration gradient across the tubing wall is fully established and no further losses due to partitioning occur since the membrane is saturated with preservative. In this phase, the diffusivity gains more importance and phenol losses start exceeding those of benzyl alcohol. The rather high divergence between theoretical and experimental data at later time points can be explained with the constant decrease of flux values that is not considered in this simple model. For the calculations, flux rates were considered constant for the time frame between two analysis time points. This discrepancy could be diminished with iterative calculations over shorter observation periods.

In summary, this simple approach assuming temporary steady state systems, equilibrium between solution and tubing inner surface as well as tubing outer surface and surrounding air, and one-directional diffusion resulted in a fair fit of experimental data. More sophisticated mathematical calculations exist and are amongst others used for the estimation of pervaporation yields [22,26,27]. During pervaporation, the herein described process is exploited on purpose for the purification of aqueous solutions from volatile substances with the help of permeable membranes like silicone rubber. All these approaches are summarized by the 'solution-diffusion model', which is based on Fick's diffusion law and reviewed in detail by Wijmans and Baker [14]. For example, Prybylski and Sloan [18] modelled flux data with the Roberts-Sloan equation. Their computations led to the conclusion that the maximum flux of substances that are present at their solubility limit only depends on the solubility in the first layers of the membrane. This again confirms our findings. Complex

mathematical formulas for all kind of different geometries and also non-steady state diffusion problems are given by Crank [28].

The criticality of preservative losses during filling line down times in biopharmaceutical drug product manufacturing can thus be assumed to be high. Especially for smaller tubing IDs that are typically employed for filling, expected losses are manifold higher due to the higher surface area to volume ratio and the often thinner tubing wall. In the present case, this adds up to a 4.9 times higher loss per mL of solution for initially comparable incubation concentrations comparing the 1.6 mm with the 6 mm ID tubing. However, pre-flushing of the tubing prior to filling might assure saturation of the tubing material with preservative and thus losses from partitioning into the polymer could be minimized. This situation is represented by the graphs in Figure VI-87 that display losses starting from 60 minutes incubation time only. 60 minutes were found to be sufficient to establish a concentration gradient across the whole tubing wall. Initial losses for tubing with an ID of 6.0 mm seem to be moderate. Therefore filling line down times of a few minutes might be acceptable. For tubing with an ID of 1.6 mm, however, a loss of 1 % is already encountered within 1.5 minutes in the case of m-cresol and after 2.4 minutes in the case of benzyl alcohol. In order to avoid products with OOS deviations arising from a reduced preservative content, the total volume inside the filling tubing would thus have to be discarded if down times exceed a critical value. A potential mean to overcome this issue are presented in the next chapter.

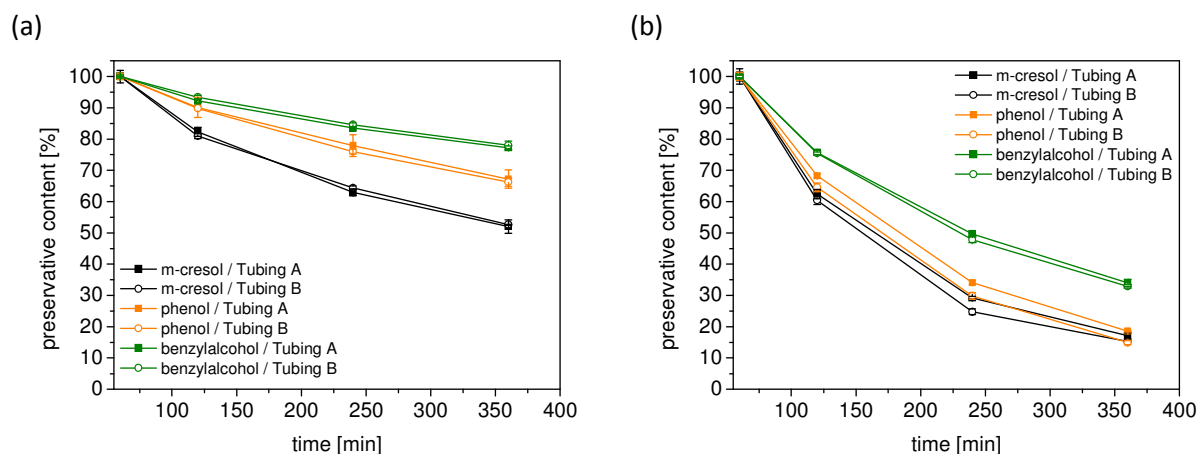


Figure VI-87: Expected loss during fill & finish for tubing with an ID of (a) 6.0 mm and (b) 1.6 mm. For this estimation, experimental data for concentrations inside the lumen at $t = 60$ min were set to 100 %.

5 SUMMARY AND CONCLUSION

The present study showed that preservative losses upon static incubation inside the lumen of silicone tubing are substantial and can be critical during filling line down times. The investigation included benzyl alcohol, phenol, and m-cresol, which are the three most commonly used preservatives in protein drugs. Losses were most pronounced with m-cresol, followed by phenol and last benzyl alcohol. In tubing with an ID of 1.6 mm, preservative concentrations were close to zero after six hours incubation time. The higher surface area to volume ratio together with the thinner tubing wall led to strongly increased losses in comparison to tubing with an ID of 6.0 mm. The type of silicone tubing as well as the starting concentration of the preservative did not influence losses. From the three physical parameters that govern the overall sorption-diffusion-desorption process, the partition coefficient was found to be most decisive. Diffusivities contributed to a reduced extent, whereas varying evaporation characteristics did not seem to have any effect. Experimental data was in good agreement with theoretically expected preservative concentrations in the lumen. Computations were based on temporary steady state systems, assuming equilibrium between solution and tubing inner surface as well as tubing outer surface and surrounding air, and one-directional diffusion following Fick's first law. In order to avoid negative effects on product quality, down times during filling of preservative-containing formulations with silicone tubing must be kept to a minimum.

6 ABBREVIATIONS

<i>A</i>	contact area per mL of solution
BA	benzyl alcohol
<i>c</i>	concentration
<i>D</i>	diffusivity
<i>d</i>	distance / thickness
<i>h</i>	height
ID	inner diameter
<i>J</i>	flux
<i>k</i>	partition coefficient
logP _{ow}	logarithm to the base of 10 of the octanol-water partition coefficient
<i>m</i>	mass
M _∞	netto mass of tubing piece used for evaporation experiments
MW	molecular weight
PDMS	polydimethylsiloxane
<i>r</i>	radius
RT	room temperature
<i>t</i>	time
OOS	out of specification

7 REFERENCES

- [1] R. Rößler, 3.1.9 Silicon-Elastomer für Verschlüsse und Schläuche, in: *Arzneibuch-Kommentar*, Wissenschaftliche Verlagsgesellschaft Stuttgart / Govi-Verlag, Pharmazeutischer Verlag GmbH, Eschborn, 2004.
- [2] S.M. Bahal, J.M. Romansky, Sorption of parabens by flexible tubings., *Pharm. Dev. Technol.* 6 (2001) 431–40.
- [3] S.M. Bahal, J.M. Romansky, Sorption of benzoic acid, sorbic acid, benzyl alcohol, and benzalkonium chloride by flexible tubing., *Pharm. Dev. Technol.* 7 (2002) 49–58.
- [4] B.K. Meyer, A. Ni, B. Hu, L. Shi, Antimicrobial preservative use in parenteral products: past and present., *J. Pharm. Sci.* 96 (2007) 3155–67.
- [5] J.R. Alford, A.C. Fowler, D.S. Wuttke, B.A. Kerwin, R.F. Latypov, J.F. Carpenter, et al., Effect of benzyl alcohol on recombinant human interleukin-1 receptor antagonist structure and hydrogen-deuterium exchange., *J. Pharm. Sci.* 100 (2011) 4215–24.
- [6] Y. Zhang, S. Roy, L.S. Jones, S. Krishnan, B.A. Kerwin, B.S. Chang, et al., Mechanism for benzyl alcohol-induced aggregation of recombinant human interleukin-1 receptor antagonist in aqueous solution., *J. Pharm. Sci.* 93 (2004) 3076–89.
- [7] R.L. Hutchings, S.M. Singh, J. Cabello-Villegas, K.M.G. Mallela, Effect of antimicrobial preservatives on partial protein unfolding and aggregation., *J. Pharm. Sci.* 102 (2013) 365–76.
- [8] B.M. Teska, J. Alarcón, R.J. Pettis, T.W. Randolph, J.F. Carpenter, Effects of Phenol and meta-Cresol Depletion on Insulin Analog Stability at Physiological Temperature., *J. Pharm. Sci.* 103 (2014) 2255–67.
- [9] National Center for Biotechnology Information, PubChem Compound Database, CID 244 (benzyl alcohol). Available online at: <http://pubchem.ncbi.nlm.nih.gov/compound/244> (accessed April 6, 2015).
- [10] National Center for Biotechnology Information, PubChem Compound Database, CID 996 (phenol). Available online at: <http://pubchem.ncbi.nlm.nih.gov/compound/996> (accessed April 6, 2015).
- [11] National Center for Biotechnology Information, PubChem Compound Database, CID 342 (m-cresol). Available online at: <http://pubchem.ncbi.nlm.nih.gov/compound/342> (accessed April 6, 2015).
- [12] S.C. George, S. Thomas, Transport phenomena through polymeric systems, *Prog. Polym. Sci.* 26 (2001) 985–1017.
- [13] A. Colas, R. Malczewski, K. Ulman, Silicone tubing for pharmaceutical processing, *PharmaChem.* (2004) 30–36.
- [14] J.G. Wijmans, R.W. Baker, The solution-diffusion model: a review, *J. Memb. Sci.* 107 (1995) 1–21.

- [15] M.S. Suwandi, S.A. Stern, Transport of heavy organic vapors through silicone rubber, *J. Polym. Sci. Part A-2 Polym. Phys.* 11 (1973) 663–681.
- [16] C.F. Most, Some filler effects on diffusion in silicone rubber, *J. Appl. Polym. Sci.* 14 (1970) 1019–1024.
- [17] D.R. Paul, D.R. Kemp, The diffusion time lag in polymer membranes containing adsorptive fillers, *J. Polym. Sci. Polym. Symp.* 41 (2007) 79–93.
- [18] J. Prybylski, K.B. Sloan, The Flux of Phenolic Compounds through Silicone Membranes., *Pharmaceutics*. 5 (2013) 434–44.
- [19] A. Amin, M. Dare, A. Sangamwar, A.K. Bansal, Interaction of antimicrobial preservatives with blow-fill-seal packs: correlating sorption with solubility parameters., *Pharm. Dev. Technol.* 17 (2012) 614–24.
- [20] A. Amin, S. Chauhan, M. Dare, A.K. Bansal, Sorption of antimicrobial agents in blow-fill-seal packs., *Pharm. Dev. Technol.* 17 (2011) 84–93.
- [21] C.M. Bell, F.J. Gerner, H. Strathmann, Selection of polymers for pervaporation membranes, *J. Memb. Sci.* 36 (1988) 315–329.
- [22] T. Lamer, M.S. Rohart, A. Voilley, H. Baussart, Influence of sorption and diffusion of aroma compounds in silicone rubber on their extraction by pervaporation, *J. Memb. Sci.* 90 (1994) 251–263.
- [23] R.M. Barrer, H.T. Chio, Solution and diffusion of gases and vapors in silicone rubber membranes, *J. Polym. Sci. Part C Polym. Symp.* 10 (2007) 111–138.
- [24] J.M. Watson, G.S. Zhang, P.A. Payne, The diffusion mechanism in silicone rubber, *J. Memb. Sci.* 73 (1992) 55–71.
- [25] J.M. Watson, P.A. Payne, A study of organic compound pervaporation through silicone rubber, *J. Memb. Sci.* 49 (1990) 171–205.
- [26] J. Sawai, N. Ito, T. Minami, M. Kikuchi, Separation of low volatile organic compounds, phenol and aniline derivatives, from aqueous solution using silicone rubber membrane, *J. Memb. Sci.* 252 (2005) 1–7.
- [27] X. Feng, R.Y.M. Huang, Separation of isopropanol from water by pervaporation using silicone-based membranes, *J. Memb. Sci.* 74 (1992) 171–181.
- [28] J. Crank, *The Mathematics of Diffusion*, 2nd ed., Oxford University Press, London, UK, 1975.

8 APPENDIX

Table VI-43: Stock solution dilutions employed for calibration curves.

Standard	Benzyl alcohol	Phenol	m-Cresol
Cal 1	1:5	1:20	1:10
Cal 2	1:10	1:40	1:20
Cal 3	1:20	1:50	1:50
Cal 4	1:50	1:100	1:100
Cal 5	1:100	1:200	1:200
Cal 6	1:200	1:500	1:500

Table VI-44: Calculation of c_2 [mg/mL] and J [g/(m²·s)] for each analysis time point and a tubing ID of 1.6 mm, based on measured preservative concentrations inside the tubing. Experimentally determined partition coefficients k and diffusivities D as presented above were used for the computations. The starting incubation concentration inside the tubing lumen was 5.5 mg/mL for all preservatives.

Analysis time point [min]	Benzyl alcohol		Phenol		m-Cresol	
	c_2	J	c_2	J	c_2	J
0	2.47	0.34	1.48	0.28	4.55	0.65
5	12.10	0.29	1.21	0.23	2.84	0.41
10	1.96	0.27	1.11	0.21	2.33	0.34
15	1.87	0.26	1.03	0.19	2.01	0.29
30	1.65	0.23	0.86	0.16	1.50	0.21
60	1.33	0.18	0.66	0.12	0.94	0.14
120	1.02	0.14	0.43	0.08	0.58	0.08
240	0.68	0.09	0.20	0.04	0.27	0.04
360	0.50	0.07	0.10	0.02	0.15	0.02

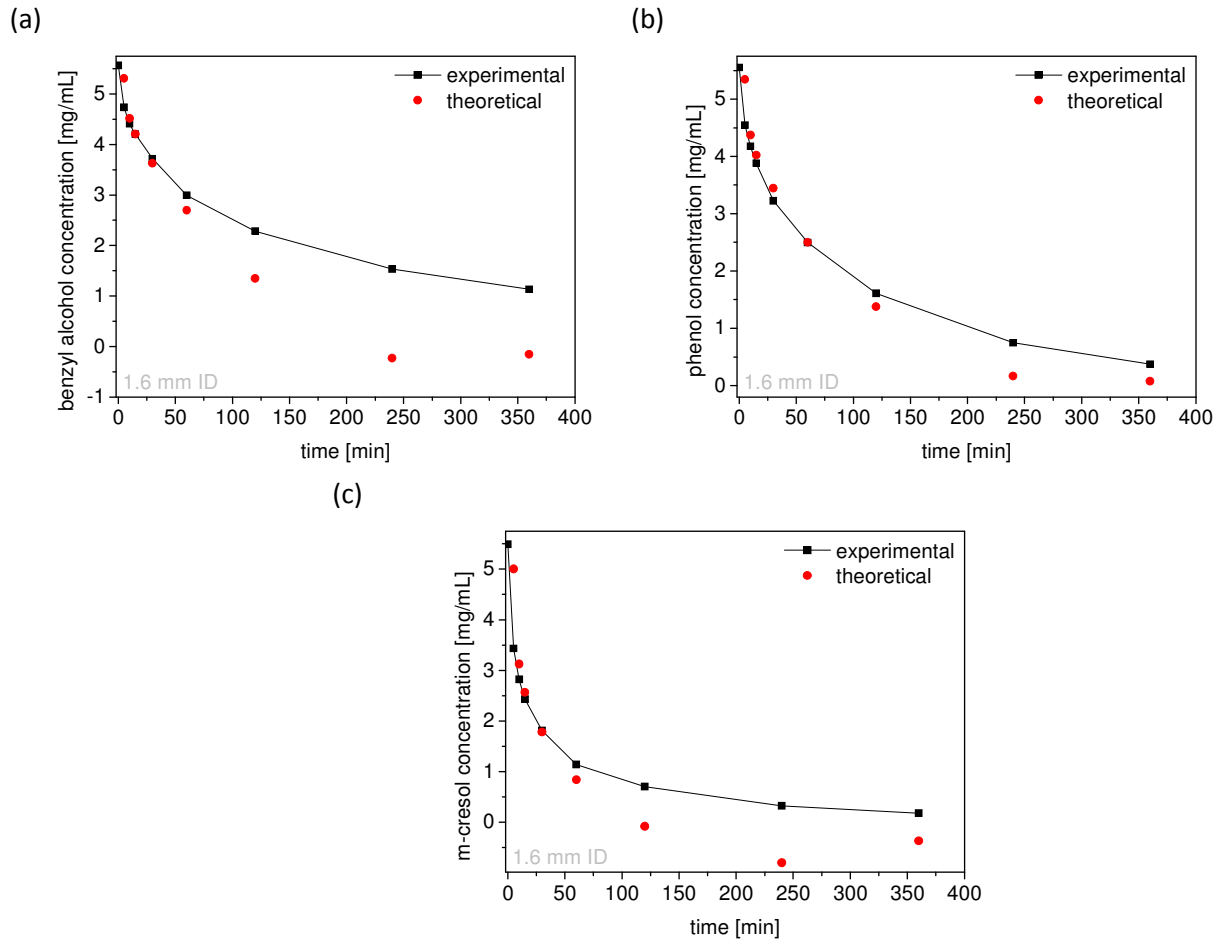


Figure VI-88: Comparison of experimental data for the preservative concentration inside the tubing lumen (ID of 1.6 mm) with theoretically determined values applying Fick's first law of diffusion. Graphs are shown for (a) benzyl alcohol, (b) phenol, and (c) m-cresol.

FLUOROPOLYMER TUBING AS AN ALTERNATIVE TO SILICONE TUBING

1 INTRODUCTION

The previous chapter highlighted the high permeability of silicone tubing for preservatives such as benzyl alcohol, phenol, and m-cresol. For filling of drug products containing preservatives, the use of alternative tubing materials with lower permeability thus needs to be evaluated. From literature, the superiority of fluoropolymer-based tubing over silicone tubing with regards to permeation characteristics is known [1–4]. The following studies are intended to extend available sorption data to the three preservatives benzyl alcohol, phenol, and m-cresol. For this purpose, the Fluidvit FPM tubing was chosen exemplarily. In contrast to most other fluoropolymer tubing, the mechanical properties of this tubing type justify not only its use as transfer tubing, but also the use in a peristaltic pump. When filling preservative-containing drug product with a peristaltic pump, disposable Fluidvit FPM tubing might thus be a suitable alternative for the commonly employed silicone tubing. In addition to permeation characteristics, the particle shedding propensity of this tubing type was evaluated via Wfl recirculation in a peristaltic pump and the previously introduced analytics [5]. Moreover, the leachable profile of the Wfl recirculates was analyzed in order to draw conclusions about the general suitability of this tubing material for filling of aqueous solutions.

2 MATERIALS AND METHODS

2.1 Materials

2.1.1 Chemicals

M-Cresol and benzyl alcohol were purchased from Merck KGaA (Darmstadt, Germany), phenol was obtained from AppliChem (Darmstadt, Germany). NaCl, Na₂HPO₄, and NaH₂PO₄ were supplied by VWR International (Darmstadt, Germany). NaOH (1 M) and HCl (1 M) were obtained from Sigma-Aldrich (Taufkirchen, Germany). Highly purified water used for buffer preparation was taken from an arium[®] pro DI Ultrapure Water System (Sartoris Stedim Biotech GmbH, Goettingen, Germany) or a USF ELGA PURELAB Plus UV/UF purification system (ELGA LabWater, Celle, Germany). Buffer filtration (volumes ≥ 500 mL) was performed with pressurized nitrogen and 0.2 μm cellulose acetate filters (47 mm ø, Sartorius Stedim Biotech GmbH).

2.1.2 Fluoropolymer Tubing

Fluidvit FPM tubing made from fluoropolymer (Viton[®]), with an ID of 6.4 mm (OD of 9.6 mm) and a hardness of 60 Shore (suitable for peristaltic pumping) was obtained from ProLiquid GmbH (Überlingen, Germany).

2.2 Methods

2.2.1 Sample Preparation

The three preservatives were dissolved in 10 mM phosphate buffer containing 145 mM NaCl at the pH and concentration stated in Table VI-38.

Table VII-45: Standard formulation and analysis parameters for the three used preservatives.

Preservative	Concentration	pH	Sampling volume	Dilution for analysis	λ_{\max}
Benzyl alcohol	10 mg/mL (= 1 %)	5	200 μL	1:5	258 nm
Phenol	5.5 mg/mL (= 0.55 %)	7	50 μL	1:20	270 nm
m-Cresol	3.15 mg/mL (= 0.315 %)	7	100 μL	1:10	272 nm

2.2.2 Sorption Experiments

40 cm long pieces of tubing were filled with 10 mL of preservative solution (n=3). Ends were clamped and the tubing pieces were incubated at RT for 5, 10, 15, 30, 60, 120, 240, and 360 minutes. Samples were withdrawn from the filled tube at every analysis time point. The exact volume of the sample aliquots is given in Table VI-38. Sample aliquots were transferred, diluted (see Table VI-38) and stored in 2R glass vials (Schott AG, Mainz, Germany) prior to analysis.

2.2.3 UV Absorption Measurements

Triplicates à 200 μL of each diluted sample as well as of each standard concentration (see Appendix, Table VI-43) and the corresponding blank buffer were transferred into a 96-well quartz well plate (Hellma Analytics, Müllheim, Germany). UV absorption was measured with a FLUOstar Omega well-

plate reader and Omega software version 1.01 (BMG Labtech GmbH, Ortenberg, Germany) after a positioning delay of 0.5 s and with 20 flashes per well in 'absorbance endpoint' mode. Absorption maxima as stated in Table VII-45 were determined from previously performed UV absorption scans in the range of 220 to 350 nm. Linear regression fit with the 'average data based on blank corrected' raw data was performed within the MARS Data Analysis Software version 1.01 (BMG Labtech).

2.2.4 Online-Turbidity Monitoring

Pumping cycles (n=2) were performed under a laminar flow cabinet to avoid external particle contamination. Tubing sets were flushed with 4 L of highly purified water and 1 L of Wfl prior to the recirculation experiment using a laboratory vacuum pump (LABOPORT, KNF Neuberger GmbH, Freiburg, Germany). Flush volumes were based on initial experiments (data not shown). The low-pressure flow-through cuvette set (HACH LANGE GmbH, Düsseldorf, Germany) as well as the outer surfaces of the ends of the tubing set were rinsed with highly purified water and Wfl until the rinsing fluid was visually free from particles. Online-turbidity monitoring was performed with 250 mL of Wfl in recirculation over 24 h with the setup described in [5]. The operation parameters of the Flexicon PD12 peristaltic pump (Watson-Marlow Flexicon, Ringsted, Denmark) were based on previous experiments (data not shown) and set as follows: dispensing mode, 180 rpm, acceleration of 60, starting filling volume of 5.0 mL. Online-turbidity monitoring was carried out with a HACH 2100AN turbidimeter connected to a computer using HachLink 2000 V.2.9 alpha software. The operation mode of the turbidimeter included activated ratio function, auto range function, and signal averaging (n=15). Data points were collected every 60 seconds. Turbidimeter functionality was confirmed with turbidity standards (< 0.15 NTU stray light standard, 0-2 / 0-20 / 0-200 / 0-2000 NTU Gelex Secondary Standards from HACH; max. deviation of $\pm 5\%$ in comparison to precedent measurement) prior to every experiment.

2.2.5 Determination of Pump Rate

A stop watch and a 250 mL measuring cylinder were used to determine the pump rate of each tubing set for approx. 10 seconds before and after the 24 h pumping cycle (n=5).

2.2.6 Dynamic Light Scattering (DLS)

Particle characterization in the nanometer range was performed by dynamic light scattering using the Zetasizer Nano-ZS (Malvern Instruments Ltd., Herrenberg, Germany). The undiluted, neither filtered nor centrifuged samples were measured in disposable Plastibrand semi-micro PMMA cuvettes (Brand GmbH, Wertheim, Germany) at a backward scatter of 173° after 20 seconds equilibration time at 25°C and with water as dispersant. Positioning, attenuation selection and measurement duration as well as number of sub runs for the three performed measurements per sample were optimized automatically for each run by the Zetasizer Software 6.32. Z-average and polydispersity index (PDI) were calculated applying the 'General purpose (normal resolution)' analysis model.

2.2.7 Light Obscuration (LO)

The final recirculate was analyzed for particles in the micrometer range by light obscuration (in analogy to USP 788 and Ph Eur 2.9.19 requirements) with a SVSS-C instrument (PAMAS, Partikelmess- und Analysesysteme GmbH, Rutesheim, Germany) within three days after the pumping cycle. After a pre-run volume of 0.5 mL, each sample was analyzed in triplicates of 0.3 mL at a filling and emptying

rate of 10 mL/min. Size channels from 1 to 60 μm were auto-scaled logarithmically. Before each run, the system was rinsed with at least 5 mL of highly purified water. Data was collected using PAMAS PMA Program V 2.1.2.0.

2.2.8 3D Laser Scanning Microscopy

Surface roughness of inner tubing walls was visualized using the 3D laser scanning microscope Keyence VK-X210 with a CF Plan 20x objective (Keyence GmbH, Neu-Isenburg, Germany). Using a scalpel, tubing pieces were cut into thin strips and placed under the microscope with horizontal flow direction. For every sample micrographs were captured with VK Viewer software in 'Easy Mode' from eight different sections. The roughness parameters arithmetic mean roughness R_a and maximum height R_z were calculated according to the JIS standard B0601:2001 in the multi-line roughness mode with VK Analyzer Plus software version 3.3.0.0 from an average of $2n+1$ horizontal lines with $n=30$ and 10 skipped lines in-between. Tubing curvature was corrected via the 'correct tilt – sec curved surf. (auto)' function. Cutoff values of $\lambda_c = 2.5 \text{ mm}$ and $\lambda_s = 8 \mu\text{m}$ were applied.

2.2.9 Leachable Analytics via GC-MS

After stir bar sorptive extraction ("Twister", Gerstel GmbH & Co. KG, Mülheim an der Ruhr, Germany) for 60 minutes at 800 rpm, leachable analysis after thermal desorption (Gerstel TDS 3) was carried out on an Agilent 6890 gas chromatograph equipped with a DB-1MS column (J&W Scientific, Folsom, CA, USA). An Agilent 5975 mass spectrometer was used as detector (Agilent Technologies GmbH, Boeblingen, Germany). For quantification purposes, the two reference substances tetrahydrofurfuryl methacrylate and di-pentyl-phthalate were used as internal standards.

3 RESULTS

3.1 Preservative Loss during Static Incubation

Preservative losses could not be identified for any of the three preservatives during static incubation for up to 6 hours (see Table VII-46). Apart from minor variations, preservative concentrations inside the tubing lumen remained constant.

Table VII-46: Preservative content for the different sampling time points. Results are stated as mean values with standard deviations (n=3, except *: n=2).

Time [min]	5	10	15	30	60	120	240	360
Benzyl alcohol	101.9 ± 1.7	102.6 ± 1.2	102.3 ± 2.8	101.5 ± 0.8	100.6 ± 1.8	100.1 ± 2.2	99.9 ± 1.2	100.9 ± 1.1
m-Cresol	99.9 ± 1.8	98.0 ± 3.9*	101.3 ± 5.6	100.1 ± 2.8	94.2 ± 2.0	99.2 ± 2.5	94.0 ± 2.2	99.8 ± 0.8*
Phenol	101.5 ± 0.5*	98.3 ± 3.7	100.7 ± 3.1	100.2 ± 3.3*	102.1 ± 2.8	100.4 ± 2.7	102.1 ± 2.9	101.6 ± 3.3

3.2 Online-turbidity monitoring

Online monitoring of the turbidity of Wfl recirculated with two sets of fluoropolymer tubing resulted in rather identical curves (see Figure VII-89). After an initial, sharp increase in turbidity values up to 0.4 and 0.5 NTU, respectively, turbidity values remained at that level for the rest of the experiment.

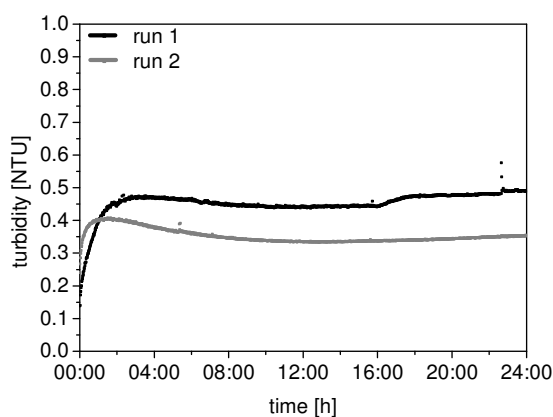


Figure VII-89: Online-turbidity monitoring of Wfl recirculated through fluoropolymer tubing.

3.3 Particle characterization

The two recirculates were characterized for particles in the nanometer range using DLS. Z-Average as well as Pdl values obtained for both recirculates differed substantially and showed high variability (see Table VII-47). This can be attributed to the multimodal size distribution (see Figure VII-90a) and the rather low count rates (on average below 100 kcps). Three distinct particle fractions at around 100 nm, 400-500 nm and 5560 nm were detected. LO particle counts were around 2000 particles $\geq 1 \mu\text{m/mL}$, with hardly any particles being bigger than $10 \mu\text{m}$. Most of the micrometer-sized particles were in the size range between 1 and $2 \mu\text{m}$ (Figure VII-90b). Table VII-52 in the Appendix lists particle counts for size bins of $\geq 2/5/10/25 \mu\text{m}$.

Table VII-47: Characteristics of particles in the Wfl recirculates determined by DLS (Z-average and Pdl) and LO (particle counts $\geq 1 \mu\text{m}$). Results are stated as mean values with standard deviations ($n=3$).

Sample	Z-Average [nm]	Pdl	Particle counts $\geq 1 \mu\text{m}$ (#/mL)
Recirculate 1	489.2 ± 221.5	0.737 ± 0.238	2421 ± 51
Recirculate 2	282.5 ± 129.0	0.575 ± 0.201	2043 ± 54

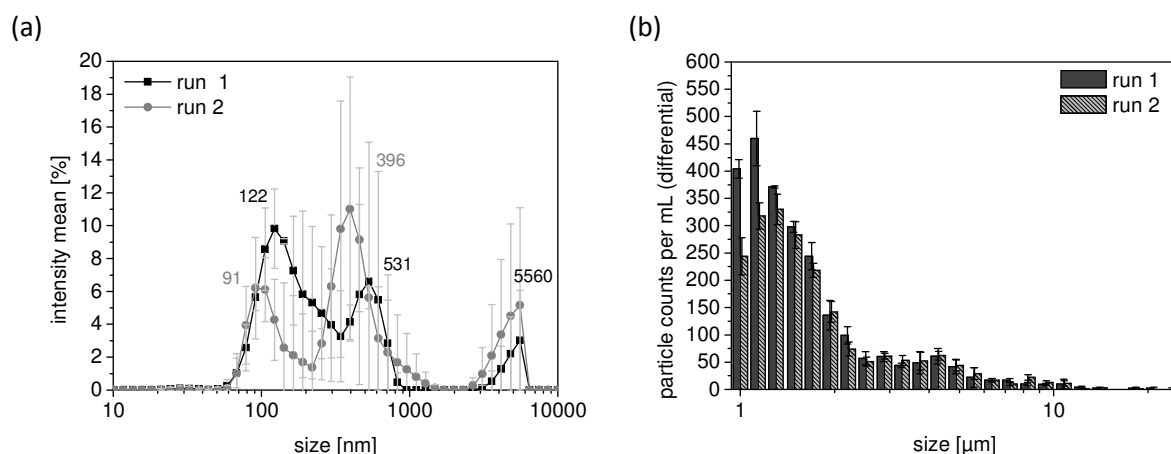


Figure VII-90: Particle size distributions of Wfl recirculates obtained from (a) DLS and (b) LO analysis.

3.4 Tubing wear

Flow rates during continuous pumping were determined as a measure for the deformation of the tubing lumen. After the 24 h pumping cycle, flow rates for both tested tubing sets were decreased by 3 to 4% (see Table VII-48).

Table VII-48: Flow rates in mL/s determined for the two tubing sets before and after the 24 h pumping cycle.

Sample	Before pumping cycle	After pumping cycle	Decrease by
Run 1	24.6 ± 0.2	23.7 ± 0.1	3.9 %
Run 2	23.8 ± 0.1	23.0 ± 0.1	3.4 %

Additionally, surface morphology of the inner tubing wall was examined using 3D laser scanning microscopy. The results in Table VII-49 do not reveal any changes in morphology for areas that were located within the pump head during pumping. In any case, the tubing surface appeared rather rough and irregularly structured. Roughness values of sections outside and within the pump head were identical.

3.5 Leachable Analytcs

Various leachables were found in concentrations below the reporting threshold of 0.05 ppm by GC-MS analytics (Table VII-50). Only acetophenone, benzothiazole, and 2,4-bis(1,1-dimethylethyl)-phenol were detected in both recirculates. Toluene, 2-(2-butoxyethoxy)ethyl acetate, and an unknown substance were present in only one of the two analyzed recirculates. In Table VII-53 in the Appendix, leachable results of Wfl recirculates obtained with two different silicone tubing types as pump tubing (Versilic and Dow APT) are shown for comparison.

Table VII-49: 3D laser scanning micrographs and roughness values of sections of fluoropolymer tubing that were placed outside and within the pump head during the pumping cycle. Roughness values are given as mean values with standard deviations (n=8).

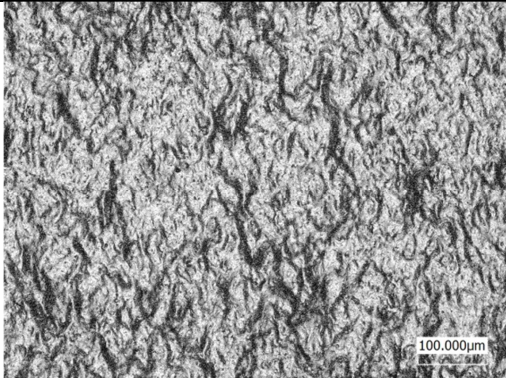
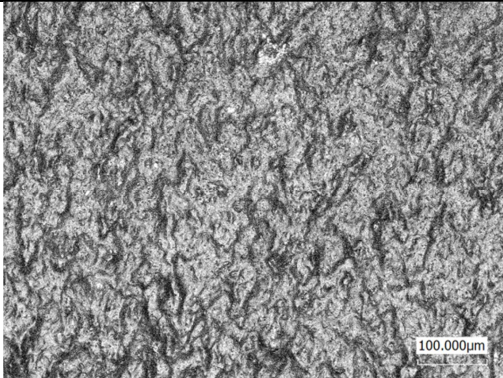
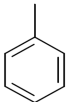
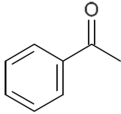
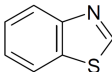
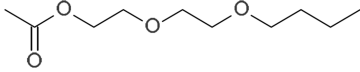
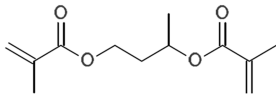
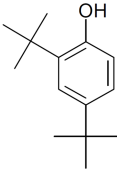
Roughness parameter	Outside pump head	Within pump head
Morphology		
Rz [µm]	13.7 ± 1.3	13.5 ± 0.7
Ra [µm]	2.4 ± 0.3	2.3 ± 0.2

Table VII-50: Results from leachable analytics via GC-MS for the two obtained recirculates. Concentrations state a potential increase in comparison to the Wfl blank.

Structure	Compound Name	Estimated concentration (in µg/g or ppm)	
		Recirculate 1	Recirculate 2
	Toluene	Not detected	< 0.05 (0.009)
	Acetophenone	< 0.05 (0.004)	< 0.05 (0.003)
	Benzothiazole	< 0.05 (0.007)	< 0.05 (0.006)
	2-(2-butoxyethoxy)ethyl acetate	< 0.05 (0.027)	Not detected
Unknown, presumably similar to 	Unknown, presumably similar to 1,3-butylene glycol dimethacrylate	< 0.05 (0.025)	Not detected
	2,4-bis(1,1-dimethylethyl)-phenol	< 0.05 (0.007)	< 0.05 (0.009)

4 DISCUSSION

The peristaltic fluoropolymer tubing tested in this study showed high resistance to preservative pervaporation. Even after six hours of static incubation with the three preservatives benzyl alcohol, phenol, and m-cresol, no losses in concentration were observed. As suggested by Bahal and Romansky [3,4,6], flexible fluoropolymer tubing might thus be the tubing of choice for filling preservative-containing drug products. The earlier studies of Bahal and Romansky were conducted with methylparaben and propylparaben as well as benzyl alcohol, sorbic acid, and benzoic acid and various types of fluoropolymer-based tubing. Tested tubing resins included fluorinated ethylene propylene (Teflon® FEP), Viton® fluoro-elastomer synthetic rubber, perfluoroalkoxy (Teflon® PFA), polytetrafluoro-ethylene (Teflon® NXT), and FEP laminated polyvinylchloride (Tygon® SE-200). All of these tubings showed good permeability characteristics. However, many Teflon® tubings are not as flexible as silicone tubing which is commonly used for peristaltic pumping. Therefore laminated tubing or the Fluidvit FPM tubing tested in this study is a promising alternative. Fluidvit FPM tubing is made from the same material as Viton® tubing from DuPont and characterized by extraordinary high chemical resistance against hydrocarbons, oil, strong acids, oxidation media, as well as aromatic and chlorinated solvents. The employed tubing was colored black, but can be obtained in FDA quality as well [7].

Advantages and drawbacks of PTFE tubing in comparison to silicone tubing were addressed by Colas *et al.* [1]. Apart from the reduced permeability and likewise reduced flexibility, PTFE tubing is claimed to show low spallation. As shown in Chapter IV, particle shedding is another important aspect that needs to be considered during tubing evaluation. Online-turbidity monitoring revealed a minor turbidity increase during the first hour of recirculation only. This indicates that particle shedding occurs to a very reduced extent since an increase in turbidity was found to be a reliable indicator for ongoing particle shedding [5]. The turbidity endpoint value for Fluidvit FPM tubing was less than 0.5 NTU and thus below the turbidity endpoint value obtained for the silicone tubing showing lowest spallation propensity (up to 1.6 NTU, comparable ID of 6.0 mm). The number of micrometer-sized particles in the recirculates was low, but similar to particle counts found for silicone tubing recirculates. The particle size distribution as obtained with LO was comparable for Fluidvit and silicone recirculates, with hardly any particles above 10 µm and a size distribution maximum between 1 and 2 µm. However, the size distribution in the nanometer range differed. Instead of only one pronounced peak at around 200 nm, two peaks with rather weak signal intensities were identified. LO and DLS results thus also point towards low spallation propensity of the fluoropolymer tubing. This observation was confirmed by surface roughness data. Despite a rather rough surface, hardly any changes in surface morphology occurred during pumping. In addition to the earlier identified parameter surface roughness, the identity of the material itself is thus a determining factor for particle shedding. The decrease in flow rate that arises from tubing deformation during pumping [1], was within the ranges determined for silicone tubing. Other types of fluoropolymer tubing for which low particle spallation propensity is claimed in literature are Chem-Sure®, a composite of PTFE and a fluoroelastomer, and Sta-Pure®, a composite of expanded PTFE and silicone [2].

The leachables profile of the Wfl recirculates seems promising due to the limited number of compounds that were found and the very low concentrations of these leachables. Although the number of leachables found in silicone tubing recirculates was even less, these differences are not considered relevant since leachable levels were below the reporting level in any case. All tested

tubing types are therefore judged to be equally suited for pumping aqueous solutions in terms of generated leachables. However, as stated by Jenke *et al.* [8], the level of leachables extracted from tubing materials under flow conditions can be assumed to be far below the total amount of leachables present in the tubing. The compound 2,4-bis(1,1-dimethylethyl)-phenol, also known as 2,4-di-*t*-butylphenol, was also found in ethanol and water extracts of Santoprene tubings [8] and in leachable studies with a single-use bag [9]. This compound is a known degradation product of polyolefines that is generated during sterilization with γ -irradiation [10]. Evaluating the origin of the found leachables is only feasible with detailed information on the qualitative composition of the tubing material. Unfortunately, this information is typically proprietary and therefore not accessible.

5 SUMMARY AND CONCLUSION

The superiority of fluoropolymer tubing over silicone tubing with regards to preservative sorption was shown exemplarily with the tubing type Fluidvit FPM. Additionally, low particle shedding propensity as well as a promising leachables profile were identified as benefits of this fluoropolymer tubing type. Fluoropolymer tubing can therefore be highly recommended for filling of preservative-containing formulations. A general replacement of silicone tubing by fluoropolymer tubing might be counteracted by associated higher material costs. Possible interactions with a fluoropolymer tubing candidate might be formulation specific and need to be addressed on a case by case basis.

6 ABBREVIATIONS

DLS	dynamic light scattering
FDA	food and drug Administration (US)
FEP	fluorinated ethylene propylene
ID	inner diameter
LO	light obscuration
NTU	nephelometric turbidity units
PdI	polydispersity index
PTFE	polytetrafluoroethylene
R _a	arithmetic mean roughness
RT	room temperature
R _z	maximum height
OD	outer diameter
ppm	parts per million
Wfi	water for injection
λ_{\max}	wavelength of adsorption maximum

7 REFERENCES

- [1] A. Colas, R. Malczewski, K. Ulman, Silicone tubing for pharmaceutical processing, *PharmaChem.* (2004) 30–36.
- [2] S.M. Bahal, J.M. Romansky, Spalling and sorption of tubing for peristaltic pumps., *Pharm. Dev. Technol.* 7 (2002) 317–23.
- [3] S.M. Bahal, J.M. Romansky, Sorption of parabens by flexible tubings., *Pharm. Dev. Technol.* 6 (2001) 431–40.
- [4] S.M. Bahal, J.M. Romansky, Sorption of parabens by fluoropolymer or fluoropolymer laminated flexible tubing., *PDA J. Pharm. Sci. Technol.* 55 417–21.
- [5] V. Saller, J. Matilainen, U. Grauschopf, K. Bechtold-Peters, H.-C. Mahler, W. Friess, Particle shedding from peristaltic pump tubing in biopharmaceutical drug product manufacturing., *J. Pharm. Sci.* 104 (2015) 1440–50.
- [6] S.M. Bahal, J.M. Romansky, Sorption of benzoic acid, sorbic acid, benzyl alcohol, and benzalkonium chloride by flexible tubing., *Pharm. Dev. Technol.* 7 (2002) 49–58.
- [7] Liquid-scan GmbH & Co.KG, Technisches Datenblatt Fluidvit FPM-Schläuche, (2012).
- [8] D.R. Jenke, J. Story, R. Lalani, Extractables/leachables from plastic tubing used in product manufacturing., *Int. J. Pharm.* 315 (2006) 75–92.
- [9] T. Weitbrecht, G. Kallmeyer, U. Klotz, T. Posset, A. Mang, Einsatz von Disposables in der Pharma-Parenteralia-Produktion, *Pharmind.* 75 (2013) 1810–1823.
- [10] P.G. Demertzis, R. Franz, F. Welle, The effects of γ -irradiation on compositional changes in plastic packaging films, *Packag. Technol. Sci.* 12 (1999) 119–130.

8 APPENDIX

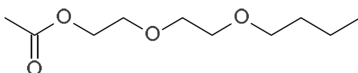
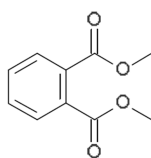
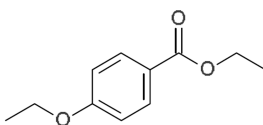
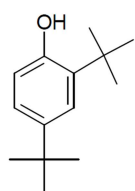
Table VII-51: Stock solution dilutions employed for calibration curves.

Standard	Benzyl alcohol	Phenol	m-Cresol
Cal 1	1:5	1:20	1:10
Cal 2	1:10	1:40	1:20
Cal 3	1:20	1:50	1:50
Cal 4	1:50	1:100	1:100
Cal 5	1:100	1:200	1:200
Cal 6	1:200	1:500	1:500

Table VII-52: LO particle counts for the two Fluidvit FPM / Wfl recirculates classified by size bins.

Sample	Particle counts / mL			
	$\geq 2 \mu\text{m}$	$\geq 5 \mu\text{m}$	$\geq 10 \mu\text{m}$	$\geq 25 \mu\text{m}$
Recirculate 1	643	138	30	0
Recirculate 2	650	153	31	1

Table VII-53: Results from leachable analytics via GC-MS for Wfl recirculates obtained with Versilic silicone tubing and a tubing set consisting of Dow APT silicone tubing in the pump head area and C-Flex tubing as transfer tubing. Concentrations state a potential increase in comparison to the Wfl blank.

Structure	Compound Name	Estimated concentration (in $\mu\text{g/g}$ or ppm)	
		Versilic recirculate	Dow APT / C-Flex recirculate
	2-(2-butoxyethoxy)ethyl acetate	Not detected	< 0.05 (0.010)
	Dimethyl phthalate	Not detected	< 0.05 (0.003)
	Ethyl-4-ethoxybenzoate	Not detected	< 0.05 (0.008)
	2,4-di-tert-butylphenol	Not detected	< 0.05 (0.010)

CHAPTER VIII

FINAL SUMMARY & OUTLOOK

As described in **Chapter I**, it was the aim of this thesis to extend current knowledge around the characteristics of disposables used for biopharmaceutical drug product (DP) manufacturing such as single-use bioprocess bags and silicone tubings for peristaltic pumping and the potential interactions of these disposables with the drug product itself. During the course of the presented studies, different types of analytical methods were tested and implemented in order to obtain information about protein adsorption phenomena, particle shedding, and sorption events.

In **Chapter II**, single-use bioprocess bags with ethylene-vinyl acetate (EVA) and ultra-low density polyethylene (ULDPE) contact layers were characterized using surface analytical techniques like laser and IR microscopy, zeta-potential / streaming potential measurements, and contact angle measurements. The impact of the different polarities and morphologies of the two surfaces on the adsorbed amount and the adsorption kinetics of an IgG1 antibody was assessed via detergent based desorption and subsequent SEC quantification. The suitability of the desorption method was demonstrated by the rather faint coloration of desorbed surfaces after gold staining. On EVA the adsorption maximum of 4 mg/m² at pH 6 was increased to 5 mg/m² when increasing the ionic strength via the addition of sodium chloride from 50 mM to 100 mM. Varying pH value and ionic strength did not affect adsorbed amounts on the ULDPE surface, which were around 3 mg/m². Modelling of adsorption isotherms with the Langmuir-Freundlich equation led to the conclusion that the affinity of IgG molecules for the nonpolar ULDPE surface was higher than for the more polar EVA material. This led also to faster surface saturation upon incubation with IgG. Experiments with fluorescently labelled IgG molecules proved the ongoing exchange of adsorbed molecules and molecules in the bulk after surface saturation.

With the quartz crystal microbalance (QCM) studies described in **Chapter III**, kinetic insights into adsorption events *in situ* were gained. EVA and PE model surfaces were prepared by dissolution of the polymers in tetrahydrofuran under moderate heating and subsequent spin-coating onto QCM sensor chips. The time dependent frequency (Δf) and damping shifts ($\Delta \Gamma$) during IgG adsorption to the coated QCM sensor surface were evaluated with regards to adsorbed amounts and viscoelastic properties of the adsorbed layer. Under most of the studied conditions and independent of the investigated surface, the adsorption process consisted of three distinct phases. The initial phase was characterized by the rigid attachment of protein molecules due to electrostatic interactions with the sensor surface. During a second phase, more molecules attached rather loosely. The final step was characterized by the rigidification of already adsorbed molecules and / or rigid attachment of additional IgG molecules. The $\Delta \Gamma / \Delta f$ ratio at the end of the adsorption process indicated that the adsorbed IgG layer in most cases except at pH 2 was rather rigid in nature. Therefore, the application of the Sauerbrey equation for transforming frequency shifts into adsorbed amounts was considered valid. The discrepancy in adsorbed amounts determined either via surfactant desorption and SEC or via QCM highlights the impact of deviating surface characteristics. Despite chemical equivalence, the

employed spin-coated model surfaces cannot fully reflect real bag surfaces during adsorption studies. An adaption of the coating process via the inclusion of an annealing step after spin-coating [1] might be beneficial. The effect of this measure especially on surface polarity should be monitored with contact angle measurements [2]. In addition to experiments with varying pH and ionic strength values, it was evaluated how non-ionic surfactants (polysorbate 20 and 80, poloxamer 188) affect adsorption. Surfactants were found to suppress protein adsorption effectively only when present during the IgG adsorption step itself.

Overall, the actual loss in IgG concentration in the bulk due to protein adsorption to bioprocess bag surfaces was found to be negligible, especially with higher concentrated bulk drug substance such as > 10 mg/mL (loss \leq 0.1 % even at 25 % filling of small-volume bags). Since potential immunogenic effects arising from an alteration of the protein structure during adsorption and the anticipated exchange with native molecules from the bulk are discussed [3–5], further studies on protein adsorption should focus on these structural aspects.

The second part of this thesis focused on particle shedding from silicone tubing during operation in a peristaltic pump. In **Chapter IV**, the mechanical stress within the pump head was identified as the root cause for particle abrasion due to morphological changes of the inner tubing surface. With 3D laser scanning microscopy, it could be visualized how the relatively rough silicone surface structure becomes smoothed during the course of the pumping cycles. Varying surface roughness between different types of silicone tubing was the determining factor for the extent of particle shedding. The extent of particle shedding was evaluated by online-turbidity monitoring and particle counting methods like light obscuration (LO), micro-flow imaging (MFI) and nanoparticle tracking analysis (NTA). With dynamic light scattering (DLS), the main fraction of shed particles was measured to be 200 nm in size. With MFI, the morphology of the micrometer sized particles was identified as silicone oil-like. Investigations did not only include different silicone tubing types, but also two different tubing inner diameter and furthermore, batch-to-batch variations were considered.

Since the pumping step for dosing is performed after sterile filtration during fill & finish of a biopharmaceutical DP, particles shed from peristaltic tubing directly end up in filled DP units. The possible impact of such particles on DP stability was assessed in **Chapter V**. Shed particles were accumulated in a limited volume by pumping placebo buffer in circulation. Particles were then spiked into two formulated IgG molecules at two relevant, but worst-case particle levels. Sample aliquots in glass vials were put on accelerated stability for up to 6 months at 2–8°C, 25°, and 40°C. Stability was monitored with SEC, LO, turbidity, MFI and visual inspection. The presence of shed particles did not alter observed IgG fragmentation and aggregation events. Particle count increases as observed with MFI in samples containing shed particles could be attributed mainly to the colloidal instability of the silicone particles and not to the formation of proteinaceous particles. A negative effect of shed silicone particles at expected concentrations on IgG stability in the final DP is thus not considered to be of concern.

From these studies it is assumed that particle shedding from peristaltic silicone tubing is not critical with regards to DP stability. Since particle levels in the final DP should be minimized, it is nevertheless recommended to use low-abrasive silicone tubing during fill & finish. Low-abrasive tubing is characterized by low surface roughness values and can easily be identified with 3D laser scanning microscopy.

Silicone tubing might also impact the quality of the final DP due to its high permeability for volatile excipients like preservatives. In **Chapter VI**, the concentration loss of the three preservatives m-cresol, phenol, and benzyl alcohol during static incubation in silicone tubing was investigated. The propensity of the three preservatives towards partitioning, diffusion, and subsequent desorption from the silicone polymer was evaluated via the analytical determination of partitioning, diffusion, and evaporation constants. The degree of partitioning from solution into the silicone polymer was identified as the most decisive parameter for the extent of preservative loss. Since silicone tubing is an integral part of typical fill & finish setups irrespective of the dosing technology, significant preservative losses might be encountered during filling of a preservative-containing DP especially with tubing of small inner diameter.

A possible solution to overcome this issue is presented in **Chapter VII**. A type of flexible fluoropolymer tubing that is equally suited for operation in a peristaltic pump was analyzed for its sorption as well as particle shedding behavior. The performance of the tested fluoropolymer tubing with regards to these properties and also in terms of potential leachables was promising. Further investigations should include the actual performance of this type of tubing on peristaltic filling lines.

The flexibility and cost-effectiveness that is inherent to disposables will definitely promote their further use for the small- to medium-scale production of DP, e.g. for clinical phases [6–9]. Due to size limitations of single-use bags [7] and bioreactors, it is questionable whether disposables will likewise capture commercial production sites for drug product and drug substance, respectively [10]. In any case, it is assumed that disposables will form integral parts of hybrid manufacturing units. The herein described phenomena of protein adsorption, particle shedding, and sorption are not considered to put any constraints on the future use of disposables since the effects of these phenomena are either minimal or controllable by choosing appropriate material. For the realization of fully disposable production sites, investigations should be likewise extended to other single-use equipment like disposable fillers and connectors.

ABBREVIATIONS

DLS	Dynamic Light Scattering
DP	drug product
Δf	damping shift
EVA	ethylene-vinyl acetate
Δf	frequency shift
LO	Light Obscuration
MFI	Micro-Flow Imaging
NTA	Nanoparticle Tracking Analysis
PE	polyethylene
QCM	Quartz Crystal Microbalance
SDS	sodium dodecyl sulfate
SEC	Size Exclusion Chromatography
ULDPE	ultra-low density polyethylene

REFERENCES

- [1] J. Vörös, The density and refractive index of adsorbing protein layers., *Biophys. J.* 87 (2004) 553–61.
- [2] S.J. Kapp, I. Larsson, M. Van De Weert, M. Cárdenas, L. Jorgensen, Competitive adsorption of monoclonal antibodies and nonionic surfactants at solid hydrophobic surfaces., *J. Pharm. Sci.* 104 (2015) 593–601.
- [3] M. Wahlgren, Protein adsorption to solid surfaces, *Trends Biotechnol.* 9 (1991) 201–208.
- [4] W. Norde, C.A. Haynes, Reversibility and the Mechanism of Protein Adsorption, in: T.A. Horbett, J.L. Brash (Eds.), *Proteins at Interfaces II - Fundamentals and Applications*, American Chemical Society, Washington, DC, 1995: pp. 26–40.
- [5] F. Felsovalyi, P. Mangiagalli, C. Bureau, S.K. Kumar, S. Banta, Reversibility of the adsorption of lysozyme on silica, *Langmuir.* 27 (2011) 11873–82.
- [6] P. Krämer, R. Müller, Single-Use-/Disposables-Prozesskomponenten: Eine Technologiealternative. Teil 1: Technologische Einsatzgrenzen aus bioverfahrenstechnischer Sicht, *Pharm. Ind.* 74 (2012) 323–327.
- [7] C. Mintz, Single-Use, Disposable Products: A “State of the Industry” Update, *Life Sci. Lead.* (July 2009).
- [8] T. Kapp, J. Boehm, J. Chase, J. Craig, K. Davis, V. Gupta, et al., Road Map to Implementation of Single-Use Systems, *Bioprocess Int.* 8 (2010) Supplement 10–19.
- [9] M. Jornitz, T. Paust, The Evolution of Single-Use Technologies in Aseptic Processing, *Pharm. Technol.* 34 (2010). Available online at: <http://www.pharmtech.com/evolution-single-use-technologies-aseptic-processing> (accessed May 9, 2015).
- [10] B. Lee, E. Langer, R. Zheng, Next-Generation Single-Use Bioreactor Technology and the Future of Biomanufacturing: A Summary from the Manufacturer’s and User’s Perspective, in: R. Eibl, D. Eibl (Eds.), *Single-Use Technology in Biopharmaceutical Manufacture*, John Wiley & Sons, Inc., Hoboken, New Jersey, USA, 2011: pp. 184–195.